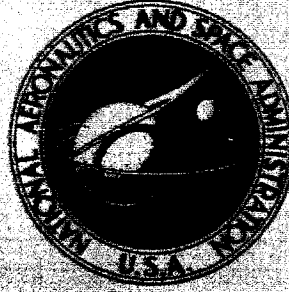


**NASA CONTRACTOR
REPORT**



NASA CR-535

NASA CR-535

GPO PRICE \$ _____

CFSTI PRICE(S) \$ 5.00

Hard copy (HC) _____

Microfiche (MF) 1.25

553 July 65

N66 36106

(ACCESSION NUMBER)

(THRU)

199

(PAGES)

1

(CODE)

CR-535

(NASA CR OR TRX OR AD NUMBER)

33

(CATEGORY)

**ANALYSIS OF HYPERSONIC PRESSURE
AND HEAT TRANSFER TESTS
ON DELTA WINGS WITH LAMINAR
AND TURBULENT BOUNDARY LAYERS**

by A. L. Nagel, H. D. Fitzsimmons, and L. B. Doyle

Prepared by

THE BOEING COMPANY

Seattle, Wash.

for Langley Research Center

ANALYSIS OF HYPERSONIC PRESSURE AND HEAT TRANSFER
TESTS ON DELTA WINGS WITH LAMINAR
AND TURBULENT BOUNDARY LAYERS

By A. L. Nagel, H. D. Fitzsimmons, and L. B. Doyle

Distribution of this report is provided in the interest of information exchange. Responsibility for the contents resides in the author or organization that prepared it.

Prepared under Contract No. NAS 1-4301 by
THE BOEING COMPANY
Seattle, Wash.

for Langley Research Center

NATIONAL AERONAUTICS AND SPACE ADMINISTRATION

For sale by the Clearinghouse for Federal Scientific and Technical Information
Springfield, Virginia 22151 - Price \$5.00

PREFACE

This is one of three final reports on a program to complete the analysis of existing aerothermodynamic test data obtained during the X-20 program. The work has been accomplished by The Boeing Company under Contract NAS 1-4301 with NASA, Langley Research Center, Hampton, Virginia. A. L. Nagel was the program manager, H. L. Giles was the principal investigator, and M. H. Bertram was the NASA contract monitor. Final reports have been prepared for each of three tasks:

- Task I - Analysis of Hypersonic Pressure and Heat Transfer Tests on Delta Wings with Laminar and Turbulent Boundary Layers.
- Task II - Analysis of Hypersonic Pressure and Heat Transfer Tests on a Flat Plate with a Flap and a Delta Wing with a Body, Elevons, Fins, and Rudders.
- Task III - Analysis of Pressure and Heat Transfer Tests on Surface Roughness Elements with Laminar and Turbulent Boundary Layers.

Results of Task I are presented in this report.

CONTENTS

	<u>Page</u>
SUMMARY-----	1
INTRODUCTION-----	2
SYMBOLS-----	3
APPARATUS AND TESTS-----	10
Test Facilities-----	10
Models and Tests-----	11
EXPERIMENTAL TECHNIQUE AND DATA REDUCTION-----	14
Pressure data-----	14
Heat transfer data-----	15
Visual data-----	17
DATA APPRAISAL-----	17
Pressure data-----	17
Heat transfer data-----	18
RESULTS AND DISCUSSION-----	20
Cylindrical leading edge-----	20
Dual radius leading edge-----	26
Data on slab portion of delta wing-----	28
Delta wing turbulent heating-----	34
CONCLUDING REMARKS-----	37
APPENDIX A - THOMAS - FITZSIMMONS CONDUCTION CORRECTION METHOD----	39
B - LAMINAR AND TURBULENT $\rho_T \mu_T$ HEAT TRANSFER METHOD----	47
C - DELTA WING FLOW FIELD CALCULATIONS-----	81
FIGURES-----	89
REFERENCES-----	193

ANALYSIS OF HYPERSONIC PRESSURE AND HEAT TRANSFER
TESTS ON DELTA WINGS WITH LAMINAR AND TURBULENT
BOUNDARY LAYERS

By A. L. Nagel, H. D. Fitzsimmons and L. B. Doyle

SUMMARY

36106



Results are presented of an analysis of slab delta wing pressure and heat transfer data with laminar and turbulent boundary layers. The data were obtained during the X-20 (Dyna-Soar) program from a parametric series of models tested in conventional wind tunnels at Mach numbers of 6, 7, and 8. Shock tunnel data at Mach numbers of 6 and 15 and shock tube data at a Mach number of 2.2 are also presented. All tests were in air. Free stream Reynolds numbers based on leading edge diameter ranged from 1×10^4 to 6×10^6 .

Turbulent leading edge heating data at Mach numbers of 6 and 8 with wing sweep angles up to 78 degrees and wing angles of attack of up to 45 degrees are compared to swept cylinder theory. Laminar and turbulent heat transfer data from blunt and sharp prow delta wings at angles of attack to 30 degrees are also presented. Lower surface centerline heating data at angles of attack up to 45 degrees are compared to two and three dimensional theories. The effect of lower surface ramp angle and a dual radius leading edge are illustrated by pressure and heating data comparisons with the blunt delta wing and cylindrical leading edge data.

Streamline data taken by a direct transfer oil flow technique are presented for both blunt prow and sharp prow delta wings at angles of attack up to 45 degrees.

Three appendices are included, containing a method for correcting heat transfer data for conduction effects, a heat transfer prediction method based on correlations of exact similarity solutions, and a method of predicting wing flow fields.

Author

INTRODUCTION

The initiation of the X-20 program in November 1959 led to an immediate and urgent need for aerodynamic heating information, since it was known that the high temperatures experienced during re-entry would impose severe constraints on its performance. There existed not only a lack of detailed knowledge of the flow over complex configurations, there were also conspicuous voids in data for simpler shapes as well. The effects of Mach number, wall temperature, and nose bluntness on turbulent boundary layer heating rates were not well established, even for flat plate flow. Laminar boundary layer theory was well established for the stagnation point; for other locations only approximate methods were available. There was also a lack of applicable experimental data. Much additional information was necessary to the success of the X-20 program.

Accordingly, an extensive analytic and experimental program was begun. It was known that the critical heating conditions for re-entry were at about 20,000 fps, a velocity that could not be completely simulated in existing test facilities. A series of parametric tests were therefore conducted in which the test conditions were systematically varied. In order to obtain the widest possible range of test conditions, geometrically similar models were tested in NASA, Air Force, and private facilities.

Much of the data from the parametric delta wing series of tests was never fully analyzed. Pertinent data were analyzed as soon as specific X-20 heating problems became known; there was little time to analyze data obtained in the parametric series. The NASA has financed their analysis and the publication of the present report.

This work complements other delta wing investigations (e.g. references 1 and 2) by providing data for additional flow conditions and model geometries. The basic model was a 73 degree swept delta wing with cylindrical leading edges having a spherical nose cap. Variations about the basic model included sharp-prow configurations in which the leading edges were extended to meet on the centerline plane, a noncylindrical leading edge, and two other angles of sweep. New information presented includes turbulent leading edge heating data at Mach numbers up to 8, direct comparisons of ideal and real gas flow about a blunt delta wing, and turbulent delta wing heating at angles of attack up to 40 degrees.

Two other reports in this series, references 3 and 4, present the results of flow separation and surface roughness testing conducted in the X-20 program.

SYMBOLS

a	speed of sound
A	boundary layer thickness parameter, $2 + (\delta^*/\theta)$
c	specific heat of model skin
c_p	specific heat at constant pressure
c_v	specific heat at constant volume
C	constant in equation (B50)
C_f	skin friction coefficient, $\tau_w / [(1/2) (\rho u^2)]$
$C_{f,r}$	skin friction coefficient evaluated for reference Reynolds number, eq. (B57)
C_m	constant in boundary layer shear law, eq. (B13)
C_p	pressure coefficient, $(P - P_\infty) / [(1/2) (\rho_\infty u_\infty^2)]$
C_x	constant in boundary layer shear law, eq. (B16)
D	leading edge diameter; nose diameter
E	crossflow momentum thickness, eq. (B7)
\bar{E}	momentum thickness ratio, E/θ
f	streamline divergence due to transverse pressure gradients, eq. (B9)
F	function of x , eq. (B11)
F_{Pr}	Prandtl number function, eq. (B22)
F_x	equivalent distance function, eq. (B55)
g	scale factor on y , eq. (B1)
G	boundary layer parameter, eq. (B16)
h	heat transfer coefficient based on temperature, $\dot{q}/(T_{aw} - T_w)$; control volume height
H	heat transfer coefficient based on enthalpy, $\dot{q}/(i_{aw} - i_w)$

i	enthalpy
i_D	energy absorbed in dissociation
J	streamwise pressure gradient parameter, eqs. (B35) and (B49)
k	thermal conductivity; constant in eq. (4)
$K = (1/u_e) (dV_{ii}/dS_{LE})_{SL}$	See Table (B1)
L	length
\mathcal{L}	Lewis number function, eq. (B22) and (B28)
m	exponent on boundary layer shear law, eq. (B13)
M	Mach number
M_n	Mach number component normal to surface, $M_\infty \sin(\alpha_{local})$
n	coordinate normal to stagnation line
N	surface distance normal to and measured from geometric stagnation line
\bar{N}_{CL}	normalized rate of change of streamline angle, eq. (G11)
N_{Le}	Lewis number
N_{Re}	free stream Reynolds number
$N_{Re,e}$	Reynolds number based on boundary layer edge conditions, eq. (B20)
$N_{Re,r}$	reference Reynolds number, eq (B54)
$N_{Re,ref}$	$N_{Re,r}$ based on model thickness
N_{St}	Stanton number, $h / (\rho_\infty u_\infty c_{p_\infty})$
$N_{St,ref}$	turbulent Stanton number, based on model thickness, for reference conditions on stagnation line of a 60° swept infinite cylinder
$N_{St,o}$	Stanton number for the stagnation point of a hemisphere with a diameter equal to the delta wing thickness
P	pressure

$P(X)$	arbitrary function of X
q	heating rate, (Btu/ft ² -sec)
\bar{q}_w	transformed heating rate, eq. (B11A)
$Q(X)$	arbitrary function of X
r	streamline divergence due to body shape, eq. (B9A); recovery factor
R	gas constant in equation of state; radius
S	surface distance measured along centerline; Reynolds analogy parameter, eq. (B22)
S_{eq}	skin friction equivalent distance, eq. (B18)
S_{LE}	surface distance normal to and measured from the leading edge flow stagnation line
\mathcal{L}	Reynolds analogy factor, eq. (B21)
t	time; boundary layer trip height from model surface
T	temperature
\bar{T}	mean temperature
\bar{T}_w	average initial temperature of model (see Appendix A)
T-F	Thomas-Fitzsimmons conduction correction
u	velocity component in x-direction
U	transformed u, eq. (B11)
v	velocity component in y-direction
V	transformed v, eq. (B11)
V_n	velocity component normal to stagnation line
w	velocity component in z-direction
W	width
x,y,z	Cartesian coordinates; curvilinear coordinates (see Appendix B)

x_{eq}	heat transfer equivalent distance, eq. (B24)
X	distance from delta wing apex measured along centerline; transformed x coordinate, eq. (B11)
X_N	distance measured normal to leading edge
X_T	distance measured along centerline downstream of boundary layer trip
X'	distance from delta wing apex measured parallel to leading edge
X'_T	distance measured parallel to leading edge downstream of boundary layer trip
Y	transformed y coordinate, eq. (B11)
Z	transformed z coordinate, eq. (B11); compressibility factor, $P/\rho RT$
α	angle of attack; Prandtl number exponent, eq. (B42); thermal diffusivity, $k/\rho c$
α_{local}	angle between free stream velocity vector and local tangent plane
α_N	effective angle of attack at stagnation line, $(90^\circ - \Lambda_{eff})$
β	wing apex angle, $(90^\circ - \Lambda)$; pressure gradient parameter, eq. (B31)
γ	ratio of specific heats, c_p/c_v
Γ	boundary layer parameter, eq. (B31)
δ	boundary layer thickness
δ^*	boundary layer displacement thickness, eq. (B7)
δ'	shock standoff distance, eq. (4)
Δ	total distance between any two streamlines
Δx	increment in x
ΔX_T	distance measured from model apex to downstream side of boundary layer trip (see figs. 8 and 9)

Δy	increment in y
ϵ	ray angle measured from delta wing centerline
θ	angle from geometric stagnation line; boundary layer momentum thickness, eq. (B7); streamline angle measured from delta wing centerline
θ_s	angle of shock with respect to free stream velocity vector
θ_{SL}	angle measured from geometric stagnation line to true flow stagnation line
θ_w	temperature difference, $T_w - T_{av}$
$\bar{\theta}$	angle measured from true flow stagnation line
Θ	transformed momentum thickness, eq. (B11A)
Λ	sweep angle
μ	absolute viscosity
ξ	shock standoff angle
ρ	density
$\rho_r \mu_r$	reference density-viscosity product (see Appendix B)
σ	partial Prandtl number for translation, rotation, and vibration only (see Appendix B)
Σ	boundary layer parameter, eqs. (B37) and (B38)
τ	shear stress; model skin thickness
$\bar{\tau}_w$	transformed shear stress, eq. (B11A)
φ	streamline angle measured from leading edge shoulder; $\Theta^{(m+1)/m}$
φ^*	streamline angle at leading edge, eq. (C3)
φ^{**}	streamline correlation function, eq. (C9)
ψ	angle of yaw
α	is proportional to

Subscripts:

a	solution to eq. (A6)
atm,SL	atmospheric conditions evaluated at sea level
aw	adiabatic wall
B	blunt
c	crossflow
cyl	cylinder
CL	centerline
D	based on diameter
e	boundary layer edge
eff	effective
eq	equivalent
h	heating rate
i	incompressible;initial
L	laminar
LE	leading edge
m	mean; measured
max	maximum
max h	corresponding to point of maximum heating
n	normal
N	nose
o	wind tunnel or plenum total condition; evaluated at stagnation reference conditions; See also B45
r	evaluated at enthalpy corresponding to $\rho_r \mu_r$

ref * reference
 R. radial
 s streamwise; static
 S evaluated at stagnation conditions
 S' evaluated at stagnation enthalpy and local pressure
 SH shoulder
 SL stagnation line
 T turbulent; trip
 v viscous
 w wall
 x_1 evaluated at $x = x_1$
 0 evaluated for $M=0$, eq. (B51)
 1 evaluated in front of shock
 2 evaluated behind shock
 ∞ freestream condition

Superscripts:

* aft of boundary layer trip
 ' evaluated for infinite cylinder

APPARATUS AND TESTS

Test Facilities

The X-20 basic delta wing program consisted of eight tests. Six tests were conducted in four conventional wind tunnels, one test in the AVCO 4-inch shock tube and one series of tests in the Cornell Aeronautical Laboratories (CAL) 24-inch and 48-inch shock tunnels. All tests were conducted in air.

The four conventional wind tunnels utilized were:

1. Boeing Hypersonic Wind Tunnel (BHWT)
2. Boeing Supersonic Wind Tunnel (BSWT)
3. Arnold Engineering Development Center Wind Tunnel B (AEDC-B)
4. Jet Propulsion Laboratory 21-inch Hypersonic Wind Tunnel (JPL)

These six facilities will be discussed briefly, starting with conventional wind tunnels.

Boeing Hypersonic Wind Tunnel.-The Boeing Hypersonic 12-inch Wind Tunnel is a blowdown type providing steady flow for periods up to two minutes, depending upon flow conditions. Maximum stagnation pressure and temperature utilized were 1400 psia and 1085°R, respectively. Axisymmetric contoured nozzles provided Mach numbers of 6.08 and 7.0 and a free stream Reynolds number to 19.3×10^6 per foot was obtained. The tunnel has an open test section with an atmospheric diffuser. Provisions were made to inject sting mounted heat transfer models into the core flow from a cooling chamber in less than 0.2 seconds. The cooling chamber, illustrated in figure 1, was found necessary to maintain heat transfer models in an isothermal condition prior to injection. The model was injected only after the flow had stabilized. Transient model temperature measurements for heat transfer data were recorded on multi-channel oscillographs. Pressure data were punched directly into IBM cards from a scanning-valve transducer system.

Boeing Supersonic Wind Tunnel.- The Boeing Supersonic Wind Tunnel provides various test conditions by the use of flexible nozzle walls adjusted by hydraulic jacks. Mach numbers used were 2.0, 2.5, and 3.0 at free stream Reynolds numbers per foot of 7.1×10^6 , 8.25×10^6 , and 9.65×10^6 , respectively. This facility is also of the blowdown type. Pressure data were punched into IBM cards from a scanning-valve transducer system. No heat transfer tests were made in this tunnel.

Arnold Engineering Development Center Tunnel B. - The Mach 8.08 Tunnel B at Arnold Engineering Development Center is of the continuous flow, closed-test-section type. Maximum stagnation pressure and temperature utilized were 805 psia and 1350°R, respectively. Free stream Reynolds numbers were varied from 0.986×10^6 to 3.43×10^6 per foot. Sting mounted heat transfer models were protected from the flow by a clamshell-type cooling shoe. To expose the model, the two halves of the shoe were retracted to opposite sides of the tunnel wall. This retraction process was accomplished in about 0.5 seconds. Model temperature data were recorded on magnetic tape from the output of a digital voltmeter which scanned each thermocouple 20 times per second. Pressure data were similarly recorded on magnetic tape from a scanivalve-transducer system. Reference 5 may be consulted for further facility information.

Jet Propulsion Laboratory Hypersonic Tunnel. - The 21-inch Jet Propulsion Laboratory Wind Tunnel provided continuous flow at Mach 8.04 and a free stream Reynolds number of 0.785×10^6 per foot. Total pressure was 250 psia at a total temperature of 1660°R. This tunnel utilized a cooling shroud to protect the sting mounted model from the flow. Shroud removal took approximately 0.25 second. Temperature and pressure data were recorded on magnetic tape directly from digital readout systems. Each thermocouple was scanned 20 times per second.

AVCO Shock Tube. - The AVCO 4-inch shock tube provided supersonic flow at Mach 2.2 and at total enthalpies from 1946 to 9598 Btu/lb for the study of real gas effects. Reynolds numbers were varied from 2×10^3 to 13×10^6 per foot. Heat transfer data in the form of temperature-time histories from thin and thick film gages were photographically recorded from oscilloscopes. No pressure instrumentation was used, although pressure information was obtained from Schlieren photography using a Mach line technique.

Cornell Aeronautical Laboratory Shock Tunnel. - The AD642 leading edge tests were conducted in a 48-inch contoured nozzle having a nominal Mach number of 15, and a 24-inch contoured nozzle having a nominal Mach number of 6. The total pressure in these tests were up to 700 psia and the total temperature was up to 5,950°R. Further facility details may be obtained from Reference 6.

Models and Tests

Figure 2 illustrates typical slab delta wing models used in these tests. The nomenclature describing model geometry is given in figure 2(a). The geometric variations included leading edge diameters from 0.332 inch to 1.5 inches, sweep angles of 68, 73, and 78 degrees, ramp angles of zero and 4 degrees, and model lengths from 3 to 16 leading edge diameters. Sharp-prow models were formed by the intersection of the cylindrical leading edges; blunt-prow models had spherical nose-caps of the same diameter as the leading edges. The one dual-radius leading edge model had a 0.25 inch upper radius and a 0.75 inch lower radius.

All of the conventional wind tunnel heat transfer models were electroformed. In fabricating models of this type, a thin shell of nickel is electrolytically deposited upon a mandrel. The model shell is then removed and machined to uniform skin thickness, smoothness and contour. This technique has the advantage of providing continuous skin free of joints even for complex geometries. A minimum of internal support structure was utilized. A typical model of this type is shown in figure 2(b). The shock tube models were shaped from solid glass. Both thick and thin film heat transfer gages were used, installed directly upon the model surface.

A brief description of each test and its associated models appears below. Nominal wind tunnel flow conditions are summarized in Table I while details of model geometry are tabulated in Table II and sketched in figure 2. In the remainder of this report the tests will be referred to by their respective Boeing Model numbers, such as AD461M-1.

Test AD461M-1.^a - Test AD461M-1 included seven sharp and blunt-prow models tested in the Boeing Hypersonic Wind Tunnel. As shown in table II, the models tests covered a range of blunt-prow diameters from 0.332 to 1.00 inches and length to diameter ratios from 4.2 to 16.2. One blunt-prow model had a four degree ramp angle. Boundary layer trips were used on all AD461M-1 models to obtain turbulent flow. Data available from these tests included heat transfer, pressure, and oil flow patterns.

Test AD461P-1.^b - Test AD461P-1 was conducted in the Boeing Supersonic Wind Tunnel to provide pressure and streamline data to aid in the analysis of shock tube data from test AD485M-1. One blunt-prow model having a length to diameter ratio of 3.0 was tested at angles of attack from -15° to +45°. Pressure measurements and oil flow patterns were available from this test.

Data reports are identified by alphabetical superscripts and may be obtained on loan from The Boeing Company, Seattle, Washington:

^aData Report BHWT Test No. 41, The Investigation of Pressure and Heat Transfer on Various Dyna-Soar Wing Models, Boeing Document D2-7614, February 20, 1962.

^bBSWT Test No. 087, High Speed Test of the DS-1 Project, Boeing Document D2-8009, December 14, 1960.

Test AD462M-1.^{c,d} - Test AD462M-1 provided blunt-prow delta wing pressure, heat transfer, and flow field data for both turbulent (tripped) and laminar boundary layers. The test was conducted in Arnold Engineering Development Center Tunnel B. Model angle of attack was varied from -25° to $+30^\circ$; sideslip angles were 0° and $\pm 5^\circ$.

Test AD465M-1.^e - Test AD465M-1 was conducted in the 21-inch hypersonic tunnel at the Jet Propulsion Laboratories. One sharp-prow delta wing was tested at Mach 8.04. The primary purpose was to study the effects of circumferential slots on leading edge heating. Tests were also made with the slots filled to obtain smooth body, sharp-prow data. The model was tested at angles of attack from 0° to 41.5° , and sideslip of 0° , 5° , and 10° . Only laminar heat transfer data and Schlieren photographs were obtained.

Test AD477M-1.^{f,g} - Test AD477M-1 provided heat transfer and pressure data on a dual-radius leading edge sharp-prow, delta wing. The test was conducted in Arnold Engineering Development Center Tunnel B at angles of attack from -5° to 55° and sideslip angles of $\pm 10^\circ$. One tripped flow run at Reynolds number 42.8×10^4 , based on leading edge diameter, provided some turbulent leading edge data.

Test AD483M-1.^h - Test AD483M-1 included two sharp-prow delta wings with sweep angles of 68° and 78° . The test was conducted at the Boeing Hypersonic Wind Tunnel. Pressure and heat transfer data for tripped turbulent boundary layers were obtained at 0° to 30° angle of attack and sideslip angles of 0° and 10° .

^cData Report AEDC - Tunnel B BAC Test No. 12 Mach 8 Heat Transfer and Pressure Test on AD462M-1 Dyna-Soar Model, Boeing Document D2-8045, June 7, 1961.

^dData Report Re-evaluated Heat Transfer Data from AEDC-B-BAC 012 Test of the AD462M-1 Model, Boeing Document D2-8045-1, October 4, 1962.

^eData Report JPL 21-82, Heat Transfer and Pressure Test on a Slotted Leading Edge Wing Model, Boeing Document D2-80491, June 27, 1962

^fData Report - AEDC-B-BAC Test No. 19, Flow Survey Probe Test and Oil Flow Study of a Dyna Soar Model.

^gData Report AEDC B-BAC Test 15 M = 8, Heat Transfer and Pressure Test on AD 477M-1, Boeing Document D2-8206.

^hData Report BHWT Test No. 044 Tests on Two AD483M-1 Parametric Models for the Dyna-Soar Program to Study the Effect of Sweepback Heat Transfer and Pressure Distribution, Boeing Document D2-80049, September 1961.

Test AD485M-1.ⁱ - Test AD485M-1 was conducted in the AVCO 4-inch shock tube to provide pressure and heat transfer data in a real gas environment. The data were obtained for both tripped turbulent and laminar boundary layers at a freestream Mach number of 2.2 for angles of attack from 0° to 30°. The three models applicable to basic delta wing studies consisted of a 73° sweep blunt-prow wing, a 45° swept blunt plate, and an unswept blunt plate. Sketches of the two blunt plate models are shown in figure 2(c). A picture of the fourth model, a sharp 25° wedge, is shown in figure 3 to illustrate the Mach line pressure technique.

AD642M-1.^j - AD642-1 included a series of basic shapes which were tested in the Cornell Aeronautical Laboratory Hypersonic Shock Tunnel. These shapes included a sharp nosed hemicylindrical leading edge tested at sweep angles of 55°, 60°, 65°, and a hemisphere cylinder tested at angles of attack of 0°, 10°, 20°, and 50°. Sketches of the two models are shown in figure 2(d). Heat transfer and pressure measurements were obtained in laminar flow at a Mach number of 15 and in turbulent flow at a Mach number of 6 over a wide range of Reynolds numbers. A sharp flat plate was also tested and reported under Task II of the present contract.

EXPERIMENTAL TECHNIQUE AND DATA REDUCTION

Pressure Data

Conventional wind tunnels. - Conventional wind tunnel pressure measuring techniques were used in tests AD461M-1, AD461P-1, AD462M-1, AD465M-1, AD477M-1, and AD483M-1. Piezoelectric pressure transducers were employed throughout. Model pressure readings were scanned prior to recording to ensure stable conditions. Data were read simultaneously with the tunnel total pressure and temperature.

Where both pressure and heat transfer data were taken from a single model, the pressure taps and thermocouples were installed on opposite sides of the model to avoid heat sink effects. Where pressure taps and thermocouples were both on centerline, they were well spaced for the same reason. Pressure taps that were closely spaced, as on the leading edges, were staggered to avoid interference effects.

ⁱData Report, Dyna Soar Real Gas Tests in the AVCO 4.0 Inch Diameter Shock Tube, Boeing Document D2-80304, June 30, 1961.

^jTurbulent Reference, Roughness Leakage and Deflected Surface Heat Transfer and Pressure Tests for The Boeing Company Conducted in the CAL 48 Hypersonic Shock Tunnel, Boeing Document D2-80910, January 3, 1963.

Shock tube. - A Mach line pressure technique (reference 7) was used with limited success in shock tube test AD485M-1. This model consists of using isentropic relationships to define the local model pressure from the local Mach angle. Mach angles are measured from Schlieren photographs such as figure 3. The Mach lines were generated by small indentations (0.001 inch wide by 0.001 inch deep) in the model surface.

Heat Transfer Data

Conventional wind tunnels. - Heat transfer data from all conventional wind tunnel tests were obtained by the well-known thin skin calorimeter technique. This method consists of measuring the rate of temperature increase of the thin metal skin of the model exposed to aerodynamic heating. A local heat balance on the thin skin relates the Stanton number, N_{St} to the skin temperature as follows:

$$N_{St} = \frac{\rho c \tau_{eff} \frac{\partial T_w}{\partial t} - k \tau \nabla^2 T_w}{\rho_\infty u_\infty c_{p_\infty} (T_{aw} - T_w)} \quad *(1)$$

where ρ , c and k are density, specific heat and thermal conductivity of the model skin. The term $\rho c \tau_{eff} (\partial T_w / \partial t)$ represents the net rate at which heat is being added to the skin; the term $k \tau \nabla^2 T_w$ represents only that rate of heat addition by conduction along the model skin. The wall temperature, T_w , was measured with No. 30 (.01 inch dia.) gage chromel-alumel thermocouples spot welded to the inside surface of the model skin. The skin was made sufficiently thin so that temperature differences through the skin were negligible. Nominal skin thicknesses for each calorimeter model are listed in table II.

Prior to each run the models were isolated from the wind tunnel flow and cooled in order to maximize the aerodynamic heating rate and to minimize conduction effects due to initial skin temperature gradients. Models were

*The Laplacian operator ∇^2 is defined by

$$\nabla^2 = \frac{\partial^2}{\partial x^2} + \frac{\partial^2}{\partial y^2} + \frac{\partial^2}{\partial z^2}$$

In the present application, temperature gradients through the model skin are neglected, so that for flat surfaces:

$$\nabla^2 T = \frac{\partial^2 T}{\partial x^2} + \frac{\partial^2 T}{\partial y^2}$$

where x and y are measured in the plane of the skin, and are orthogonal.

then exposed to the flow by model injection (BHWT) or shroud removal (AEDC-B and JPL) as quickly as possible. The exposure time varied from 1/10 second for model injection up to 1/2 second for shroud removal. Temperature data were usually recorded for 5 to 10 seconds, depending upon the severity of the heating rate. The nickel model skin properties were determined from data shown in figure 4. Also shown are three least squares fitted equations that were used in these tests for computer data reduction. These equations agree within 1 percent at temperatures for which the heat transfer data were reduced. The density of nickel was taken constant at 555 lb/ft³. The term τ_{eff} in equation (1) is the measured model skin thickness, τ , for flat surfaces; equal to $\tau(1 - \tau/D)$ for cylindrical surfaces; and approximately equal to $\tau(1 - \tau/D)^2$ for spherical surfaces. The recovery temperature, T_{aw} , was computed approximately from the true local angle of attack, α_{local} , with the following equation.

$$\frac{T_{aw}}{T_o} = r + (1 - r) \frac{2 + (\gamma - 1) (M_\infty \sin \alpha_{local})^2}{2 + (\gamma - 1) M_\infty^2} \quad (2)$$

The recovery factor, r , was taken as 0.85 for laminar flow and 0.90 for turbulent flow. As discussed later, the temperature rise rate, $\partial T_w / \partial t$ is required at several different times during a single test run. Early in the X-20 program $\partial T_w / \partial t$ was evaluated from a least squares, second degree curve fitted to the first 11 temperature data points, which encompassed 1 second of real time. The $\partial T_w / \partial t$ was then evaluated each 0.1 second from the fitted curve. Later in the program, a curve fit through each separate interval of data was made for each different time that a value was desired. This technique was used since the best estimate of slope using the least squares curve fit technique is obtained at the midpoint of the interval of data over which the curve fit is made. The curve was still fitted to 1 second of data; however, 21 data points were now used.

All thin skin calorimeter data of the present tests were corrected for lateral conduction by use of the previously unpublished Thomas-Fitzsimmons method (described in Appendix A and referred to, in this report, as the T-F method). The method basically consists of extrapolating the curve of heat transfer coefficient versus time (or temperature) back to an effective start of the test run. For data reduction purposes, the test run was assumed to start at the time the model entered the inviscid core of the tunnel flow.

Shock tube. - Test AD485M-1 (AVCO Shock Tube) utilized thin film heat transfer gages for heating rates less than about 880 Btu/ft²-sec., and thick film gages for higher heating rates. These gages have the necessary rapid response time for use in shock tubes. Thin film gages consist of a platinum film resistance thermometer vacuum deposited over a pyrex glass substrate. The surface temperature history of the glass defines the aerodynamic heating rate by use of the solutions of the heat conduction equation for a semi-infinite slab as indicated in the data report footnote i. The thick film

gage consists of a platinum resistance thermometer that serves also as a calorimeter. Data were reduced by an equation similar to equation (1). Because of the short test times, lateral conduction of the type experienced in thin skin calorimeters is insignificant.

Shock tunnel. - Thin film heat transfer gages on model AD642 similar to those described above were employed in the Cornell Aeronautical Laboratory shock tunnel. The semi-infinite slab solutions used by CAL are described in references 8 and 9.

Visual Data

Schlierens or shadowgraphs were taken on all tests by standard techniques.

Oil flow pictures were used to determine streamline angles in test AD461M-1. A mixture of lampblack and No. 60 high temperature oil was spread over the model which was then protected from disturbance until tunnel flow was established. The model was injected into the flow and the oil pattern allowed to develop for 10 to 15 seconds, after which the model was retracted and removed. Photographs of the patterns were made as well as permanent impressions. The impressions were obtained by applying transparent adhesive tape to the wing and then applying the tape to vellum paper. This impression technique allowed the oil flow pattern on the curved leading edge to be layed flat, facilitating the measurement of streamline angles and stagnation line locations.

DATA APPRAISAL

Pressure Data

Conventional wind tunnel pressure data. - No unusual difficulties arose in the measurement of pressure data in conventional wind tunnels except in test AD465M-1. These pressure data exhibited a significant variation with time. As sharp-prow delta wing data were available from other tests, AD465M-1, pressure data have been omitted from this report. Pressure data from other conventional wind tunnel tests exhibited good repeatability.

Shock tube pressure data. - The Mach line technique used to measure AD485M-1 model pressures in the shock tube worked well on the lower surface centerline. However, streamline inflow or outflow occurred at locations away from the centerline causing Mach lines to be photographed at false angles. No acceptable correction was found; only data from Mach lines originating on the centerline were used. In order to provide an exact location of each Mach line origin, center punch marks .001 inch in diameter and .001 inch deep were spaced along the plane to be measured. Experience in the use of this technique showed that the true pressure was obtained by measuring the Mach angle from the line originating from the rear of the punch mark. A Schlieren picture of the Mach lines has been shown in figure 3.

Heat Transfer Data

Heat transfer data are subject to numerous and often large sources of error, which may be either systematic or random. Systematic errors may arise from conduction, model thermal distortion, or gage temperature effects. Random errors may arise from lack of complete control of test conditions, measurement errors, and human error. The importance of heating rate prediction in the design of the X-20 stimulated attempts to improve the quality of aerodynamic heating data, and considerable progress was made during the course of the program. Most of this progress must be attributed to the efforts of the operators of the test facilities involved; however, it is felt that the conduction correction method presented in Appendix A is an important contribution as well.

In the present study, careful consideration was given to sources of error and steps were taken to prevent, minimize or correct for them wherever possible. Due to the large quantity of data in the present report, individual attention could not be given to all apparent data discrepancies. Data obviously erroneous were omitted whenever noticed. In turbulent flow, data from several different, but similar, models and tests are presented. Agreement between such data is, at times, only fair and is attributed to differences in the trip strips utilized and to transitional flow. The major problems encountered and the corrective action taken are described below.

Conduction effects. - For the thin skin calorimeter heat transfer models, the major systematic error was lateral conduction in the model skin. To estimate the degree to which the present data are affected by conduction errors, samples of data uncorrected for conduction and corrected by the method of Appendix A have been compared with well established laminar stagnation point and stagnation line theories. Two such comparisons are given in figure 5 and 6. In these figures test data are presented as ratios to the corresponding theoretical values. The nonlinear percentile abscissa is graduated such that the classic normal distribution of random errors plots as a straight line. On such a plot, the linearity of data is a measure of the randomness of errors, while the slope is a measure of the data scatter. The value of the data at the 50th percentile is a measure of systematic error. Figure 5 presents measurements of stagnation point* heat transfer to the spherical nose. The model was electroformed nickel, tested at Arnold Engineering Development Center Tunnel B and otherwise similar to present delta wings. The data indicated by open symbols were reduced 0.87 seconds after test start (earliest available data) and are not conduction corrected. When compared to theory, discrepancies as large as -40 percent are in evidence. The mean error at the 50th percentile is -10 percent. The same data when corrected by the method used in this investigation have a mean error of

*These data were taken at various angles of attack and a few points are as much as 20° removed from the stagnation point. All data were corrected to stagnation point; with the $\rho_r \mu_r$ theoretical distribution. The maximum correction was 8 percent.

only -3.5 percent and a maximum error of -7.5 percent. Figure 6 is a similar presentation of delta wing leading edge stagnation line data from the present investigation. Again, the mean of the corrected data is within 3 percent of the theoretical value.

Other systematic errors.- Other systematic errors in heating data have been considered. The heat sink effect of #30 gage thermocouple wire has been estimated to contribute less than 1 percent error. Errors due to radiation are similarly considered negligible. Model skin thickness was carefully controlled in manufacture and locally measured to 0.0005 inch, or approximately 1 percent. The specific heat of the nickel skin perhaps accounts for the second largest systematic error, but is known to about 3 percent, based on the data of figure 4.

Another measure of heat transfer data quality is the repeatability of data from run to run. Repeatability is a check upon the degree to which tunnel flow conditions, instrumentation, data reduction, conduction and other corrections are consistent and predictable. A statistical plot is shown in figure 7 of samples of delta wing laminar and turbulent leading edge heating data from repeat runs for tests AD461M-1, AD462M-1, and AD477M-1. The ordinate is the difference of the measured heating rate in the repeat data run from the measured heating rate from the repeated, or first run. For the laminar data at the 50th percentile, the data from the repeat run seem to be biased positively, but only by about 2 percent. The standard deviation of the laminar repeatability, based upon the faired normal distribution line, is 2.6 percent about the mean. The turbulent leading edge repeatability is not biased and exhibits a standard deviation of 6.5 percent. The higher standard deviation of the turbulent data repeatability is attributed to trip strip effects, and to the use of oscillograph temperature recorders as opposed to the digital system used for the laminar data. Overall repeatability is considered good.

Boundary layer tripping devices. - Boundary layer tripping devices were used to obtain turbulent flow on some of the delta wing models. For all but the AD462M-1 model the trips were made of sand glued to the surface. For the AD462M-1 model a glove of wire screen was fitted over the blunt model prow. The screen was .015 inch diameter wire with a mesh size of .04 inches and covered the whole prow aft for 1.25 inches on the instrumented surface as indicated in figure 54.

The possible adverse effects of trips on heating measurements was realized at the time the tests were run. Every effort was made to minimize possible adverse effects by making the trips as small as possible. However, it was found that tripping was possible only with relatively large trips. The data were examined for trip effects with the aid of plots such as figures 8 and 9. Only data believed to be free of trip effects are presented.

CAL Gage Calibration. - The CAL heat transfer data are obtained with a gage that consists of a thin film of platinum fused to a glass substrate. The platinum film is used as a resistance thermometer to measure the increase

in substrate surface temperature during the test. The heating rate can be determined from the temperature increase if the density, specific heat, and thermal conductivity of the substrate are known. The quantity actually required is the square root of their product ($\rho c k$) which is determined from a calibration procedure in which a step pulse electric current is passed through the platinum film. The small amount of resistance heating causes a slight temperature increase and allows $\sqrt{\rho c k}$ to be determined at the initial gage temperature. The variation of $\sqrt{\rho c k}$ with temperature is obtained by preheating the gage in an electric oven and repeating the electric pulse heating calibration.

Some time after the AD642 tests were completed, CAL made new measurements of $\sqrt{\rho c k}$ that lead to a considerably different variation with temperature than previously indicated. It was not feasible to rereduce the data at the time this report was written. It was determined, however, that the laminar data shown would be lowered by 0 to 6 percent on the basis of the new calibration. The highest heating rate data (obtained on the leading edge model in turbulent flow) would be reduced by up to about 30 percent.

After examining the effects of the "new" calibration would have on the data, particularly such trends as heating rate versus time during the test run, the authors feel that some uncertainty in calibration remains. A test will be made in 1966 as a part of an Air Force research contract that is expected to provide additional information.

The data are presented as originally reduced.

RESULTS AND DISCUSSION

Cylindrical Leading Edge

Pressure data at low angles of attack. - Leading edge pressure data for 73 degree swept delta wings at angles of attack up to 15 degrees are shown in figures 10 and 11. Figure 10 shows the downstream variations of leading edge pressures; figure 11 presents the circumferential distribution. For nonzero angles of attack, the leading edge stagnation line location (shift) was calculated by the relationship

$$\tan \theta_{SL, cyl} = \frac{\sin \alpha}{\cos \alpha \cos \Lambda + \tan \psi \sin \Lambda} \quad (3)$$

The axial pressure distributions presented in figure 10 are seen to differ significantly from infinite cylinder theory (normal component stagnation pressure) for at least 6 leading edge diameters.

The blunt-prow pressure data of figure 10 show a characteristic over-expansion from the spherical nose shoulder followed by a return to values

higher than infinite cylinder theory. At 10 degrees angle of attack the pressure appears stabilized after about 6 diameters, but at zero degrees angle of attack the pressure is not stabilized at less than 9 diameters on the stagnation line and is still rising at 30 degrees from the stagnation line. Note also that the minimum pressure point moves forward with increasing local angle of attack. This effect is similar to that observed on the lower surface and will be discussed more fully under Delta Wings.

No completely corresponding sharp-prow data are available. However, data from the sharp-prow dual-radius model at an angle of attack of 10 degrees* show that the stagnation line pressure decreases with distance aft, asymptotically approaching a constant value. It is not clear whether the final value will agree with the infinite cylinder predictions or is approaching some slightly higher value. However, the observed trend is in agreement with the "finite length cylinder theory" curve, which does approach the cylinder value as a limit. It is assumed in this finite length cylinder theory that the leading edge shock angle decreases exponentially from a wedge shock at the apex to a parallel shock infinitely far aft or in terms of shock standoff distance, δ' , as

$$\frac{\delta'}{D} = \frac{\delta'_{cyl}}{D} \left[1 - e^{-k_{\delta}(X'/D)} \right] \quad (4)$$

where δ' is the infinite cylinder shock standoff distance. (Both δ' and δ'_{cyl} are measured normal to the cylinder axis). The constant k_{δ} is determined from the initial shock angle, which is given by oblique shock theory. There results

$$\frac{\delta'}{D} = \frac{\delta'_{cyl}}{D} \left[1 - e^{-(\tan \xi)(X'/\delta'_{cyl})} \right] \quad 4(a)$$

where ξ is the angle between the shock and the surface as predicted by oblique shock theory, and X' is the distance along the cylinder stagnation line. The pressures are assumed to vary similarly:

$$P' = P_{cyl} \left[1 + \left[\frac{P'_{wedge}}{P_{cyl}} - 1 \right] e^{-(\tan \xi)(X'/\delta'_{cyl})} \right] \quad (5)$$

*The use of data from the dual-radius leading edge model (AD477M-1) in this and other comparisons is limited to angles of attack of 10 degrees or above, and at locations away from the geometric stagnation line. It is believed that this allows a valid comparison to cylindrical leading edge data.

where P' is the stagnation line pressure and P'_{wedge} is the oblique shock theory prediction.

Circumferential distributions at low angles of attack are presented in figure 11. Since stagnation line values are different than cylinder theory near the wing apex, only data well downstream are shown. Data are normalized with respect to infinite cylinder theory, and compared to infinite cylinder predictions by three methods: Newtonian theory, an empirical method by Gregorek and Korcan (ref. 15) and an empirical method developed during the X-20 program. The latter method is essentially identical to that of Bertram and Everhart (ref. 1). As shown, all data from the present program tend to be higher than the predicted distributions; as much as 100 percent higher at the leading edge shoulder. However, the trend is consistent with other low Reynolds number data.

The cylinder formula, equation (3), predicts a stagnation line shift of 42.5 degrees at an angle of attack of 15 degrees for a 73 degree swept wing. Since the sonic line (in the crossflow plane) is approximately 50 degrees from the stagnation line, it might be expected that at low angles of attack the lower surface would have little effect on pressures in the subsonic portions. This is borne out by the data; it will be seen in figure 11 that significant departures from the predicted values occur only for $\alpha > 40$ degrees.

Pressure and streamline data at high angles of attack.- Cylindrical leading edge pressure distribution data for both sharp and blunt-prow models at angles of attack between 15 and 40 degrees are shown in figure 12. Again, distribution data are normalized by infinite cylinder theoretical values. Dual-radius model data (AD477M-1) have again been used only where cylindrical leading edge behavior is expected. Considerably more scatter is apparent in figure 12 than in figure 11, which is believed to be at least partly due to lower surface effects.

An examination of oil flow and pressure data has shown that one of the effects of the lower surface is to cause an additional stagnation line shift over and above that predicted by equation (3). The observed stagnation line shift is shown in figure 13, and is compared to the infinite cylinder theory of equation (3). It is seen that the stagnation line follows the infinite cylinder prediction only up to about 15 degrees angle of attack. At higher angles, it moves much more rapidly than the infinite cylinder theory predicts, and moves onto the lower surface at about 40 degrees angle of attack.

Also shown in figure 13 are some data by Zakkay and Fields (ref. 16) obtained at a Mach number of 6 on an unswept two-dimensional wedge with a cylindrical leading edge. These data were made comparable by considering the Mach 6 free stream flow as the normal component to the leading edge of a 73° swept delta wing at angle of attack. The agreement of Zakkay's data with the delta wing data implies that the delta wing lower surface effect upon stagnation line shift is essentially two-dimensional. As will be shown later, there is a three-dimensional effect near the nose of the model, indicated by a variation in stagnation line location with distance from the

apex. The data of figure 13 are all for the downstream region where no such variation was measured. Examples of the leading edge oil flow streamline data used to determine stagnation line shift are shown in figure 14. The faired curve of figure 13 is used in other parts of this report. For example, the data of figure 12 are replotted in figure 15 against distance from the observed stagnation line. Although differences in location of as much as 15 degrees are involved, there is not a large effect on the agreement of the present pressure data with previous prediction methods, and considerable scatter is still evident.

Laminar heat transfer at low angles of attack.- Laminar leading edge heat transfer data for blunt and sharp-prow delta wings at angles of attack up to 15 degrees are presented in figures 16 through 18. As with the pressure data already presented, experimental values are normalized by swept infinite cylinder theory, in this case the laminar $\rho_r \mu_r$ method described in Appendix B. Stagnation line data are presented in figure 16 as a function of the effective sweep angle, which for zero angle of attack is just the wing sweep angle. For delta wings at angles of attack the effective sweep angle is given by

$$\sin \Lambda_{\text{eff}} = \cos \psi \cos \alpha \sin \Lambda - \sin \psi \cos \Lambda \quad (6)$$

Agreement with the theory is generally excellent. The AD462M-1 blunt nose data are examined far aft where bluntness effects are expected to be small. The AD477M-1 dual-radius leading edge data (average of 21 points) are presented only for an angle of attack of 10 degrees, where no appreciable dual-radius effect is expected (see the later discussion of the Dual-Radius Leading Edge). For these conditions and geometries, good agreement with the theory is to be expected.

The downstream extent of blunt and sharp-prow effects upon cylinder stagnation region heat transfer are shown in figure 17. The AD477M-1 gages were located at the true stagnation line which was 30 degrees away from the geometric stagnation line. All AD462M-1 data were within 22 degrees of the stagnation line. Two zero-degree angle of attack repeat runs are shown for this blunt-prow model. Blunt-prow model data all exhibit a minimum in the heating rate, at approximately 2.5 diameters aft, which is 35 percent below infinite cylinder theory. The location of the minimum heating point is nearly independent of angle of attack, which contrasts with the movement of the minimum pressure point shown in figure 10. The reduced heating level due to bluntness extends about 8 and 6 diameters aft at zero and 10 degrees angle of attack, respectively. The variation of the extent of the blunt-prow effect with angle of attack is consistent with that shown by the pressure data. At $X'/D = 1.9$, the blunt-prow data are consistent with hemisphere theory at the shoulder of the spherical nose, as indicated on this figure.

The sharp-prow data of figure 17 exhibit a gradual decrease in level with distance aft. This sharp-prow characteristic is exhibited also in the

pressure data. The sudden increase in heating 8 diameters ait may be due to flow transition, since the lower surface data at this condition are transitional. Nevertheless, the overall agreement with $\rho_r \mu_r$ infinite cylinder theory is excellent.

The distribution of laminar heating around blunt and sharp-prow delta wing cylindrical leading edges is shown in figure 18, also compared to $\rho_r \mu_r$ infinite cylinder theory. The theory has been calculated using the X-20 empirical cylinder pressure distribution of figure 11. The negative angle of attack AD462M-1 data are highly consistent up to 107 degrees from the flow stagnation line. The maximum angle of attack has been limited to 15 degrees to minimize lower surface effects. The most significant effect shown in figure 18 is the rapid departure of the blunt-prow data from cylinder theory with increasing angle from the stagnation line. The data are approximately 150% higher than infinite cylinder theory at an angle of 90 degrees. These data were closely examined because of this unexpected result, but the further study confirmed the trend. As with the pressure data previously discussed, little influence of the lower surface is expected at angles of attack of 15 degrees or less. It will be recalled, however, that the pressure data do show a similar trend. Since the effect is much more pronounced in the blunt-prow model data, the conclusion has been reached that these data exhibit a prow bluntness effect away from the stagnation line which increases, rather than decreases, the heating level. This is further confirmed by the fact that the heating rates from the shoulder instruments are higher for the blunt-prow than the sharp-prow model.

Lower surface effects on laminar heat transfer.- Wing lower surface effects on cylindrical leading edge heat transfer for angles of attack up to 45 degrees are illustrated in figures 19, 20, and 21. All X-20 data are for 73 degree swept wings at a Mach number of 8.

Figure 19 presents leading edge heat transfer distributions normalized with respect to the theoretical stagnation line value. Two trends are apparent in figure 19; the point of maximum heating moves less rapidly with angle of attack than does the flow stagnation line, and the maximum heating rate decreases with respect to the theoretical prediction for a cylinder.

The movement of the point of maximum heat transfer with respect to the flow stagnation line is attributed to a reduction in velocity gradient at the stagnation line, such that the maximum velocity gradient occurs at a more leeward location. Since the heating rate depends on both the pressure and the velocity gradient, the point of maximum heating is shifted in the same direction. The reduction of the velocity gradient at the stagnation line is attributed to the change in stagnation line pressure relative to that on the lower surface. The effect does not occur when the sonic point is on the leading edge, of course. With increasing angle of attack the difference in pressure between the stagnation line and the lower surface decreases. The resulting decrease in pressure gradient also decreases the

velocity gradient. This decrease would occur only on the windward side, there being no similar effect on the upper surface. Since the point of maximum heating occurs at a location where the pressure is somewhat less than the stagnation line value, the reduction in heating rate is not surprising. As with the stagnation line shift results, discussed previously, the reduction in stagnation line velocity gradient is consistent with that exhibited by the unswept model data of reference 16. Close examination of the reference 16 data also shows that the location of the local maximum velocity gradient is not on the stagnation line. Although heat transfer measurements were not presented, an estimate of the location of the point of maximum heating can be made by observing the point at which the product $P(\partial u/\partial s)$ was a maximum. This estimate is compared with the present delta wing data in figure 20, where the angle between the flow stagnation line and the line of maximum heating is plotted versus wing angle of attack. The data of reference 16 are adjusted to equivalent delta wing angles of attack such that the quantity $(\theta_{SL,cyl} - \theta_{SH})$ is matched. As shown, the location of the line of maximum heating relative to the flow stagnation line is consistent between the two sets of data, even though the data of reference 16 are for a constant normal Mach number of 6 while that of the delta wing data varied from 3 to 6. This agreement implies that the maximum heating shift, relative to the stagnation line, is essentially two-dimensional.

Referring to the theory lines shown in figure 19, it will be noted that the maximum heating rate is predicted by

$$N_{St,max} = N_{St}(\bar{\theta}_{max h}) \quad (7)$$

where $N_{St}(\bar{\theta}_{max h})$ is the infinite cylinder theory evaluated at $\bar{\theta}_{max h}$ which is taken from figure 20. The distribution of heating about the point of maximum heating is seen to be essentially unchanged from the infinite cylinder distribution. The heating rate distribution can therefore be calculated from

$$\frac{N_{St}}{N_{St,max}} = \left[\frac{N_{St}}{N_{St,max}} \right]_{cyl} \quad (8)$$

provided that $(N_{St} N_{St,max})_{cyl}$ is based on distance from the point of maximum heating. This method has been found to predict the observed trends in both laminar and turbulent flow when θ_{SL} is taken from figure 13 and $\bar{\theta}_{max h}$ is taken from figure 20. One such comparison is shown in figure 21 which presents maximum leading edge heating rate to a blunt and sharp delta wings as a function of angle of attack.

Turbulent heat transfer at low angles of attack.- Turbulent heat transfer data on a delta wing cylindrical leading edge at angles of attack up to 15 degrees are presented in figures 22 and 23. Figure 22 presents stagnation line data for effective sweep angles up to 78 degrees; turbulent

circumferential distribution data are shown in figure 23 for wing sweep angles of 68, 73 and 78 degrees. Turbulent leading edge flow could be obtained only by the use of boundary layer trips, and diverse downstream effects of these devices were observed as discussed and illustrated under Data Appraisal. Consequently, only data at distances greater than 3 diameters aft of the trip strip were used.

Turbulent stagnation line data are compared in figure 22 to $\rho_r \mu_r$ infinite cylinder theory. Some trip effect is present, but the overall repeatability is acceptable. Delta wing data from the present program are indicated. The AD485M-1 shock tube data at 45 degrees sweep exhibit greater scatter, which is thought to be partly the result of the flow not being fully turbulent. The model had only two gages, and as may be seen in figure 22, the upstream gage generally indicated lower heating rates than did the downstream gage. Generally, the agreement of the data with the $\rho_r \mu_r$ method is good over the entire range of sweep angles, including some data (AD485M-1) in which real gas effects were present.

The circumferential distribution of turbulent leading edge heating is compared with the $\rho_r \mu_r$ infinite cylinder theory in figure 23. The scatter is somewhat greater for these turbulent data than for the laminar data shown in figure 18, but the data indicate substantial agreement with the theory up to 50 degrees from the stagnation line. The data at the shoulder depart from cylinder theory as in laminar flow. The data in figure 23 are from sharp-prow delta wings. Data from the blunt-prow models were not of sufficient quality to determine the existence of an effect similar to that shown in the laminar data of figure 18.

The effect of angle of attack on the maximum observed turbulent delta wing leading edge heating rate is shown in figure 24. In order to compare data from several different test conditions the data are normalized by a reference value of the Stanton number ($N_{St, ref}$) which is the theoretical turbulent stagnation line value ($\rho_r \mu_r$ theory) for a 60 degree swept cylinder with a diameter equal to the wing thickness.

The data of figure 24 exhibit trends similar to those shown by the laminar data in figure 21, agreeing well at low angles of attack with $\rho_r \mu_r$ infinite cylinder theory, but showing less increase with angle of attack. This decrease, relative to the theory is attributed to a lower surface effect similar to that observed in laminar flow. The amount of data available is not so extensive as in the laminar comparison, and the possibility of higher values than those plotted cannot be entirely discounted. However, the observed trend agrees well with the leading edge theory corrected for lower surface effects as described in connection with figure 21.

Dual-Radius Leading Edge

Model AD477M-1 was provided with a dual-radius leading edge where the larger radius was 3 times the smaller radius (see figure 2). As shown, the model had a sharp-prow and sweep angle of 73 degrees. The dual-radius

configuration could have reduced X-20 leading edge heating in flight, but was not adopted because of poor low speed aerodynamic characteristics.

Pressure data and stagnation line shift. - Pressure distributions on the dual-radius leading edge model are shown in figure 25. In this case, data are normalized with respect to the observed maximum pressures, P_{max} . P_{max} is up to 9 percent higher than calculated stagnation line pressure; it is used since leading edge sonic point locations will be of interest later. This stagnation line pressure discrepancy is felt to be due to a finite length effect, on the basis of the comparison shown in figure 10. The quality of the AD477M-1 pressure data is considered to be excellent.

Two methods were used to determine the location of the stagnation line and sonic lines from the faired data of figure 25:

- 1) the θ at which $P/P_{max} = 1$ and 0.528 for each angle of attack, and
- 2) the angle of attack at which $P/P_{max} = 1$ and 0.528 for each instrument location.

The results are presented in figure 26. The displacements predicted by the X-20 and infinite cylinder methods are shown for reference. A maximum difference of about 12 degrees from the cylindrical leading edge theory was observed at zero and negative angles of attack.

It is of interest to determine the angle of attack limits of the dual-radius effect. An examination of figure 26 shows that the stagnation line location agrees with the previously determined cylinder values except at low angles of attack. It is also seen that the convergence of the dual-radius model data to the cylinder values coincides with the movement of the upper sonic line onto the large radius portion of the leading edge. These trends are in agreement with the expected behavior, considering two-dimensional flow in the plane normal to the leading edge axis. On the basis of these data and the crossflow analogy it has been concluded that the smaller radius affects the leading edge flow only at angles of attack less than 14 degrees, and that there is no measurable effect above 10 degrees.

Heat transfer data. - Circumferential heat transfer data for the AD477M-1 dual-radius leading edge are presented in figure 27. All data are normalized with respect to $\rho_r \mu_r$ infinite cylinder stagnation line theory based on the larger radius. The theoretical distribution for the large radius is shown, adjusted to be consistent with the stagnation line location of figure 26. This adjustment improves data-theory agreement considerably over that obtained using the cylindrical leading edge stagnation line location. For this model the line of maximum heating coincides with the true flow stagnation line. Heating distributions on the larger radius are essentially unaffected by the dual-radius geometry, as indicated by the theory curves. However, cylinder theory based on the smaller radius does not agree with data obtained on that part of the leading edge.

Also shown in figure 27, at zero angle of attack, are the only turbulent dual-radius data available from the test. Data and theory both exhibit essentially the same distribution as the laminar values when normalized by the theoretical $(\rho_r \mu_r)$ stagnation line value. Incomplete transition to turbulent flow may account for the slightly reduced heating level of these data, indicated by the maximum value of $N_{St}/N_{St, SL}$ theory of about 0.90.

It appears from these data that the larger of the two radii determines the stagnation region heating level, even when the stagnation line is on the smaller radius ($\theta_{SL} = -5^\circ$ at -5 degrees angle of attack). It is expected that the smaller radius would dominate at larger negative angles of attack, but no such data were obtained. The observed behavior suggests that the shock shape in the stagnation region is determined primarily by the large radius. Although this shock shape could not be photographed, the behavior of the stagnating streamlines near the wall can be determined from the stagnation line locations, and the direction of the free stream flow determined from purely geometric considerations. Comparisons of this type (see figure 28) show that the stagnation streamline does not coincide with the free stream vector at low angles of attack.

Data on Slab Portion of Delta Wing

Pressure data--sharp prow model.— Lower surface pressure data from the centerline region of sharp prow models are shown in figure 29. At high angles of attack the data are seen to be essentially constant and in good agreement with the indicated theoretical values. The latter are based on the well-known wedge equation:

$$C_p = \frac{2[\sin \alpha][\sin(\alpha + \xi)]}{\cos \xi} \quad (9)$$

where α is the angle of attack or wedge angle and ξ is the difference between the shock wave angle and the angle of attack. Values of ξ were calculated from equation (10):

$$\xi = 70 \left(\frac{\rho_\infty}{\rho_2} \right) \left(\frac{\tan \alpha}{\tan \Lambda} \right)^{.566} \quad \text{degree} \quad (10)$$

Equation (10) is an empirical fit to numerical solutions of the flow field over a sharp leading edge delta wing by the method of reference 18. A comparison of shock wave angles predicted with equation (10) with some data from the sharp-prow dual-radius model AD477M-1 is shown in figure 30. Although the model has blunt leading edges, equation (10) is seen to agree very well with the observed shock angles.

In order to more easily compare the data with other prediction methods, the data of figure 29 are replotted in figure 31. As shown, the high angle of attack data are in fair agreement with wedge, cone, and Newtonian theories;

however, equation (9) provides the best agreement.

At low angle of attack a strong axial pressure gradient was observed, which is attributed to combined viscous interaction and leading edge bluntness effects. The viscous interaction effect was calculated with reference 19 by Bertram, which is identical to his earlier method (ref. 20) at zero angle of attack. The bluntness contribution was calculated from:

$$C_{PB} = .374 \left(\frac{\gamma - 1}{\gamma} \right)^{1/3} \left(\cos^2 \Lambda \right) \left(\frac{C_{D,LE}}{x_n/D} \right) - \frac{.52}{\gamma M_\infty^2} \quad (11)$$

The leading edge drag coefficient, $C_{D,LE}$ is to be evaluated for the Mach number normal to the leading edge. Equation (11) is based on reference 21, modified to relate the effect of the swept leading edge to the free stream dynamic pressure.

The predictions of the viscous interaction and bluntness methods are shown in figure 29. Good agreement is obtained with simple addition of the effects except in the downstream portion of the Mach 6 data, where the effect of the final term in equation (11) becomes dominant. The agreement obtained is quite surprising, since equation (11) results from purely formal operations on an expression developed for quite different conditions. Not only is the normal Mach number very low, but the condition of symmetry with respect to the centerline plane would be expected to have an effect as well. Indeed, it could be argued that the leading edge contribution should be doubled at the centerline, since the wing has two leading edges. However, it is expected that linear addition of both leading edge contributions would over predict centerline pressures.

The spanwise pressure distributions shown in figure 32 exhibit similar trends in that the high angle of attack data are essentially constant except on the leading edge itself. At angles below about 10 degrees the data are badly scattered, but do not seem to show any gradient comparable with that predicted by equation (11), except for the 0 degree angle of attack data shown in figure 32(a). The Mach 6 and 7 data actually seem to show a minimum at the leading edge shoulder. The Mach 8.08 data from the dual radius model may not provide a proper comparison at angles of attack less than about 15 degrees.

The effect of yaw on spanwise pressure distributions for the sharp prow dual-radius model is shown in figure 33. As expected, the effect is largest on the leading edge and at low angles of attack. No comparable data are available from the Mach 6 and 7 tests.

Pressure data-effect of nose bluntness.-Lower surface centerline pressure data from a blunt prow delta wing are presented in figure 34. At high angles of attack the data agree well with equations (9) and (10) except near the nose.

The poorest agreement is shown by the Mach 7 data, which were taken very early in the X-20 program, and are considered to be the poorest quality data. The Mach 8.08 data, which are in excellent agreement with equations (9) and (10) are also considered to be the best quality data. With the relative quality of the data taken into account, it is considered that there is no large effect of nose bluntness on the high angle of attack data.

The available information regarding shock shape is consistent with this observation. As shown in figure 35, the shock wave is well predicted by matching the sharp delta wing shock shape, equation (10), to a hemisphere shock, reference 22 and that the matching point is very near the nose at high angles of attack.

At low angles of attack nose bluntness was found to increase centerline pressures. A prediction of this increase was made with the correlation equation given by Van Hise (ref. 22) which is based on the blast wave analogy for hemisphere cylinders:

where

$$C_{P_n} = \frac{.060 \left[\frac{M^2}{(x/D)} \right] [C_{D_n}]^{1/2} - .45}{\frac{\gamma}{2} M_\infty^2} \quad (12)$$

C_{D_n} = nose hemisphere drag coefficient

(X is in this case measured from the geometric stagnation point and along the model axis.) The value obtained was then superimposed onto the previously described viscous and leading edge bluntness contributions so that the final theoretical pressure coefficient is:

$$C_P = C_{P_v} + C_{P_B} + C_{P_n} \quad (13)$$

Equation (13) is in fair agreement with the data in figure 34 for X/D less than about 6; at greater distances the Mach 8.08 data are well above the prediction. This latter trend persists to angles of attack of 15 degrees, and may be due to sting interference, although there is no other evidence of interference effects. Near the nose the data fall below the prediction for all but the highest angles. This effect is believed to be a characteristic overexpansion of the flow from the nose, similar to that observed on hemisphere-cylinders by Van Hise (ref. 22) and others.

Spanwise pressure distributions for zero yaw are shown in figure 36. As with the centerline data, no large effect of nose bluntness was observed at high angles of attack. At zero angle of attack the data of figure 36c show a consistent increase over data shown in figure 32b. However, at all other attitudes no consistent difference is apparent.

The effect of yaw on spanwise pressures on the blunt prow model is shown in figure 37. The results are very similar to those shown in figure 33 for the sharp prow model, allowing for the different yaw angles in the two tests.

The effect of ramp angle is shown in figure 38. Based on the previous comparisons equation (9) is expected to apply to the forward portion of the wing for high angles of attack. Also, far downstream of the fold line equation (9) should again apply, as the effect of the ramp cannot extend infinitely far. Immediately downstream of the fold line, however, equation (9) is expected to over-predict the local pressure, since a local flow expansion calculation would show a greater pressure drop at the fold than does equation (9). Based on the data shown, it appears that the effect of the ramp extends at least 16 nose diameters, or at least twice the length of the ramp. However, these data, which were taken early in the X-20 program, are of relatively poor quality, and are not considered definitive for the relatively small effect shown.

Real gas effect.- Centerline pressure data from blunt prow delta wing models tested in a supersonic wind tunnel and a shock tube are presented in figure 39. The shock tube data were taken in conjunction with tests to determine real gas effects on heat transfer. Pressure data are available from only the low enthalpy shock tube tests, since the pressures obtained in high enthalpy tests could not be contained by the shock tube windows. Dissociation levels were up to 10 percent ($Z = 1.1$) for the data shown, however. The wind tunnel data were taken to provide comparable ideal gas pressures, to provide more detailed distributions than could be obtained with the Mach line technique used in the shock tube tests, and to provide streamline data for analyzing shock tube heat transfer data.

The shock tube data are found to be somewhat lower than the wind tunnel data which are well-predicted by simple cone theory.

Shock tube pressure data could not be obtained at angles of attack greater than about 37 degrees. As stated earlier, shock tube pressure data were obtained by reading local Mach angles. The absence of Mach lines at higher angles is interpreted as indicating that the lower surface flow had become subsonic.

Delta Wing streamline data.- Streamline pattern data were taken in several of the tests by the direct transfer technique described under EXPERIMENTAL TECHNIQUE AND DATA REDUCTION. The direct transfer technique was used in order to obtain true flow patterns rather than the projected views that photographs provide. Some examples of the direct transfer streamline patterns are shown in figure 40. Although difficult to reproduce, the flow patterns were found to be more easily read quantitatively from the original direct transfers than from photographs. Samples of streamline angle readings are presented in figure 41; the faired results of other readings are presented in figure 42.

Both the blunt and sharp prow streamline patterns exhibit more outflow near the trailing edge than near the apex. The observed behavior is consistent with the variation of the streamline angle at the leading edge shoulder, shown in figure 43. The condition of symmetry about the centerline requires that the outflow angle begin from zero at the intersection of the leading edge shoulders, while far downstream it is expected to agree with the sharp delta wing predictions presented in appendix C. As shown, in figure 43 the streamline angle at the leading edge is still increasing at the trailing edge of the model for angles of attack greater than 35 degrees. The comparison of observed streamline angles on blunt and sharp prow models presented in figure 44 shows similar trends.

It should be noted that oil flow patterns do not necessarily indicate the true direction of the external flow. Laminar flow theory for yawed cylinders and yawed cones (references 23 and 24) indicate that the outflow angle as indicated by the direction of the shear force at the surface may be a factor of two or more greater than the outflow angle of the external flow. The magnitude of the effect in turbulent flow cannot be calculated, but is thought to be much less.

Laminar-heating--sharp prow model.- Laminar heating data were obtained on two sharp prow models in the present program, the cylindrical leading edge model AD465M-1 and the dual-radius leading edge model AD477M-1. Data from the centerline regions normalized by a theoretical hemisphere stagnation point value, are presented in figure 45. Data are shown only for angles of attack greater than 20°. At lower angles the data were of poor quality and apparently transitional. As discussed previously in the section on dual radius effects, it is believed that there is no significant effect of the smaller radius on lower surface flow in this angle of attack range.

Comparisons have been made with two theoretical methods: two-dimensional $\rho_r \mu_r$ flat plate theory, and a three-dimensional method using outflow calculations based on Appendix C. Both methods are strictly applicable only to sharp leading edge models, so that some equivalent boundary layer origin must be selected. Accordingly the $\rho_r \mu_r$ theory is evaluated for two different distances, as indicated on the figure.

Far forward, and at low angles of attack, the data are seen to agree best with the two-dimensional theory, while farther aft and at higher angles the data agree better with the three-dimensional theory. These trends are consistent with the discussion of flow patterns, which showed less outflow near the apex than farther aft.

Spanwise heating distributions on the dual-radius sharp prow model at zero and 10 degrees yaw are presented in figure 46, again in the angle of attack range for which the effect of the smaller radius is thought to be negligible. The theoretical prediction for the stagnation line of an infinite cylinder is shown for each angle of attack and for both the unyawed and yawed attitudes. The data for the unyawed case are seen to fall well

below the theory, as was noted in a previous section. The stagnation line data for the yawed case show much less reduction. It will be noted that the observed effect of yawing the model 10° on stagnation line heating is approximately constant throughout the angle of attack range at about 40%, in contrast to the infinite cylinder prediction that the effect decreases to less than 10% at 40 degrees angle of attack.

The theoretical curves shown in figure 46 were computed by equating the flow to that on an unyawed blunt wedge. The free stream Mach number is taken to be the actual free stream component normal to the leading edge stagnation line, and the equivalent angle of attack is given by the stagnation line shift (see figure 28). It was known that this analogy provides excellent estimates of pressure and heat transfer coefficient near the stagnation line of a yawed cylinder.

The method is seen to predict the heat transfer distribution on the leading edge reasonably well, but the predicted heating rates fall well below the data near the center of the wing.

Laminar heating--bluntness effects.-- Centerline heat transfer data from blunt prow delta wing model AD462M-1 are presented in figure 47, normalized with respect to the stagnation point theoretical value. Comparison of these data with figure 45 show a reduction of 30% or more below the corresponding sharp prow data, except near the hemisphere tangent point.

Three $\rho_r \mu_r$ theoretical values are presented for comparison. Each value was computed assuming that the effects of three-dimensional flow on heat transfer is not significantly influenced by cross flow pressure gradients. The sharp delta wing $\rho_r \mu_r$ method previously described is seen to greatly overpredict the data, even when based on the distance from the theoretical apex. The two blunt prow curves were calculated by the method of Appendix B using pressure data from figure 34. Both calculations are matched to the hemisphere shoulder value. The three-dimensional calculation incorporates the sharp delta wing prediction of outflow angles described in Appendix C. Since the observed outflow angles on the blunt delta wings were found to be much less than this method predicts, the two-dimensional theory is also shown. Streamwise pressure gradients are taken into account in both blunt prow calculations.

The data are seen to fall below the blunt prow theories except at the highest angles of attack, and except for a short distance aft of the nose. No streamline data are available from these specific tests. The lower Mach number data from AD461M-1 tests all indicate the existence of some outflow, from which it would appear that three-dimensional effects do not explain the tendency of the data to fall below the theory. However, the oilflow data of reference 1 demonstrate the existence at low angles of attack of a much more complex flow field than is assumed by the theory shown here, which apparently reduces the local heat transfer. As the angle of attack increases, the agreement with the theory generally improves. The exception, the high data point at $X/D = 12$ for 30° angle of attack is thought to be transitional.

Spanwise distributions of laminar heat transfer on the blunt prow delta wing are presented in figure 48. The sharp-prow zero yaw data and theory from figure 46 are also replotted for comparison. The blunt prow data are seen to follow trends that are consistent with the previous observations, the sharp prow leading edge data being generally higher than the blunt prow model data. There appears to be a trend wherein prow bluntness increases heating inboard of the leading edge at low angles, but causes a reduction at high angles.

Spanwise distribution of laminar heat transfer data and theory on a yawed blunt prow delta wing are shown in figure 49. The data and theory shows trends similar to those shown in figures 46 and 48 for the zero yaw case. The cross flow theory tends to overpredict the heat transfer distribution at the leading edge, and underpredicts the heating rates on the lower surface. The effect of yaw on blunt delta wing centerline heat transfer presented in figure 50 indicates the presence of transition effects.

Delta Wing Turbulent Heating

Delta wing heating rates with turbulent boundary layer flow are presented in figures 51 through 56. The majority of the data were obtained in the Boeing Hypersonic Wind Tunnel which provided a much higher Reynolds number than was available in other facilities, but whose small test section limited model size to about 7 inches. For this reason it was not possible to instrument the models as thoroughly as was desired. As on the leading edge models, turbulent flow could be obtained only with the aid of boundary layer trips, which invalidated some of the data. However, turbulent data were obtained for many conditions that are believed to be of good quality. Particularly interesting are the shock tube data, since these are the only known delta wing data taken under conditions for which real gas effects are present.

Sharp-prow models. - Turbulent heating data from the sharp-prow models are presented in figures 51, 52, and 53. Centerline data are presented in figure 51, together with theoretical predictions according to the $\rho_r \mu_r$ method given in Appendix B. As previously discussed in connection with figure 45 there is no clear choice of an equivalent sharp delta wing apex for beginning boundary layer calculations. The effective origin of the laminar boundary layer is expected to lie someplace between the sharp-prow and the intersection of the leading edge shoulders. Since turbulent flow could not be obtained without a boundary layer trip it is believed that the flow remained laminar up to the trip. The effective origin of the turbulent boundary layer may therefore be downstream of the leading edge shoulder intersection. The data indicate, however, fully turbulent flow just downstream of the trip so that the effective origin cannot be downstream of the trip.

Accordingly, three possible applications of the theory are shown: three-dimensional theory based on distance from the model apex, and two- and three-dimensional theory based on distance from the trip. The

three-dimensional theories include streamline divergence based on sharp delta wing streamlines as predicted by the method of Appendix C.

The data are well predicted by the theory based on distance from the trip. It is not possible to demonstrate the existence of a three-dimensional flow effect, however, as the predicted effect is less than the uncertainties in the data. It is felt that the high angle of attack data are the most reliable, for several reasons:

1. Heating rates are highest, minimizing instrument errors.
2. Pressures are least affected by bluntness or viscous interactions.
3. Three-dimensional effects are largest, hence most easily observed.
4. Transition occurred very near (or on) the trip.
5. Total pressure losses (due to small shocks caused by the trip) are less because the local Mach number is small.

In contrast, the lowest angle of attack data appear to be only partially tripped. Considering the relative data quality, it appears that the present tests do not support the predicted existence of a streamline divergence effect in turbulent flow. In this connection, it will be recalled that the leading edge data clearly establish the existence of streamline divergence effects in turbulent flow (since otherwise the heating rate would vary with distance along the stagnation line) and that predictions based on Appendix B including the three-dimensional effect agree well with the experimental leading edge results. It is clear, however, that three-dimensional effects are not appreciably larger than the theory predicts and that two-dimensional theory is adequate to predict the present delta wing data up to angles of attack of 40°.

The spanwise distributions of turbulent heating on the sharp-prow model are presented in figure 52. The theoretical curve shown is based on the two-dimensional and three-dimensional centerline theory just described and the turbulent infinite cylinder theoretical distribution. A curve has been interpolated by

$$N_{St} = \frac{N_{St,SH}}{\left\{ \frac{\left(\frac{N}{D}\right)_{SH} - \left(\frac{N}{D}\right)_{CL}}{\left(\frac{N}{D}\right)_{CL} - \left(\frac{N}{D}\right)_{SH}} \left[\left(\frac{N_{St,SH}}{N_{St,CL}}\right)^5 - 1 \right] + 1 \right\}^{1/5}} \quad (14)$$

As shown, the interpolation agrees well with the data when the centerline heat transfer coefficient was the two-dimensional value, as well as those based on the three-dimensional centerline value. Again, the three-dimensional effect is small, so that no firm conclusions should be drawn.

The effect of yaw on the lower surface turbulent heating is shown in figure 53 to be small. A low angle of attack case ($\alpha = 10^\circ$) is shown as an example, since yaw effects tend to be more pronounced for this condition. Although heating on the windward side appears slightly higher for the yawed condition, the increase is of the same magnitude as the data scatter. This result was also found in examining the sharp-prow laminar heating data (figure 46).

Bluntness Effects.- Turbulent data presented in figure 54 show that, as with the laminar case, heating near the nose is reduced by nose bluntness. As indicated by the theory curves the effect of bluntness is much larger than the three-dimensional flow divergence effect, whereas in laminar flow (figure 47) the three-dimensional effect dominates. Only one set of theory curves is shown, the effect of the Mach number and Reynolds number variations being negligible in the normalized method of presentation. There is considerable scatter in the data near the nose which may be the result of flow disturbances due to the boundary layer trips. However, it will be noted that the data for any particular Reynolds number usually exhibit quite consistent trends, and may be showing a characteristic transitional flow behavior.

Farther downstream the data show two overall trends: the lower Reynolds number data are consistently higher, and the data tend to rise relative to the theoretical predictions. Both trends are consistent with the expected bluntness effects. At low angles of attack the air that has passed through the strong shock created by the blunt nose will remain near the centerline of the wing, and so may be expected to affect the boundary layer for a considerable distance. The effect of the strong shock is to cause much of the energy of the inviscid stream to be transferred from the kinetic form (velocity) to internal modes (temperature, dissociation, etc.) reducing both the local density and velocity. A reduction in boundary layer heat transfer also results. Ultimately, however, the air that has passed through the strong shock will be absorbed into the boundary layer, and the bluntness effect will disappear. The lower the Reynolds number, the thicker the boundary layer, and hence the more rapidly the bluntness effect will be lost. At high angles of attack the oil flow data show that the streamlines diverge, and it is clear that the air that passes through the strong bow shock will be spread out over a much wider region of the wing, and therefore absorbed by the boundary layer in a shorter distance. The 30-degree angle of attack data would indicate that the bluntness effect disappears in only about 6 nose diameters, or less, for that case.

Centerline data from a blunt delta wing model tested in the 4-inch shock tube are presented in figure 55. As shown, the data are in excellent agreement with the $\rho_r \mu_r$ theory under conditions much different from those of the previous figures. Although the free stream Mach number is low, that total temperature is much higher than in the wind tunnel tests, due to the very high free stream static temperature. The stagnation point gas temperature is calculated to be 9000°R, and the corresponding dissociation level is 10 percent ($Z = 1.1$). Calculations used the ideal gas hemisphere and sharp cone pressure theories of figure 39.

Effect of forward ramp. - The effect of ramp angle on the turbulent heat transfer to the centerline of a blunt-prow delta wing is illustrated by the data of figure 56. Also presented are data for a flat delta wing at the same angle of attack. As expected, the heating is always higher on the ramp, since the ramp is at a higher angle of attack with respect to the free stream flow. Heating rates downstream of the ramp are seen to be slightly less than on the flat wing. This trend is also to be expected. The higher shear forces and heating rates on the ramp imply greater losses of momentum and energy from the boundary layer than on the corresponding flat delta wing, leading to lower heating rates aft of the ramp.

CONCLUDING REMARKS

An analysis has been made of delta wing pressure and heat transfer test data taken during the X-20 program. The data were taken in conventional wind tunnels, a shock tunnel, and a shock tube. Test Mach numbers were from 2.2 to 15; test Reynolds numbers per foot were from 2×10^4 to 17×10^6 . Angles of attack were from zero to 45 degrees with yaw angles of 0 to 10°. Laminar and turbulent boundary layer data were obtained. The turbulent data were obtained by adding trips in the nose region of the models.

The basic model tested was a 73-degree swept leading edge blunt delta wing having equal nose and leading edge diameters. Lengths of the models were from 3 to 15 nose diameters. Variations about the basic model included sharp prow configurations formed by the intersection of the cylindrical leading edges, sweep angles of 68 and 78 degrees, and a dual radius configuration with the lower radius three times larger than the upper radius.

Both the heating and the pressure data from the sharp prow model leading edges were higher than infinite cylinder stagnation line theory for several nose diameters. Leading edge heating and pressure data from the blunt prow model show good agreement with hemisphere theory at the tangent point, followed by a sudden decrease to approximately 30 percent less than the cylinder theory. Both the pressure and the heating data then slowly increase toward the cylinder theory.

The stagnation line of the delta wing leading edges was found to move more rapidly with angle of attack than predicted by infinite cylinder theory, moving onto the wing lower surface at about 35 degrees angle of attack. However, the point of maximum heating moves less rapidly than predicted by infinite cylinder theory or indicated by data defining the stagnation line location. These effects are accompanied by a reduction in the maximum heating rate relative to infinite cylinder theory that begins at about 15 degrees angle of attack and increases to about 30 percent at 30 degrees angle of attack. The observed reduction in heating rate is about the same in laminar and turbulent boundary layers. An empirical method for predicting the reduction was devised based on infinite cylinder theory that is in good agreement with the observed trends.

The presence of the smaller radius on the delta wing having a dual radius was found to influence the stagnation line shift angle at small angles of attack. Location of maximum heating appears to coincide with the flow stagnation line, however. At zero angle of attack the maximum heating rate is about 10 percent higher than infinite cylinder theory based on the larger radius, but at high angles of attack heating on the larger radius was seemingly unaffected by the smaller radius.

At high angles of attack delta wing centerline pressure coefficients were found to be well predicted by wedge theory, when the shock wave angle is based on numerical solutions of the sharp delta wing flow field given by a correlation formula. The predictions are in excellent agreement with observed shock wave angles for both blunt and sharp prow models. At low angles of attack strong axial pressure gradients were observed in all tests. The data are in good agreement with predictions for viscous interaction and bluntness induced pressure effects. Yawing the model 10 degrees was found to produce sizeable increases in pressure and heating on the windward side, even at the highest angles of attack tested.

Aerodynamic heating data from the centerline region of the sharp prow delta wings were compared to a previously unpublished prediction method and were found to be in good agreement for angles of attack up to 40 degrees. High angle of attack laminar heating data were well above two dimensional theory, but in good agreement with three-dimensional theory. The blunt prow delta wing data, however, were in the best agreement with two-dimensional theory at all angles of attack. Spanwise distributions of laminar heat transfer coefficients in the vicinity of the leading edge were compared to normal component theory and found to agree well only on the leading edge. Inboard, the data are well above the theory.

Turbulent data from the centerline region of sharp prow models are also well predicted by the three-dimensional theory for angles of attack up to 40 degrees. However, the predicted three-dimensional effects in turbulent flow are small, so that the data are also in good agreement with the two-dimensional theory. The calculations show a large effect of bluntness on turbulent heating that is observed at low angle of attack. The data indicate that the bluntness effects are decreased as the angle of attack is increased.

APPENDIX A

THOMAS-FITZSIMMONS CONDUCTION CORRECTION METHOD

(T-F METHOD)

By A. L. Nagel, A. C. Thomas, and H. D. Fitzsimmons

Introduction

The thin skin calorimeter technique has proved to be one of the simplest and most reliable methods for obtaining heat transfer data in conventional wind tunnels. However, conduction within the skin can often lead to large errors in evaluating heat transfer. The effect is most severe when the aerodynamic heating distribution has large gradients, and always reduces the measured heating rate at points of peak heating.

Although every effort is made to uniformly cool the model before each test, experience has shown that small temperature differences cannot be avoided. Even small temperature differences can cause large gradients over small distances, and can give rise to substantial conduction rates at the test start. Examples of this effect will be shown.

The most common method of correcting for conduction is to calculate the conduction heating rate directly from measured model skin temperatures. However, this calculation requires the second derivative of temperature (actually $\nabla^2 T$) which is difficult to obtain accurately. Finite difference approximations to the second derivatives can be written, but in application this approach is subject to several disadvantages: 1) closely spaced thermocouples are required, 2) thermocouples are required surrounding the point where corrections are made, and 3) small errors in the absolute temperature measurement can lead to large errors in the calculated correction.

Attempting to overcome these objections, an entirely different approach was developed by Conti, reference 25. Noting that for an initially isothermal model conduction effects arise solely from uneven aerodynamic heating, Conti, calculated the approximate temperature response of a thin skin for various assumed aerodynamic heating distributions. His results are presented in equations and charts for plates, wedges, cones, cylinders, and spheres, and are useful in designing tests so as to minimize conduction errors. However, the correction of measured heating rates by this method is possible only if the distribution of aerodynamic heating is known. Usually, however, the purpose of the test is to determine the aerodynamic heating distribution, so that Conti's method can be applied

only in an iterative manner. The method also fails to account for initial model non-isothermality due to unequal cooling or to flow disturbances at initiation of the test.

The method described here was developed in 1960 and 1961 independently of Conti's work but following a similar line of thought. The method avoids the requirement for spatial derivatives of either the model temperature or heating rate, and does consider an initially non-isothermal model. The method is well adapted for computer programming since all calculations are based on temperature-time data from a single thermocouple. The method is currently computer programmed and in use at Arnold Engineering Development Center, as well as at The Boeing Company.

Derivation

The heat balance for a differential element of a model skin may be written as

$$\rho c \tau \frac{\partial T_w}{\partial t} = h (T_{aw} - T_w) + \nabla (k \tau \nabla T) \quad (A1)$$

provided that the skin thickness, τ , is sufficiently small that the temperature at the inside surface is not appreciably different from that at the outside surface. Neglecting the variation of ρ , c , and k with temperature, equation (A1) may be written

$$\frac{\partial T_w}{\partial t} = \frac{h}{\rho c \tau} (T_{aw} - T_w) + \alpha \nabla^2 T_w \quad (A2)$$

The Laplacian operator ∇^2 is defined by

$$\nabla^2 = \frac{\partial^2}{\partial x^2} + \frac{\partial^2}{\partial y^2} + \frac{\partial^2}{\partial z^2}$$

In the present applications, temperature gradients through the model skin are neglected, so that for flat surfaces:

$$\nabla^2 = \frac{\partial^2 T}{\partial x^2} + \frac{\partial^2 T}{\partial y^2}$$

where x and y are measured in the plane of the skin, and are orthogonal.

Equation (A2) in terms of the temperature excess, θ_w , above the average initial temperature of the model, \bar{T}_w , becomes

$$\frac{\partial \theta_w}{\partial t} = \frac{h}{\rho c \tau} (\theta_{aw} - \theta_a) + \alpha \nabla^2 \theta_w \quad (A3)$$

where

$$\theta_w = T_w - \bar{T}_w$$

$$\theta_{aw} = T_{aw} - \bar{T}_w$$

The temperature excess, θ_w , is now defined to consist of two terms such that

$$\theta_w = \theta_a + \theta_i \quad (A4)$$

With this definition, equation (A3) becomes

$$\frac{\partial \theta_a}{\partial t} + \frac{\partial \theta_i}{\partial t} = \frac{h}{\rho c \tau} (\theta_{aw} - \theta_a) + \alpha \nabla^2 \theta_a + \alpha \nabla^2 \theta_i - \frac{h}{\rho c \tau} \theta_i \quad (A5)$$

Since θ_a is still arbitrary, we now require

$$\frac{\partial \theta_a}{\partial t} = \frac{h}{\rho c \tau} (\theta_{aw} - \theta_a) + \alpha \nabla^2 \theta_a \quad (A6)$$

and that

$$\theta_a(x, y, t = 0) \equiv 0$$

Defined in this way, θ_a is seen to be the temperature response of the model in an ideal test wherein the model is initially exactly isothermal. The term $\alpha \nabla^2 \theta_a$ arises only from non-uniform aerodynamic heating and is called the "impressed conduction."

From equations (A5) and (A6) it follows that:

$$\frac{\partial \theta_i}{\partial t} = \alpha \nabla^2 \theta_i - \frac{h}{\rho c \tau} \theta_i \quad (A7)$$

From the definitions given, θ_i at the time zero is seen to represent the initial temperature distribution. The conduction term $\alpha \nabla^2 \theta_i$ which results from initial temperature gradients is called "initial conduction." It is seen that θ_a does not appear in the equation for θ_i . This separation of initial and impressed conduction effects is the essential step in the development of the present method. If the initial model temperature distribution were known, θ_i could be calculated for later times from equation (A7). Although θ_i is in general not known, its behavior can be deduced from equation (A7) as follows:

At the location where $|\theta_i|$ is at its maximum

$$\frac{\partial |\theta_i|}{\partial t} < 0 \quad (A8)$$

Equation (A8) follows from equation (A7), provided only that α and h are positive. Since $|\theta_i|_{\max}$ is always decreasing, then*:

$$\lim_{t \rightarrow \infty} \theta_i(x, y) = 0$$

*In actual practice, this limit is approached very quickly. Since the error in data reduction is due to the derivative $\partial \theta_i / \partial t$ rather than to θ_i , the time the effect persists is approximately

$$(\partial \theta_i / \partial t) \Delta t \approx \theta_i$$

which implies that no large errors can be of long duration unless θ_i is large. Numerical and experimental examples are given later.

In an actual test θ_a is unknown and θ_i is known only at time zero. Only the sum θ_w , is measured and known at all times. For this reason it is now convenient to introduce the measured heat transfer coefficient, h_m , and the ideal heat transfer coefficient, h_a ;

$$h_m = \frac{\rho c \tau}{T_{aw} - T_w} \frac{\partial T_w}{\partial t}; \quad h_a = \frac{\rho c \tau}{\theta_{aw} - \theta_a} \frac{\partial \theta_a}{\partial t} \quad (A9)$$

Note that h_m is not necessarily equal to the true aerodynamic heat transfer coefficient at any time. However, at time zero h_a is exactly the true heat transfer coefficient. Therefore, h_a is expanded about $t = 0$ as follows:

$$h_a = h_a(0) + t \left. \frac{\partial h_a}{\partial t} \right|_0 + \frac{t^2}{2!} \left. \frac{\partial^2 h_a}{\partial t^2} \right|_0 + \dots \quad (A10)$$

Compare series (A10) with the series

$$h_m = A + B t + C t^2 + \dots \quad (A11)$$

where the coefficients A, B, . . . , etc., are determined by fitting a curve to the h_m data. The discussion of initial conduction shows that

$$\lim_{t \rightarrow \infty} h_m = h_a$$

Therefore,

$$\begin{aligned} A &\approx h_a(0) = h \\ B &\approx \left. \frac{\partial h_a}{\partial t} \right|_0 \\ C &\approx \frac{1}{2} \left. \frac{\partial^2 h_a}{\partial t^2} \right|_0 \end{aligned} \quad (A12)$$

provided that the curve is fitted in a time interval after the effects of initial conduction are negligible.

Without specifying θ_i the accuracy of approximations (A12) cannot be established analytically. The number of terms used in equation (A11) must be limited; otherwise, initial conduction effects and (in actual practice) measurement errors will have a large effect on the coefficients of the high order terms. It has been found, both by computer simulations and with actual data, that the series (A11) should contain only three terms for best results.

To summarize, the data reduction procedure by the T-F method consists of:

1. Computing a history of measured heat transfer coefficients, h_m (equation A9).
2. Establishing time zero, the time at which aerodynamic heating begins.
3. Establishing a time at which initial conduction effects become negligible, t_a .
4. Fitting a least squares, second degree curve to the h_m values at times greater than t_a and evaluating the constant coefficient h in equation (A11) at time zero.

Some examples of numerical computations and data will now be given to verify the foregoing analysis.

Verification

The rapid decay of initial conduction with time is illustrated by the numerical calculations of figure 57 for a nickel slab. Initial non-isothermality was $\pm 4^\circ\text{R}$ upon which was superimposed a flat plate heating distribution. Initial conduction, compared to the aerodynamic heating rate, is negligible in this case after about one second. This time is indicated in figure 57 by t_a ; after time t_a only impressed conduction remains. Note that even for this small, but typical non-isothermality, the initial conduction is substantial. This conduction effect is governed by equation (A7).

Numerical calculations illustrating the rapid increase of impressed conduction with time are typically shown in figure 58 for a nickel leading edge model. Here, an initially isothermal model was exposed to a circumferential heating rate distribution similar to that for a delta wing leading edge. Impressed conduction is seen to become substantial at one second, particularly at the shoulder where the spatial derivatives of the aerodynamic heating rate are large. This impressed conduction effect is governed by equation (A6).

Figure 59 illustrates the results of the T-F conduction correction method when applied to the impressed conduction case of figure 58. The solid line of figure 59 is the input heat transfer coefficient distribution. Open symbols represent the uncorrected "data" reduced at 0.3 seconds; their departure from the solid line indicates the amount of impressed conduction error at this time. The filled symbols show the conduction corrected values. The input heating rate is predicted well by "data" corrected positively in the stagnation line region and negatively near the shoulder. The experimental conduction effect simulated by the computer studies of figures 58 and 59 is illustrated in figure 60. Here, AD461M-1 leading

edge data are shown reduced at 0.3 seconds (open symbols) and conduction corrected (filled symbols). Initial conduction was present. Positive corrections near the stagnation line are again in evidence. A negative 7.7 percent correction was applied at the shoulder location. Typical experimental heat transfer coefficient histories for this test are shown versus time in figure 61. Impressed conduction rates are seen to be up to 100 percent per second near the lower surface apex. The solid line connecting the data points represents equation (A11).

An example of data severely affected by initial conduction is given in figure 62. Figure 62 (a) shows the temperature history taken 40 degrees from a spherical nose stagnation point. Unsteady flow occurred during the first 0.5 seconds (shock impingement or tunnel blockage), causing the temperature to rise abruptly. A plot of the measured heat transfer coefficient, figure 62 (b), shows initial conduction caused the measured data to be 4.25 times the theoretical value at 0.4 seconds. In figure 62 (b) initial conduction effects are still evident at one second; in fact, by expanding the scale as in figure 62 (c), initial conduction is seen to last up to two seconds. The T-F method applied to the data interval between 2.9 and 8.9 seconds predicts a corrected heat transfer coefficient about three percent from theory. In this special case, time zero has been taken as 0.5 seconds, the end of the unsteady flow period, or the beginning of aerodynamic heating. It is pointed out that the measured heat transfer coefficient history before two seconds is not necessarily typical in shape and decay time with that at any other model location; any "agreement" with theory in this time period is fortuitous. Data closer to the stagnation point, but having similar initial conduction, were used to make the statistical accuracy study shown in figure 5 under DATA APPRAISAL.

Practical Application

Depending upon the facility, time zero may be the time the model reaches the edge of the tunnel core, the time flow is established over the model or, if the model exposure time is short, simply the time at which the test is initiated. Unless the impressed conduction rates are extremely high, small errors in time zero (possibly 1/4 to 1/2 second) are acceptable. Establishment of t_a , the time at which initial conduction effects become negligible, is somewhat more arbitrary. Examination of typical measured heat transfer coefficient histories will generally disclose a time at which only impressed conduction is present. If initial conduction effects are weak, little accuracy is lost by picking an arbitrary time for t_a of the order of 0.5 to one second. The method of computing $\partial T_w / \partial t$ was discussed previously in this report under DATA REDUCTION. It is generally necessary to compute h_m over the initial conduction time period in order to help establish time t_a . The initial conduction affected values of h_m may then be left unused in the curve fitting process of equation (A11). If the h_m history is substantially linear in time or exhibits excessive experimental scatter or irregularity, it is more practical to substitute a linear least squares curve fit for equation (A11).

If the h_m history is highly curved or the initial conduction severe, the demands upon the least squares technique to define equation (All) require accurate data over a longer time period. The use of a third or higher degree curve fit in an attempt to account for higher terms in equation (All) has been found unsatisfactory. The data scatter or irregularity usually present in the h_m history is interpreted in the least squares calculation as actual curvature. Highly erroneous corrections may appear. The possible advantage, therefore, is limited by practical problems.

Lastly, the T-F conduction correction method does not eliminate the usual requirements upon the experimentalist for good judgment and "custom" care in the handling of experimental heat transfer data. The method, however, does provide a useful tool for significantly improving heat transfer data quality, even in data severely affected by conduction.

Temperature Extrapolation

The essence of the method described so far is the representation of impressed conduction as a power series in time. Since the conduction is actually a function of temperature rather than time, it appears that the variation of h_m with temperature would be more nearly linear than the time series (All). Also, the extrapolation against temperatures has a well defined end point, the initial temperature, avoiding the aforementioned uncertainty in time zero.

In practice, there appears to be no clear-cut improvement with the temperature extrapolation process, however. In most cases the h_m versus temperature curve is slightly more linear but no large change in the corrected heat transfer coefficient is observed. The small difference that has been observed usually increases the corrected heat transfer coefficient slightly, as illustrated by the comparison of figure 63. It is seen that scatter of the corrected data is essentially the same; the mean value is about 3% higher according to the temperature extrapolation process.

A sample h_m versus temperature curve is shown in figure 64. Figure 64 is for the same data as figure 62 (c).

APPENDIX B

LAMINAR AND TURBULENT $\rho_r \mu_r$ HEAT TRANSFER METHOD

The $\rho_r \mu_r$ method used for theoretical predictions throughout this report was developed by Richard A. Hanks in the course of the X-20 program. The method is based on the integral form of the boundary layer momentum equation. This equation is transformed into an equivalent incompressible form that is then solved to yield a generalized equation that includes the usual boundary layer thickness and form factors as undetermined functions. For laminar flow these functions were evaluated by equating the generalized equation to exact numerical solutions of the differential equations for self-similar boundary layers. Two apparently universal boundary layer functions were evaluated that allow a general heat transfer equation to be written that agrees with essentially all of the exact similarity solutions to within about 3 percent, including the effects of fluid property variations, finite streamwise and crossflow pressure gradients, and streamline divergence. The two functions are:

1. a reference value of the density-viscosity product $\rho_r \mu_r$ that depends only on the density-viscosity products evaluated at the wall, edge, and stagnation enthalpies, and
2. a boundary layer profile parameter, Γ , that depends only on the density evaluated at a linear combination of the wall, edge, and stagnation enthalpies.

No analytic expressions for these functions were derived, and all results in this report were calculated with the aid of curves given in this appendix. Recently, however, simple expressions have been found that agree closely with the plotted curves.

The extension to turbulent flows was guided by the laminar results, physical considerations, and comparisons with experimental results. The functions $\rho_r \mu_r$ and Γ are retained in the turbulent flow method, and are equal to the laminar values. However, the expressions used to calculate the heating are of course somewhat different, and so the effects of $\rho_r \mu_r$ and Γ on the heating rate are also somewhat different. The general form of the basic momentum integral equation allows turbulent flow heat transfer data from different sources to be compared on a consistent and systematic basis. During the X-20 program extensive comparisons to experimental data were made in which no data were consciously ignored. The method described here reflects those comparisons. Although the derivation given is restricted to the vicinity of a plane of symmetry, the resulting expressions have been applied to infinite cylinder distributions with good results.

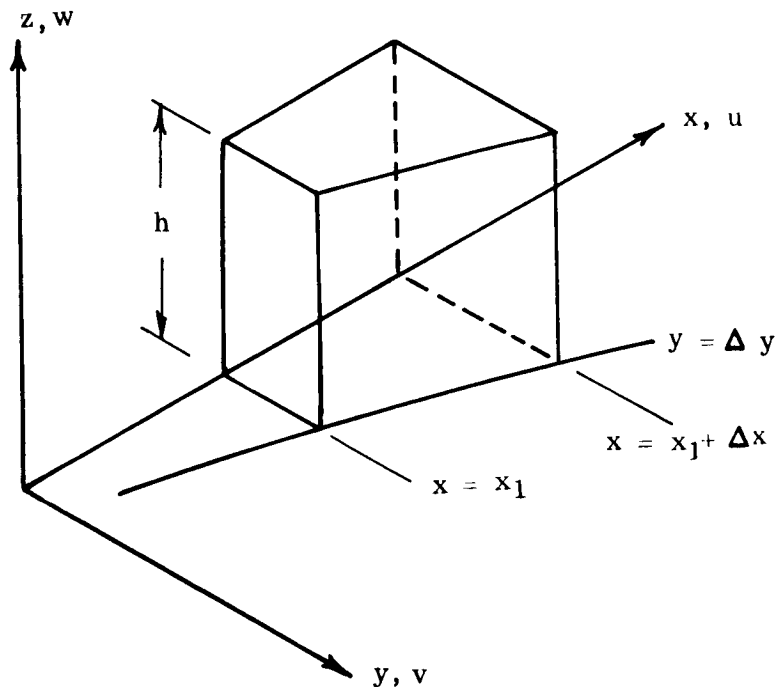
The following discussion describes the method as it is now programmed for digital computers and as it was used in the preparation of the present report. Some modifications of the method have been made under NASA contract

NAS8-11321 which are not included in the present calculations. These modifications are primarily for flow conditions other than those of the data discussed in this report, and do not lead to appreciable numerical differences here. Further information regarding the later modifications may be obtained from reference 40. The following description of the derivation and application of the method is in six parts:

1. Derivation of a general form of the boundary layer momentum integral equation.
2. Transformation of the integral equation to an equivalent incompressible form.
3. Correlation of exact laminar solutions.
4. Evaluation of turbulent boundary layer parameters.
5. Combined laminar and turbulent method.
6. Summary of method and simplified equations.

DERIVATION OF THE MOMENTUM INTEGRAL EQUATION

A derivation of the boundary layer momentum integral equation in a general curvilinear coordinate system will now be given. The derivation is restricted to the vicinity of a plane of symmetry as well as by the usual boundary layer assumptions. A control volume is defined as shown in the sketch below:



The length elements in the x and z directions are unity. However, the length element for y is determined by the function $g = g(x)$, which is considered arbitrary (subject to the restriction that dg/dx remains finite). Later it will be seen that in some cases the most convenient choice of g is determined by the shape of the body under consideration. The height of the control volume, h , is constant and must be larger than the boundary layer thickness but is otherwise arbitrary. The surface $y = 0$ coincides with the straight streamline; hence $v = 0$ when $y = 0$. However, v is not necessarily zero nor even constant on any other surface of constant y .

Mass conservation. - The mass entering the control volume through the surface $x = x_1$ is given by:

$$\Delta y \left[g \int_0^h \rho u dz \right]_{x_1}$$

The mass leaving at $x = x_1 + \Delta x$ is given by a similar expression. Expanding in a Taylor series, and retaining only the first order term yields:

$$\begin{aligned} & \Delta y \left[g \int_0^h \rho u dz \right]_{x_1 + \Delta x} \\ &= \Delta y \left[g \int_0^h \rho u dz \right]_{x_1} + \Delta y \Delta x \frac{\partial}{\partial x} \left[g \int_0^h \rho u dz \right] \end{aligned} \quad (B1)$$

so that the mass remaining within the control volume is:

$$- \Delta y \Delta x \frac{\partial}{\partial x} \left[g \int_0^h \rho u dz \right] \quad (B2)$$

Applying this technique over all six surfaces of the control volume, and requiring steady flow, yields:

$$\Delta x \Delta y \frac{\partial}{\partial x} \left[g \int_0^h \rho u dz \right] + \Delta y \Delta x \frac{\partial}{\partial y} \left[\int_0^h \rho v dz \right] + g \Delta x \Delta y \left[\rho w \right]_{z=0}^{z=h} = 0 \quad (B3)$$

Since $w(0) = 0$ there results in the limit as Δx and Δy approach zero:

$$\frac{\partial}{\partial x} \left[\int_0^h \rho u dz \right] + \frac{1}{g} \frac{\partial g}{\partial x} \left[\int_0^h \rho u dz \right] + \frac{1}{g} \frac{\partial}{\partial y} \int_0^h \rho v dz + \rho_e w_e = 0 \quad (B4)$$

x-momentum. - In a similar manner the following expression for x-momentum is obtained:

$$\begin{aligned} & \frac{\partial}{\partial x} \left[g \int_0^h \rho u^2 dz \right] + \frac{\partial}{\partial y} \left[\int_0^h \rho u v dz \right] + g \left[\rho u w \right]_{z=0}^{z=h} \\ & = g \left[+\tau \right]_{z=0}^{z=h} - h \frac{\partial}{\partial x} [g p] + h p \frac{\partial g}{\partial x} \end{aligned} \quad (B5)$$

Combining (B5) with the previous result for mass conservation, and noting that $\tau(h) = 0$:

$$\begin{aligned} & \frac{\partial}{\partial x} \left[g \int_0^h \rho u^2 dz \right] - u_e \frac{\partial}{\partial x} \left[g \int_0^h \rho u dz \right] + \frac{\partial}{\partial y} \left[\int_0^h \rho v (u - u_e) dz \right] \\ & = -g \tau_w - h g \frac{\partial p}{\partial x} \end{aligned} \quad (B6)$$

Introducing the usual boundary layer thickness parameters:

$$\text{momentum thickness} \quad \theta = \int_0^h \frac{\rho}{\rho_e} \left[\frac{u}{u_e} - \left(\frac{u}{u_e} \right)^2 \right] dz \quad (B7)$$

$$\text{displacement thickness} \quad \delta^* = \int_0^h \left(1 - \frac{\rho u}{\rho_e u_e} \right) dz$$

$$\text{crossflow momentum thickness ratio} \quad \frac{E}{\theta} = \bar{E} = \frac{1}{\theta} \int_0^h \frac{\rho v}{\rho_e v_e} \left(1 - \frac{u}{u_e} \right) dz$$

leads to the following expression for Δx and Δy approaching zero:

$$\frac{\tau_w}{\rho_e u_e^2} = \frac{\partial \theta}{\partial x} + \left[\frac{1}{u_e} \frac{\partial u_e}{\partial x} \left(2 + \frac{\delta^*}{\theta} \right) + \frac{1}{\rho_e} \frac{\partial \rho_e}{\partial x} + \frac{1}{g} \frac{\partial g}{\partial x} + \frac{E}{\theta} \frac{1}{g u_e} \frac{\partial v_e}{\partial y} \right] \theta \quad (B8)$$

Definition of $g(x)$. - Since the definition of g is still arbitrary, it seems desirable to make a definition that will simplify equation (B8) if possible. It might appear that if g were selected such that $v_e \equiv 0$ (i.e., streamline coordinates) the last term would be made zero also. Such is not necessarily the case however, since v_e is a divisor in the definition of E . It will be seen that in the limit for small y , the product

$$\frac{\partial v_e}{\partial y} E$$

becomes

$$\frac{1}{y} \int_0^h \frac{\rho v}{\rho_e} \left(1 - \frac{u}{u_e}\right) dz$$

An additional condition, $\partial v / \partial y \equiv 0$ does cause this term to go to zero. An examination of the complete boundary layer differential equation shows that $\partial v / \partial y \equiv 0$ occurs only if

$$\partial p / \partial y = 0$$

and

$$\partial^2 p / \partial y^2 = 0$$

These conditions are met only if the body is: 1) two-dimensional, or 2) axisymmetric and at zero angle of attack. In both cases the surfaces $y = \text{constant}$ follow streamlines if $g \propto r$, the local body radius. In the case of an axisymmetric body at angle of attack the streamlines will not follow surfaces of constant y however. The additional divergence is denoted by f , defined by

$$\frac{1}{f} \frac{\partial f}{\partial x} = \frac{1}{u_e g} \frac{\partial v_e}{\partial y} \quad (\text{B9})$$

where v_e is measured with respect to the y, x coordinate system. In terms of r and f equation (B8) becomes

$$\frac{\tau_w}{\rho_e u_e^2} = \frac{\partial \theta}{\partial x} + \theta \left[\frac{1}{u_e} \frac{\partial u_e}{\partial x} \left(2 + \frac{\delta^*}{\theta}\right) + \frac{1}{\rho_e} \frac{\partial \rho_e}{\partial x} + \frac{1}{r} \frac{\partial r}{\partial x} + \frac{E}{\theta} \left(\frac{1}{f} \frac{\partial f}{\partial x}\right) \right] \quad (\text{B10})$$

Physically, the term r may also be thought of as streamline divergence due to body shape while the term f represents streamline divergence due to transverse pressure gradients. The quantities r and f are related by

$$rf = \Delta \quad (\text{B9A})$$

where Δ is the total distance between any two streamlines. In the absence of transverse pressure gradients the final term in equation (B9) will be zero.

TRANSFORMATION OF THE MOMENTUM INTEGRAL EQUATION

In order to obtain a more useful form of the momentum equation (B10) a modified Stewartson transformation suggested by Mager (ref. 27) is adopted in which:

$$\begin{aligned} X &= \int_0^x F \frac{\rho_r \mu_r}{\rho_o \mu_o} dx \\ Y &= y \\ Z &= F \int_0^z \frac{\rho}{\rho_o} dz \\ U &= u/F, \quad V = v/F \end{aligned} \quad (\text{B11})$$

where X , Y , Z , U and V are the transformed coordinates and velocities. The stagnation values of density and viscosity, ρ_o and μ_o , are required to be constant, and F is an unspecified function of x only. With these definitions, the momentum thickness, skin friction at the wall, and heat transfer rate in the transformed coordinate system are, respectively:

$$\begin{aligned} \Theta &= \int_0^\infty \left(\frac{U}{U_e} - \left(\frac{U}{U_e} \right)^2 \right) dZ = F \frac{\rho_e}{\rho_o} \theta \\ \bar{\tau}_w &= \frac{\tau_w}{F^2} \left(\frac{\rho_o \mu_o}{\rho_r \mu_r} \right) \\ \bar{q}_w &= \frac{\dot{q}_w}{F} \left(\frac{\rho_o \mu_o}{\rho_r \mu_r} \right) \end{aligned} \quad (\text{B11A})$$

The transformed momentum integral equation becomes

$$\begin{aligned} \frac{\bar{\tau}_w}{\rho_e U_e^2} &= F \frac{d}{dX} \left(\frac{1}{F} \frac{\rho_o}{\rho_e} \Theta \right) + \frac{\rho_o}{\rho_e} \Theta \left[\frac{\Lambda}{U_e F} \frac{\partial}{\partial X} (U_e F) + \frac{1}{\rho_e} \frac{\partial \rho_e}{\partial X} \right. \\ &\quad \left. + \frac{1}{r} \frac{dr}{dX} + \frac{E}{\theta} \frac{1}{f} \frac{df}{dX} \right] \end{aligned} \quad (\text{B12})$$

in which $A = 2 + \frac{\delta^*}{\theta}$; \bar{E} and A are unchanged by the transformation .

Solution of the transformed integral equation.- It is assumed that the local friction coefficient in the transformed plane is given by

$$\frac{\bar{\tau}_w}{\rho_o U_e^2} = \frac{C_m}{\left(\frac{\rho_o U_e \Theta}{\mu_o}\right)^{1/m}} \quad (B13)$$

Equation (B13) is substituted into equation (B12) yielding an equation of the form:

$$\frac{d\Theta}{dX} + P(X)\Theta = \Theta^{-\frac{1}{m}} Q(X)$$

which becomes a linear first order equation with the change of variable:

$$\varphi = \Theta^{\frac{m+1}{m}}$$

The solution obtained is:

$$\frac{\bar{\tau}_w}{\rho_o U_e^2} = \frac{C_m \left(F^{A-1} U_e^{A-1} r f \bar{E} \mu_o \right)^{1/m}}{\left\{ \int_0^X C_m \left(\frac{m+1}{m} \right) \rho_o \mu_o^{\frac{1}{m}} U_e^{\frac{A(m+1)-1}{m}} F^{(A-1)\frac{m+1}{m}} \left(r f \bar{E} \right)^{\frac{m+1}{m}} dx \right\}^{\frac{1}{m+1}}} \quad (B14)$$

In the untransformed physical plane, (B14) is:

$$\frac{\tau_w}{\rho_r \mu_r u_e} = \frac{C_m \mu_o^{\frac{1-m}{m}} \rho_r \mu_r u_e^{\frac{A+m-1}{m}} \left(r f \bar{E} \right)^{1/m}}{\left\{ \int_0^x C_m \left(\frac{m+1}{m} \right) \mu_o^{\frac{1-m}{m}} \rho_r \mu_r u_e^{\frac{A(m+1)-1}{m}} \left(r f \bar{E} \right)^{\frac{m+1}{m}} dx \right\}^{\frac{1}{m+1}}} \quad (B15)$$

Neither ρ_o nor F appear in this equation, and their definitions are therefore immaterial.

Remembering that C_m , m , and μ_o are assumed to be independent of x , and defining

$$C_x = C_m \frac{m}{m+1} \left(\frac{m}{m+1} \right)^{\frac{1}{m+1}} \quad (B16)$$

$$G = \rho_r \mu_r u_e r^{\frac{m+1}{m}}$$

(B15) can then be reduced to:

$$\frac{\tau_w}{u_e} = \frac{C_x \mu_o^{\frac{1-m}{1+m}} [\rho_r \mu_r u_e]^{\frac{m}{m+1}}}{\left[\frac{1}{G \left(f \bar{E} u_e^{A-1} \right)^{\frac{m+1}{m}}} \int_0^x G \left(f \bar{E} u_e^{A-1} \right)^{\frac{m+1}{m}} dx \right]^{\frac{1}{m+1}}} \quad (B17)$$

Noting that the quantity within the brackets in the denominator on the right hand side has the units of length, we can define

$$S_{eq} = \left[\frac{1}{G \left(f \bar{E} u_e^{A-1} \right)^{\frac{m+1}{m}}} \int_0^{x_1} G \left(f \bar{E} u_e^{A-1} \right)^{\frac{m+1}{m}} dx \right]_1 \quad (B18)$$

where the subscript 1 indicates evaluation at the current point of interest x_1 . All effects due to flow three-dimensionality, streamwise and transverse pressure gradients, and upstream history are now included in S_{eq} , if $\rho_r \mu_r$ is assumed to be independent of these phenomena (the validity of this assumption will be demonstrated subsequently). Thus S_{eq} can be considered to be the "equivalent flat plate distance" for skin friction at the point of interest x_1 .

With (B18), (B17) can be rewritten:

$$\frac{\tau_w}{u_e} = \frac{C_x \mu_o}{S_{eq}} \left[\frac{\rho_r \mu_r u_e S_{eq}}{\mu_o^2} \right]^{\frac{m}{m+1}} \quad (B19)$$

which is identical in form to the corresponding expression for low speed flat plate flow,

$$\frac{\tau_w}{u_e} = c \frac{\mu}{x} N_{Re,e}^{\frac{m}{m+1}} \quad (B20)$$

One approach to the solution of a boundary layer integral equation, such as developed in the preceding analysis, involves the assumption and integration of boundary layer profiles to obtain the required boundary layer thickness parameters (see, for instance, Beckwith and Gallagher (ref. 28)). In that approach it is necessary to derive the energy equation corresponding to (F15). An alternative method is used here, wherein a general form of Reynolds analogy is assumed

$$H = \frac{q}{i_{aw} - i_w} = \int \frac{\tau_w}{u_e} \quad (B21)$$

It is of course well known that the Reynolds analogy factor \mathcal{S} has the value unity for constant property, unit Prandtl number, flat plate flow. It will be subsequently demonstrated that, in the presence of more realistic gas properties, \mathcal{S} is for laminar flat plate flows still a function only of the Prandtl number and (in dissociated flow) the Lewis number. For convenience denoting these flat plate flow functional relationships by F_{Pr} and \mathcal{L} respectively, (B21) is rewritten

$$H = \frac{\mathcal{L}}{F_{Pr} S} \frac{\tau_w}{u_e} \quad (B22)$$

where the factor S incorporates all effects of flow three-dimensionality, streamwise and transverse pressure gradients, and upstream history on Reynolds analogy.

Combining (B17), (B18) and (B22) leads to:

$$H = \frac{\mathcal{L}}{F_{Pr}} \frac{C_x}{S} \frac{\mu_o}{(\rho_r \mu_r u_e)} \frac{1}{(S_{eq})^{\frac{1}{m+1}}} \quad (B23)$$

Since S_{eq} includes all effect of flow history and pressure gradient on skin friction, and S performs a similar function on Reynolds analogy, the definition of an equivalent distance for heat transfer suggests itself. Accordingly, we define

$$x_{eq} = S^{m+1} S_{eq}$$

or

$$x_{eq} = S^{m+1} \int_0^{x_1} \frac{G \left(\bar{f} \bar{E} u_e (A-1) \right)^{\frac{m+1}{m}}}{\left[G \left(\bar{f} \bar{E} u_e (A-1) \right)^{\frac{m+1}{m}} \right]_{x_1}} dx \quad (B24)$$

leading to a general expression for heat transfer of the form

$$H = \frac{C_x \rho_r \mu_o}{F_{Pr} x_{eq}} \left[\frac{\rho_r \mu_r u_e x_{eq}}{\mu_o^2} \right]^{m/(m+1)} \quad (B25)$$

Means of evaluating the various parameters appearing in (B25) are presented in the following sections.

EVALUATION OF LAMINAR BOUNDARY LAYER PARAMETERS

Exact solutions of the similarity form of the laminar boundary layer equations were used to evaluate the parameters appearing in equation (B25). This was done in an orderly manner, beginning with two-dimensional constant-property constant-pressure flow, and progressing to the most complex conditions for which exact solutions are available. The evaluations determined from the simpler cases were retained or amplified in analyzing the more complex cases. Thus, the constant C for laminar flow is always taken to be 0.33206, the value given by Howarth in reference 29 for incompressible flat plate flow. The effects of pressure gradients, wall cooling, etc., are accounted for in other terms of equation (B25).

In some cases alternative definitions were possible. For example, the authors of references 32 and 35 incorporated (in effect) pressure gradients into the term $\rho_r \mu_r$ appearing in equation (B10), while in the present formulation such effects appear in the equivalent distance, X_{eq} . The latter definition is to be preferred as the former cannot be made consistent with the results of reference 30, which presents solutions for various pressure gradients, but with $\rho \mu$ held constant. The definitions used here were adopted only after an examination of several possible alternatives. The criteria for selection were consistency between the results of the various special cases, consistency with physical considerations, accuracy, simplicity, and freedom from interdependencies.

General considerations.- As a matter of physical consistency, it is required that if the fluid properties ρ and μ are constant through the boundary layer, the reference values of the fluid properties be equal to those constant values. This principle is extended to constant products as well, i.e., it is required that when in a given numerical calculation, e.g., references 30 and 31, the product of density and viscosity is held constant at some base value (usually the wall) the reference density viscosity product $\rho_r \mu_r$ must also be equal to that base value. The functions F_{Pr} and \mathcal{L} are equal to 1.0 when σ and N_{LE} are equal to 1.0, and $\mathcal{L} = 1.0$ for ideal gases. Also, in flat plate flow the equivalent distance is equal to the physical distance from the leading edge.

Two-Dimensional Flat Plate Flow

The special case of two-dimensional flat plate flow is examined first since the effect of fluid property variations within the boundary layer can be examined without the additional complexity of streamwise variations. For the case of constant fluid properties the solutions of Howarth show that $m = 1$ and $C_x = .332$, so that equation (B25) becomes

$$H = .332 \frac{\mathcal{L}}{F_{Pr}} \left[\frac{\rho_r \mu_r u_e}{x_{eq}} \right]^{1/2} \quad (B26)$$

$$= .332 \frac{\mathcal{L}}{F_{Pr}} \left[\frac{\rho_e \mu_e u_e}{x} \right]^{1/2} \quad (B27)$$

where (B27) follows from the principles stated under "General Considerations". For this special case the only undetermined quantity is the Reynolds analogy factors \mathcal{L} and F_{Pr} . Note that the reference stagnation viscosity, μ_0 , no longer appears.

Reynolds analogy factors.- The Prandtl number effect on Reynolds analogy in flat plate flow, usually given as $F_{Pr} = \sigma^{2/3}$ for constant σ , is slightly better represented by $\sigma^{.645}$ as may be seen in figure 65. Following the practice of reference 32, for example, the Prandtl number effect is correlated in terms of σ , the partial Prandtl number for translation, rotation, and vibration.

For variable Prandtl number there is an uncertainty as to which value should be used in correlating its effect. All solutions in the literature for which the Prandtl number is variable also involve variable $\rho\mu$, so that $\rho\mu$ is not necessarily equal to $\rho_e\mu_e$. For such cases it was found that the Prandtl number should be evaluated at the enthalpy and pressure corresponding to $\rho_r\mu_r$. This value of the Prandtl number is hereafter denoted as σ_r . The adequacy of this evaluation is demonstrated by the agreement of the three sets of calculations presented in figure 65, which also serves to establish the lack of dependency of F_{Pr} on anything other than σ_r .

With the Prandtl number effect correlated in terms of the partial Prandtl number the effect of energy transport by diffusion must be treated separately. This effect was first calculated by the authors of reference 32, wherein the expression

$$\mathcal{L} = \frac{\dot{q}_{N_{Le} \neq 1}}{\dot{q}_{N_{Le} = 1}} = 1 + (N_{Le}^{.52} - 1) \frac{i_{D,S}}{i_S} \quad (B28)$$

was found to agree well with exact solutions for $N_{Le} = 1.4$, in stagnation point flow. In high Mach number flows, however, equation (B28) may predict a significant diffusion effect under conditions for which no dissociation actually exists, since the temperatures within the boundary layer are always well below the stagnation value. To avoid this inconsistency, equation (B28)

was modified to operate on the local static enthalpy, rather than the stagnation value. The modified expression,

$$\mathcal{L} = 1 + (N_{Le}^{.52} - 1) \frac{i_{D,e}}{i_e} \quad (B29)$$

of course reduces to (B28) for stagnation point flow. Equation (B29) was used for all calculations in the present report, although later publications, reference 34, for example, indicate that equation (B29) overestimates the heating rate by 5 to 10% in some cases.

Reference density-viscosity product.- The reference density-viscosity product was first evaluated for zero Mach number with various degrees of wall cooling using the solutions of references 33, 35, and 36, and some unpublished solutions by Halvorson and Cassmeyer of The Boeing Company, as shown in figure 66.

For edge Mach numbers greater than zero it was found that the reference density-viscosity product $\rho_r \mu_r$ can be represented as a function only of $\rho_e \mu_e$, $\rho_w \mu_w$ and $\rho_s \mu_s$, where the latter is the density-viscosity product evaluated at stagnation enthalpy but the local pressure. Using the solutions of references 33 and 35 an effective edge value of $\rho \mu$ was determined that allows the use of figure 66 for Mach numbers other than zero. The effective $\rho \mu$ product $(\rho_e \mu_e)_{eff}$ was found to be a function of $\rho_s \mu_s$ and $\rho_e \mu_e$ only. The curve that defines this relation is given in figure 67 (a). All of the solutions discussed so far are well represented by the faired curve of figure 66 when plotted against $(\rho_e \mu_e)_{eff}$ as may be seen in figure 67 (b).

Subsequent investigations described below have shown that $\rho_r \mu_r$ is independent of pressure gradients. The values of $\rho_r \mu_r$ obtained from figures 66 and 67 were used for all calculations appearing in this report.*

Pressure Gradient Effects - Similar Flows

Referring to equation (B25), and recalling the earlier comment that C_x , m , F_{Pr} and \mathcal{L} are by definition taken as the flat plate values it is seen that all pressure gradient effects are reflected in $\rho_r \mu_r$ and X_{eq} . These effects can be evaluated for similar flows from the solution published (for example) in references 30 and 35, which consider streamwise pressure gradients, and references 31 and 34 which consider cross-flow pressure gradients.

*Recently some simple expressions have been found which approximate curves of figures 66 and 68 closely. The expressions are given in the final section of this appendix.

Beginning with the simplest possible case, two-dimensional flow of an ideal gas with unit Prandtl number, and the viscosity proportional to temperature, the equivalent distance effects can be isolated. Since $\rho\mu$ is always equal to $\rho_e\mu_e$, $\rho_r\mu_r$ is also equal to $\rho_e\mu_e$. (Note that $\rho\mu$ is not necessarily constant through the flow field, but varies with the local boundary layer edge pressure.) With these values incorporated, the equivalent distance expression (B24), is reduced to

$$x_{eq} = S^2 \frac{\int_0^{x_1} (P u_e) u_e^{2(A-1)} dx}{\left[(P u_e) u_e^{2(A-1)} \right]_{x_1}} \quad (B30)$$

In equation (B30) the term $(P u_e)$ reflects the effects of upstream variations in $\rho_e\mu_e u_e$, while the terms S^2 and $u_e^{2(A-1)}$ account for local pressure gradient effects on the boundary layer profiles.

Equation (B30) can be evaluated if S and A are known, and although laborious, they could be determined from the numerical solutions. Fortunately, specific evaluation of these parameters has proven to be unnecessary, since a convenient simple correlation has been found for the combined effect of S and u_e^{A-1} , which may be written as

$$S^2 \int_0^{x_1} \frac{(P u_e) (u_e^{2(A-1)}) dx}{\left[(P u_e) u_e^{2(A-1)} \right]_{x_1}} = \frac{1}{1 + \Gamma \sqrt{\beta}} \int_0^{x_1} \frac{P u_e dx}{(P u_e)_{x_1}} \quad (B31)$$

where β is the dimensionless pressure gradient parameter similar to that defined by the authors of reference 30.* The profile parameter Γ is a single valued function of a mean boundary layer density, ρ_m , calculated by

$$\frac{\rho_m}{\rho_e} = \frac{2 T_e}{(T_w + T_e)} \quad (B32)$$

Subsequent investigations of exact solutions for nonunit Prandtl number and nonlinear viscosity laws have shown that expressions of the form of (B31) are valid for these more complex conditions as well, either for two-dimensional flows with streamwise pressure gradients, or for yawed cylinder flow. The expressions finally developed are:

*The definition of β is given in equation (B41).

$$(\rho_r \mu_r)_{\beta} = (\rho_r \mu_r)_{\beta=0} \quad (B33)$$

and a generalization of (B31)

$$x_{eq,L} = \frac{1}{J_L} \int_0^{x_1} \frac{G f^2 \bar{E}_L}{\left[G f^2 \bar{E}_L \right]_{x_1}} dx \quad (B34)$$

where J_L is given by

$$J_L = \left[1 + \Gamma_s \sqrt{\beta_s} \right] \sigma_r \alpha \sqrt{\beta_s} \quad (B35)$$

and

$$\bar{E}_L = \left[1 + \Gamma_c \sqrt{\beta_c} \right] \sigma_r \alpha \sqrt{\beta_c} \quad (B36)$$

where the subscripts "s" and "c" are introduced to distinguish between streamwise and crossflow pressure gradients; it should be noted that J_L is concerned only with streamwise pressure gradient effects and \bar{E}_L only with crossflow effects; also note that $J_L = 1.0$ for $\beta_s = 0$ and $\bar{E}_L = 1.0$ for $\beta_c = 0$.

The function Γ is given for either streamwise or crossflow pressure gradients by the curve of figure 68 as a single-valued function of a parameter Σ defined by:

$$\Sigma_s = \frac{\rho_s}{\rho_{m,s}} = \frac{(Z T)_{m,s}}{(Z T)_s} \quad (B37)$$

for streamwise pressure gradients, and as

$$\Sigma_c = \frac{\rho_{e,SL}}{\rho_{m,c}} = \frac{(Z T)_{m,c}}{(Z T)_{e,SL}} \quad (B38)$$

for crossflow pressure gradients. The subscript "m" denotes evaluation at a mean boundary layer enthalpy, defined by:

$$i_{m,s} = \frac{1}{2} (i_s + i_w) \quad (B39)$$

and

$$i_{m,c} = \frac{1}{2} (i_{e,SL} + i_w) + .206 (i_S - i_{e,SL}) \sigma_r \sqrt{\frac{\rho_S \mu_S}{\rho_e \mu_e}} \quad (B40)$$

The second equality in equations (B37) and (B38) follows from the condition of constant pressure across the boundary layer (all evaluations are made at the local pressure). Again, (B37) through (B40) are the generalizations of equations (B31) and (B32).

While figure 68 and equations (B34-40) were developed solely on the basis of providing the best fit to the available data within the framework of the form of equation (B31) the obvious similarity of (B39-40) to the various reference enthalpies appearing in the literature provides some analytical justification for these correlations.

The streamwise pressure gradient parameter β_s is herein defined as:

$$\beta_s = 2 \frac{i_S}{i_e} J_L \left(\frac{x_{eq,L}}{x} \right) \frac{d(\ln u_e)}{d(\ln x)} \quad (B41)$$

With a minor modification to the definition of $x_{eq,L}$ (to be discussed in the next section), it is easily shown that this definition of β_s is identical to the corresponding parameter of reference 34. In the present report β_c is evaluated only for yawed cylinder flow, in which case $\beta_c = 1.0$, also consistent with the results of reference 34. Except as otherwise noted in the text, a value of unity was used for all leading edge theory calculations, while a value of zero (corresponding to $\bar{E} = 1.0$) was assumed for lower surface theory calculations.

The exponent α in equations (B35) and (B36) is given by

$$\alpha = .090 \left(\frac{\rho_S \mu_S}{\rho_w \mu_w} \right) \quad (B42)$$

which is also based on fits to the solutions of references 30, 31, 32 and 34. The accuracy obtained through the use of equations (B33) through (B42) is illustrated in figure 69, wherein solutions from references 30 and 34 are presented in terms of $\bar{\Gamma}$ and $\bar{\Sigma}$. As may be seen by comparing the spread of the individual numerical solutions with the indicated error band, the present method provides excellent agreement with all solutions.

Application to Nonsimilar Flow

The equations presented in this section have all been developed from similarity solutions to the boundary layer equations, and so are strictly applicable only in those situations for which similarity applies. However, based on discussions given in references 34 and 35, it is to be expected that the same correlations could provide good estimates for nonsimilar flow conditions as well, provided their streamwise variations are taken into account. This has been done by incorporating the factor J_L appearing in equation (B35) into the integrand. The expression for equivalent distance then becomes:*

$$x_{eq, L} = \frac{1}{J_L^2} \int_0^{x_1} \frac{G f \frac{2 \bar{E}_L}{J_L} dx}{(G f \frac{2 \bar{E}_L}{J_L})_{x_1}} \quad (B43)$$

It is easily seen that for similar flows, wherein J_L is constant, (B43) reduces to (B34). Evaluated for two-dimensional flows ($f \equiv 1.0$) the use of (B43) in (B41) results in a definition of β_s identical to that of reference 34, while the use of (B34) in (B41) provides a value of β_s that corresponds to the "local similarity" approach of reference 35, wherein the upstream history of profile effects are neglected (that is, the boundary layer profiles are assumed to adjust instantaneously to the local pressure gradient).

Equation (B43) assumes the crossflow parameter \bar{E}_L to be independent of streamwise pressure gradient effects; however, the presence of the β_s crossflow terms in the resulting definition of β_s provide a coupling between the transverse and streamwise pressure gradient effects, as might be expected. The overall effect predicted is in qualitative agreement with the results of reference 37; unfortunately, the difficulty of relating the correlating parameters of that reference to the present system has so far prevented quantitative comparisons.

Finally, for the general case of curved streamlines (i.e., away from a line of symmetry), it is assumed that the foregoing analysis and correlations are valid if the distance parameter x is taken to be measured along the streamline. As previously noted, the definition of β_c for the general case is obscure, and all calculations herein other than leading edge values, have been made on the basis of $\beta_c = 0$ ($\bar{E}_L = 1$), which corresponds to the "zero crossflow" method of reference 38 as far as three-dimensional effects are concerned. All present calculations do retain the effect of streamwise pressure gradients, however.

*Note that by these definitions β_s and J_L are interrelated, so that an iterative method is required for their evaluation, as also stated in reference 34.

TURBULENT FLOW

There are no exact calculations of turbulent boundary layer flow, so that a development of the type just given is not possible. However, equation (B25) still serves to identify the important parameters, and provides a basis for consistently comparing experimental results. In particular, the transformation introduced with equations (310) and (B11) allows an empirical incompressible skin friction law to be used in place of the (nonexistent) exact flow solutions. As stated in the section "Transformation of the momentum integral equation," the transformation used is based on the work of Mager, reference 27. A discussion of the reasoning behind the transformation itself is given in his paper. The present method departs from the suggestions of Mager, however, in the evaluation of the various boundary layer parameters. Mr. Hanks was guided in the evaluations by the values of the corresponding laminar parameters, an approach which was suggested by the very successful results of the first such attempt, wherein the laminar values of $\rho_r \mu_r$ were used without modification for turbulent flow. The resulting predictions were in excellent agreement with recently obtained free flight data, some of which (notably, that from the X-15 program) were not in agreement with any of the well known methods.

The author was also guided by the requirements of a design project, and so was constrained to make conservative approximations where approximations were required. Thus, the effects of streamwise and transverse pressure gradients on the turbulent boundary layer profiles were included in the calculations, even though it was known that the effects were small and could only be crudely estimated. The available evidence indicated that such effects would increase heat transfer, so that neglecting them would be unconservative.

Incompressible flow friction law.- In order to determine C_x and m a formula for skin friction in incompressible turbulent flow is required. After a survey of proposed incompressible friction formulas a minor modification of the Schultz-Grunow (ref. 39) equation was selected:

$$C_f = \frac{.370}{[\log_{10} (N_{Re} + 3000)]^{2.584}} \quad (B14)$$

The modification that was made is the addition of the constant (3000) to the Reynolds number that appears in the denominator. This modification was made because the authors felt that the high values of C_f predicted by the unmodified equation at Reynolds number below 10^4 were not realistic in view of the well supported prediction of stability theory that the incompressible laminar boundary layer is stable at Reynolds less than about 60,000.

The modified and unmodified expressions are shown in figure 70, together with some other proposed methods. As shown, there is little difference between the various methods, except that the Blasius equation falls low at high values of Reynolds number. Equation (344) was originally selected because of its slight conservatism, although any other expression could have been used.

The form of equation (B44) does not lead itself to calculations in the framework of equation (B23) due to the variation of m with Reynolds number. However, comparisons have been made that show that $m=4$ is an adequate approximation for evaluating geometric effects. For example, if m is evaluated at particular values of Reynolds number using equation (B44) the following comparisons are obtained:

N_{RE}	$m = \frac{1}{1 + \frac{d(\ln C_f)}{d(\ln N_{RE})}}$	$\frac{h_{\text{cone}}}{h_{\text{flat plate}}}$	$\frac{h_{\text{cylinder}}}{h_{\text{cylinder, } m=4}}$
10^5	3.45	1.20	.99
4.2×10^5	4.0	1.17	1.00
10^6	4.34	1.16	1.00
10^8	6.12	1.11	1.01

Thus the effect of variations in m is seen to be small. Accordingly, $m=4.0$ has been selected for the calculation of geometric effects (e.g., $h_{\text{cone}}/h_{\text{flat plate}}$) used herein. However, for actual calculations of C_f equation (344) was used as there can be considerable error in $m = \text{constant}$ approximations for absolute values of C_f . An example of such a friction law is the Blasius method, for which $m = 4$. As shown in figure 70 the Blasius equation falls well below the other methods at high Reynolds numbers.

Density-Viscosity product; Reynolds Analogy Factor.- As already noted the reference density-viscosity product for turbulent flow is taken to be the laminar value. This basic identity was suggested by the fact that $\rho_r \mu_r$ appears only in connection with the laminar shear terms of the turbulent boundary layer equations.* It is also assumed the effects of Prandtl number and Lewis number on turbulent flat plate heat transfer are also identical to the laminar values. The use of the laminar flow Prandtl number effect is common practice. The use of the laminar flow Lewis number effect is thought to be a conservative upper limit.

*See, for example, equation 13 in reference 27.

Reference stagnation viscosity.- Since the reference stagnation viscosity μ_0 does not appear in the laminar equations, no information regarding its evaluation can be obtained by examining the laminar solutions. The reference stagnation viscosity is assumed by Mager (ref. 27) to be the viscosity evaluated at stagnation conditions. For real gases with the viscosity dependent on the pressure it seems more realistic to consider the local flow composition rather than the composition corresponding to stagnation conditions. Accordingly μ_0 is calculated with the Sutherland law and μ_r using the value of specific heat corresponding to $\rho_r \mu_r$. The result is:

$$\mu_0 = \mu_r \left(\frac{i_S}{i_r} \right)^{3/2} \left[\frac{T_r + 200}{T_r \left(\frac{i_S}{i_r} \right) + 200} \right] \quad (B45)$$

Pressure gradient effects.- As in the laminar case, pressure gradient effects appear primarily in the equivalent distance, which (for $m = 4$) is given by:

$$x_{eq, T} = S^5 \int_0^{x_1} \frac{G_T f^{5/4} \bar{E}_T u_e^{5/4 (A-1)} dx}{\left[G_T f^{5/4} \bar{E}_T u_e^{5/4 (A-1)} \right]_{x_1}} \quad (B46)$$

It is assumed that there exists an analog to the laminar correlation (equation B43) of the form:

$$x_{eq, T} = \frac{1}{J_T^2} \int_0^{x_1} \frac{G_T f^{5/4} \bar{E}_T J_T dx}{\left[G_T f^{5/4} \bar{E}_T \right]_{x_1}} \quad (B47)$$

It is to be expected that:

$$(J_T - 1)^{1/5} \approx (J_L - 1)^{1/2}$$

which expresses the well known fact that pressure gradient effects on turbulent heat transfer are much smaller than those in laminar flow. After an examination of available experimental data the value

$$\frac{J_T - 1}{J_L - 1} = .48 \quad (B48)$$

was selected. By analogy to (B35) it is assumed that:

$$J_T = \left[1 + .48 \Gamma_S \sqrt{\beta_S} \right] \sigma_r^\alpha \sqrt{\beta_S} \quad (B49)$$

where Γ_S and β_S are the previously described laminar values. The small exponent α is assumed equal to the laminar value (eq. B42) although its ultimate effect on the predicted heating rate is only about 0.3% for $\beta_S = 1.0$.

Similarly, the behavior of \bar{E} in turbulent flow can be described only qualitatively, and most published analyses neglect its effect. However, its effect is to increase heating rates, and was therefore included in the present method. As in the streamwise pressure gradient case, the values actually used were based on modifications of the corresponding laminar correlations. Unlike the streamwise parameter J_L however, \bar{E}_L is strongly influenced by Mach number, as evidenced in equations (B38) and (B40), so that a dual modification is indicated.

Considering first the case for zero Mach number flow, it is seen from the definitions of (B7) that the upper limit on \bar{E} is δ^*/θ unless the transverse velocity component v within the boundary layer exceeds the external value. Laminar solutions (ref. 31) show that these velocity overshoots do not occur for cold wall zero Mach number flow, hence a correction factor of the following form is suggested:

$$\frac{\bar{E}_{T,0} - 1}{\bar{E}_{L,0} - 1} = \frac{\left[\frac{\delta^*}{\theta} + C \right]_T}{\left[\frac{\delta^*}{\theta} + C \right]_L} \quad (B50)$$

The precise value of the constant C in this expression cannot be calculated, of course. For the previously mentioned upper limit case, C of course is equal to -1 ; however, in the interests of conservatism, a value of $C = +1$ was selected to represent an upper limit. Consistent with equations (B48) and (B49), then:

$$\frac{\bar{E}_{T,0} - 1}{\bar{E}_{L,0} - 1} = 0.77 \quad (\text{B51})$$

In equations (B51) $\bar{E}_{L,0}$ is just \bar{E}_L evaluated for Mach number equal to zero. For Mach number zero equation (B40) reduces to

$$i_{m,c,0} = \frac{1}{2} (i_{e,SL} + i_w)$$

since

$$(i_s - i_{e,SL}) = 0$$

at zero Mach number.

The effect of Mach number on \bar{E}_T was determined from observation of empirical trends in turbulent yawed cylinder stagnation line heat transfer data, as

$$\frac{\bar{E}_T}{\bar{E}_{T,0}} = \left(\frac{\bar{E}_L}{\bar{E}_{L,0}} \right)^{m_T} \quad (\text{B52})$$

An equivalent form that is more convenient for computer applications has been used for all calculations in this report:

$$\frac{x_{eq,T}}{x_{eq,T,0}} = \left[\frac{x_{eq,L}}{x_{eq,L,0}} \right]^{m_T}$$

where, in general

$$\begin{aligned} x_{eq,T,0} &= \frac{1}{J_T} \int_0^{x_1} \frac{G_T J_T f^{5/4} \bar{E}_{T,0} dx}{\left[G_T J_T f^{5/4} \bar{E}_{T,0} \right]_{x_1}} \\ x_{eq,L,0} &= \frac{1}{J_L} \int_0^{x_1} \frac{G_L J_L f^2 \bar{E}_{L,0} dx}{\left[G_L J_L f^2 \bar{E}_{L,0} \right]_{x_1}} \\ x_{eq,L} &= \frac{1}{J_L} \int_0^{x_1} \frac{G_L J_L f^2 \bar{E}_L dx}{\left[G_L J_L f^2 \bar{E}_L \right]_{x_1}} \end{aligned} \quad (\text{B53})$$

It is easily demonstrated that for infinite yawed cylinder stagnation line flow, (B53) is exactly equivalent to (B52). For other types of flow (B52) and (B53) are not exactly equivalent. However, since (B52) is based on yawed cylinder data, (B52) and (B53) are equally valid assumptions, and (B53) has been found to be more convenient. In any case, the final effect on the predicted heating rate is small.

COMBINED LAMINAR-TURBULENT METHOD

A comparison of the equivalent distance expressions for laminar and turbulent boundary layers shows that in general the two values are not equal, so that the Reynolds number based on the equivalent distance will depend on the boundary layer state. This inconsistency can be avoided by employing the following definition of a reference Reynolds number:

$$N_{Re,r} = \left[\frac{\rho_r \mu_r u_e x_{eq,L,0}}{F_x^2 \mu_o^2} \frac{x_{eq,L,0}}{x_{eq,L}} \right] \quad (B54)$$

where

$$F_x = \left[\frac{x_{eq,T,0}}{x_{eq,L,0}} \right]^{\frac{1}{m_T-1}} \quad m_T = 4 \quad (B55)$$

When $N_{Re,r}$ and F_x are used in equation (B25) there results

$$H = \frac{\dot{q}}{i_{aw} - i_w} = \frac{\mathcal{L}}{2F_{Pr}} \frac{F_x \mu_o}{x_{eq,L,0}} \left[(N_{Re,r}) (C_{f,r}) \right] \quad (B56)$$

if

where $C_{f,r}$ is the friction coefficient evaluated for the reference Reynolds number. The formulas used in the present report are:

$$C_{f,r,L} = \frac{.664}{[N_{Re,r}]^{1/2}} \quad (B57)$$

and

$$C_{f,r,T} = \frac{.370}{[\log_{10} (N_{Re,r} + 3000)]^{2.584}} \quad (B58)$$

Note that in equation (B56) only $C_{f,r}$ depends on the boundary layer state.

It is easily shown that the laminar form of (B56) reduces identically to any of the special cases previously given. For example, considering only the various equivalent distance terms, and employing the general power law form for $C_{f,r}$ corresponding to equation (B25), there results

$$H \sim F_x^{-\frac{m-1}{m+1}} x_{eq,L,0}^{-\frac{1}{m+1}} \left(\frac{x_{eq,L}}{x_{eq,L,0}} \right)^{-\frac{m}{m+1}} \quad (B59)$$

For laminar flow, $m = 1$, and all terms except $(x_{eq,L})^{-1/2}$ disappear as desired. For turbulent flow, on the other hand, (B59) together with the definitions of F_x given in (B55), becomes:

$$H_T \sim \left[x_{eq,T,0} \left(\frac{x_{eq,L}}{x_{eq,L,0}} \right)^m \left(\frac{x_{eq,T,0}}{x_{eq,L,0}} \right)^{\frac{m-4}{3}} \right]^{\frac{-1}{m+1}} \quad (B60)$$

The term in the brackets differs from the previous definition of $x_{eq,T}$ given in (B53) only by the factor

$$\left(\frac{x_{eq,T,0}}{x_{eq,L,0}} \right)^{\frac{m-4}{3}}$$

arising from the use of a nominal value of $m_T = 4$ in the definition of F_x . For all cases of practical interest, this term will have a negligible effect on heat transfer - on the order of one percent or less.

Use of a skin friction law of the form of (B58) in the heat transfer equation (B56) has the effect of automatically introducing the local value of m in (B60), so that the proper compressibility effect on \bar{E}_T is obtained.

SUMMARY OF METHOD AND SAMPLE CALCULATIONS

This section summarizes the calculation procedure for the method. Table B1 lists specific values of the various parameters for several special cases. Since the calculation depends on the functions $\rho_e \mu_{e,eff}$, Γ and $\rho_r \mu_r$ which exist only as the faired curves of figures 66, 67, and 68 numerical values are given in Tables B2, B3 and B4 from which the reader can construct the necessary plots. Also given in Tables B2, B3 and B4 are simple curve fit expressions that are shown to agree closely with the values from the faired curves. The curve-fit expressions were not discovered until after the bulk of the analysis was complete, however, and were not used for any of the comparisons presented in this report.

It is assumed in the following discussion that the following quantities are known:

$$P_e, u_e, i_S, i_e, i_w$$

$$T_{S'}, T_e, T_w, \mu_e, \mu_w, \mu_{S'} = f(i_S, P_e)$$

$$\rho_e, \rho_w, \rho_{S'} = f(i_S, P_e)$$

The basic equations are independent of units, so that any consistent set of units desired can be used.

The basic equations to be solved for each case in general form are

$$H = \frac{\mathcal{L}}{\sigma_r^{.645}} \left(\frac{\mu_o F_X}{x_{eq,L,0}} \right) \frac{(N_{Re,r}) (C_{f,r})}{2} \quad (B61)$$

where

$$C_{f,r,L} = .664 / \sqrt{N_{Re,r}} \quad (B62)$$

$$C_{f,r,T} = \frac{.370}{\left[\log_{10} (N_{Re,r} + 3000) \right]^{2.584}} \quad (B63)$$

$$N_{Re,r} = \frac{\rho_r \mu_r u_e x_{eq,L,0} x_{eq,L,0}}{F_x^2 \mu_o^2 x_{eq,L}} \quad (B64)$$

$$F_x = \left[\frac{x_{eq,T,0}}{x_{eq,L,0}} \right]^{1/3} \quad (B65)$$

$$x_{eq,L} = \int_0^{x_1} \frac{G_L f^{2\bar{E}_{L,J_L}} dx}{\left[G_L f^{2\bar{E}_{L,J_L}^2} \right]_{x_1}} \quad (B66)$$

$$x_{eq,L,0} = \int_0^{x_1} \frac{G_L f^{2\bar{E}_{L,0} J_L} dx}{\left[G_L f^{2\bar{E}_{L,0} J_L^2} \right]_{x_1}} \quad (B67)$$

$$x_{eq,T,0} = \int_0^{x_1} \frac{G_T f^{\frac{5}{4} \bar{E}_{T,0} J_T} dx}{\left[G_T f^{\frac{5}{4} \bar{E}_{T,0} J_T^2} \right]_{x_1}} \quad (B68)$$

$$G_L = \rho_r \mu_r u_e r^2 \quad (B69)$$

$$G_T = \rho_r \mu_r u_e r^{5/4} \quad (B70)$$

$$J_L = \left[1 + \Gamma_s \sqrt{\beta_s} \right] \sigma_r \alpha \sqrt{\beta_s} \quad (B71)$$

$$J_T = \left[1 + .48 \Gamma_s \sqrt{\beta_s} \right] \sigma_r \alpha \sqrt{\beta_s} \quad (B72)$$

$$\bar{E}_L = \left[1 + \Gamma_c \sqrt{\beta_c} \right] \sigma_r \alpha \sqrt{\beta_c} \quad (B73)$$

$$\bar{E}_{L,0} = \left[1 + \Gamma_0 \sqrt{\beta_c} \right] \sigma_r \alpha \sqrt{\beta_c} \quad (B74)$$

$$\bar{E}_{T,0} = \left[1 + .77 \Gamma_0 \sqrt{\beta_c} \right] \sigma_r \alpha \sqrt{\beta_c} \quad (B75)$$

$$\alpha = .090 \sqrt{\frac{\rho_s \mu_s}{\rho_w \mu_w}} \quad (B76)$$

If only laminar flow is required (e.g., stag point):

$$H = .332 \frac{L}{\sigma_r^{.645}} \left[\frac{\rho_r \mu_r u_e}{x_{eq, L}} \right]^{1/2} \quad (B77)$$

The general procedure for a given case is as follows:

a. Examine x_{eq} equations to reduce them to minimum form consistent with the given problem. For example, the flat plate values of ρ_e , u_e and P_e are all independent of x and $J = 1$, so that $x_{eq} = x$ in all cases.

b. Find $\rho_r \mu_r$ using figures 66 and 67 or Tables B2 and B3. Recently the following expressions have been found for $(\rho_e \mu_e)_{eff}$ and $\rho_r \mu_r$:

$$(\rho_e \mu_e)_{eff} = \rho_{S'} \mu_{S'} \left[1.85 - .85 \frac{\rho_{S'} \mu_{S'}}{\rho_e \mu_e} \right] \quad (B78)$$

$$\rho_r \mu_r = (\rho_e \mu_e)_{eff} \left[1.6 - .6 \frac{(\rho_e \mu_e)_{eff}}{(\rho_w \mu_w)} \right] \quad (B79)$$

As may be seen from the values tabulated in Tables B2 and B3, eq. (B78) and (B79) agree with the curves of Figures 66 and 67 to within about 3%, corresponding to a 2 to 3 percent error in the predicted heating rate, and so are considered adequate for most purposes.

c. Find

1. $(Z T)_r$ from $\rho_r \mu_r$, P_e
2. i_r from $(Z T)_r$, P_e
3. σ_r from $(Z T)_r$
4. μ_o from i_s , i_r , $(Z T)_r$ and equation (B45)

(Note that μ_0 is required only for turbulent flow calculations.) Any gas properties may be used in these calculations. In the present report the gas properties of reference 41 were used.

d. Determine the streamline divergence parameters r and f . For arbitrary bodies at angle of attack these parameters are often not known, although their product Δ may be estimated from the pressure distribution or oil flow patterns such as figure 40. The values of r and f for several special cases are given in Table B1.

e. Find β_s if required. Note that the general case, exact evaluation of β_s requires an iterative solution, since

$$\beta_s = 2 \frac{i_s}{i_e} \left[J_L \frac{x_{eq,L}}{x} \right] \frac{d(\ln u_e)}{d(\ln x)} \quad (B80)$$

and the term in brackets is in itself a function of β_s . In practice however, a finite difference integration along the streamline is performed for the bracket parameter

$$\left[J_L \frac{x_{eq,L}}{x} \right] = \frac{1}{\left[G_L f^{2\bar{E}_L} J_L x \right]_{x_1}} \int_0^{x_1} G_L f^{2\bar{E}_L} J_L dx \quad (B81)$$

and the local value of β_s at $x = n\Delta x$ can be evaluated with sufficient accuracy (if the step size is small) by

$$[\beta_s]_{x=n\Delta x} = 2 \left[\frac{i_s}{i_e} \frac{d(\ln u_e)}{d(\ln x)} \right]_{x=n\Delta x} \left[J_L \frac{x_{eq,L}}{x} \right]_{x=(n-1)\Delta x} \quad (B82)$$

f. Find Σ_s , Σ_c , and Σ_0 using equations (B37, B38, B39, and B40). As discussed in connection with equation (B50), the subscript 0 denotes evaluation for zero Mach number.

g. Find Γ from Σ using figure 68 or Table B4. Recently, the following expression was found:

$$\Gamma = [.96 \Sigma^{.55} - .5] \quad (B83)$$

The error in heating resulting from the use of (B83) rather than figure 68 is less than 1% for $\beta < 10$.

h. Evaluate J , E , x_{eq} and F_x , and $N_{Re,r}$ from the definitions given earlier in this section.

i. Find $i_{D,e}$, $i_{D,e}/i_e$ and f from i_e , P_e

j. The heat transfer coefficient H can now be calculated from equations (B61) through (B63). Specific values of the various boundary layer parameters are given in Table B1.

Simplified equations for normalizing heat transfer data.- The heat transfer data presented in this report have been normalized with theoretical Stanton numbers calculated from information presented in Appendix B. The reference Stanton number coefficients used for normalization of laminar and turbulent data were respectively: the hemisphere stagnation point value (h_0) and the value stagnation line of a 60° swept infinite cylinder (h_{ref}). Some of the leading edge data were also normalized with theoretical stagnation line values.

Calculations for the reference Stanton numbers have been correlated and the following simplified relations developed (for wind tunnel condition):

Laminar - Hemisphere Stagnation Point

$$N_{St,0} = \frac{.004}{\rho_\infty u_\infty c_{p_\infty}} \frac{(M_\infty)^{1.18} (T_\infty)^{.12}}{(D/2)^{.5}} \left(\frac{P_\infty}{P_{atm,SL}} \right)^{.5} \quad (B84)$$

Turbulent - 60° Swept Infinite Cylinder Stagnation Line

$$N_{St,ref} = \frac{.0435}{(\rho_\infty u_\infty c_{p_\infty})} \frac{(M_\infty)^{1.46} (T_\infty)^{-.114}}{(D/2)^{.2}} \left(\frac{P_\infty}{P_{atm,SL}} \right)^{.8} \quad (B85)$$

These expressions are accurate within $\pm 3.5\%$ of the $\rho_r \mu_r$ theory values in the following environmental range.

M_∞	5 to 22
T_∞	60 to 120 °R
P_∞	10^{-5} to 10^{-1} Atmospheres

The above equations do not apply to the AD 485M-1 AVCO tests. However, h_{ref} for figure 55 is .53 Btu/ft² sec °R.

Infinite cylinder stagnation line heat transfer coefficients can be obtained from equations (B84) or (B85) and figure 71. The effective sweep angles can be computed with equation 6.

Case (β_s)	$\frac{\rho_r \mu_r}{(\rho_r \mu_r) x_1}$	$\frac{u_e}{(u_e) x_1}$	$\frac{r}{(r) x_1}$	$\frac{f}{(f) x_1}$	$\frac{J}{(J) x_1}$	(x_{eq}, L) at x_1	$(x_{eq}, L, 0)$ at x_1	$(x_{eq}, T, 0)$ at x_1
1. Flat Plate (0)	1	1	1	1	1	x_1	x_1	x_1
2. Stag Line of Un- yawed Cyl (1)	1	x/x_1	1	1	1	$\frac{x_1}{2JL}$	$\frac{x_1}{2JL}$	$\frac{x_1}{2JL}$
3. Hemispherical Stag Pt (1/2)	1	x/x_1	x/x_1	1	1	$\frac{x_1}{4JL}$	$\frac{x_1}{4JL}$	$\frac{x_1}{4JL}$
4. Stag Line of Inf Yawed Cyl (0)	1	1	1	e^{-KZ}	1	$\frac{1}{2K \bar{E}_L}$	$\frac{1}{2K \bar{E}_L, 0}$	$\frac{4}{5K \bar{E}_T, 0}$
5. Unyawed Cone (0)	1	1	x/x_1	1	1	$x_1/3$	$x_1/3$	$\frac{4x_1}{9}$

$\triangle 1$ Not applicable — laminar flow only.

$$\triangle 2 \quad K = \frac{1}{u_e} \left(\frac{dV_n}{dS} \right)_{LE} SL$$

$$\beta_c = 1.0$$

Table B1. - Streamline divergence parameters for several special cases.

TABLE B2

TABULATION OF VALUES OF $\rho_r \mu_r$

$\frac{(\rho_e \mu_e)_{eff}}{\rho_w \mu_w}$	$\frac{\rho_r \mu_r}{\rho_w \mu_w}$	
	From fig. 66	From eq. (B79)
.15	.226	.226
.20	.290	.296
.25	.354	.362
.30	.414	.426
.35	.485	.486
.40	.532	.544
.5	.641	.650
.6	.739	.744
.7	.818	.826
.8	.892	.896
.9	.950	.954
1.0	1.000	1.000
1.1	1.04	
1.2	1.08	
1.3	1.12	eq. (B79)
1.4	1.15	not valid
1.5	1.18	for hot
1.6	1.21	wall case.
1.7	1.25	
1.8	1.26	

TABLE B3

TABULATION OF VALUES OF $(\rho_e \mu_e)_{eff}$

$\frac{\rho_g \mu_g}{\rho_e \mu_e}$	$\frac{(\rho_e \mu_e)_{eff}}{\rho_e \mu_e}$	
	From fig. 67(a)	From eq. (B78)
.2	.335	.336
.3	.478	.478
.4	.610	.604
.5	.715	.713
.6	.791	.804
.7	.850	.879
.8	.905	.936
.9	.955	.976
1.0	1.000	1.000

TABLE B4

TABULATION OF VALUES OF Γ

Σ	Γ	
	From fig. 68	From eq. (B83)
.5	.164	.155
.6	.232	.224
.8	.360	.349
1.0	.475	.460
1.5	.710	.700
2.0	.925	.905
3.0	1.27	1.26
4.0	1.56	1.56
5.0	1.83	1.82
6.0	2.07	2.07
7.0	2.30	2.30
8.0	2.50	2.51
9.0	2.70	2.72
10.0	2.87	2.90

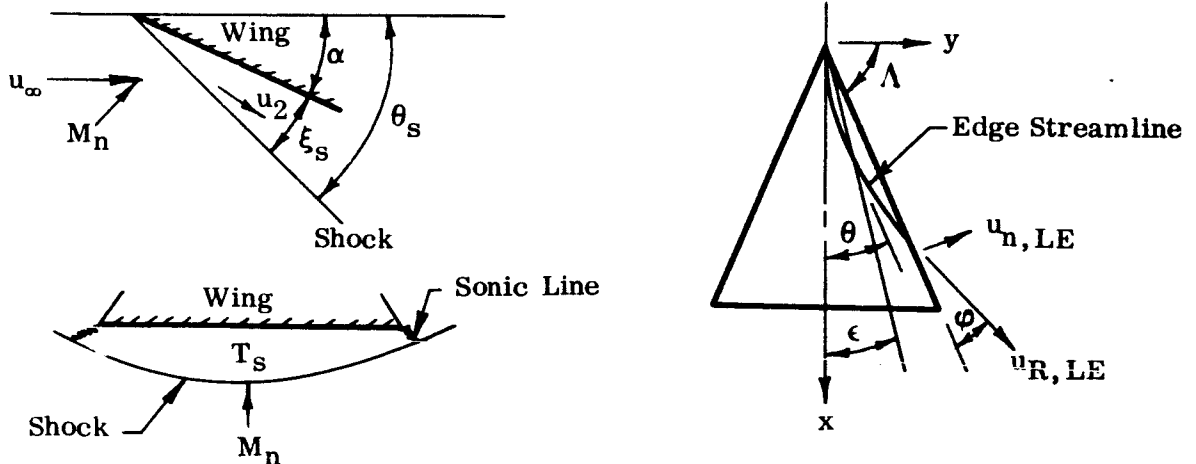
APPENDIX C

DELTA WING FLOW FIELD CALCULATIONS

Calculations of this report include predictions of three-dimensional flow effects on delta wing centerlines. The flow field parameters required for those calculations are the local velocity, pressure, and streamline divergence rate. The predictions used in this report are based on numerical solutions by the method of Kennet (ref. 18) and wedge theory. The method of reference 18 is valid only at high angles of attack such that the shock wave is detached from the leading edges, while wedge theory is applicable only at low angles of attack. There is an intermediate range where neither method applies. This appendix presents the results of the two calculations and describes the method of normalizing those results so that the flow behavior in the intermediate range can be estimated.

High Angle of Attack

First define the following physical terms relating to the boundary layer edge flow direction on a delta wing lifting surface:



For a wing with sharp leading edges the component of surface flow normal to the leading edge has the value of the local speed of sound:

$$\begin{aligned}
 u_{n,LE} &= a_S \left[\frac{a_{LE}}{a_S} \right] \\
 &= a_S \sqrt{\frac{T_{s,LE}}{T_S}}
 \end{aligned}
 \tag{C1}$$

$$T_{s,LE} = \frac{1}{1 + \frac{\gamma-1}{2} M_{LE}^2}$$

$$M_{LE} = [M_n^2 + M_R^2]^{1/2} = \left[1 + \left(\frac{u_R}{u_n} \right)^2 \right]^{1/2}, \quad M_{n,LE} = 1$$

u_R and u_n are the radial and normal components of total inviscid surface velocity. The streamline angle at the leading edge is then

$$\phi^* = \tan^{-1} \left(\frac{u_n}{u_R} \right)_{LE}
 \tag{C2}$$

and with the substitution of equation (C1) and for a perfect gas,

$$\phi^* = \tan^{-1} \left[\frac{\gamma-1}{\gamma+1} \left(\frac{2}{\gamma-1} \left(\frac{a_S}{u_{R,LE}} \right)^2 - 1 \right) \right]^{1/2}$$

In terms of total conditions,

$$\left(\frac{a_S}{u_\infty}\right)^2 = \frac{1 + \frac{\gamma - 1}{2} M_\infty^2}{M_\infty^2} \quad (C3)$$

and ϕ^* becomes

$$\phi^* = \tan^{-1} \left[\frac{\gamma - 1}{\gamma + 1} \left[\left(1 + \frac{2}{(\gamma - 1) M_\infty^2}\right) \left(\frac{u_\infty}{u_{R, LE}}\right)^2 - 1 \right] \right]^{1/2} \quad (C4)$$

Analysis of computer results from the lifting delta wing theory of Kennet reference 18 has shown that $u_{R, LE}/u_\infty$ is well approximated by the total velocity ratio u_2/u_∞ which is obtained from the shock angle at the wing centerline in the following manner:

$$\left(\frac{u_R}{u_\infty}\right)_{LE}^2 \approx \left(\frac{u_2}{u_\infty}\right)_{\underline{C}_L}^2 = 1 - 4 \sin^2 \theta_s \frac{(M_n^2 - 1)(\gamma M_n^2 + 1)}{(\gamma + 1)^2 M_n^4} \quad (C5)$$

The shock deattachment angle ξ_s at the wing centerline can be correlated by the relation

$$\theta_s - \alpha = \xi_s = 70 \frac{\rho_\infty}{\rho_2} \left(\frac{\tan \alpha}{\tan \Lambda}\right)^{.566} \text{ degree} \quad (C6)$$

for high angles of attack.

Low Angle of Attack

At very low angles of attack two-dimensional theory may be applied in the vicinity of the leading edge of a sharp delta wing provided that the normal flow is supersonic both in the free stream and on the wing surface. From equations (3) and (6) of this report it is seen that the free stream Mach number and angle of attack in the plane normal to the leading edge are given by:

$$M_n = M_\infty \sin \alpha_n \quad (C7)$$

$$\alpha_n = \tan^{-1} \left(\frac{\sin \alpha}{\cos \alpha \cos \Lambda} \right) \quad (C8)$$

The results of the normal flow wedge calculation are then combined with the flow component parallel to the leading edge to obtain the delta wing values. Since the wedge flow solutions are valid only near the leading edge, the streamline angle distribution is assumed to exhibit a sinusoidal variation. The sinusoidal distribution is chosen because it matches the streamline angle at the centerline and leading edge, and the gradient at the centerline.

Correlation of Results

The discussion under High Angle of Attack suggests the use of ϕ^* and ξ as parameters for normalizing the results of the above calculations. However, the above equations (C3), (C4) and (C5) predict two physically impossible conditions at zero angle of attack. They are:

In equation (C5), $\xi_s \rightarrow 0$ as $\alpha \rightarrow 0$

and in equation (C3), $\phi^* \rightarrow$ to a finite positive value as

$$\alpha \rightarrow 0, \quad \frac{u_\infty}{u_{R,LE}} \rightarrow 1$$

These inconsistencies are avoided if equations (C3) through (C6) are modified as follows:

Replace equation (C6) by

$$\theta_s = \left[\xi_m^2 + (\xi_s + \alpha)^2 \right]^{1/2} \quad (C9)$$

$$\xi_m = \sin^{-1} \frac{1}{M_\infty}$$

and in equation (C4) replace

$$\frac{2}{(\gamma - 1) M_\infty^2} \quad \text{by} \quad \left(\frac{2}{(\gamma - 1) M_\infty^2} \right) \left(\frac{M_n^2 - 1}{M_n^2} \right)$$

This results in a change of equation (C6) to a correlation parameter now defined as:

$$\phi^{**} = \tan^{-1} \left[\frac{1}{6} \left(\left[1 + \frac{5}{M_\infty^2} \left(\frac{M_n^2 - 1}{M_n^2} \right) \right] \left(\frac{u_\infty}{u_2} \right)^2 - 1 \right) \right]^{1/2} \quad (C10)$$

$$\gamma = 1.4$$

The correlation was found to be most successful when angles are normalized by both ϕ^{**} and the wing apex angle $\beta \equiv 90 - \Lambda$. The results of the exact solutions are presented in figure 72 in terms of the normalized rate of change of streamline angle with respect to ϕ :

$$\overline{N}_{\xi} = \frac{\left[\frac{d\theta}{d\epsilon} \right]_{\xi}}{1 + \phi^{**}/\beta} \left(\frac{M_n^2 + 1}{M_n^2} \right) \quad (C11)$$

As shown, the wedge theory calculations are well normalized in terms of \overline{N}_{ξ} but are limited to ϕ^{**}/β less than about one-half. The delta wing results are seen to converge to a single curve at ϕ^{**}/β slightly above 1.0. The range between the two solutions is represented by the indicated fairing. The actual values of $d\theta/d\epsilon$ used in this report are given in figures 73 and 74. The derivative $(1/\Delta)(d\Delta/dx)$ required for the boundary layer calculation is related to θ by

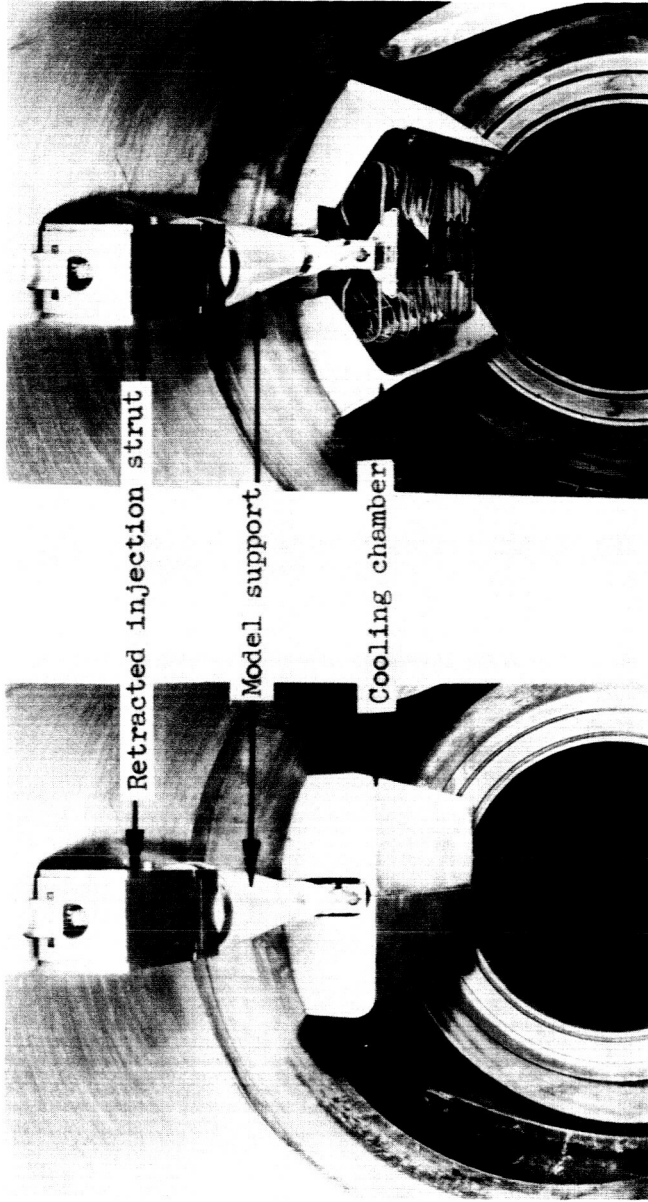
$$\frac{1}{\Delta} \frac{d\Delta}{dx} = \frac{1}{x} \left[\frac{d\theta}{d\epsilon} + 1 \right] \quad (C12)$$

TEST	TEST FACILITY	Mach No. M_∞	Free Stream Reynolds No. Millions Ft	Total Press. P_o PSIA	Model Temp. T_w °R	Angle of Attack α Degrees	Angle of Yaw ψ Degrees	Boundary Layer Flow	Laminar Reference Stanton number $N_{st,0} \sim 10^{-3}$	Turbulent Reference Stanton number $N_{st,ref} \sim 10^{-3}$	Diameter for $N_{st,ref}$ inch
AD461M-1	BHWT	6.08	15.6	1100	500	0 to 45	0, 10	Lam.	Pressure Data Only		
			19.3	1300	500			Turb.	4.74	.9	
			10.3	1200	500			Turb.	(6.07)7.4	(.9).332	
AD461P-1	BSWT	7.0	12.6	1400	500	-10 to 55	0, 10	Turb.		7.1	.332
			7.1	26.8				Lam.	Pressure Data Only		
			8.25	39.3							
AD462M-1	AEDC-B	8.08	0.986	200	450	-25 to 30	0, ±5	Lam.	26.5		
			2.02	480	500			Lam, Turb.	11.89	9.15	1.02
AD465M-1	JPL-21"	8.04	0.785	250	480	0 to 41.5	0, 5, 10	Lam.	35.2		
AD477M-1	AEDC-B	8.08	2.13	500	460	-5 to 55	0, ±10	Lam.	15.65		
			3.43	805	460			Turb.	12.35	7.44	1.5
AD483M-1	BHWT	6.10	17.0	1110	460	0 to 30	0, 10	Turb.		4.1	.9
AD485M-1	AYCO 4" Shock Tube	2.2	0.002 to 13	151946 to 9584 Btu/lb	540	0 to 30	0	Lam, Turb.	Varies from Run to Run		
AD642M-1	CAL 48" Shock Tunnel	6 15	0.06 15.7	700 3900	520	0 to 50		Turb. Lam.	Varies from Run to Run		

TABLE I: NOMINAL WIND TUNNEL FLOW CONDITIONS

TEST	MODEL DESIGNATION	PROW	NOMINAL SKIN THICKNESS INCHES	SWEEP ANGLE, Λ DEGREES	LEADING EDGE DIAMETER, D, INCHES	LENGTH DIAMETER L/D	FREE STREAM REYNOLDS NUMBER BASED ON DIAMETER		
							M_{∞}	P_0	$Re, D \sim 10^4$
AD461M-1	W ₁	Blunt	0.03	73	1.00	4.2	7.0	1200	6.08
	W ₂	Blunt	0.05	73	0.90	7.2	1400	1100	
	W ₃	Blunt	0.05	73	0.332	16.2	105	130	
	W ₃ + Nose	Sharp	0.05	73	0.332	16.2	28.5	34.8	43.1
	W ₅ (4° Ramp Wing)	Blunt	0.05	73	0.332	16.2	77.2	94.5	117
AD461P-1	W ₂ + Nose	Sharp	0.05	73	0.90	7.2	77.2	94.5	117
	W _{9A}	Sharp	0.05	73	0.90	7.2	145 ($M_{\infty} = 7.0, P_0 = 1300$)		
	W ₁	Blunt	0.05	73	1.00	4.2	59.2,	68.8,	80.4
	W ₁	Blunt	0.05	73	1.02	16.0	8.38, 17.2		
	W _{3A1}	Sharp	0.05	73	0.75	10.9	4.91		
AD477M-1	W ₁	Sharp	0.04	73	$D_1 = 0.50$ $D_2 = 1.50$	8.7	26.6,	42.8	
	W ₁	Sharp	0.05	78	0.90	7.2	128		
AD483M-1	W ₂	Sharp	0.05	68	0.90	7.2			
	1 (Wing)	Blunt		73	0.50	4.2	0.00833		
	2 (Cylinder-Plate)	Blunt		0	0.50	s/D = 3.3	to 54		
AD485M-1	3 (Cylinder-Plate)	Sharp		45	0.50	3.0			
	Cylinder-Plate	Sharp		55,60,65	4.0	8.0	M_{∞}	5.0	15.0
	Hemisphere Cylinder	Blunt		5.0	2.0		65.0	4.0	
							to 52.2	to 4.3	
							M_{∞}	6.0	15.0
							91.6	1.1	
							to 600	to 10.4	

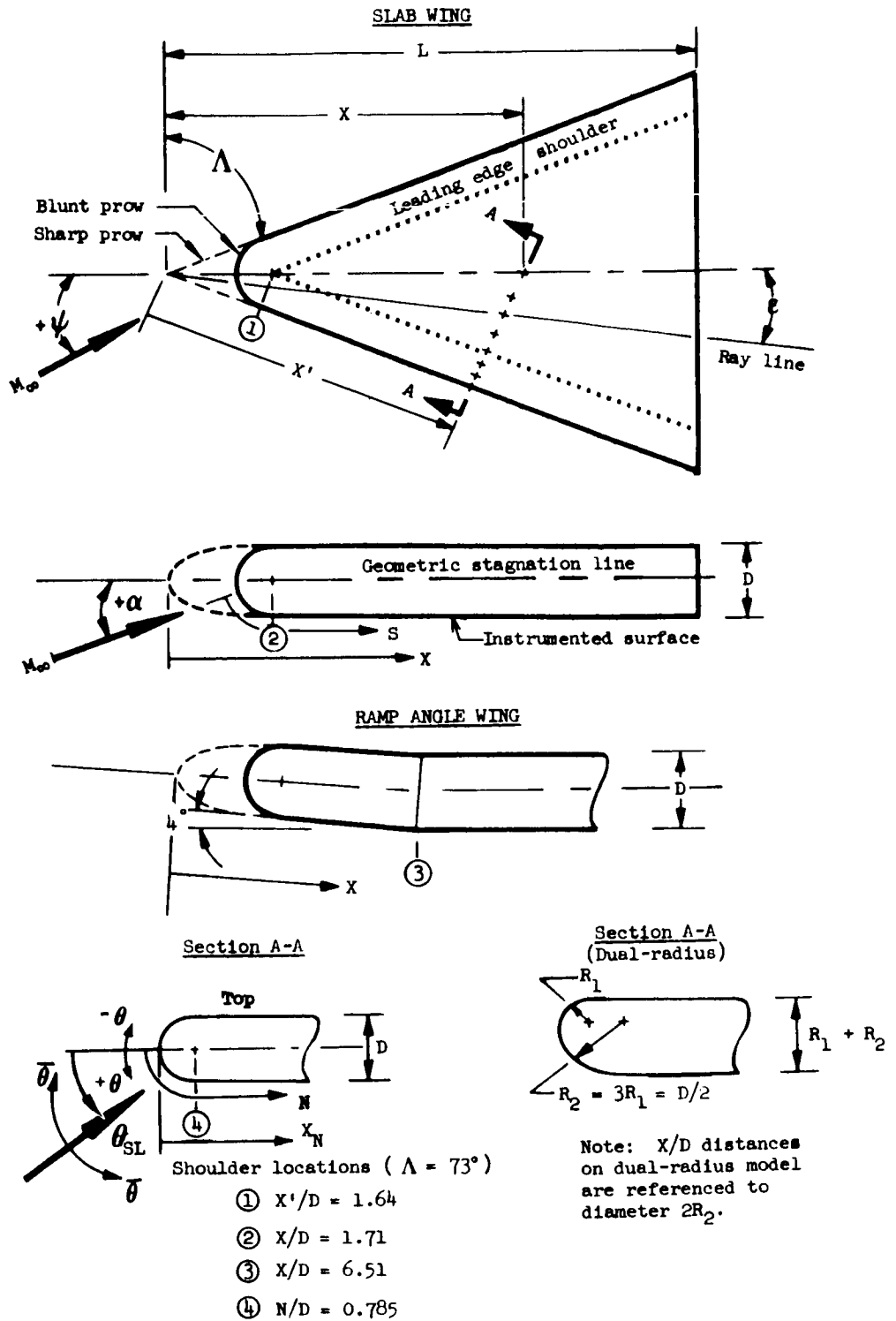
TABLE II: WIND TUNNEL MODELS



Cooling chamber closed

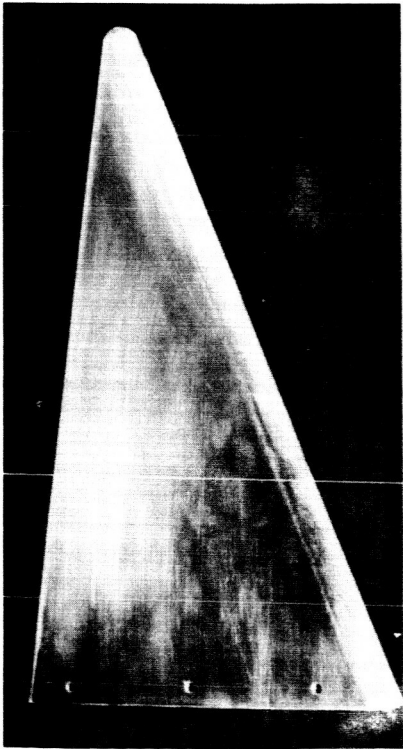
Cooling chamber open,
cooling air manifold and model exposed

Figure 1.- Model installation in 12" Boeing hypersonic wind tunnel.

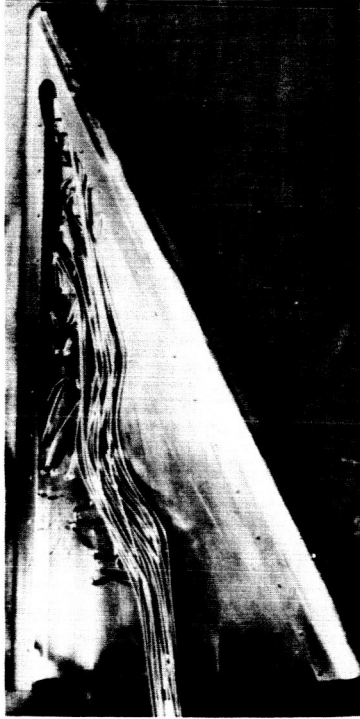


(a) Delta wing models

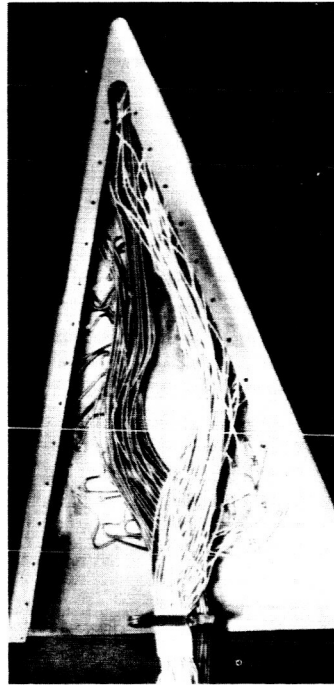
Figure 2.- Model geometry.



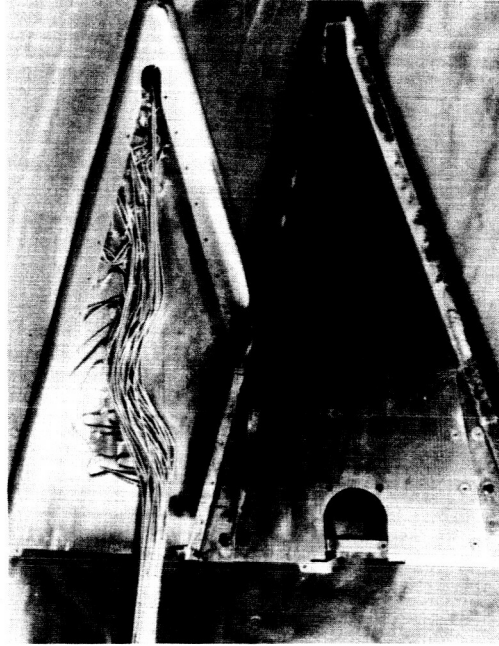
Contoured shell showing test surface attachment holes



Typical pressure tube installation



Typical thermocouple installation

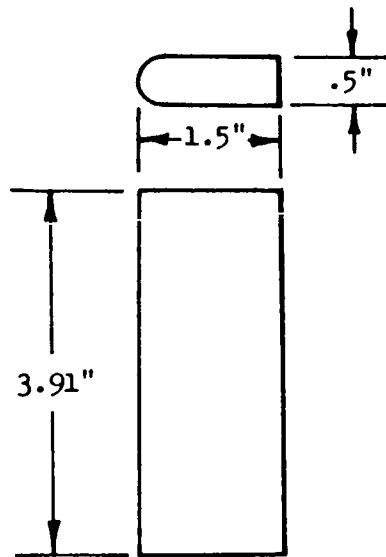


Instrumented shell and structure

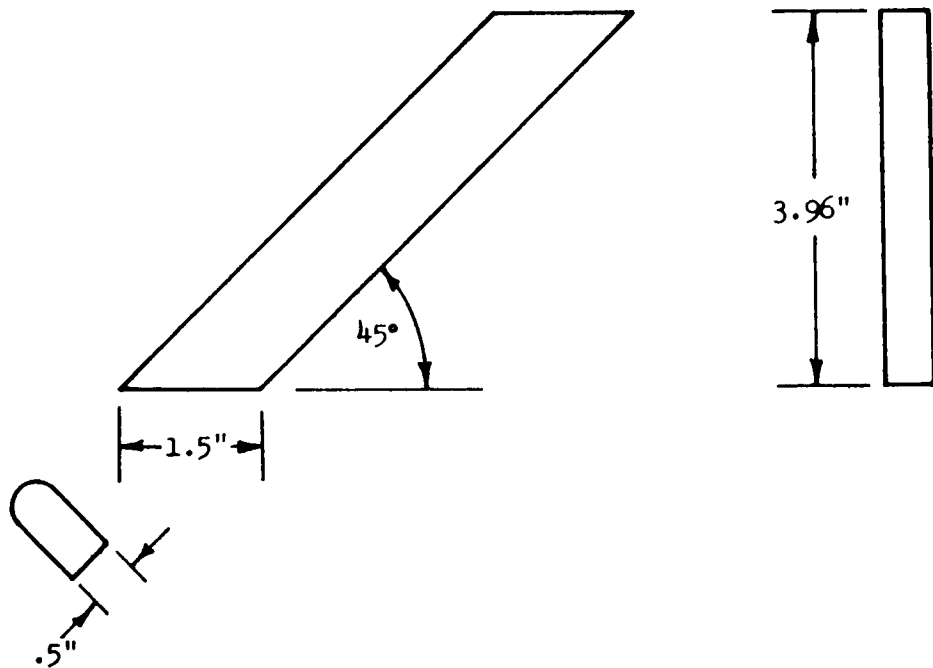
(b) Electroformed model construction

Figure 2.- Continued.

Blunt plate model

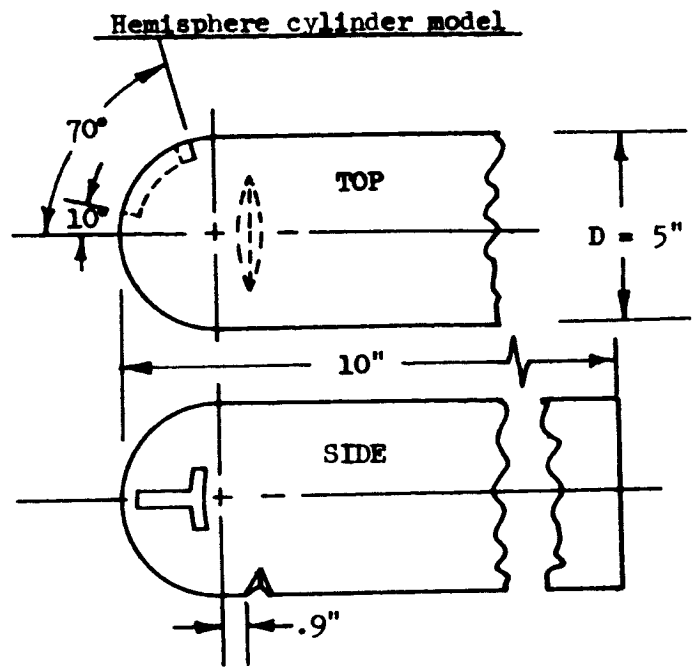


Yawed cylinder model



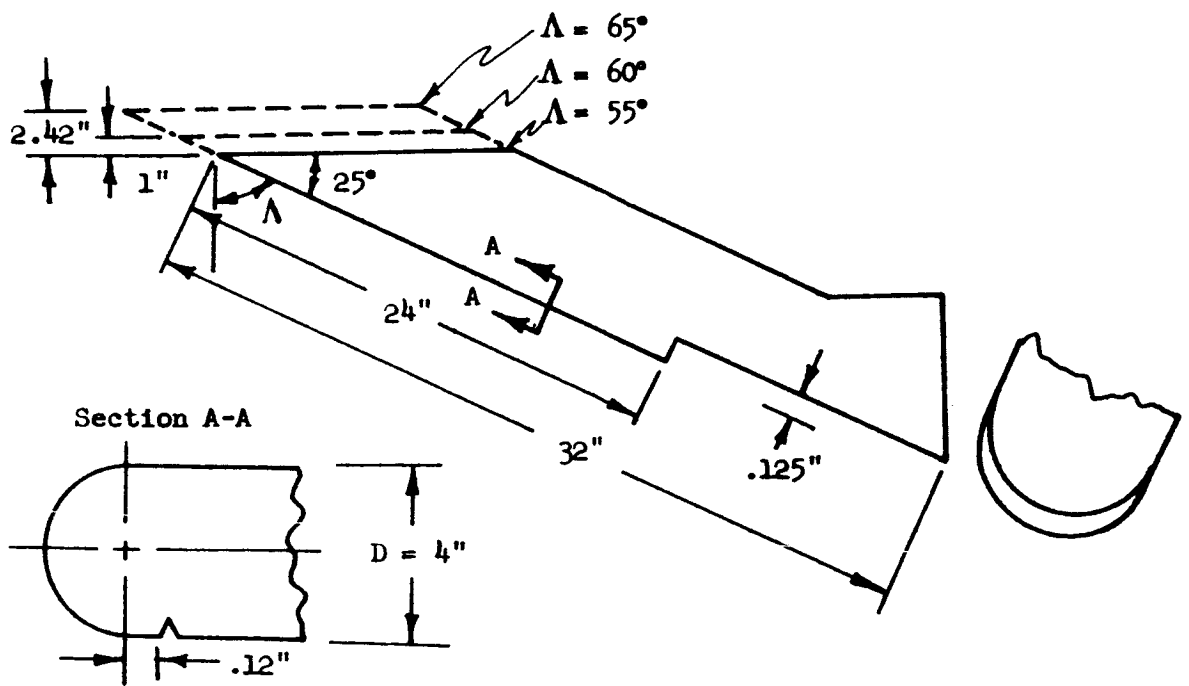
(c) AD485M-1 models

Figure 2.- Continued



Swept hemicylinder leading edge model

Span extensions for



(d) AD642M-1 models

Figure 2.- Concluded

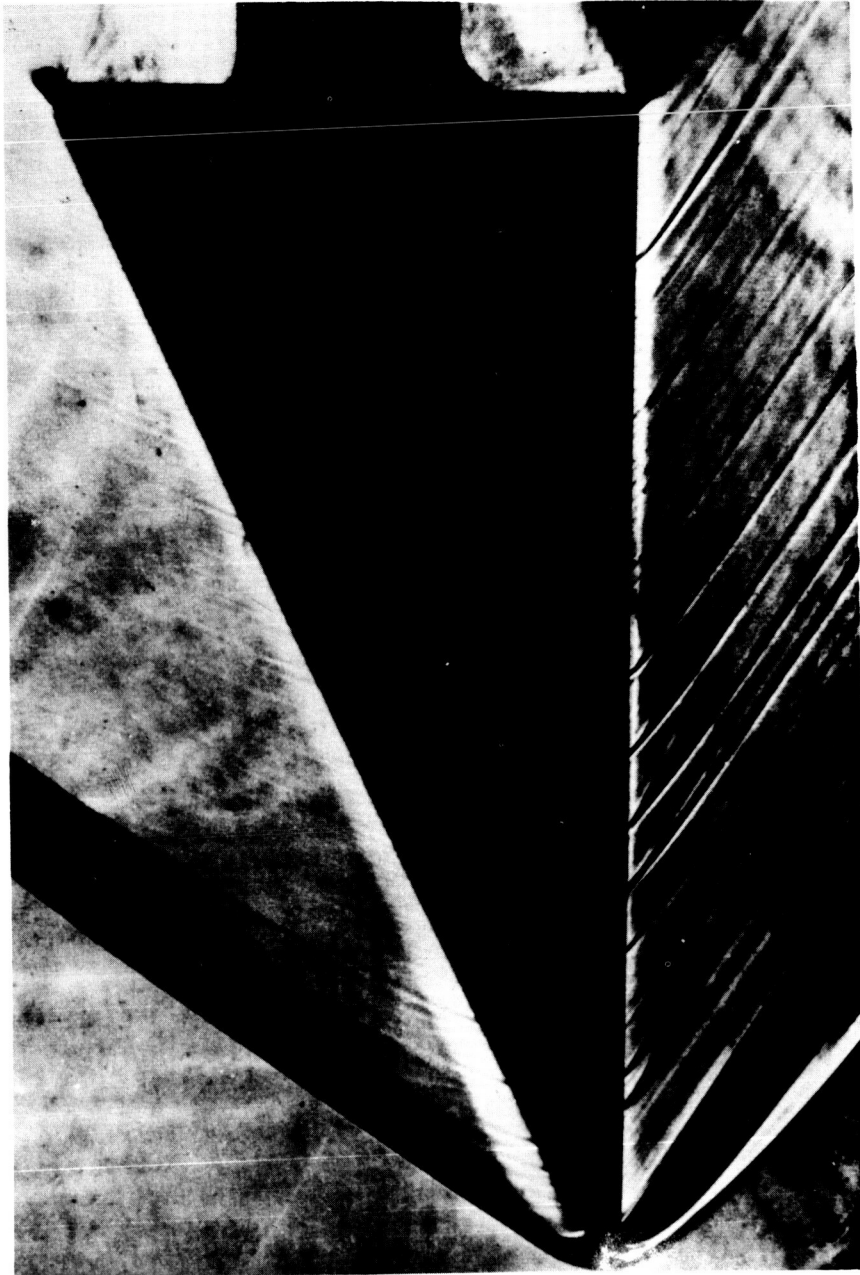


Figure 3.- Mach line schlieren photograph.
AD485M-1; $\alpha = 0^\circ$.

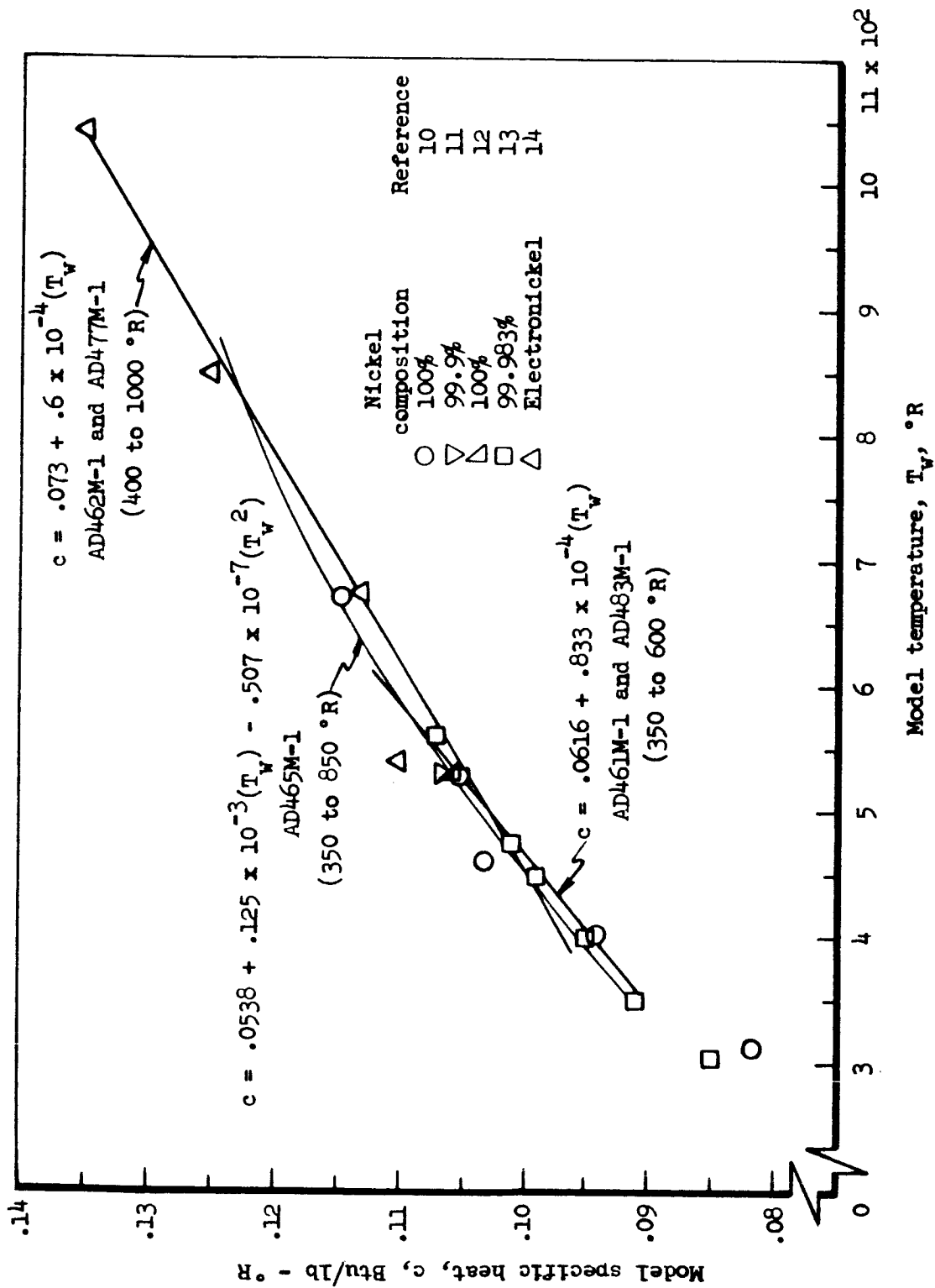


Figure 4.- Specific heat of nickel calorimeter material.

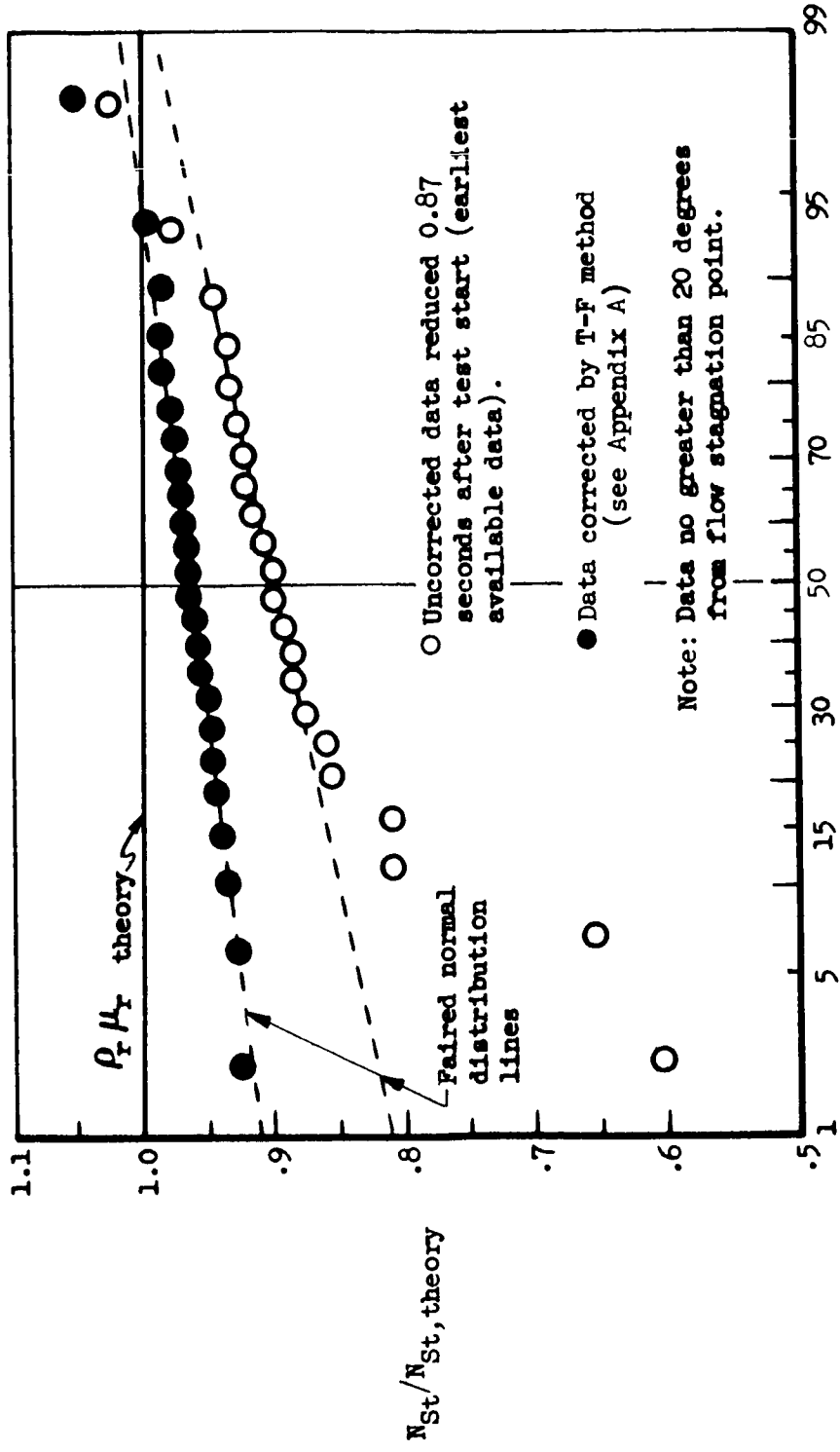


Figure 5. - Heat transfer data accuracy, spherical nose. AD463M-1;
 $M_\infty = 8.08$; $Re,D = 50.5 \times 10^4$.

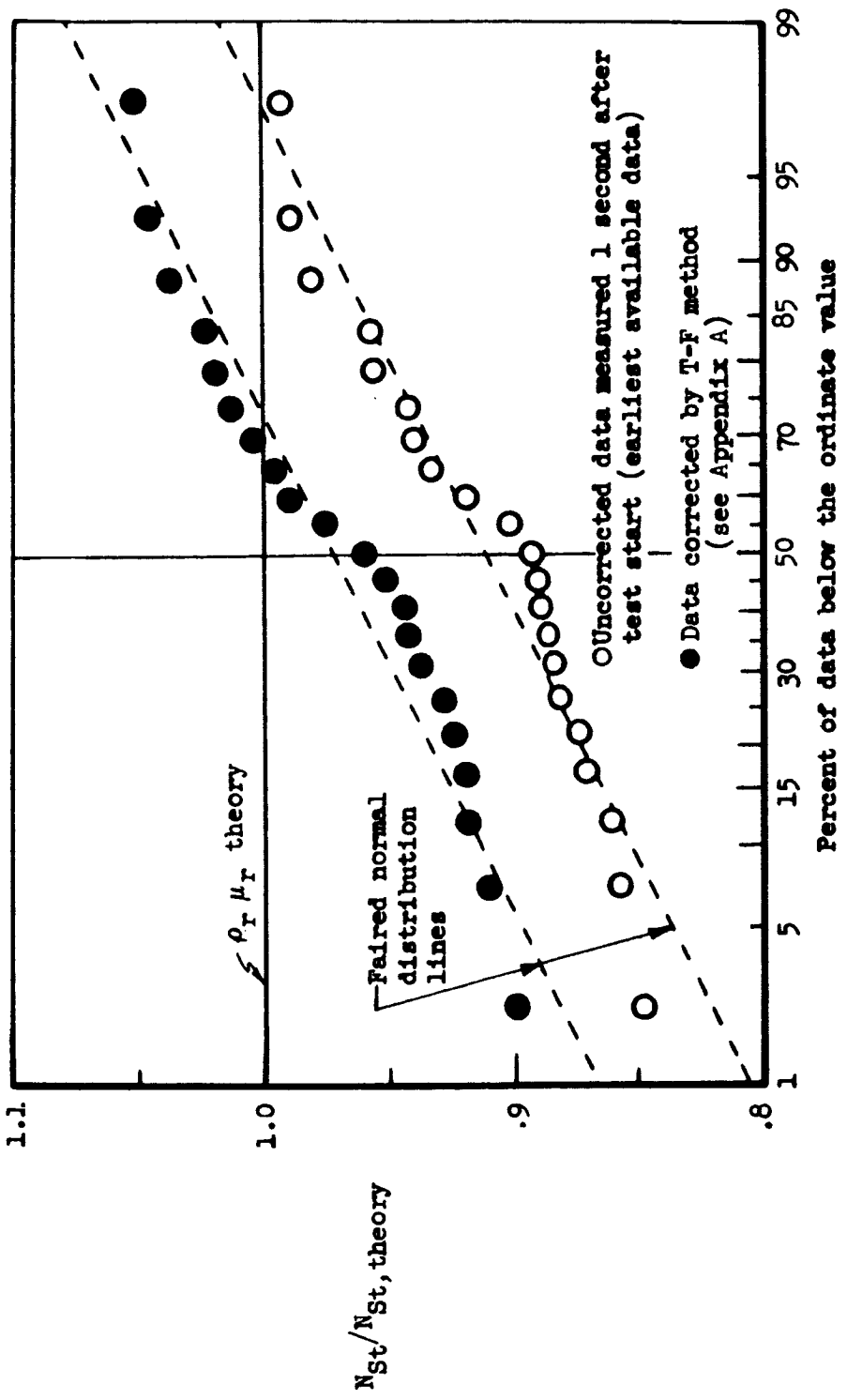


Figure 6. - Heat transfer data accuracy, laminar stagnation line. AD477M-1;
 $M_\infty = 8.08$; $\alpha = 10^\circ$; $\Lambda = 73^\circ$; $\psi = 0^\circ$;
 $N_{St,\sigma} / N_{St,theory} = 4.76$.

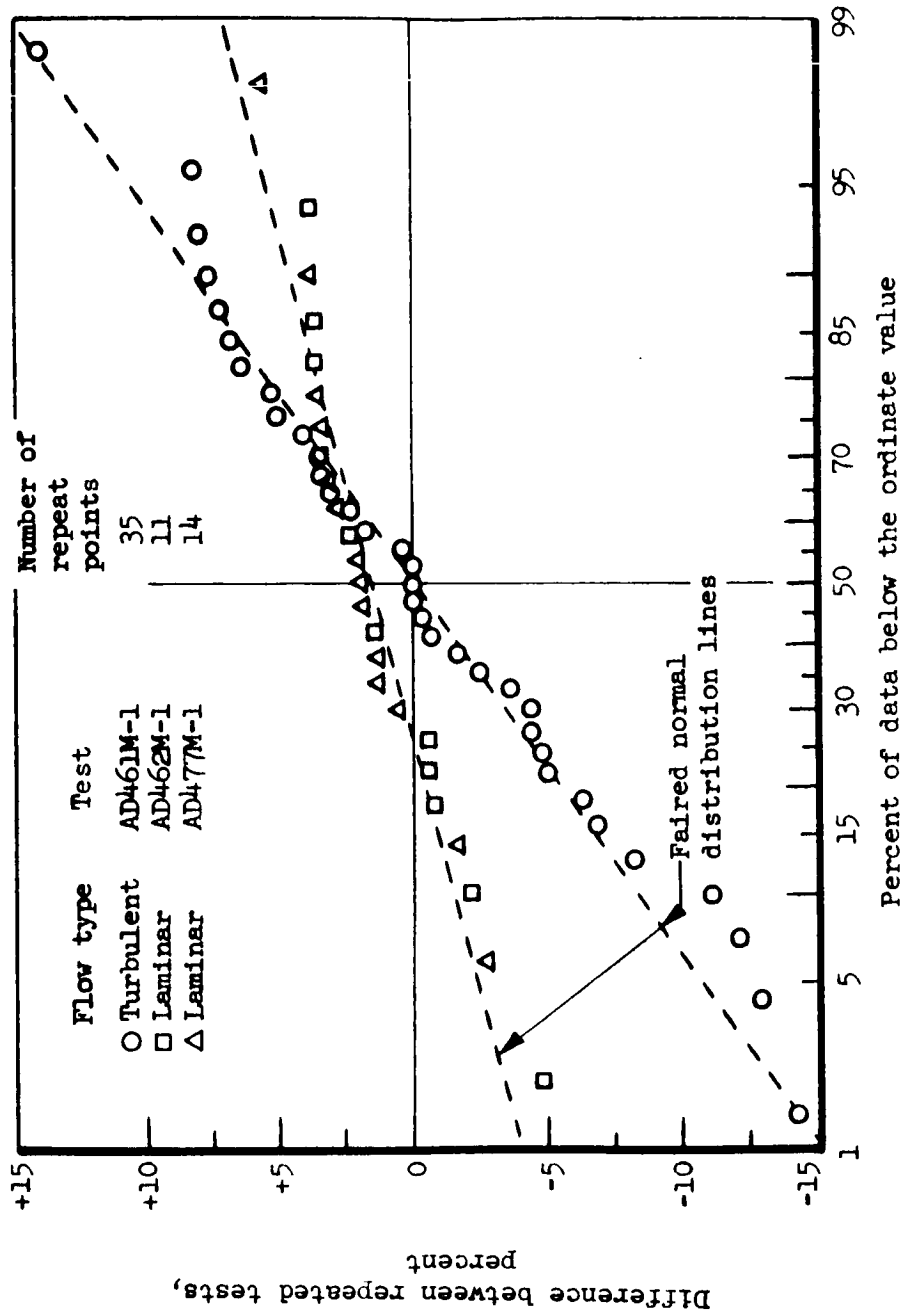


Figure 7. - Heat transfer data repeatability, turbulent and laminar leading edge.

Trip type	t/D	W/D	$\Delta X_T/D$	Prow	$\Lambda_{eff}, \text{deg}$	M_∞	$N_{Re,D}$	Test	
□	①	.033	.268	1.33	Sharp	73.0	6.08	145×10^4	AD461M-1
○	②	.022	.110	1.33	Blunt	70.35	7.04	77.2×10^4	AD461M-1
○	②	.022	1.110	1.33	Blunt	70.35	7.04	77.2×10^4	AD461M-1
△	③	.011	.167	1.28	Blunt	78.0	6.10	128×10^4	AD483M-1
△	③	.011	.167	1.28	Blunt	68.0	6.10	128×10^4	AD483M-1

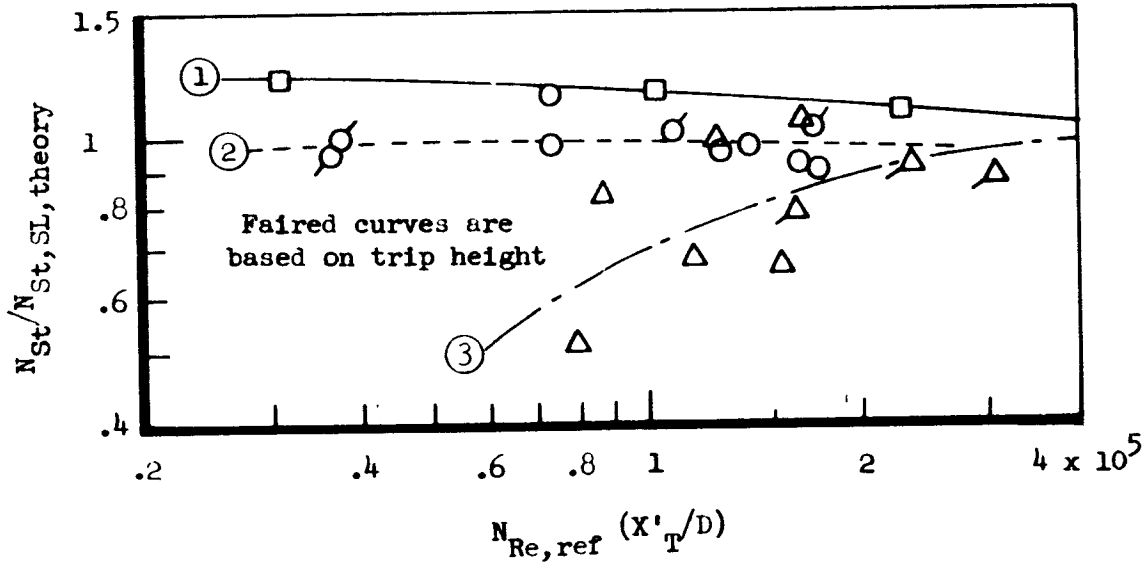
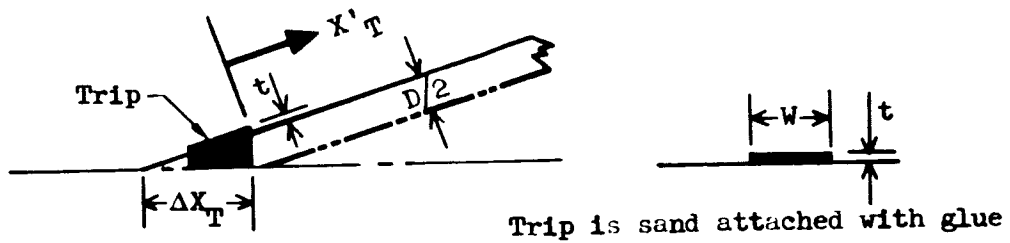
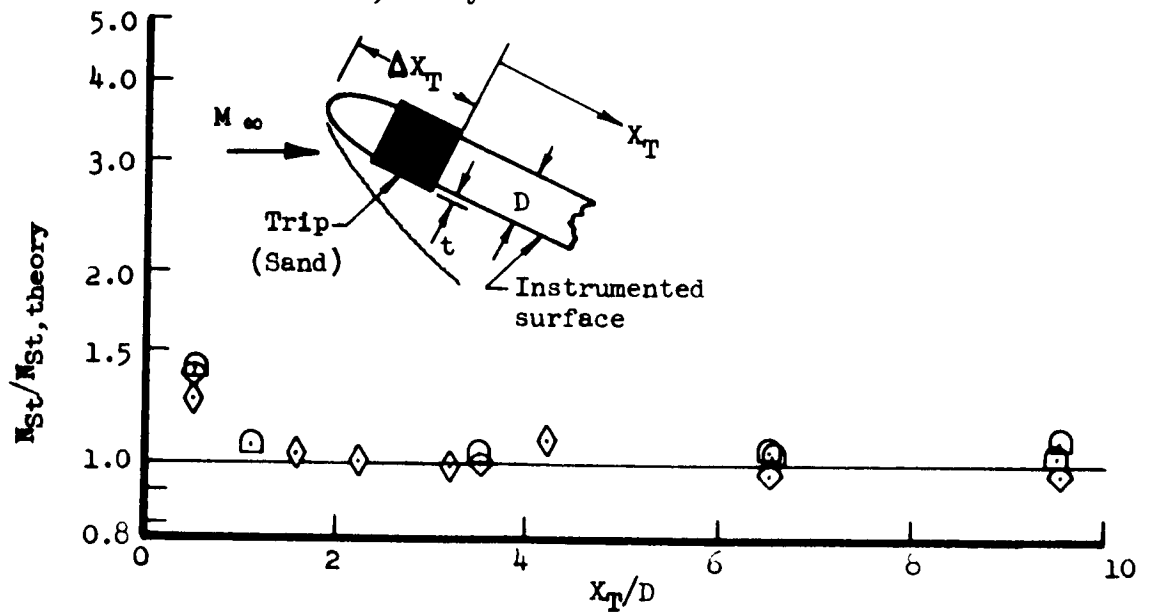


Figure 8.- Heating on cylindrical leading edge stagnation line downstream of boundary layer trip.

	α	$N_{Re,D}$	t/D	M_∞	Test	$\Delta X_T/D$	W/D
□	15°	28.5×10^4	.06	7.0	AD461M-1	3.00	.301
◇	30°	77.2×10^4	.022	7.0	AD461M-1	1.35	1.110
◇	40°	34.8×10^4	.06	7.0	AD461M-1	3.00	.301

$N_{St,theory}$ is the solid theory line shown on figure 51.

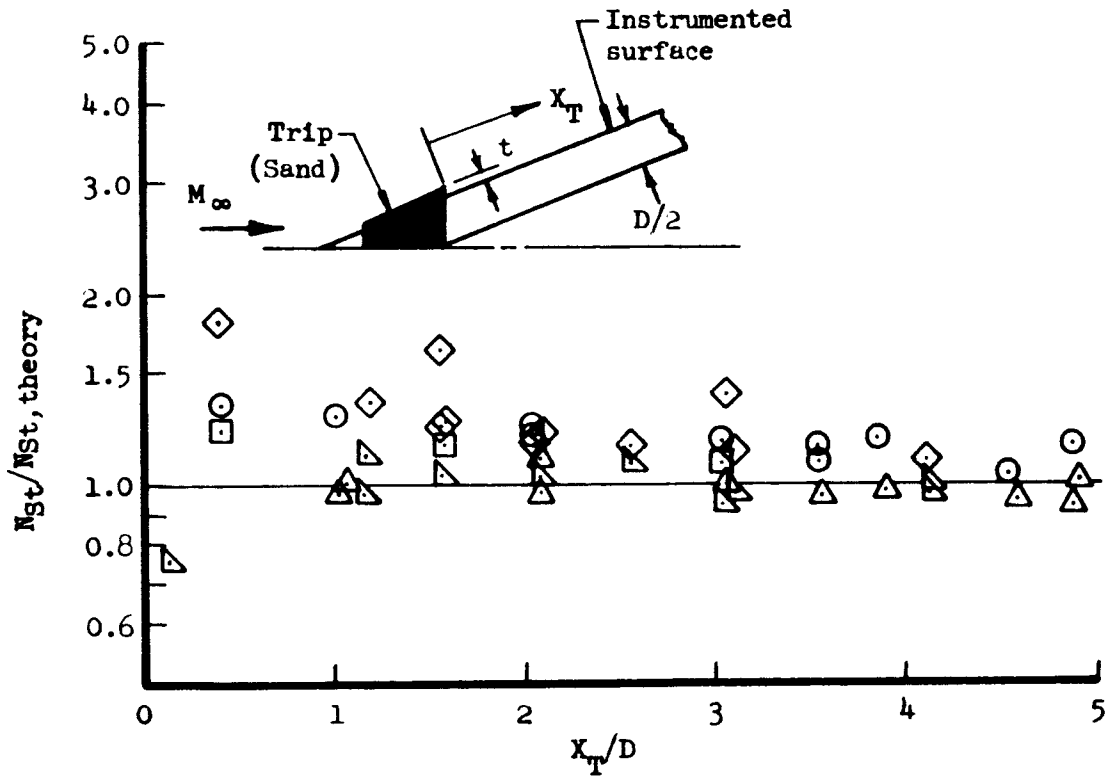


(a) Sharp-prow;
delta wing centerline

Figure 9.- Turbulent heating downstream of boundary layer trips.

	α_{Local}	$N_{\text{Re},D}$	t/D	M_{∞}	Test
◇	8.45°	77.2×10^4	.022	7.0	AD461M-1
○	14.5°	77.2×10^4	.022	7.0	AD461M-1
□	17.0°	145.0×10^4	.033	6.1	AD461M-1
△	16.8°	77.2×10^4	.022	7.0	AD461M-1
▽	19.6°	77.2×10^4	.022	7.0	AD461M-1

$N_{\text{St,theory}} = \text{Local cylinder theory based on } \rho_r \mu_r$



(b) Sharp prow;
cylindrical leading edge

Figure 9.- Concluded.

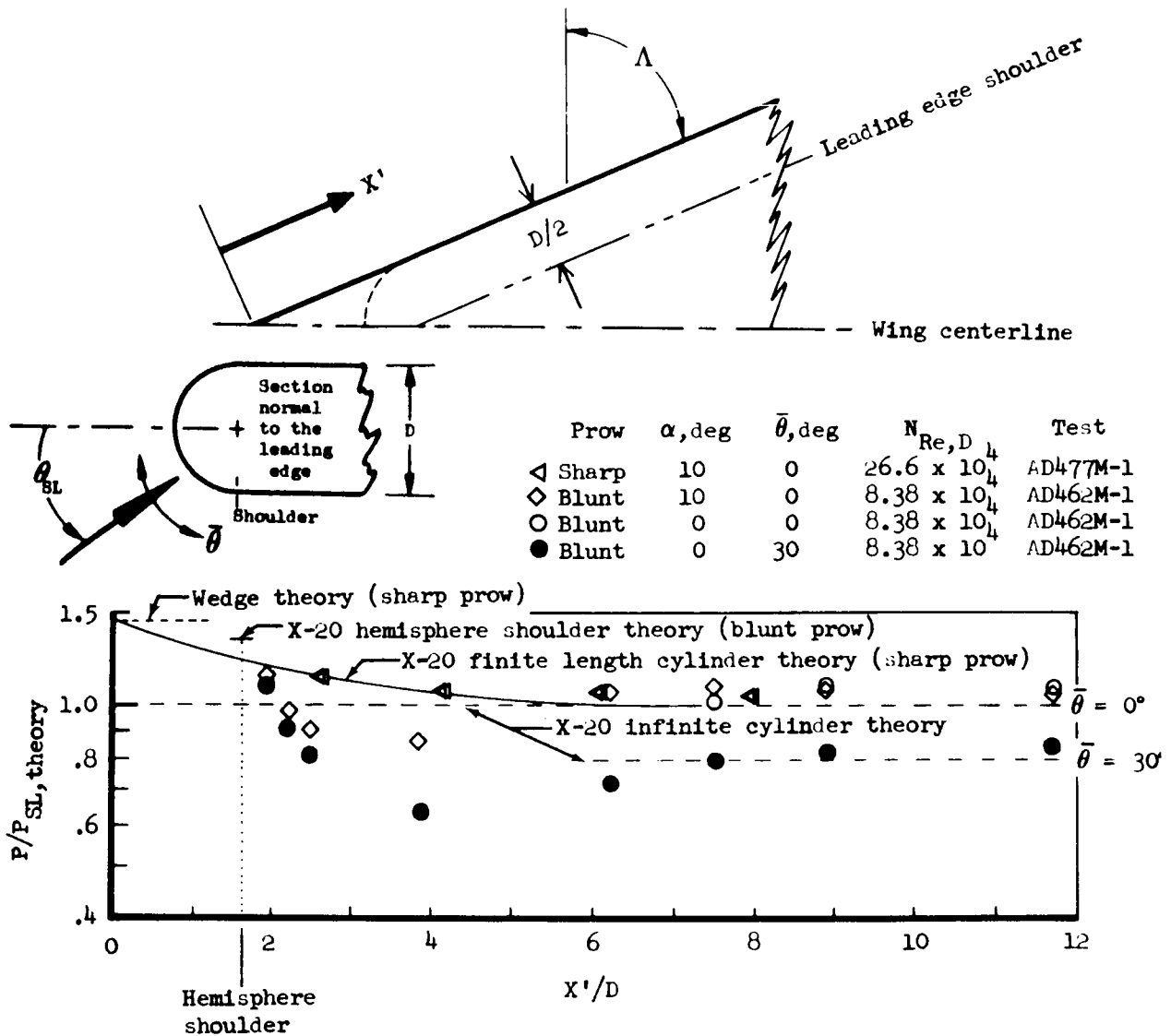


Figure 10.- Prow effect on pressures along the leading edge. $M_\infty = 8.08$; $\Lambda = 73^\circ$; $\psi = 0^\circ$.

$N_{Re,D}$	X/D	Prow	M_∞	Test
□ 117×10^4	4.06 → 6.56	Sharp	6.08	AD461M-1
△ 17.2×10^4	12.25	Blunt	8.08	AD462M-1
○ 8.38×10^4	12.25	Blunt	8.08	AD462M-1

$\bar{\theta}$ is measured from the true flow stagnation line
 Filled symbols indicate shoulder instruments

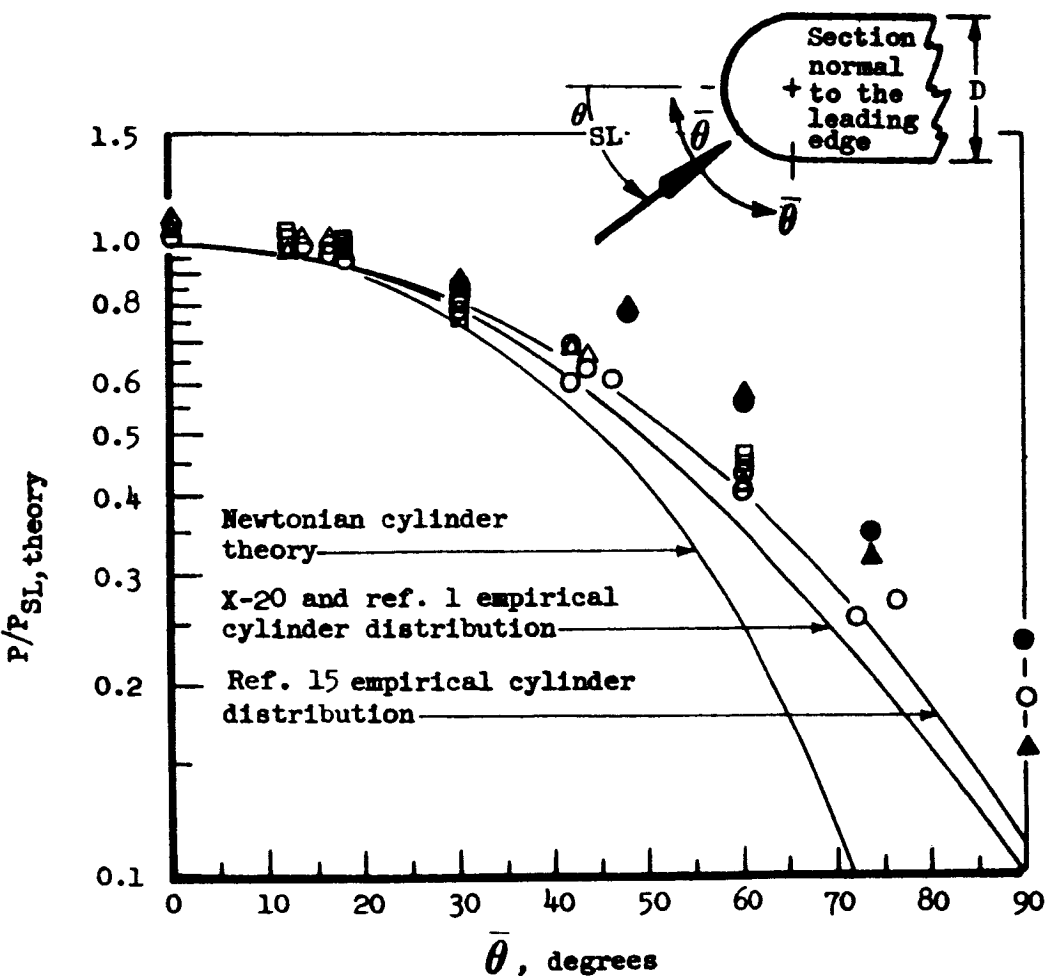


Figure 11. - Pressure distribution on a delta wing cylindrical leading edge.
 $\alpha \leq 15^\circ$; $\Lambda = 73^\circ$; $\psi = 0^\circ$.

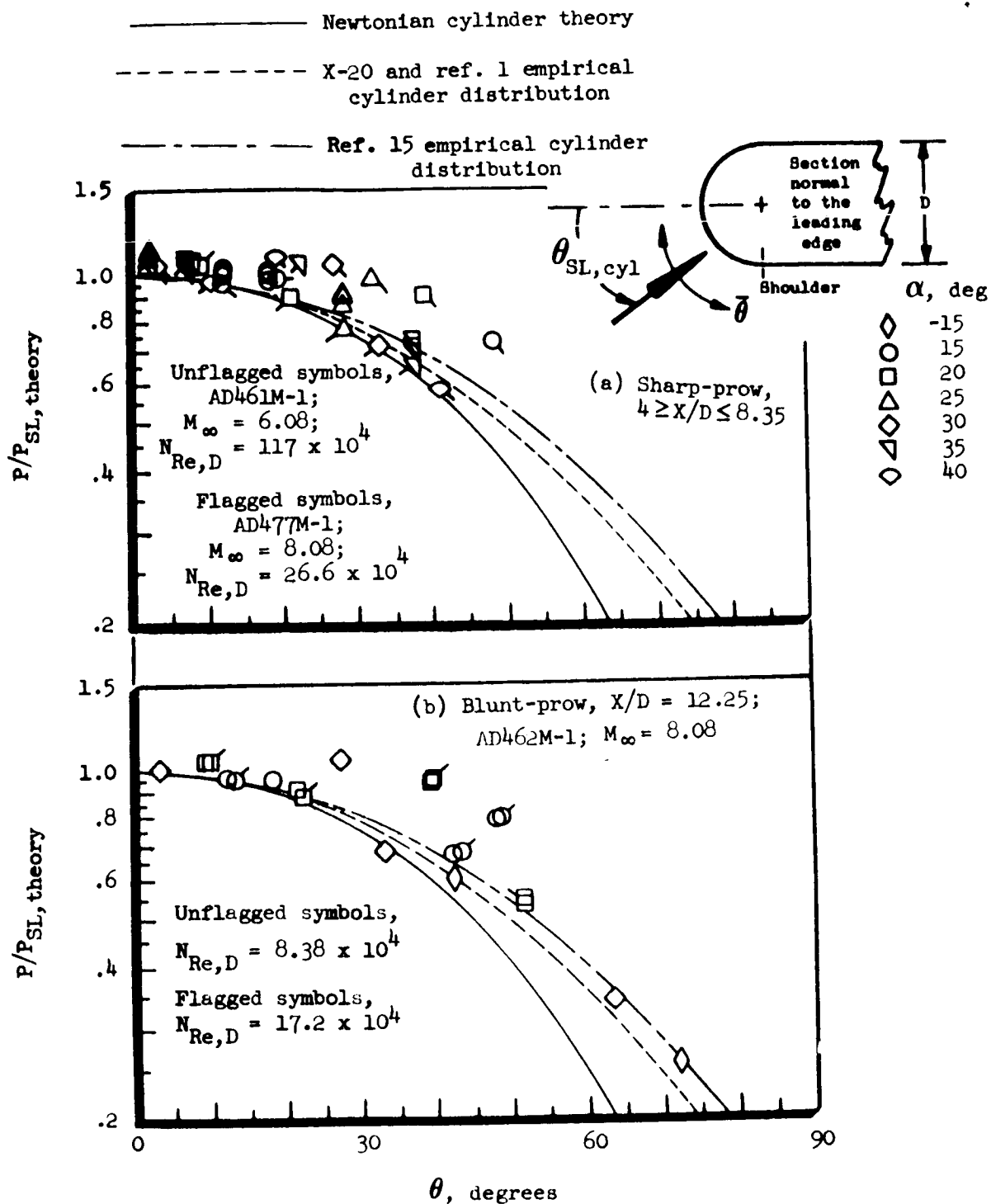


Figure 12.- Cylindrical leading edge pressure distribution, data located relative to infinite cylinder stagnation line (see figure 13).
 $\Lambda = 73^\circ$; $\psi = 0^\circ$.

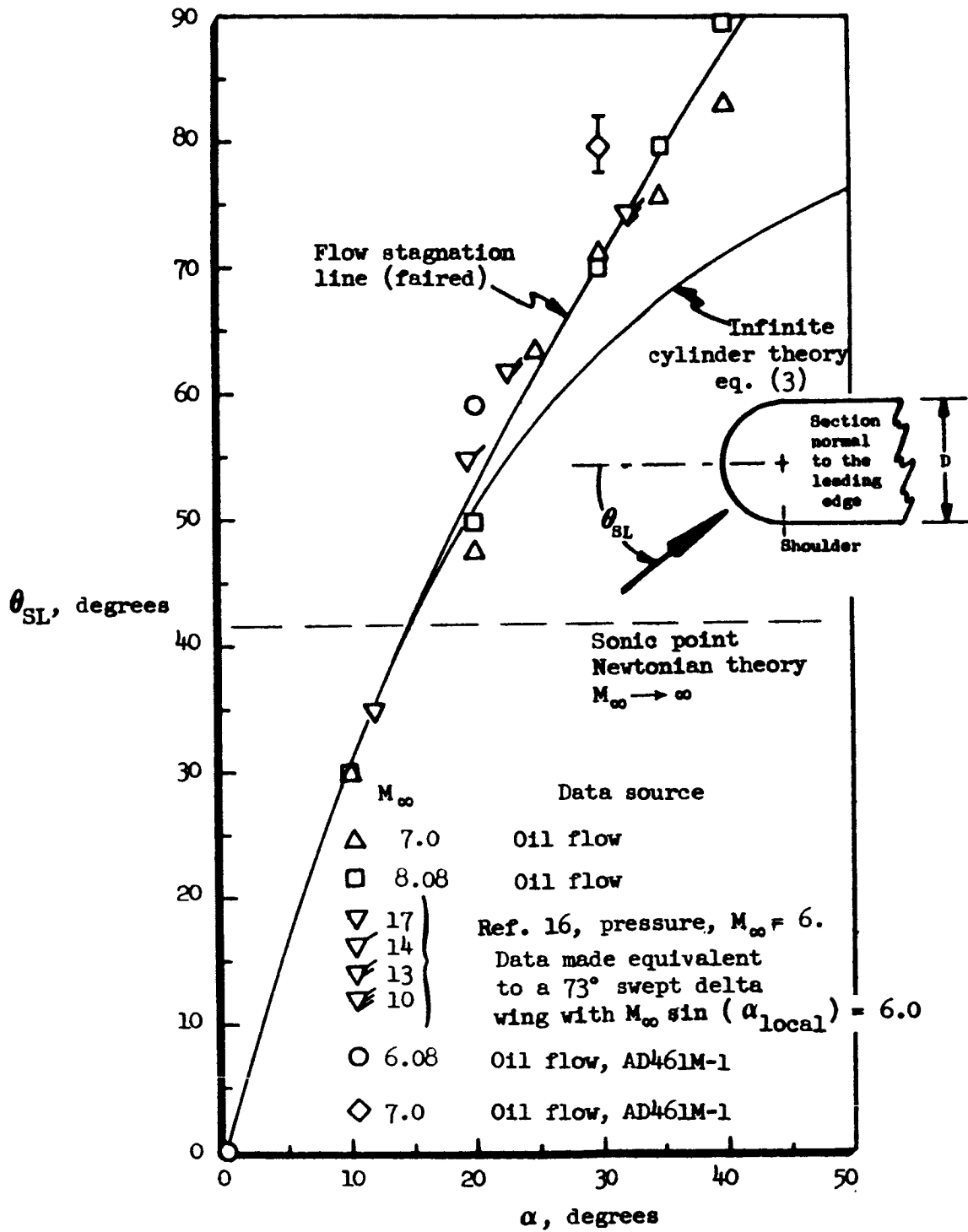


Figure 13.- Lower surface effect upon leading edge stagnation line shift.
 $\Lambda = 73^\circ; \psi = 0^\circ$.

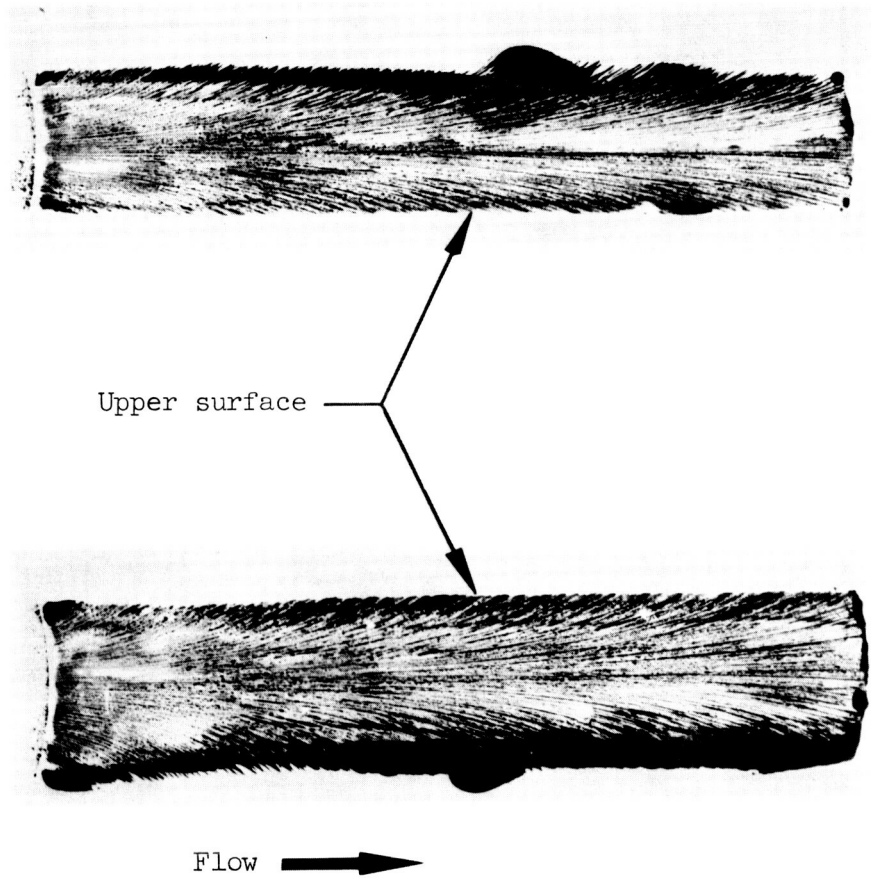


Figure 14.- Oil slicks on a delta wing cylindrical leading edge.
AD461M-1; $M = 6.08$; $\Delta = 73^\circ$; $\alpha = 0^\circ$.

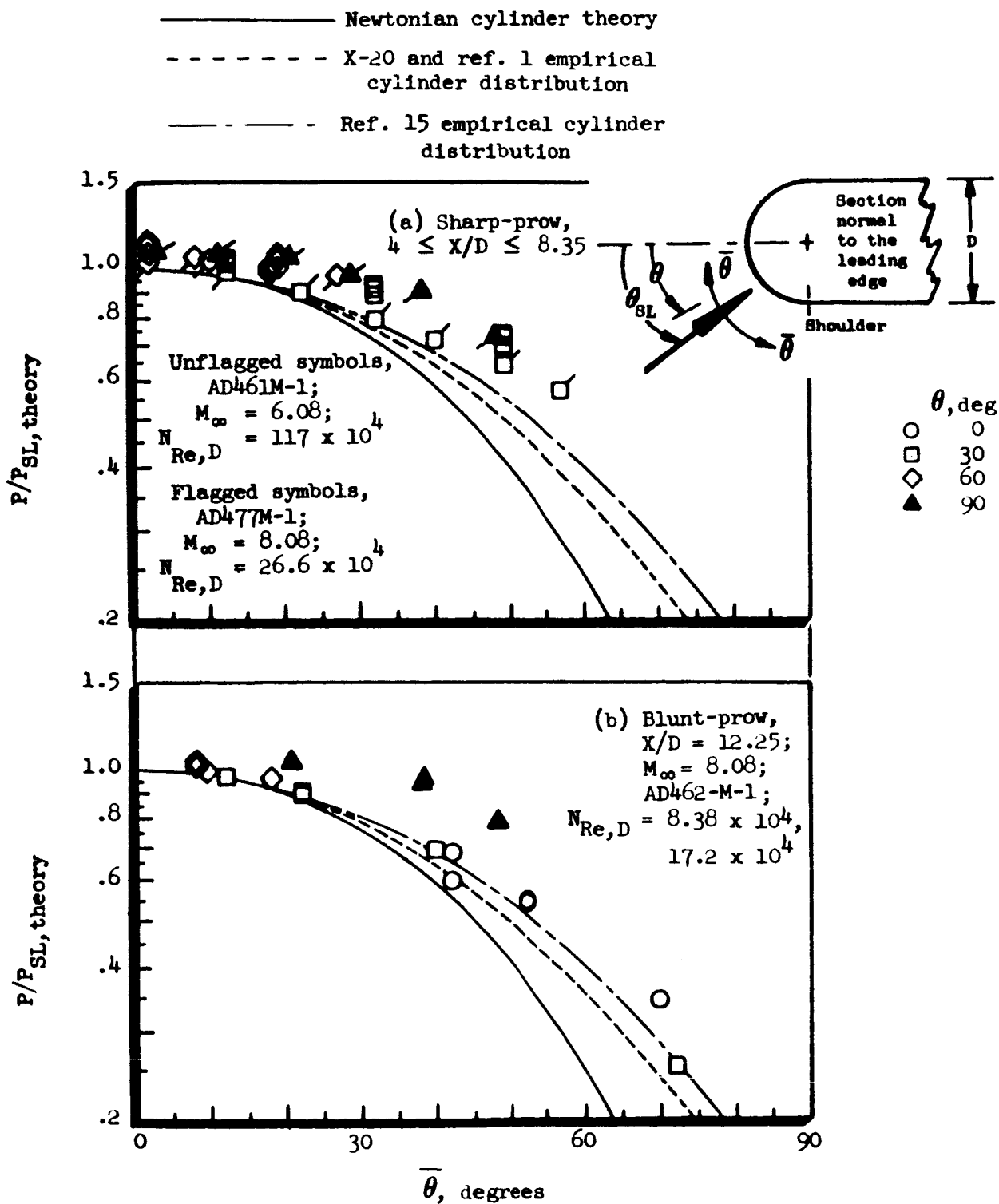


Figure 15.- Cylindrical leading edge pressure distribution, data located relative to flow stagnation line.

$$\alpha \geq 15^\circ; \Lambda = 73^\circ; \psi = 0^\circ.$$

	Λ , deg	M_∞	Test
○	73 wing	8.08	AD462M-1
□	73 wing	8.08	AD477M-1 (av 21 pts)
△	0 cyl. plate	2.2	AD485M-1 (av 21 pts)
▽	45 cyl. plate	2.2	AD485M-1
◇	55,60,65 cyl. plate	15	AD642M-1

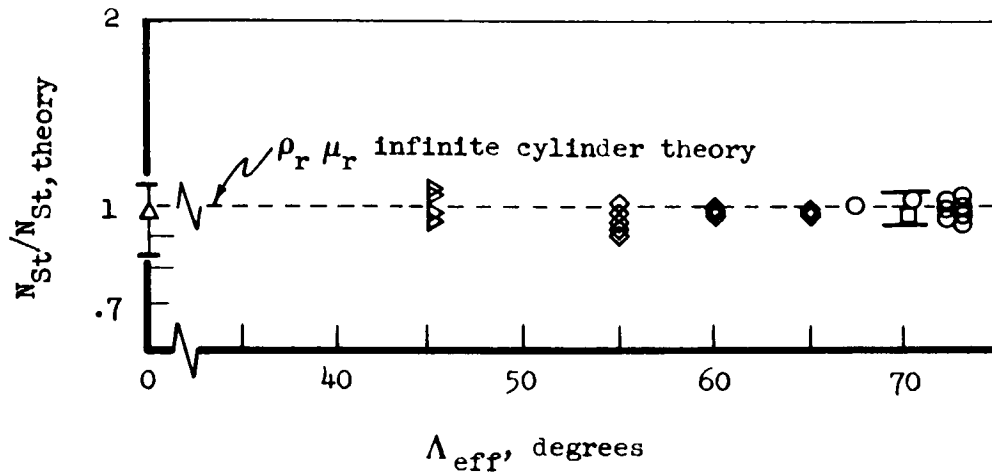


Figure 16.- Laminar stagnation line heat transfer on a cylindrical leading edge.

	α , deg	Prov	$N_{Re,D} \sim 10^4$	Test
○	0	Blunt	8.38, 17.2	AD462M-1
□	5	Blunt	8.38, 17.2	AD462M-1
◇	10	Blunt	8.38, 17.2	AD462M-1
△	10	Sharp	26.6	AD477M-1

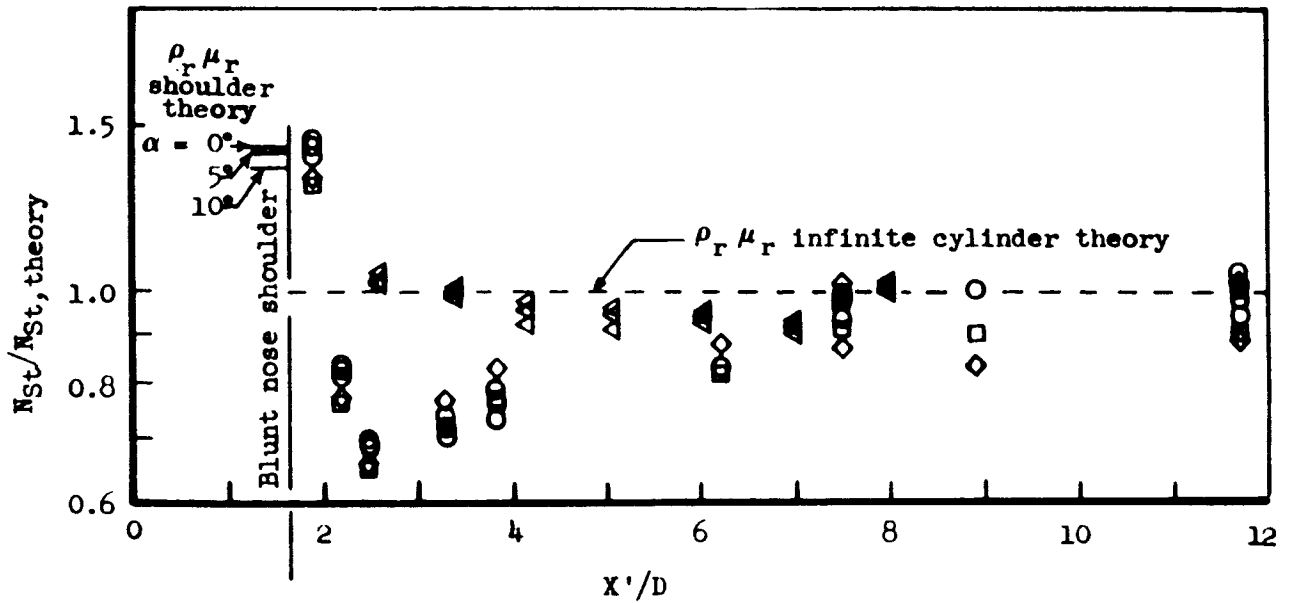


Figure 17.- Extent of blunt prov effect on leading edge heat transfer. Laminar flow; $M_\infty = 8.08$; $\Lambda = 73^\circ$; $\psi = 0^\circ$.

	X/D	Prow	$\bar{N}_{Re,D}$	Test	α , deg
○	12.25	Blunt	8.35×10^4	AD462M-1	-15 to 0
△	12.25	Blunt	17.2×10^4	AD462M-1	0 to 15
□	5.34, 8.35	Sharp	26.6×10^4	AD477M-1	10, 15
▽	6.50	Sharp	4.9×10^4	AD465M-1	0

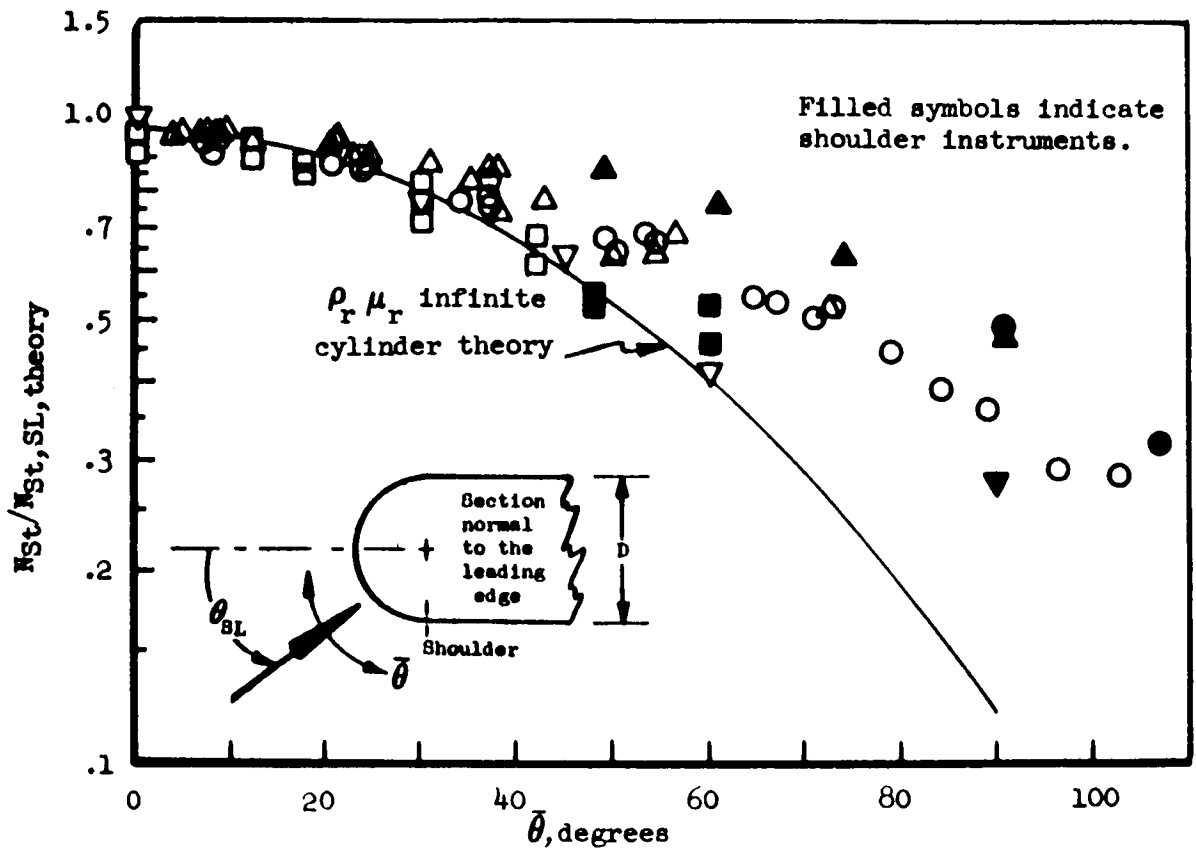


Figure 18.- Laminar heat transfer distribution on a delta wing cylindrical leading edge. $M_\infty = 8$; $\Lambda = 73^\circ$; $\psi = 0^\circ$.

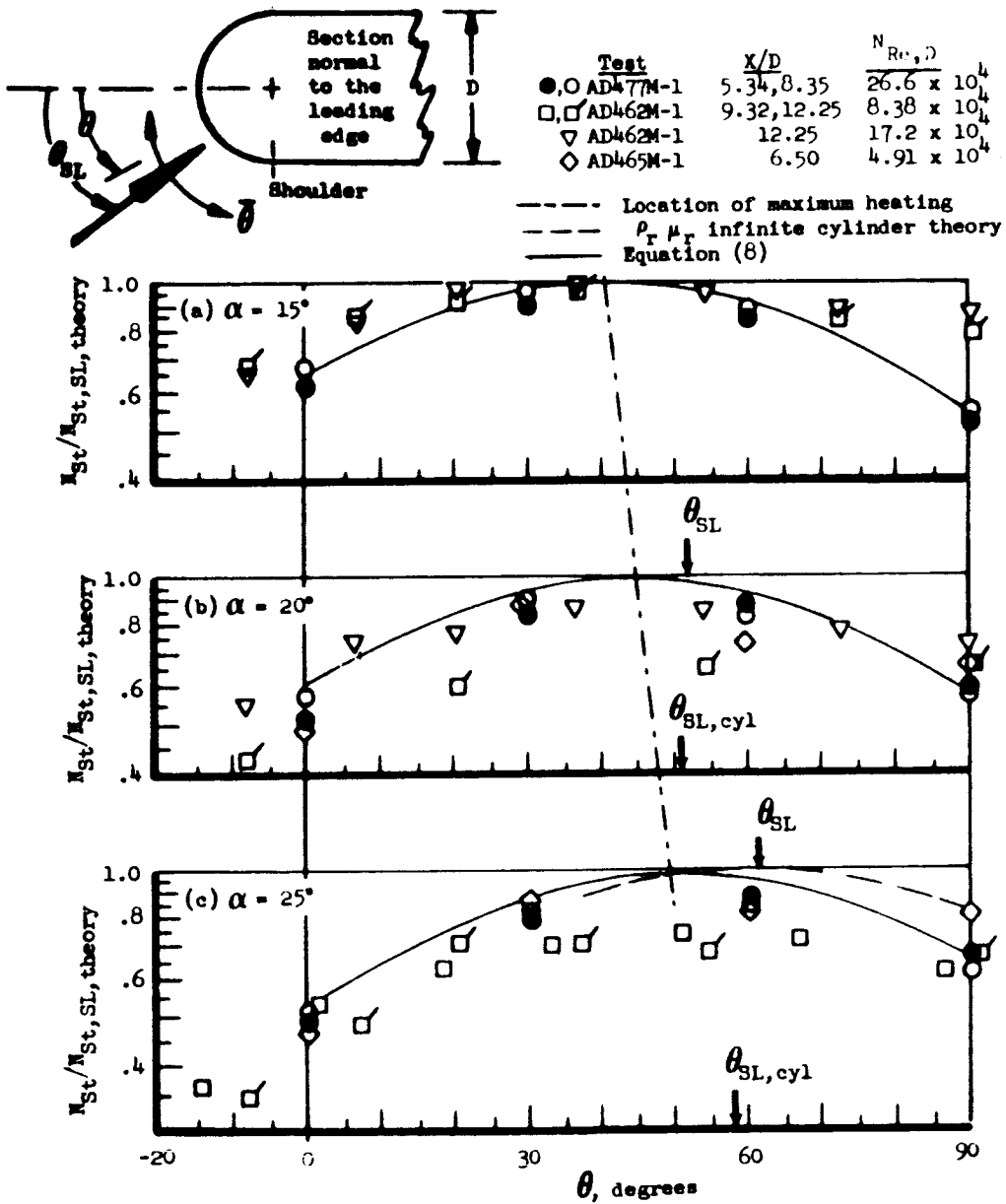


Figure 19.- Laminar heating distributions on delta wing cylindrical leading edges. $M_\infty = 8.08$; $\Lambda = 73^\circ$; $\psi = 0^\circ$.

Test	X/D	Re _D	
● ADA77M-1	5.34, 8.35	26.6 × 10 ⁴	--- Location of maximum heating
□ ADA62M-1	9.32, 12.25	8.38 × 10 ⁴	--- ρ _r μ _r infinite cylinder theory
◇ ADA62M-1	12.25	17.2 × 10 ⁴	— Equation (8)
◇ ADA65M-1	6.50	4.91 × 10 ⁴	

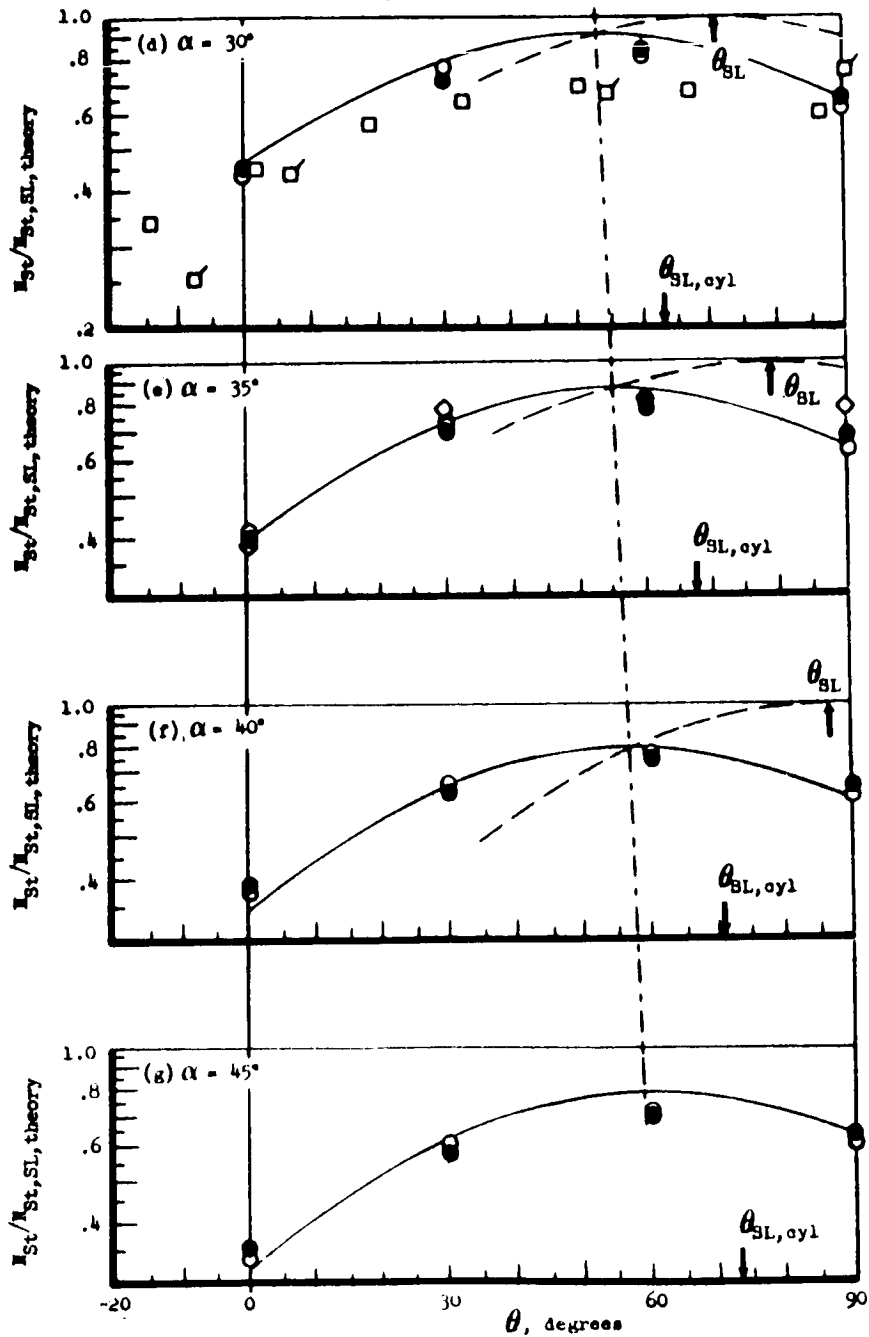


Figure 19.- Concluded.

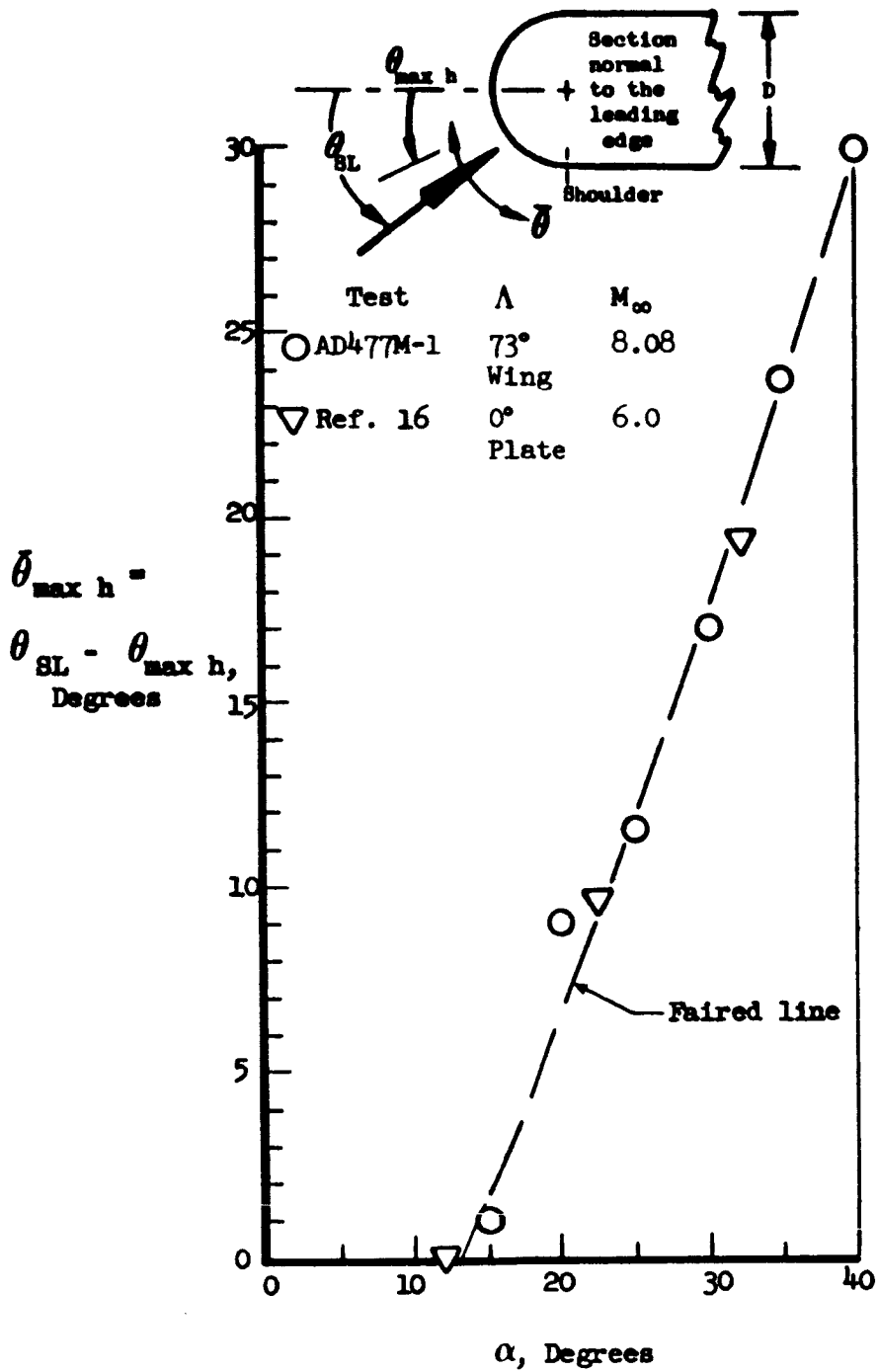


Figure 20.- Location of line of maximum heat transfer on a delta wing leading edge.

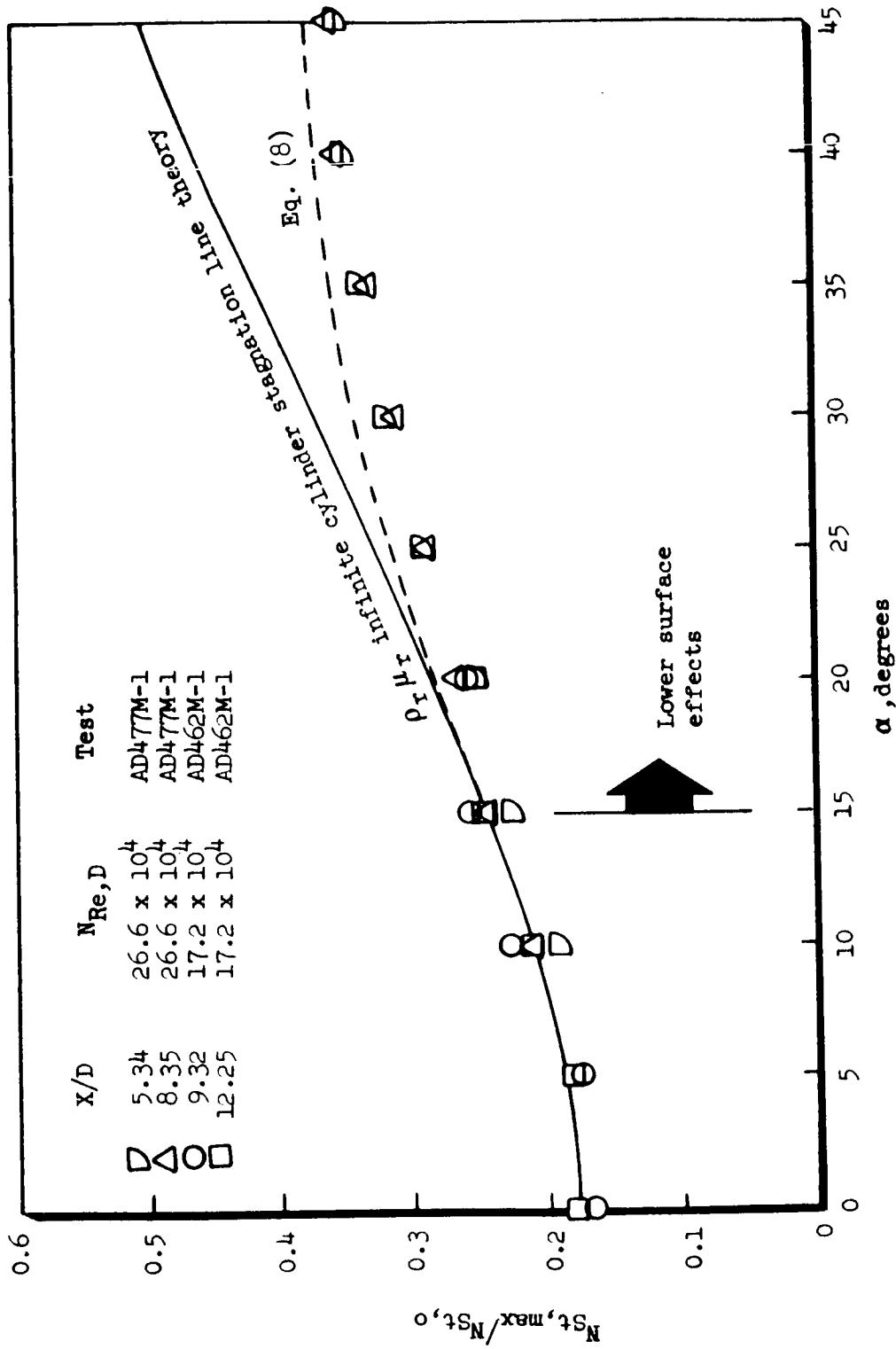


Figure 21.- Maximum laminar heating to a delta wing cylindrical leading edge. $M = 8.08$;
 $\Lambda = 73^\circ$; $\psi = 0^\circ$.

	Λ , deg	M_∞	Test
Present data	○ 73 wing	6.08	AD461M-1
	◻ 73 wing	7.0	AD461M-1
	◁ 78 wing	6.10	AD483M-1
	○ 68 wing	6.10	AD483M-1
	▽ 45 cyl. plate	2.2	AD485M-1
	◇ 55,60,65 cyl. plate	5.6 to 7.9	AD642M-1
Other data	□ 30,60,75 cyl.	6	Unpublished Boeing data

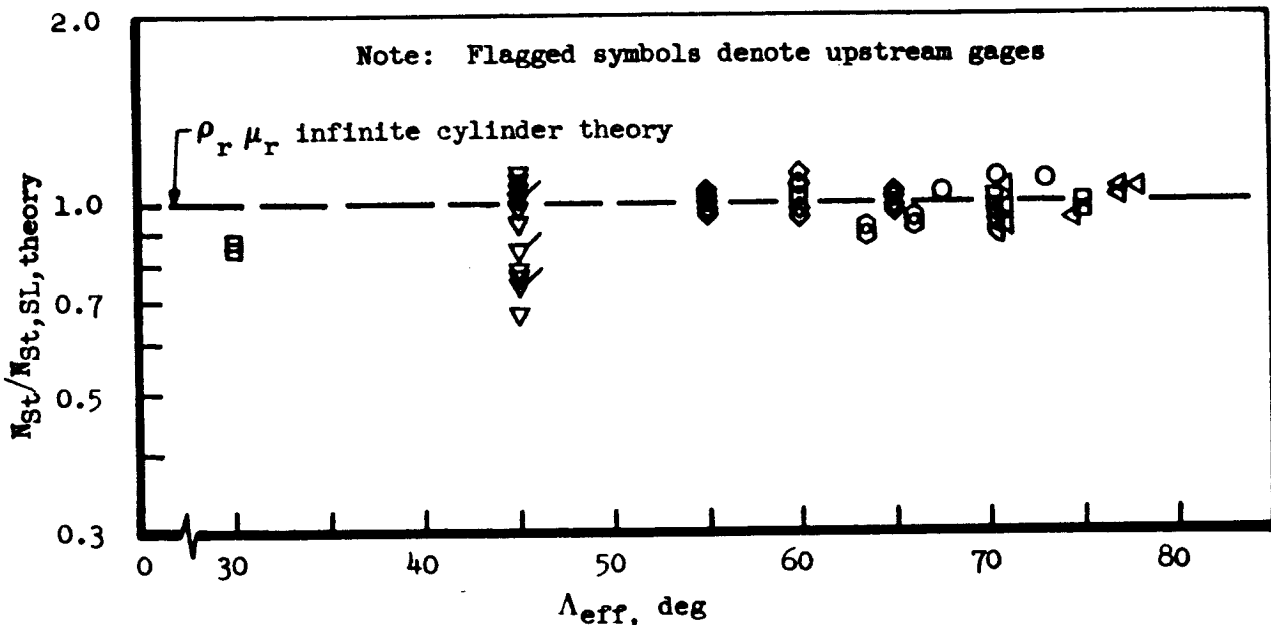


Figure 22.- Turbulent stagnation line heat transfer on a cylindrical leading edge.

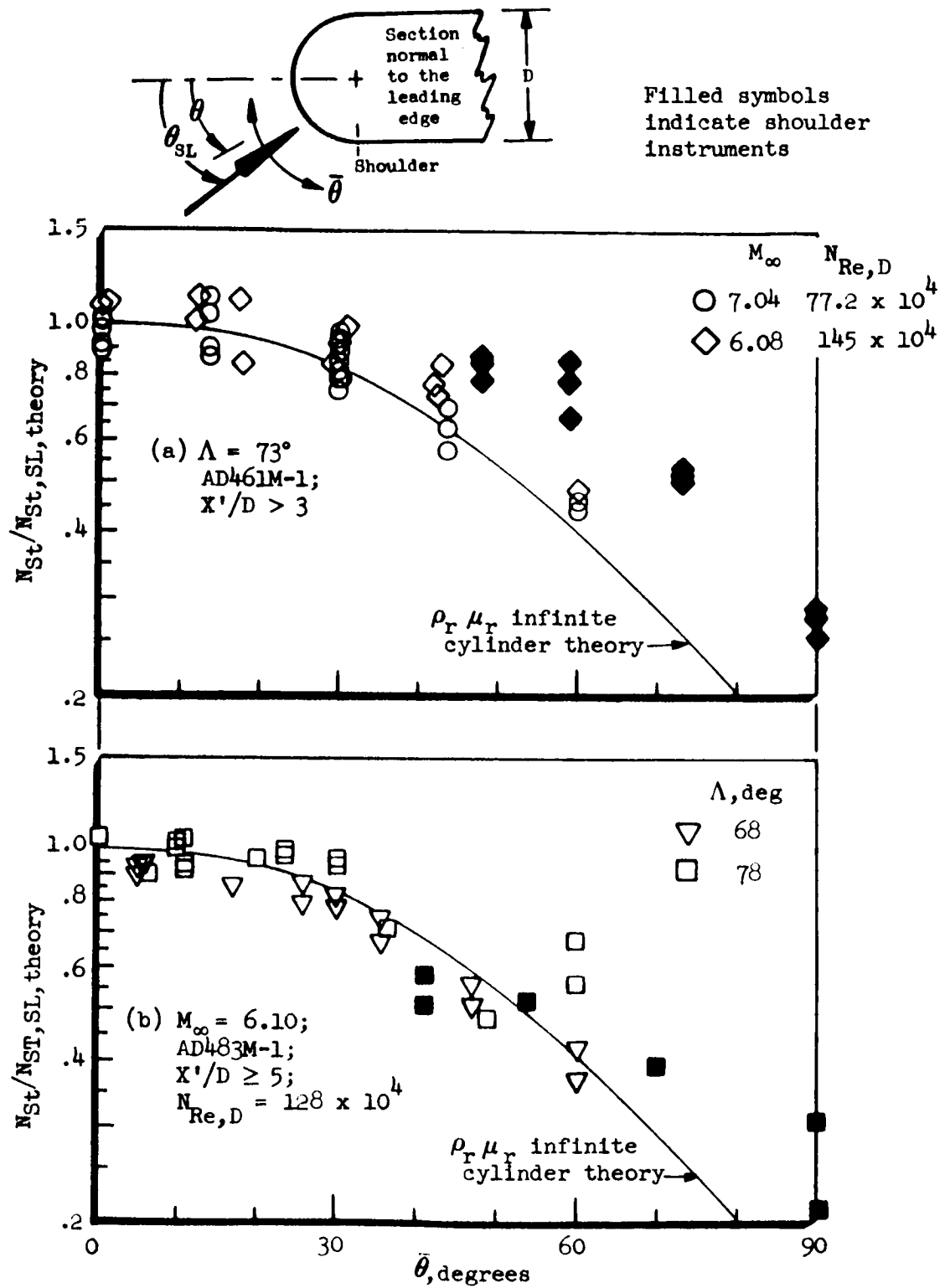


Figure 23.- Turbulent heating distribution on cylindrical leading edges of sharp-prow delta wings.
 $\alpha \leq 15^\circ$; $\psi = 0^\circ$.

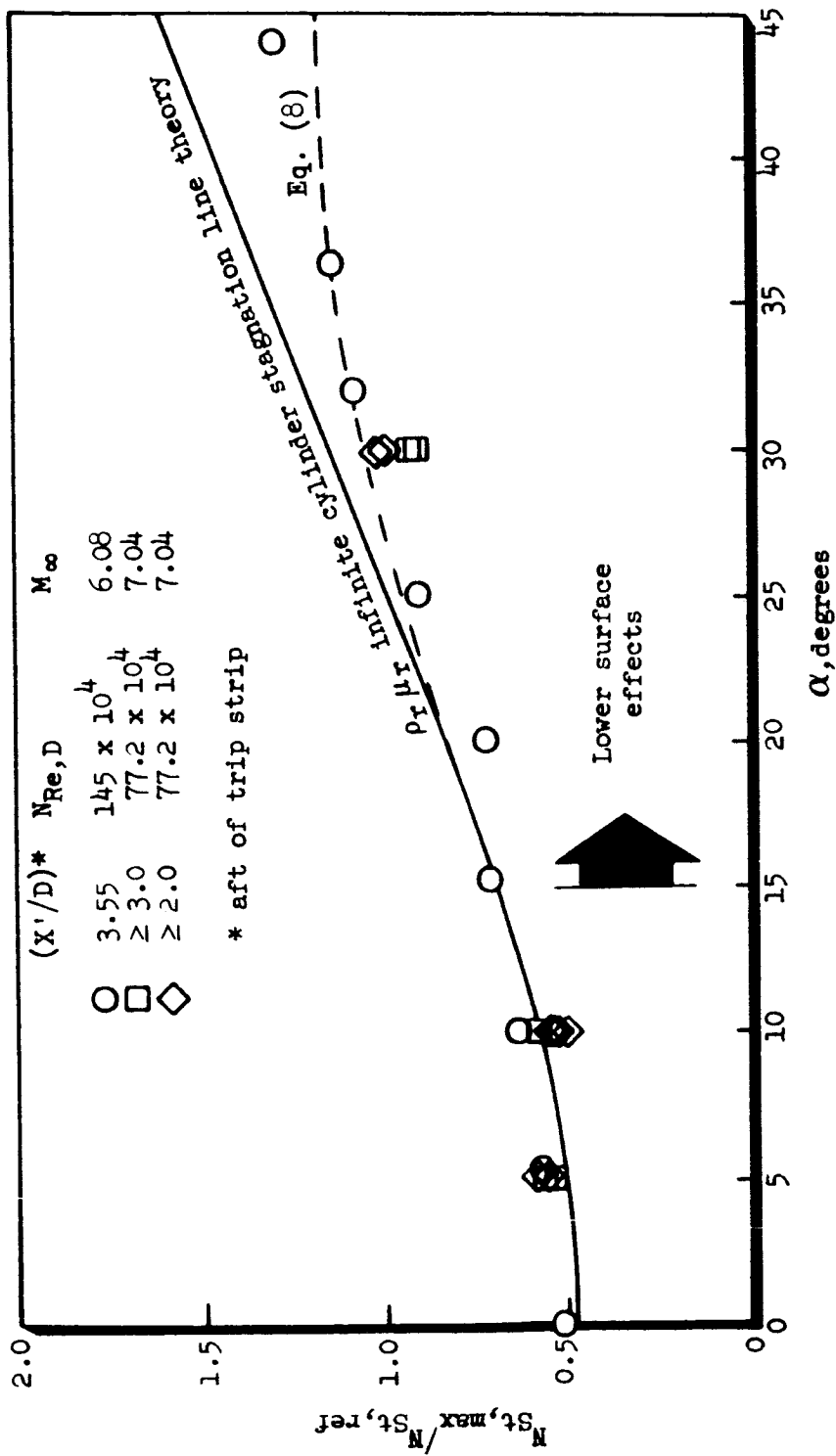


Figure 24.- Maximum turbulent heating observed delta wing cylindrical leading edges. AD46LM-1; $\Lambda = 73^\circ$; $\psi = 0^\circ$.

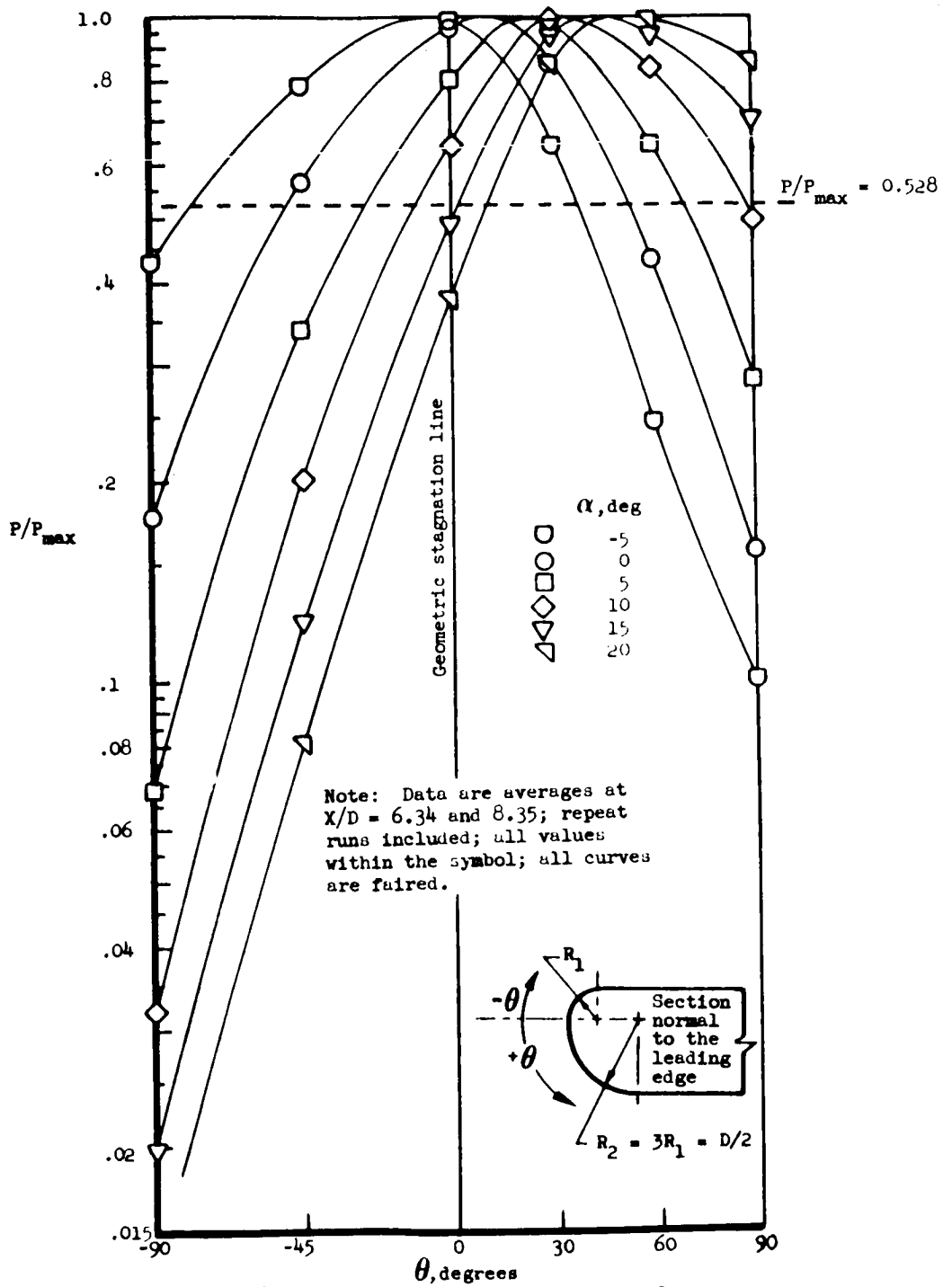
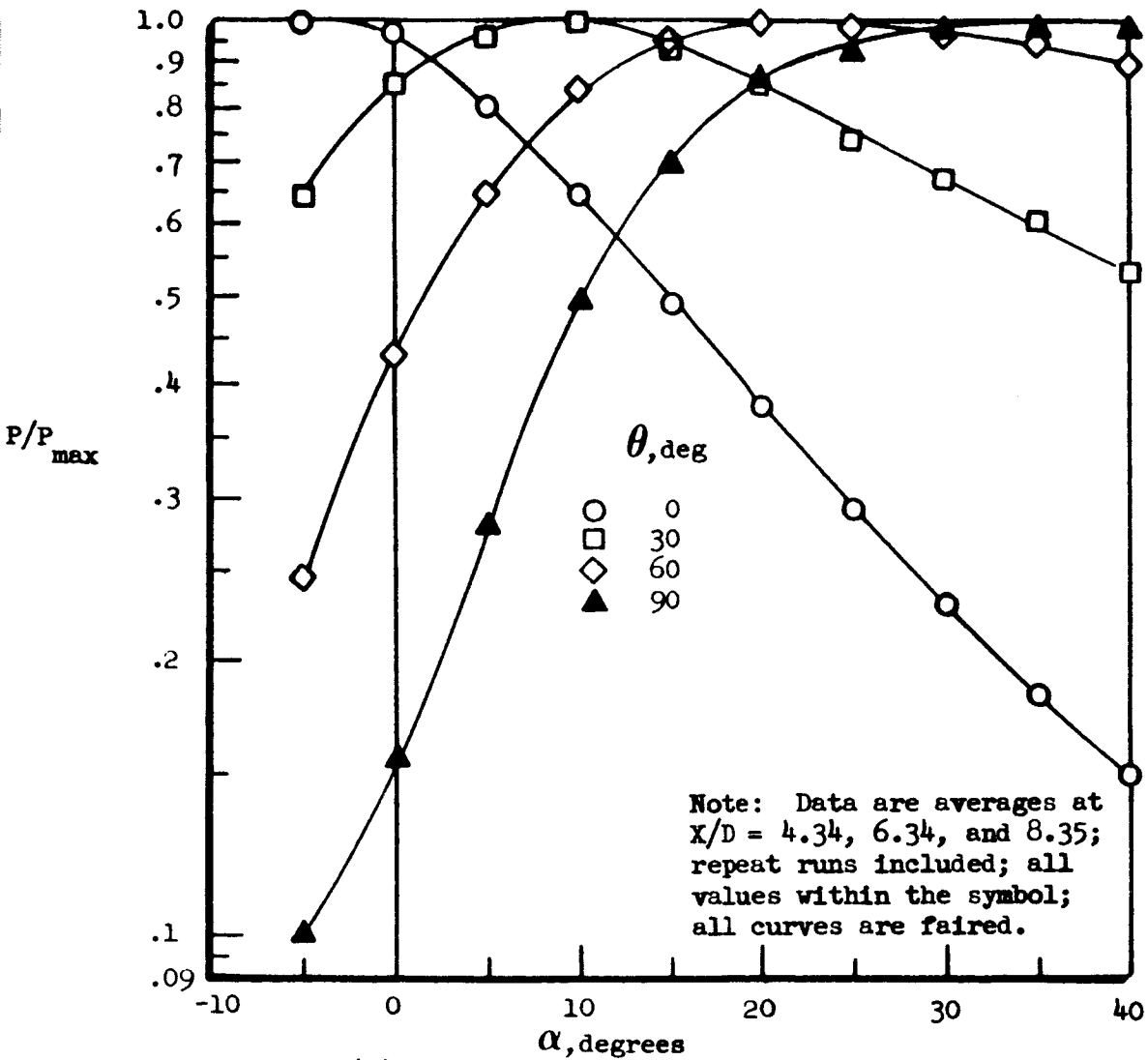
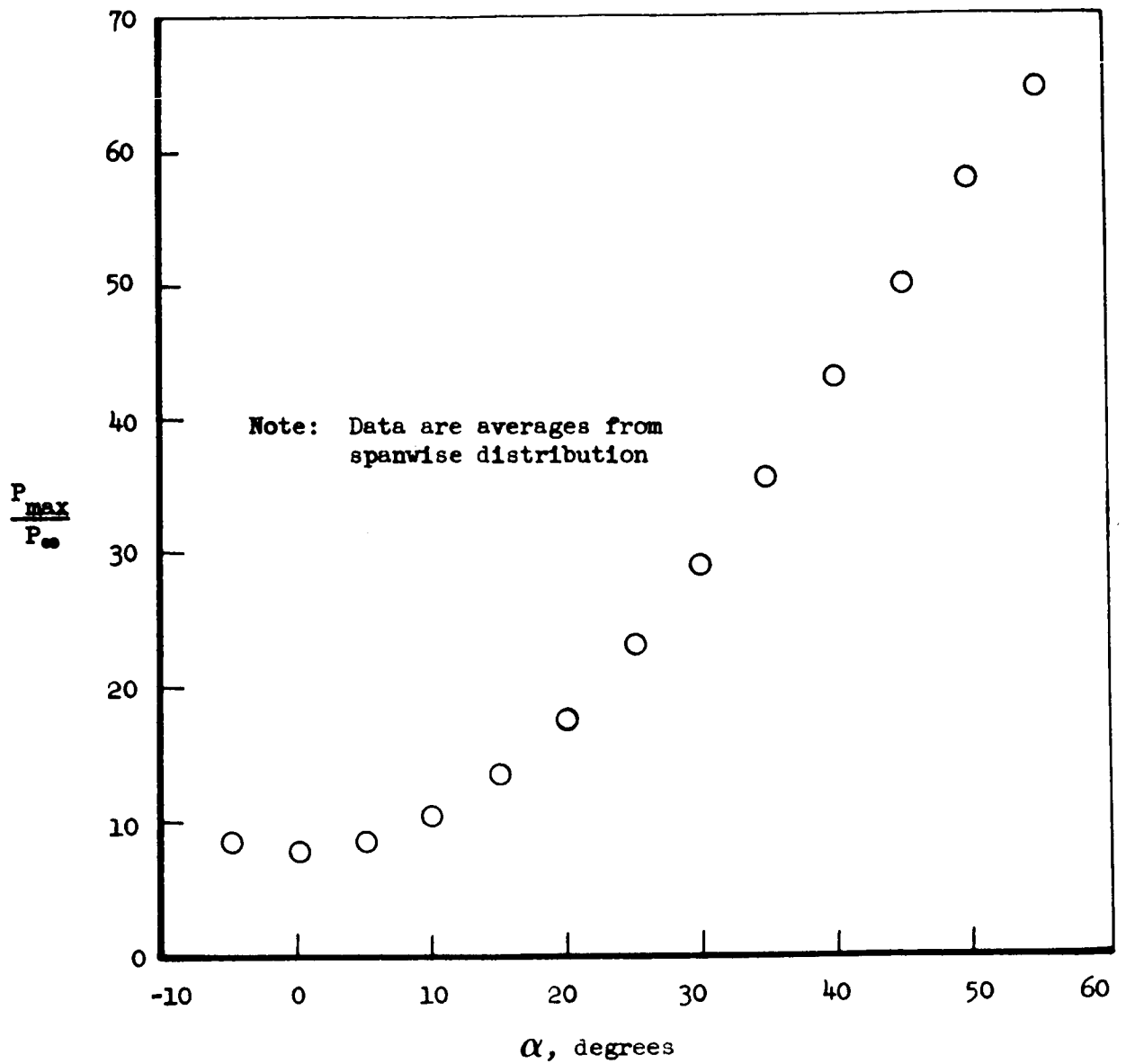


Figure 25.- AD477M-1 Dual-radius leading edge pressures.



(b) Variation with angle of attack.

Figure 25.- Continued.



(c) Maximum pressures. $X/D = 8.35$.

Figure 25.- Concluded.

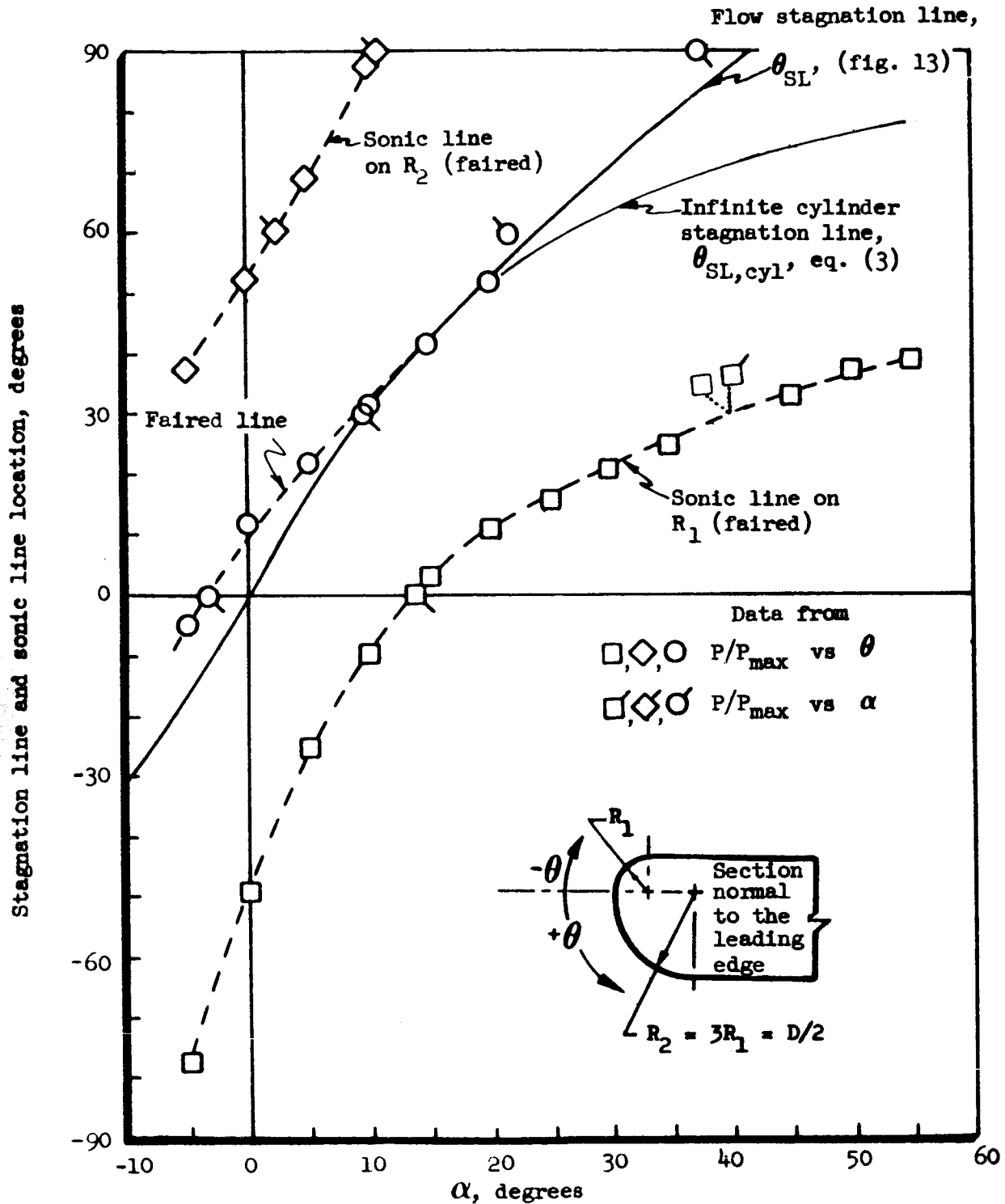


Figure 26.- Dual radius leading edge stagnation line and sonic line location. AD477M-1; $M_\infty = 8.08$; $\Lambda = 73^\circ$; $\psi = 0^\circ$.

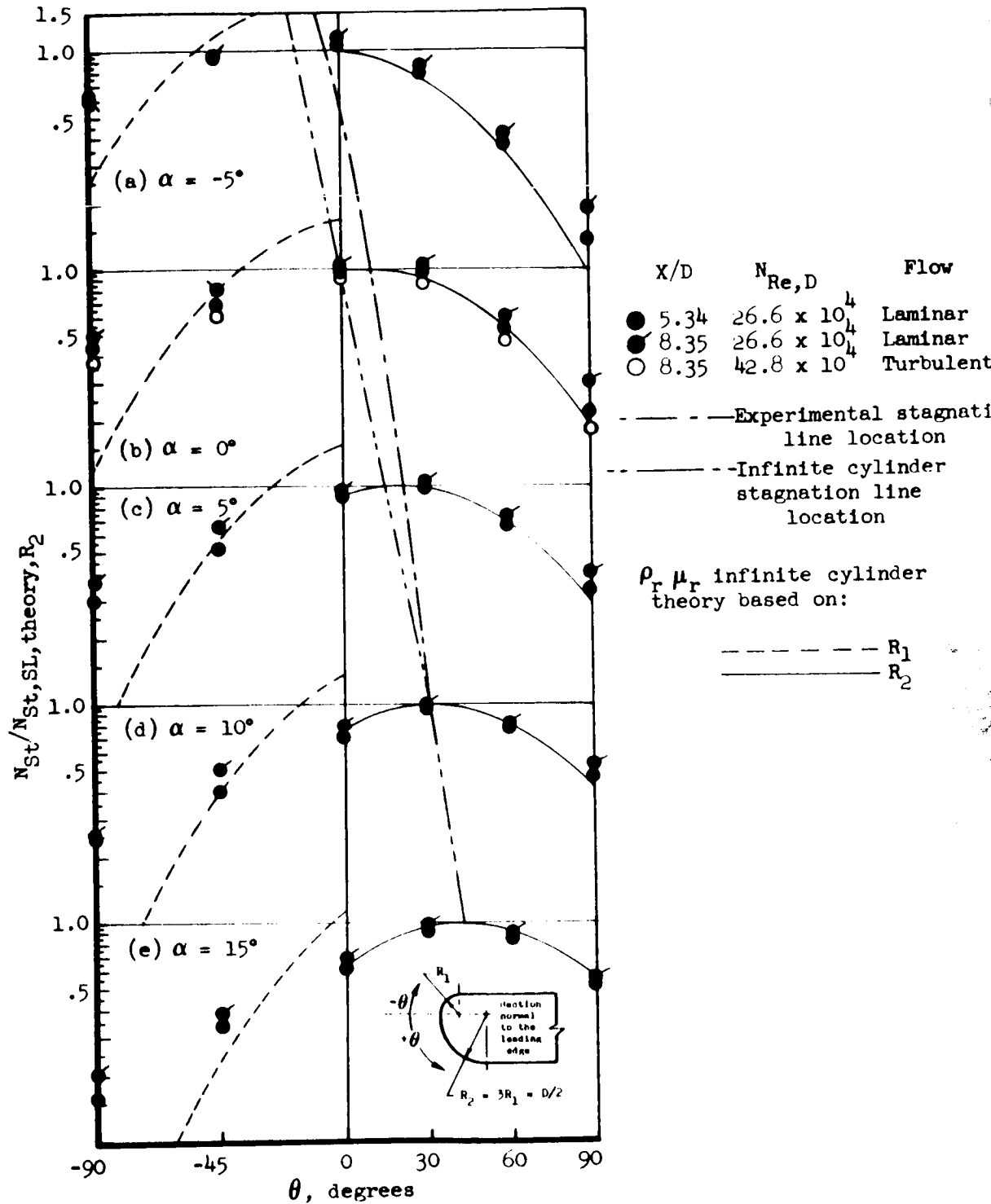


Figure 27.- Heat transfer distributions on a dual-radius leading edge.
 AD477M-1; $M_\infty = 3.08$; $\Lambda = 73^\circ$; $\psi = 0^\circ$.

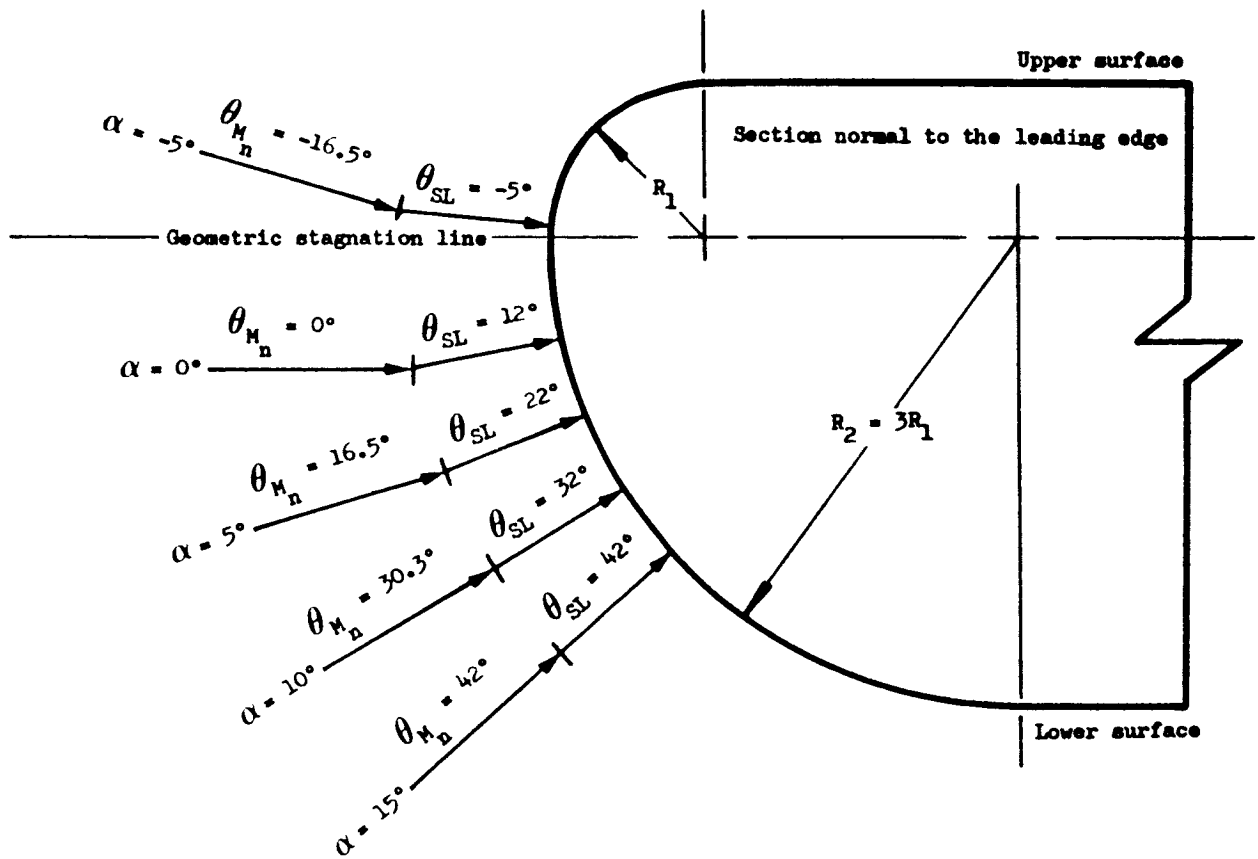
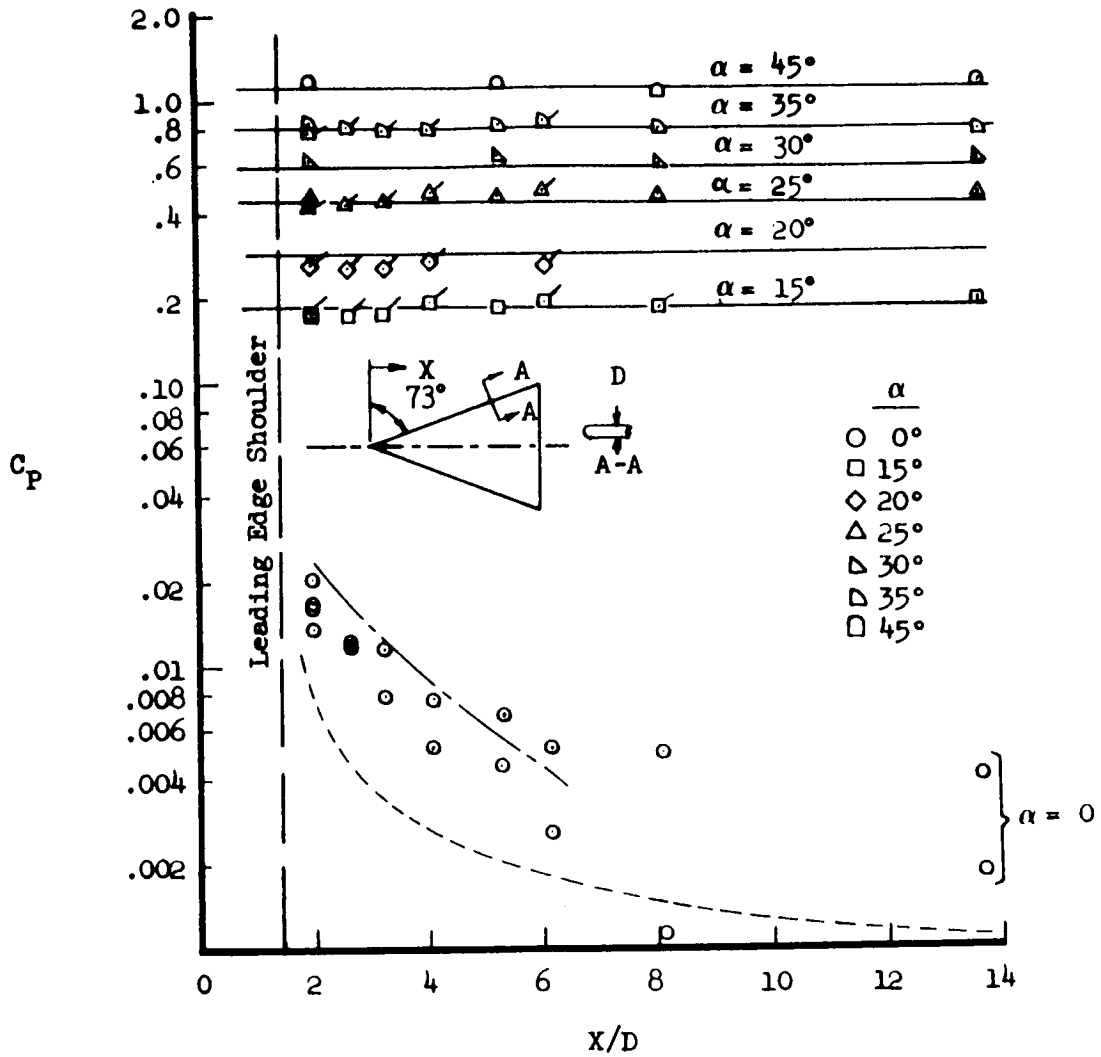


Figure 28.- Dual-radius leading edge stagnation streamlines. AD477M-1; $M_\infty = 8.08$; $\Lambda = 73^\circ$; $\psi = 0^\circ$.

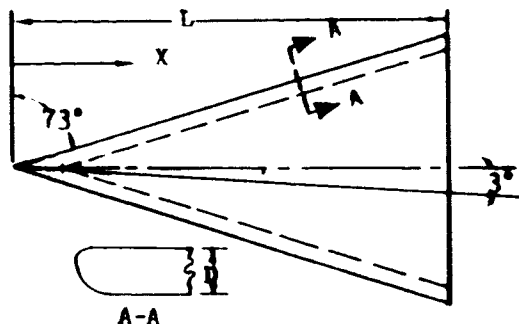
$\diamond \triangle \square \circ$ $M_\infty = 7.0; N_{Re, D} = 94.5 \times 10^4$
 $\triangle \square \circ$ $M_\infty = 6.08; N_{Re, D} = 43.1 \times 10^4$

————— Eq. (9)
 - - - - - Ref. 19, $M_\infty = 6$
 - · - · - Eq. (11) + Ref. 19

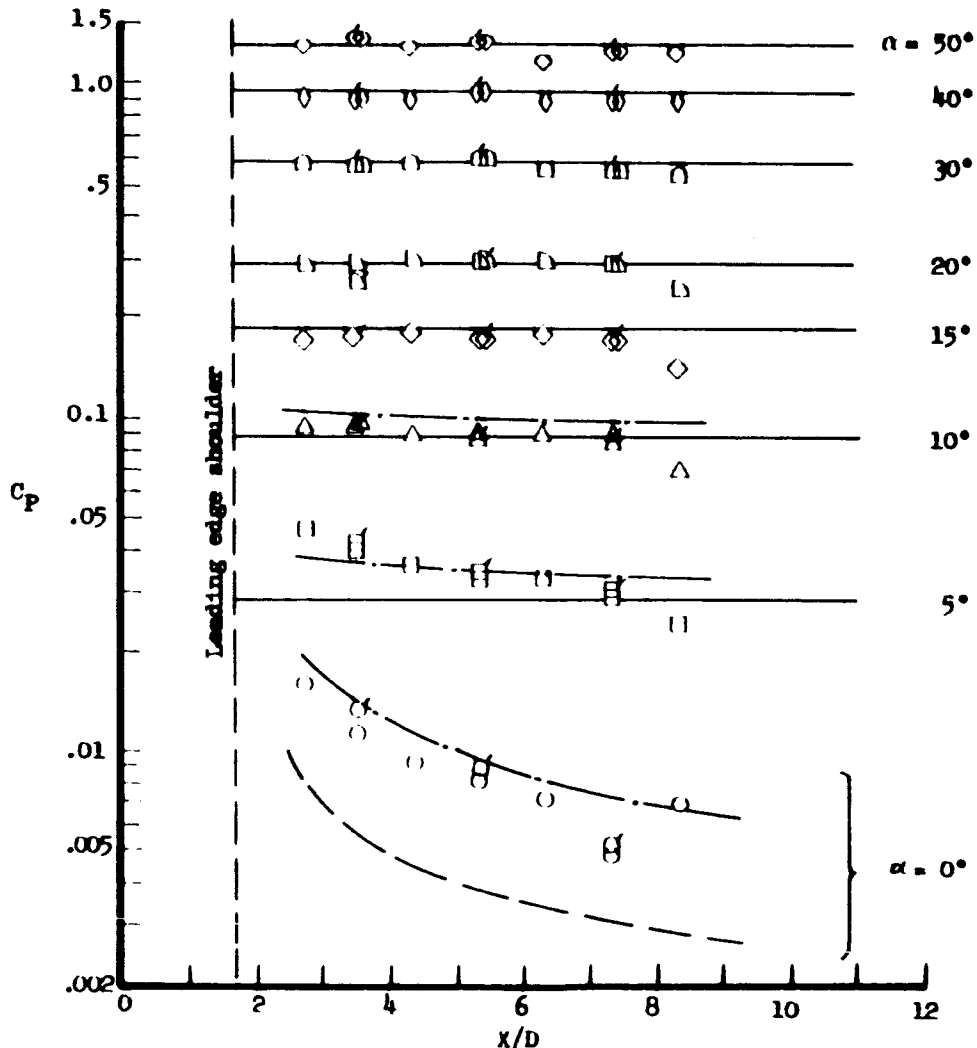


(a) Centerline pressures at Mach 6 and 7

Figure 29.- Sharp-prow delta wing pressure measurements. AD461M-1



Flagged symbols-centerline data
 Unflagged symbols-3° ray line data
 ——— Eq. (9)
 - - - Ref. 19
 - · - · Eq. (11) + Ref. 19



(b) Lower surface pressures. AD47/M-1; $M_\infty = 8.08$; $N_{Re,D} = 26.2 \times 10^4$

Figure 29.- Concluded.

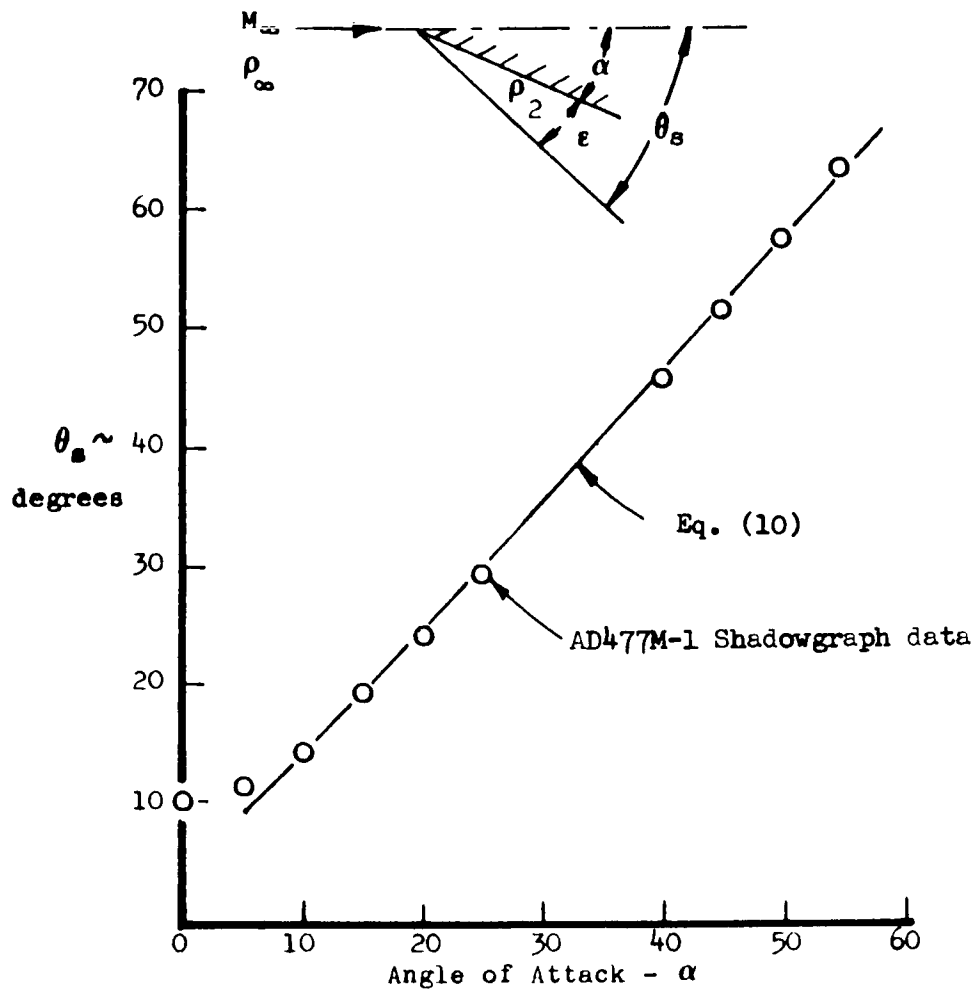


Figure 30.- Comparison of measured and predicted delta wing shock wave angles. $M_\infty = 8.08$, $\Lambda = 73^\circ$.

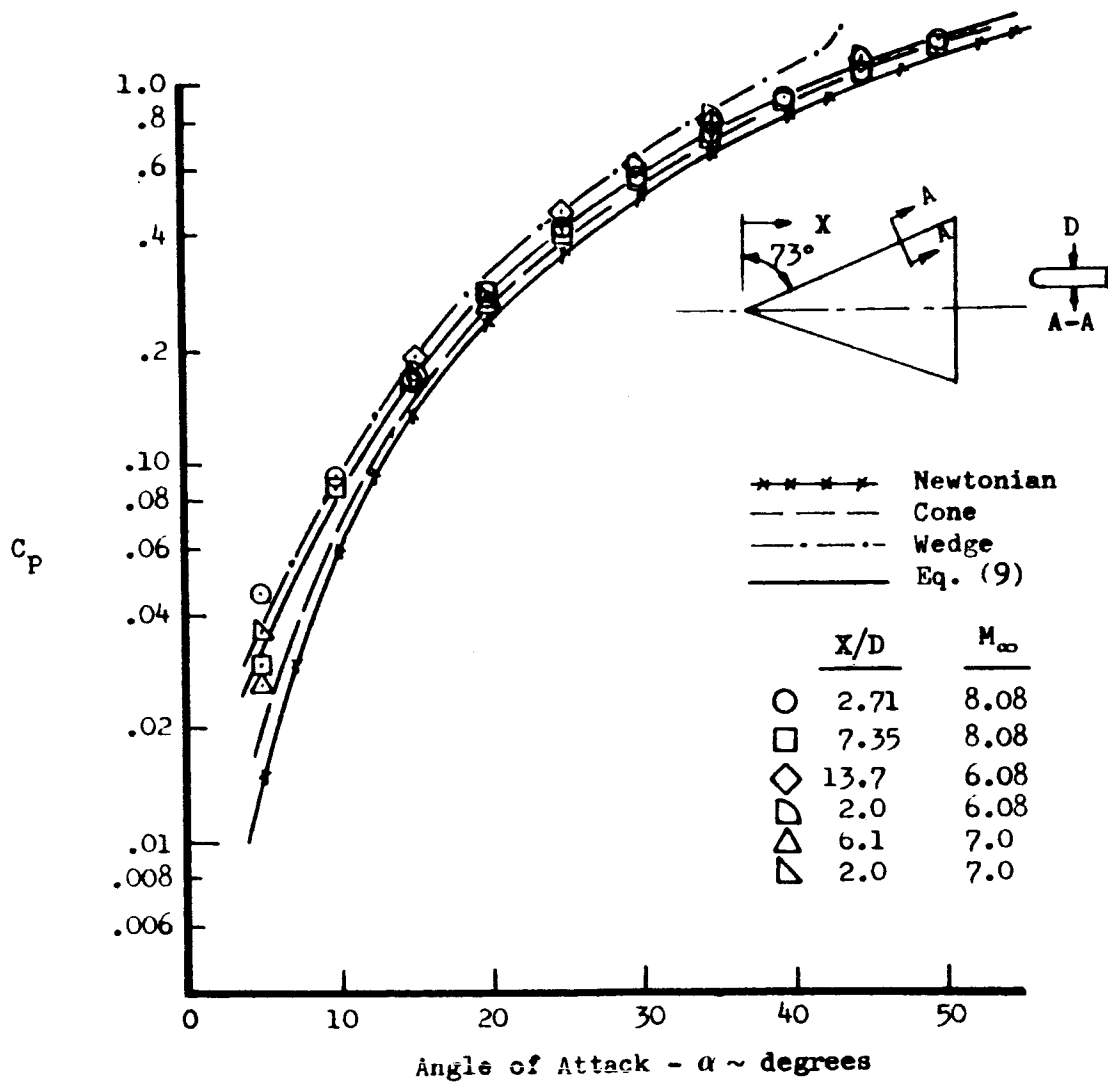
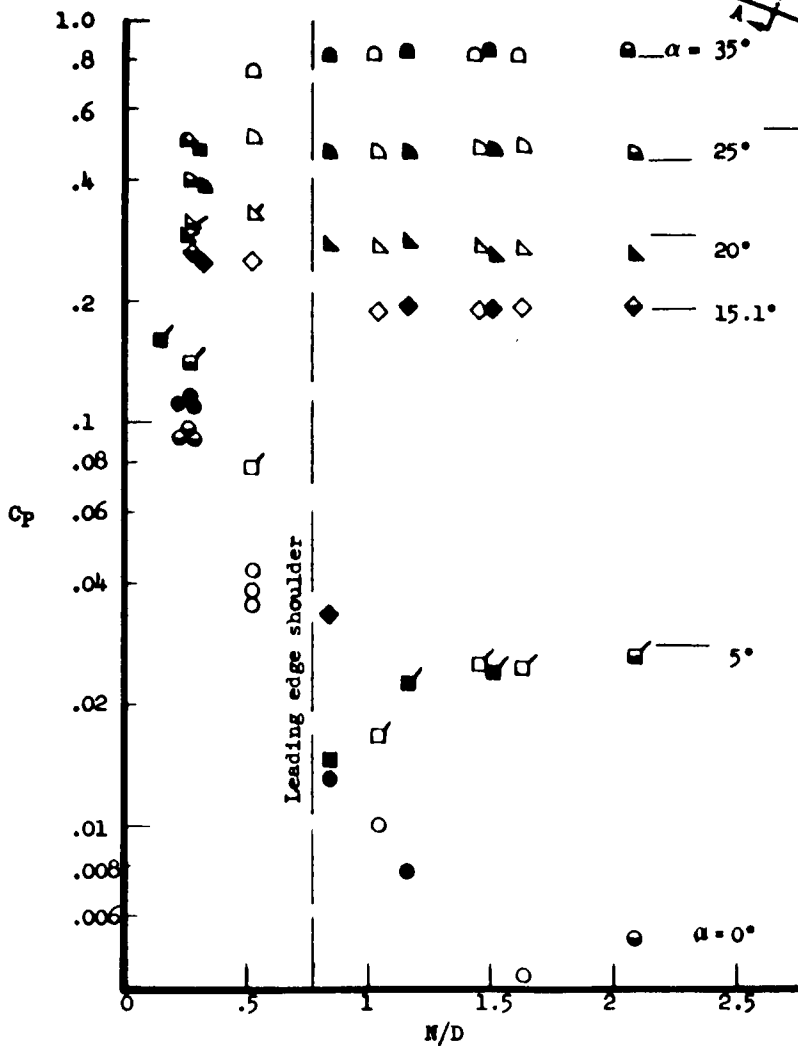
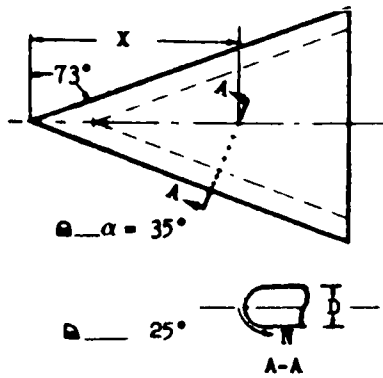


Figure 31.- Comparison of theories with sharp prow delta wing pressures at Mach 6, 7, and 8.

	M_∞	$Re_{D,D}$
Flagged symbols	6.08	117×10^4
Unflagged symbols	7.00	94.5×10^4

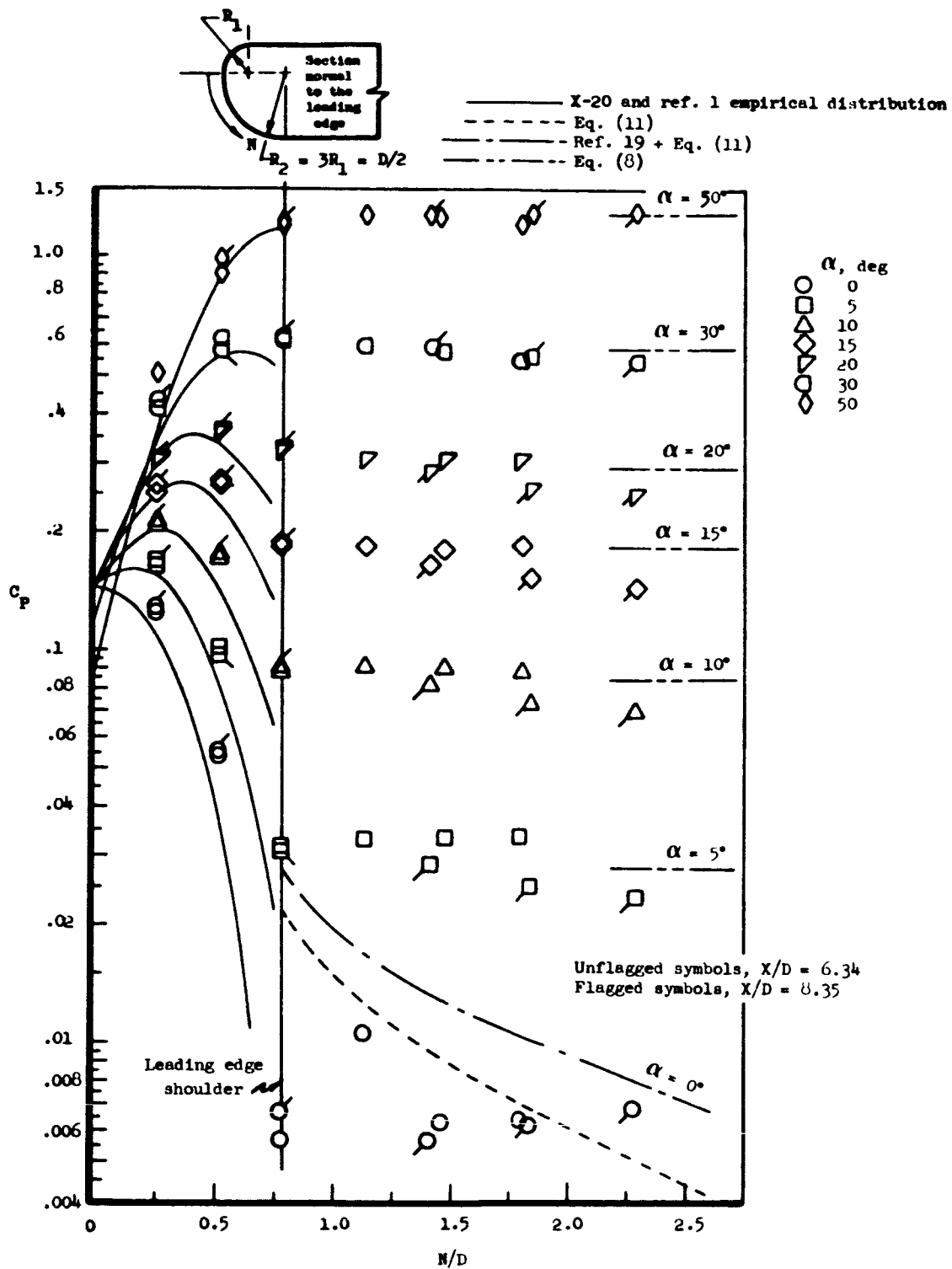
	X/D	(N/D) to f
○	5.65	1.94
●	6.18	2.09
●	6.56	2.20

— Eq. (9)



(a) Cylindrical leading edge

Figure 32.- Spanwise pressure distributions on sharp-prow delta wings. AD461M-1 models.



(b) Sharp-prow with dual-radius leading edge. AD477M-1; $M_\infty = 8.08$;
 $\Lambda = 73^\circ$; $\psi = 0^\circ$; $Re_D = 26.6 \times 10^4$

Figure 32.- Concluded.

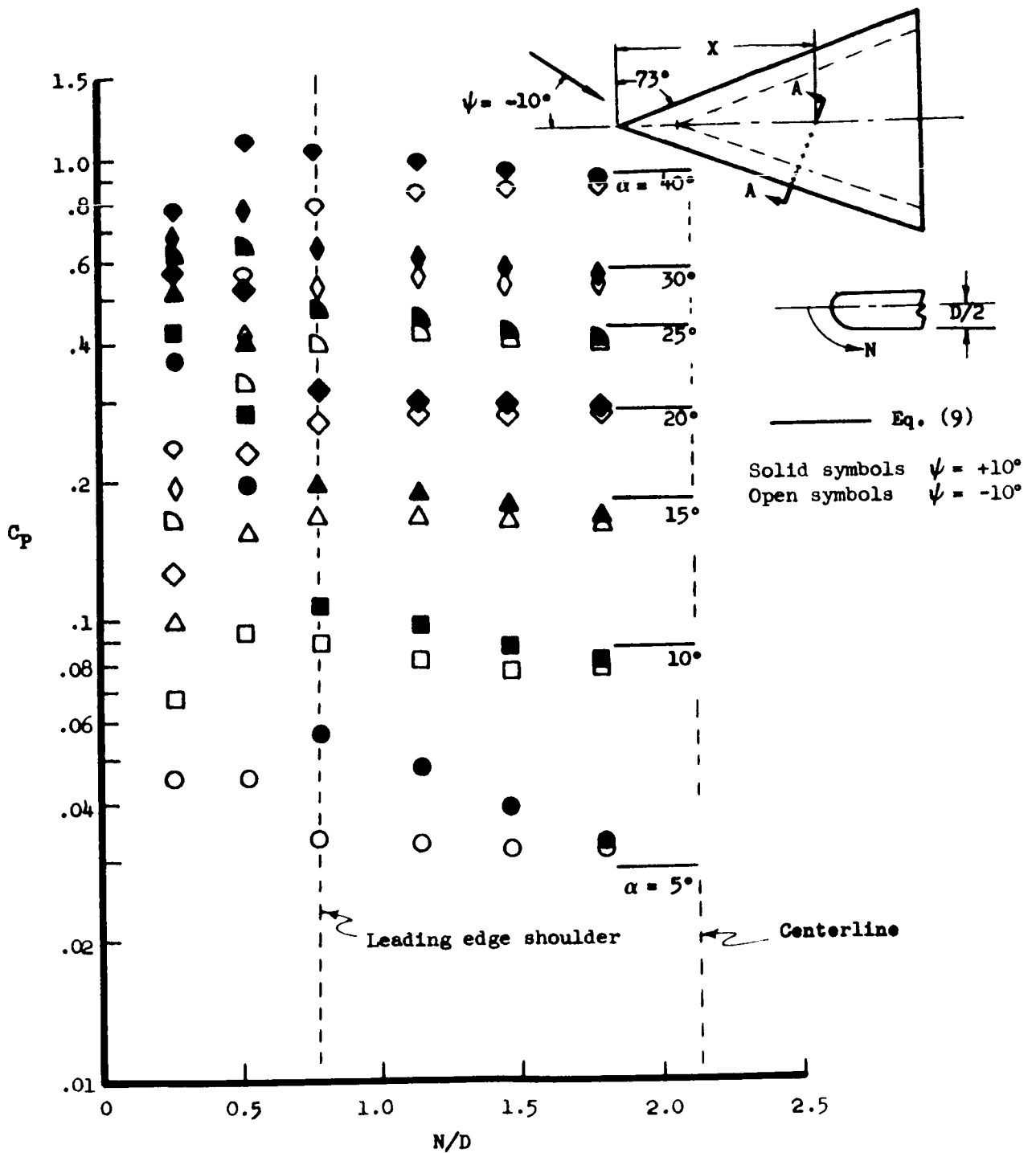
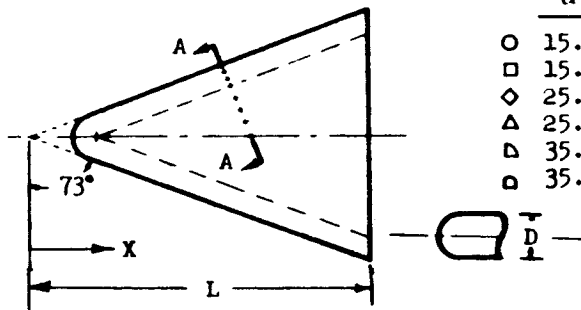


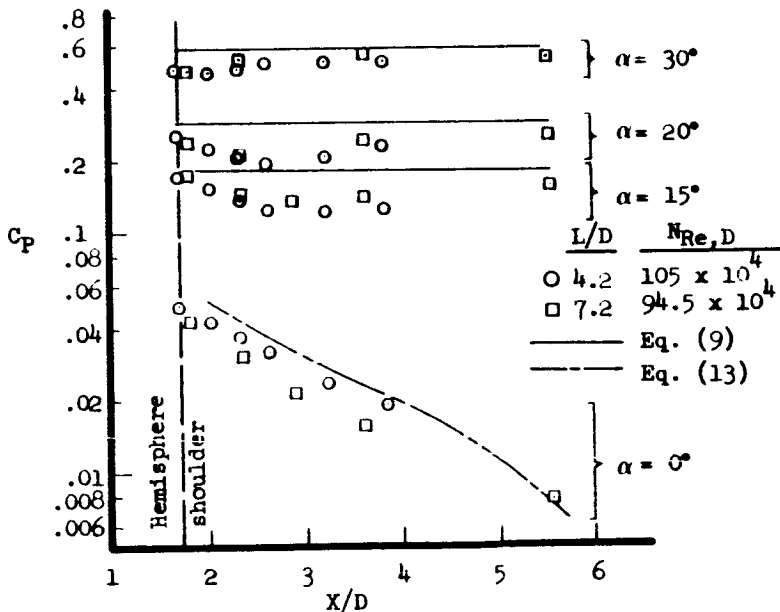
Figure 33.- Yaw effect on lower surface pressures on a sharp-prow delta wing. AD 477M-1; $M_\infty = 8.08$; $N_{Re,D} = 26.6 \times 10^4$; $X/D = 6.34$



	α	L/D	$N_{Re,D}$
○	15.7	4.2	130×10^4
□	15.3	7.2	117×10^4
◇	25.5	4.2	130×10^4
△	25.7	7.2	117×10^4
▽	35.6	4.2	130×10^4
◻	35.3	7.2	117×10^4



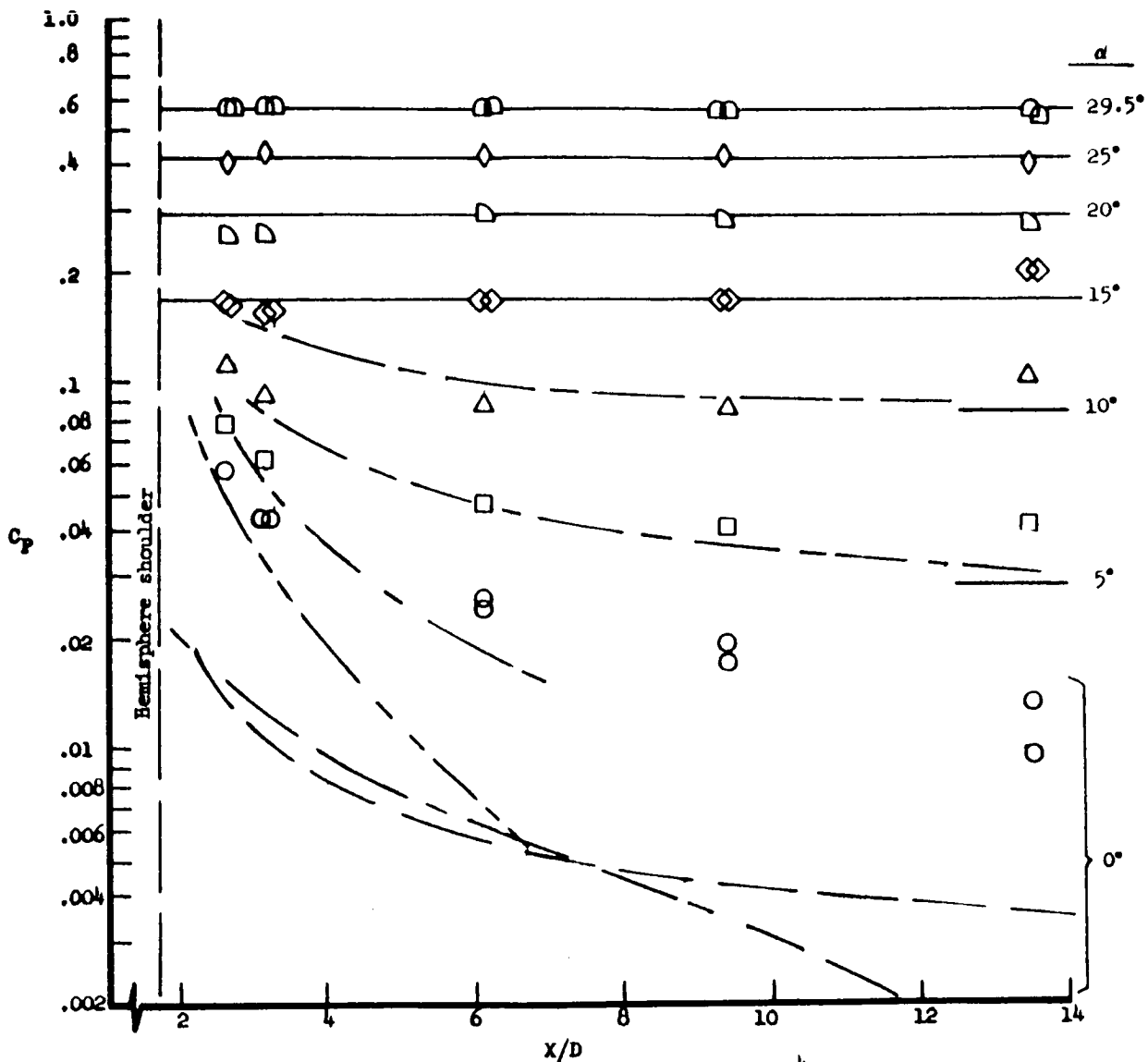
(a) AD461M-1; $M_\infty = 6.08$



(b) AD461M-1; $M_\infty = 7.0$

Figure 34.- Lower surface pressures on the centerline of blunt-prow delta wings.

- Eq. (9) Wedge
- - - - - Ref. 19 Viscous interaction
- Eq. (12) Nose bluntness
- - - - - Eq. (11) Leading edge bluntness
- Eq. (13) Overall effect



(c) AD462M-1; $M_\infty = 8.08$, $N_{Re,D} = 8.34 \times 10^4$

Figure 34.- Concluded.

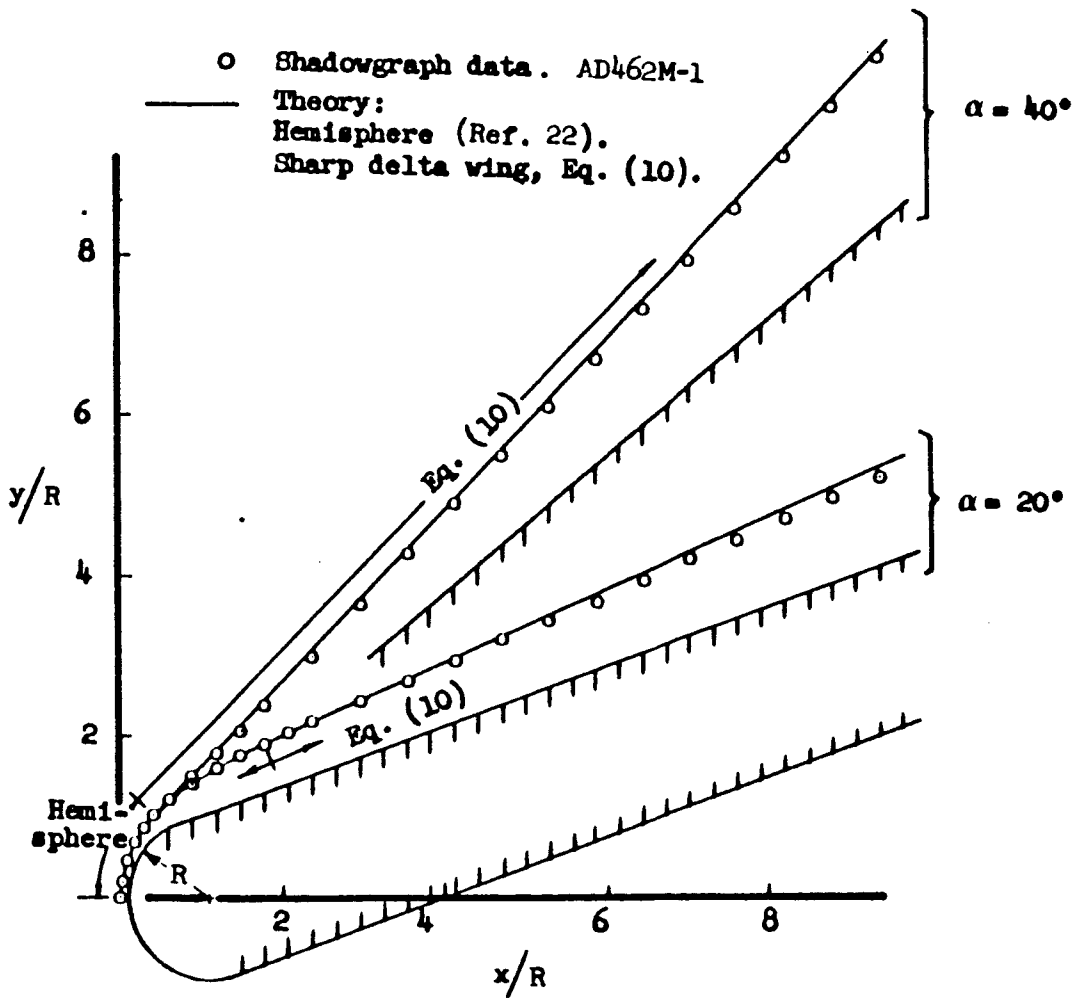
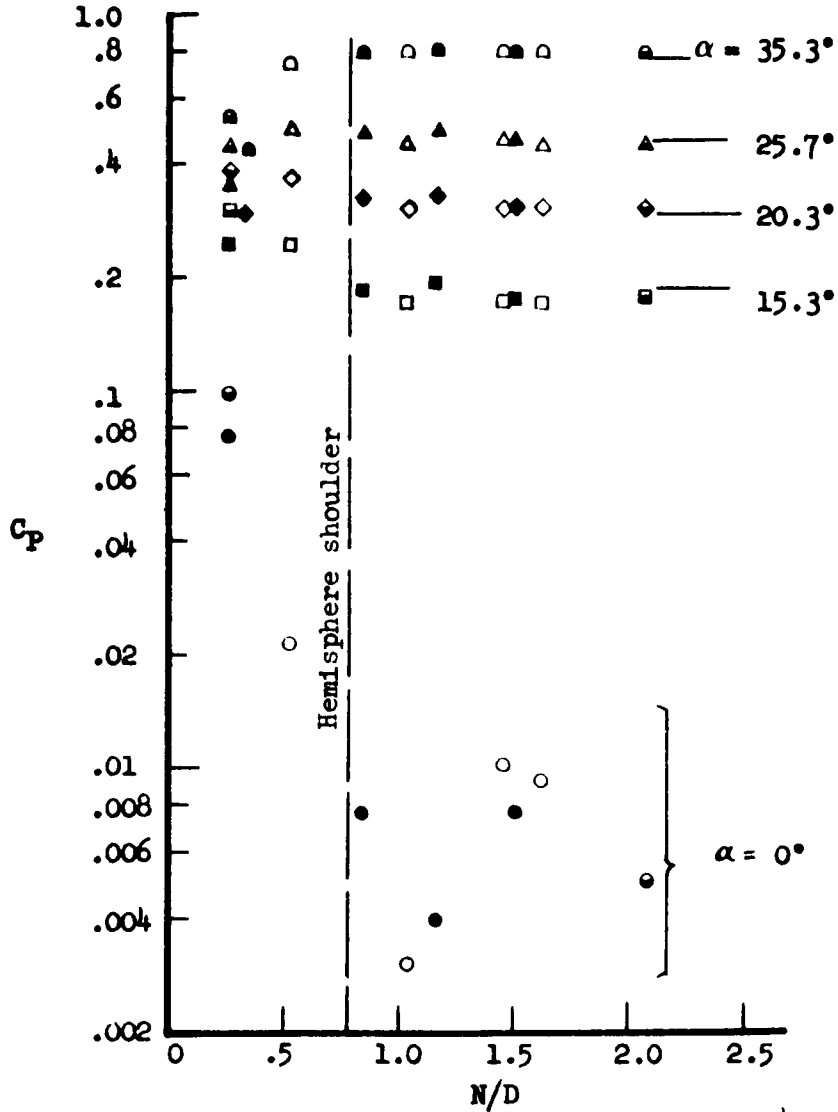
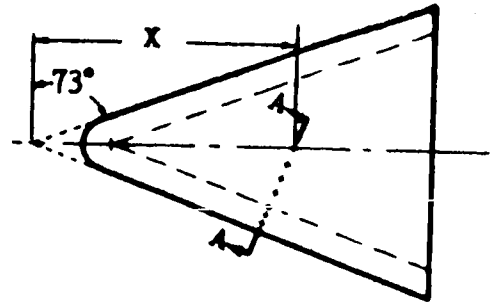


Figure 35.- Blunt prow delta wing shock shape prediction.
 $M_\infty = 8.08$.

	X/D	N/D to ζ
○	5.65	1.94
●	6.18	2.09
●	6.56	2.20

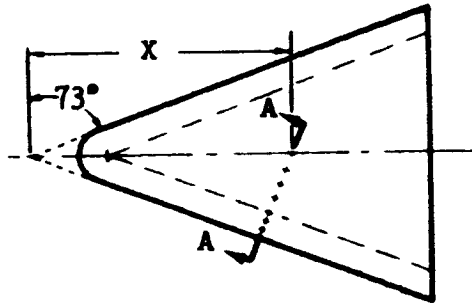
Eq. (9)



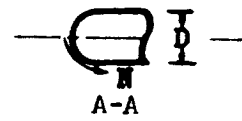
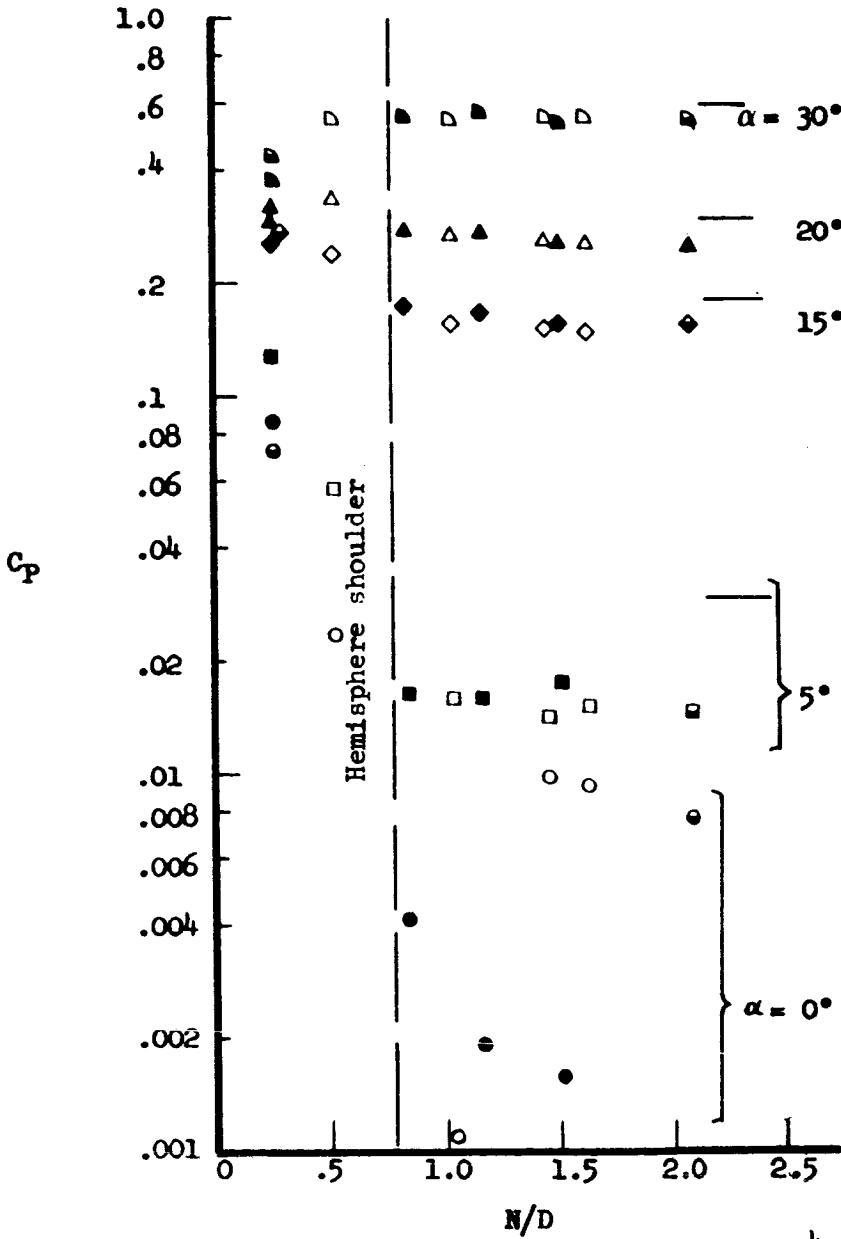
(a) AD461M-1; $M_\infty = 6.08$; $N_{Re,D} = 117 \times 10^4$

Figure 36.- Lower surface pressures on a blunt-prow delta wing.

X/D	N/D to ζ
○ 5.65	1.94
● 6.18	2.09
● 6.56	2.20

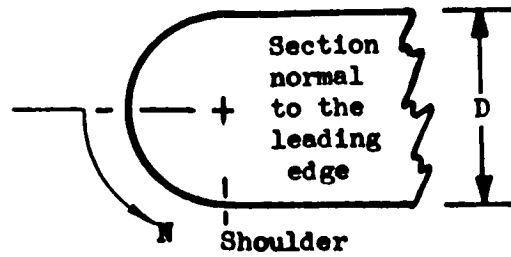


Eq. (9)

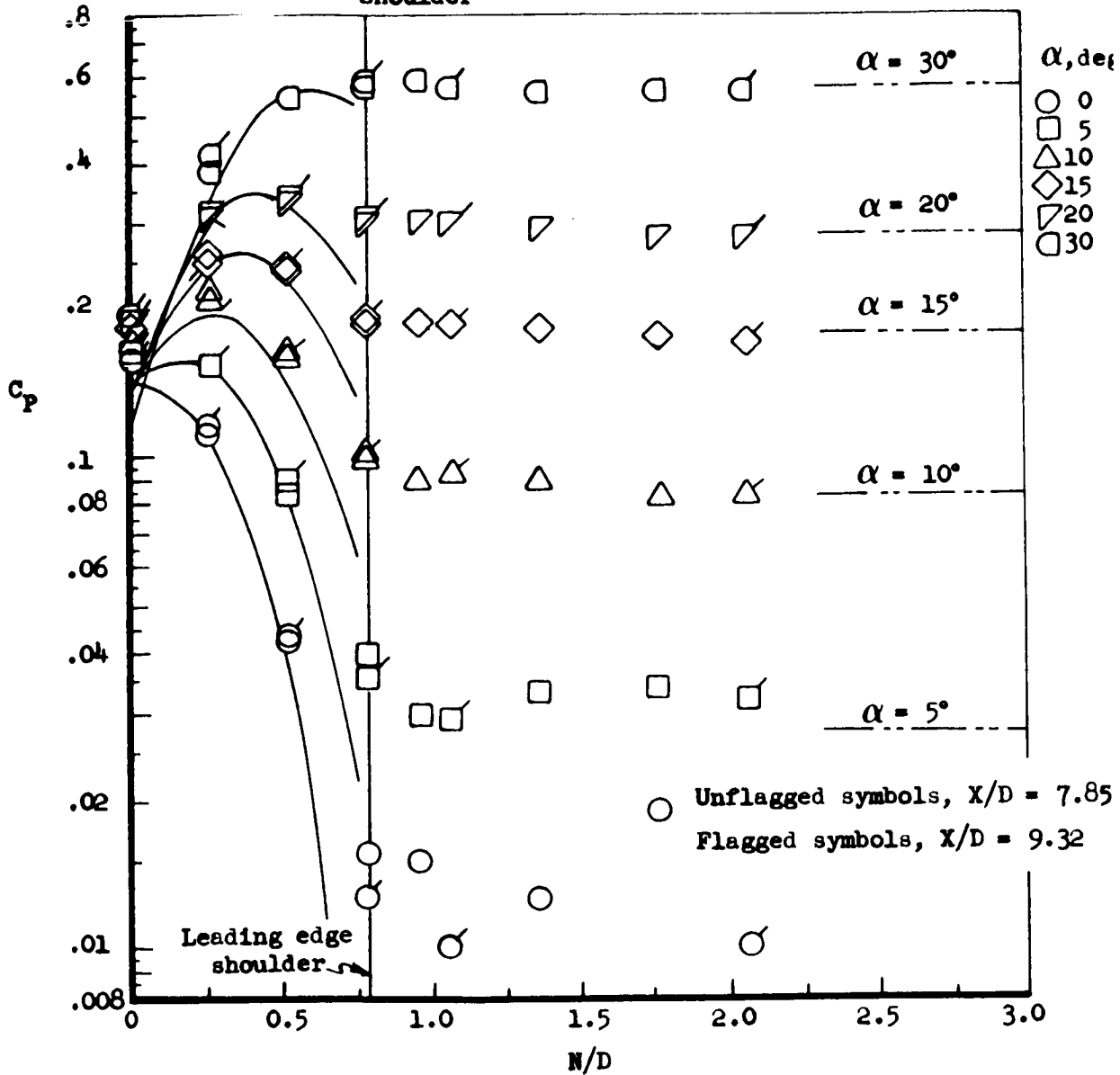


(b) AD461M-1; $M_\infty = 7$; $N_{Re,D} = 94.5 \times 10^4$

Figure 36.- Continued.



— X-20 and ref. 1 empirical distribution
 - - - Ref. 19 + eq. (11)



(c) Blunt prow with cylindrical leading edge.
 AD462M-1; $M_\infty = 8.08$; $N_{Re,D} = 8.34 \times 10^4$.

Figure 36.- Concluded.

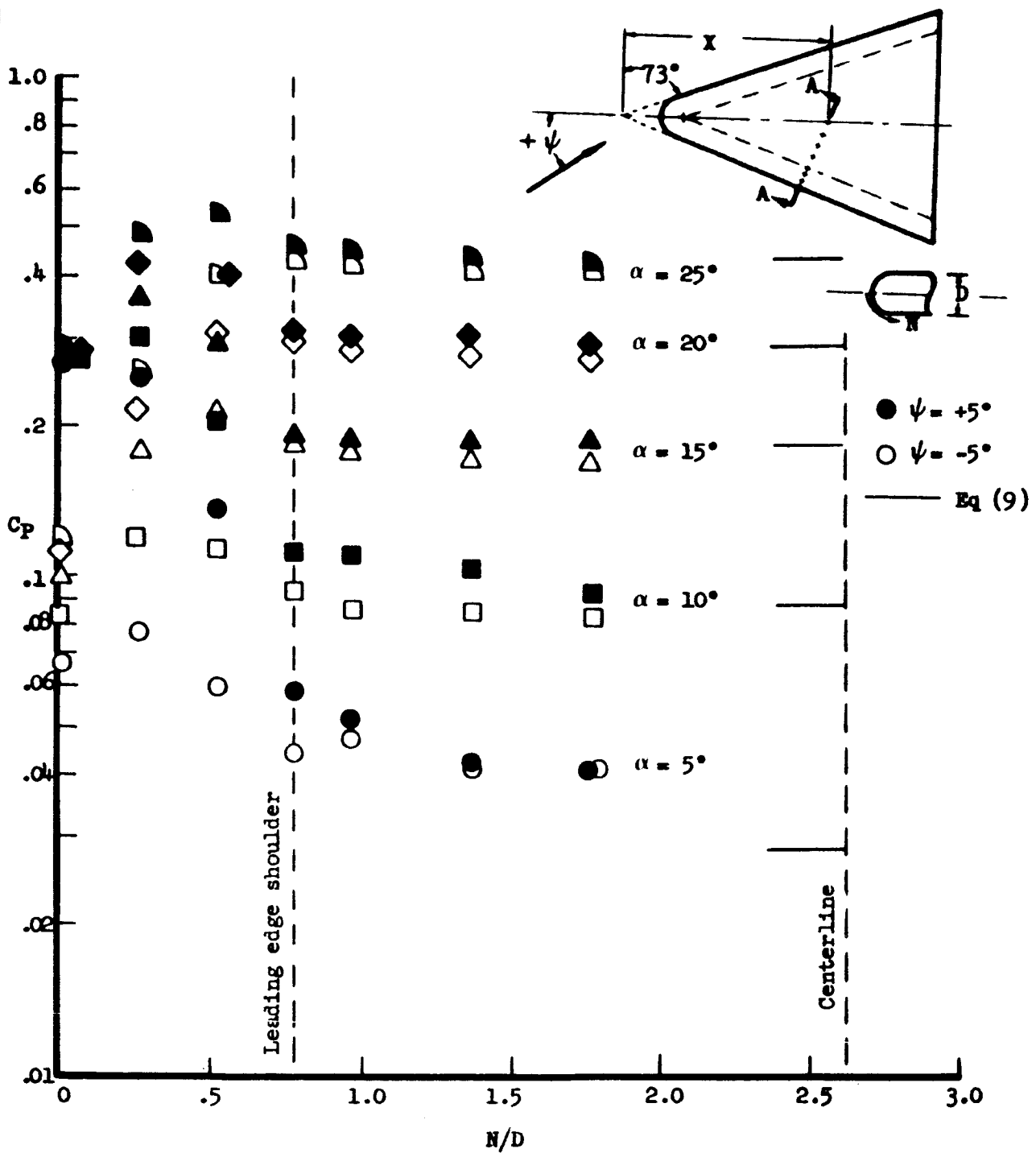


Figure 37.- Lower surface pressures on a blunt-prow delta wing for 5° of yaw.
 AD462M-1; $M_\infty = 8.08$; $N_{Re,D} = 8.34 \times 10^4$; $X/D = 6.34$

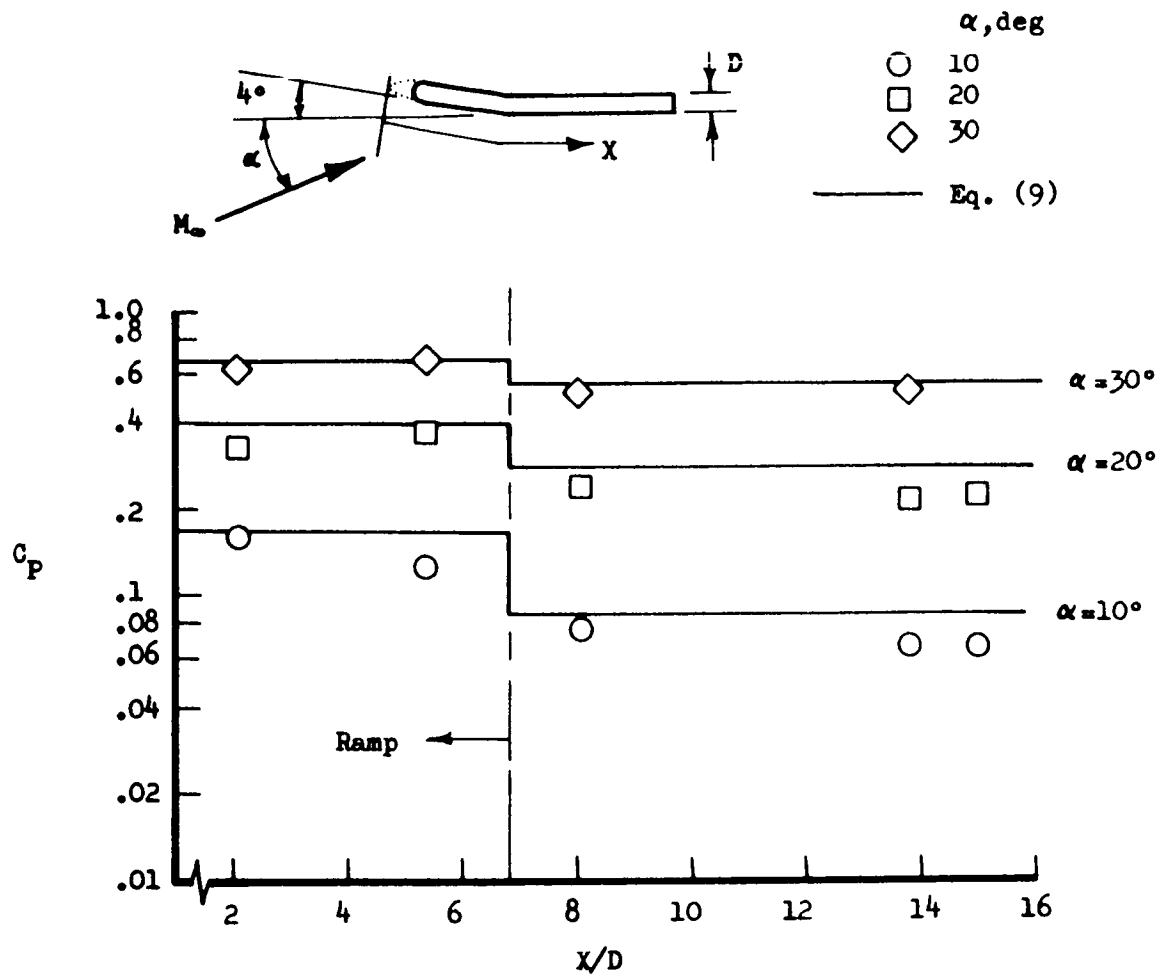


Figure 38.- Effect of a 4° ramp angle on centerline pressure data for a blunt-prow wing . AD461M-1; $M_\infty = 7.0$; $\Lambda = 73^\circ$

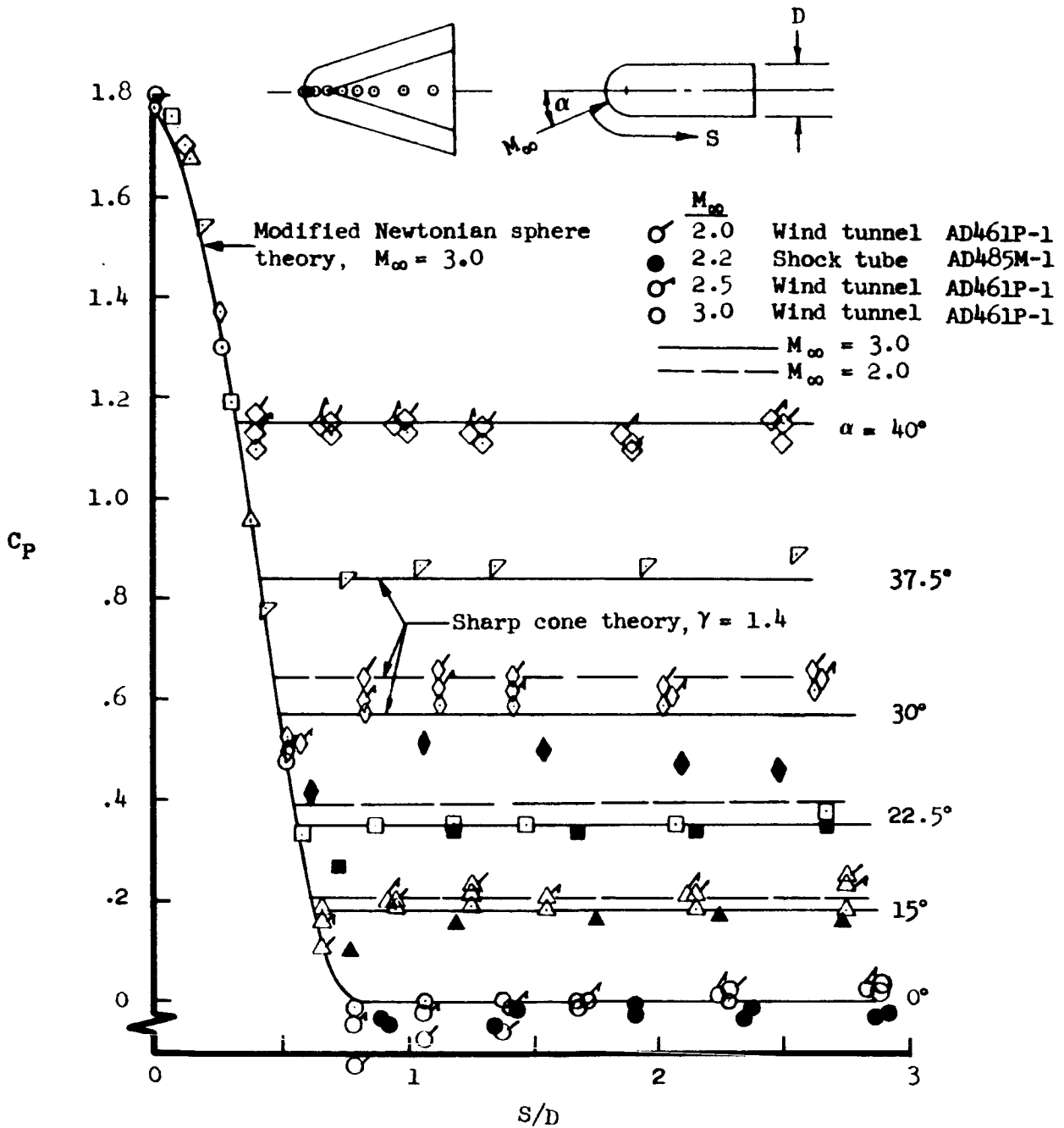


Figure 39.- Comparison of real and ideal gas pressures at low mach numbers on a blunt-prow delta wing.

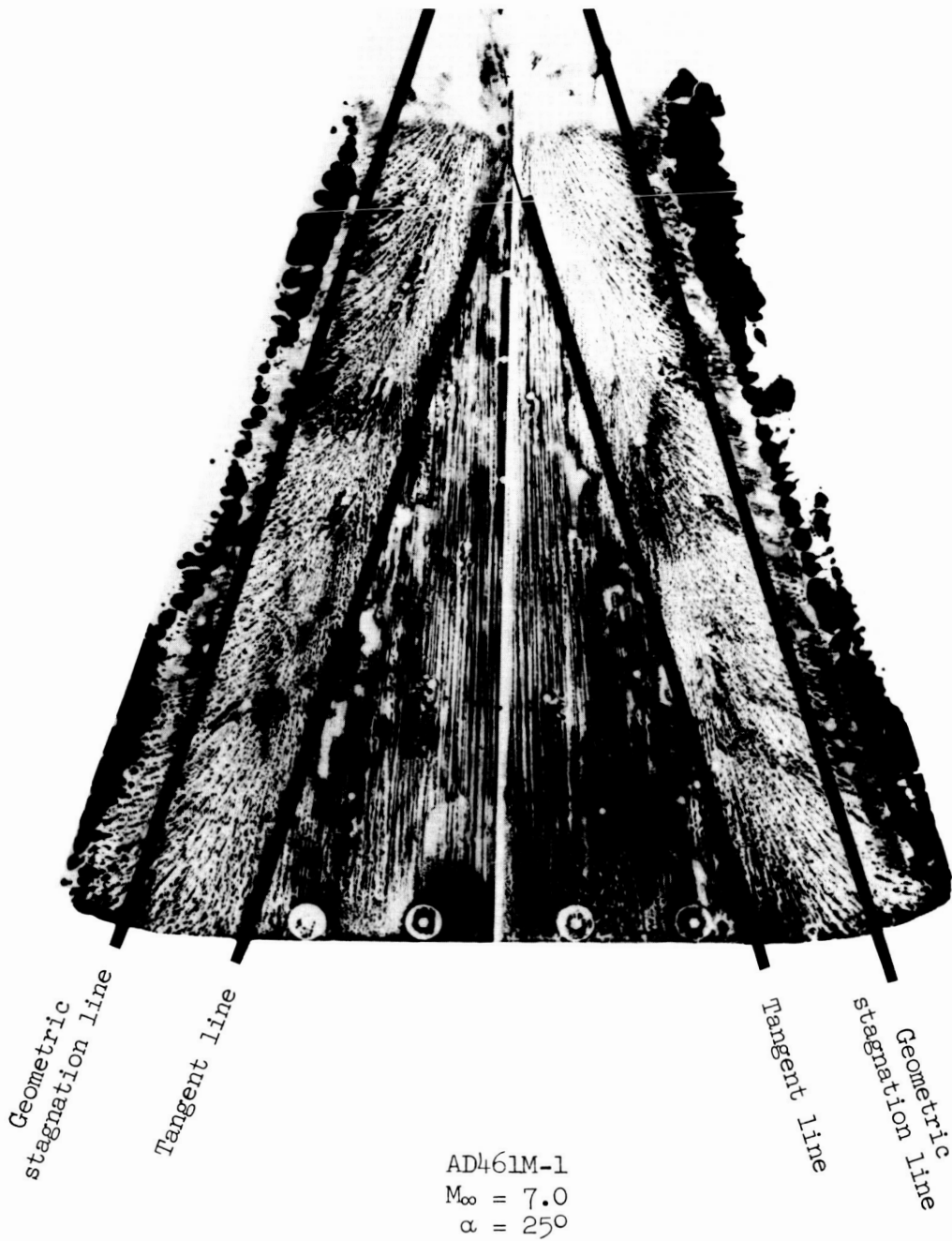
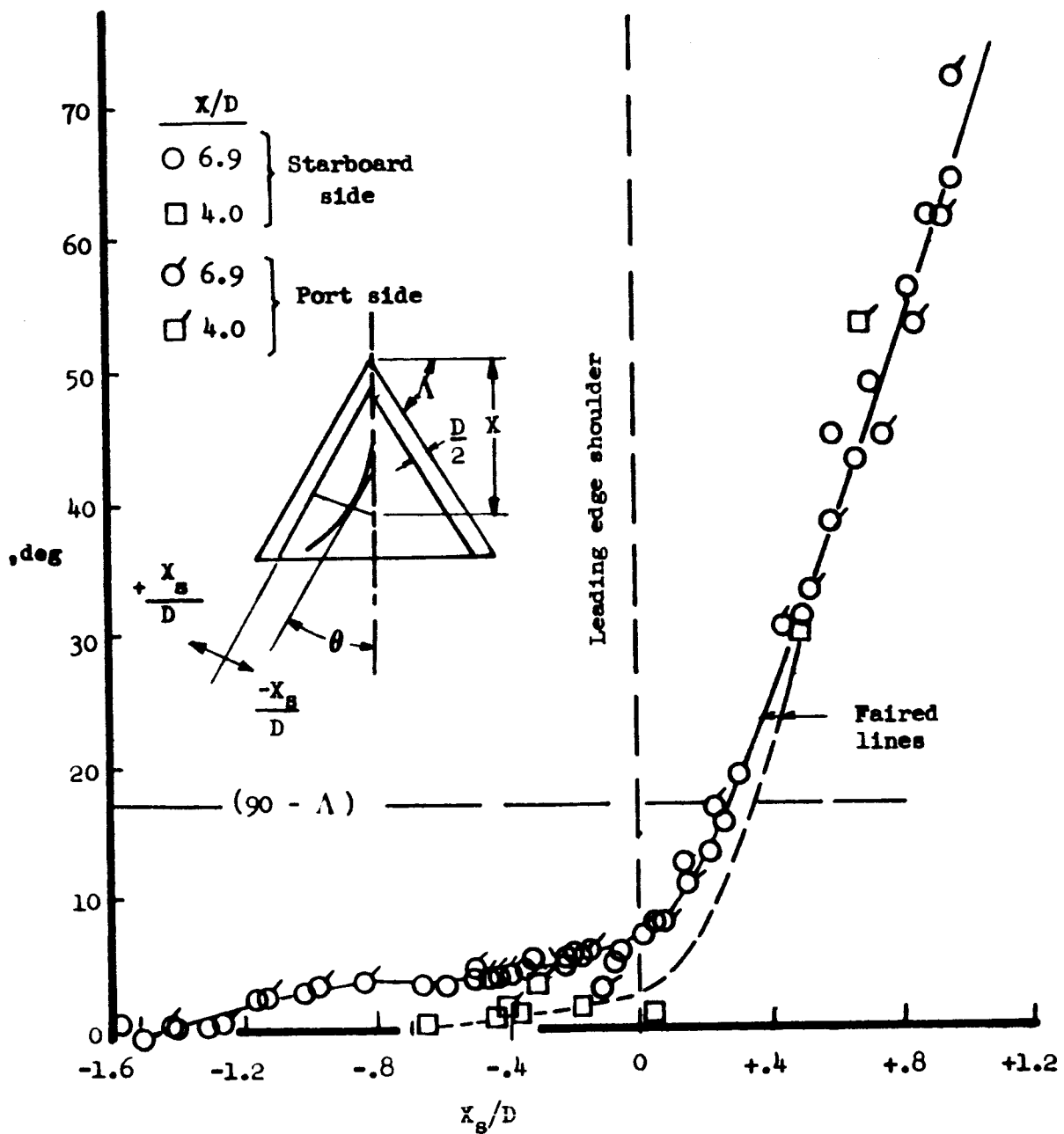
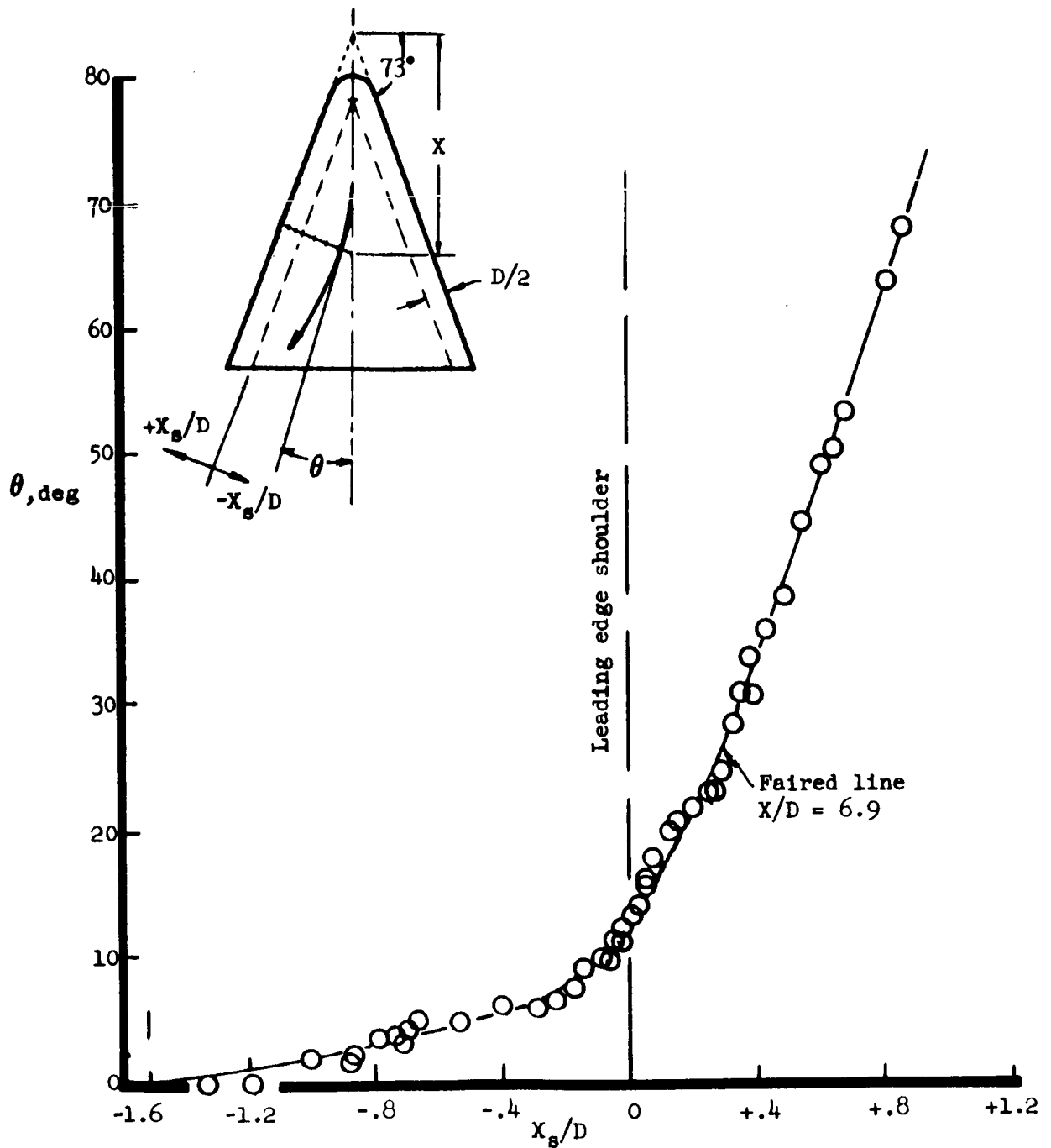


Figure 40.- Typical direct-transfer oil-flow streamline data.



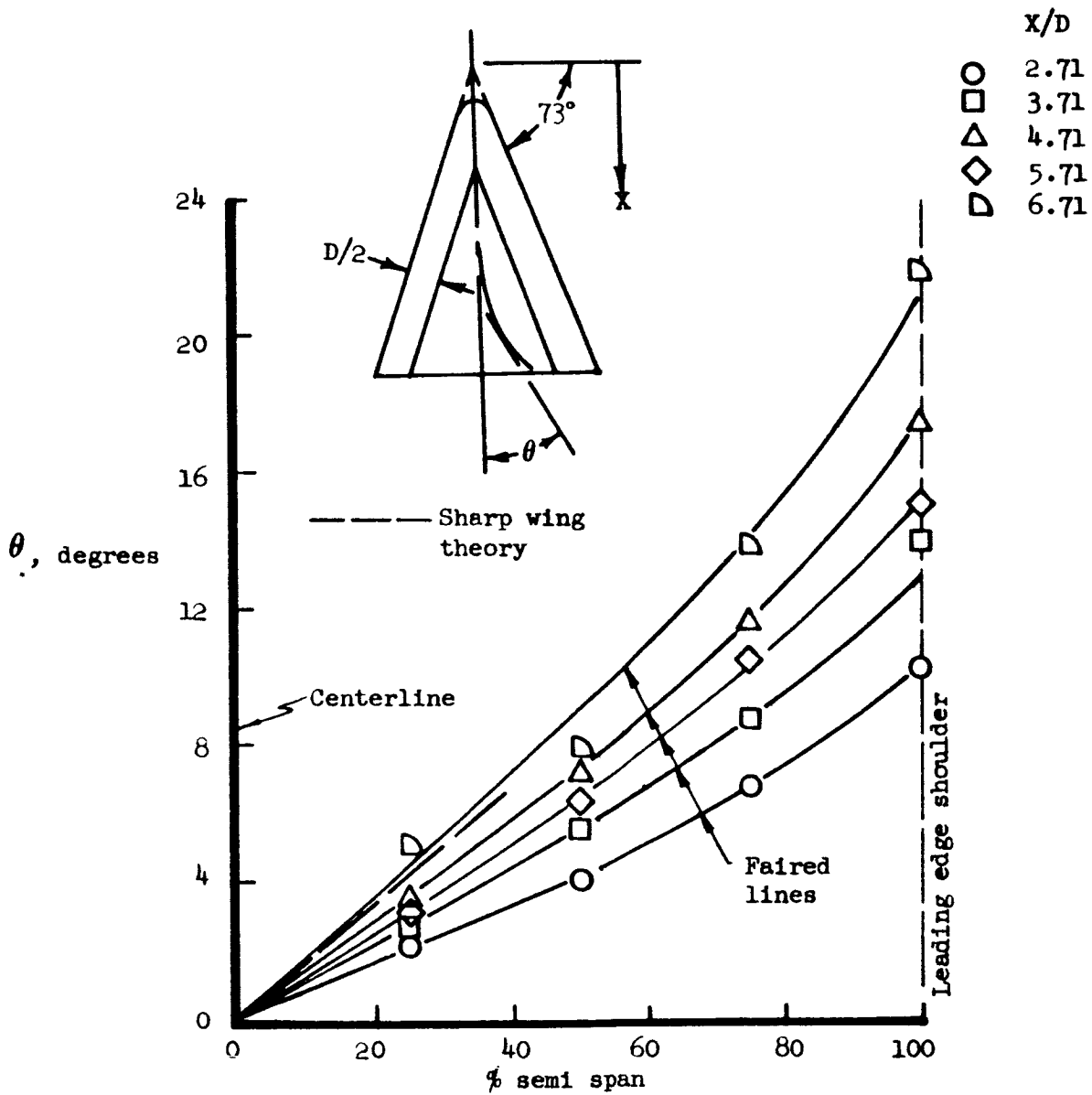
(a) Turbulent flow on the sharp-prow delta wing model W_{9A} . $\alpha = 20^\circ$;
 $\Lambda = 73^\circ$; $M_\infty = 6.08$; $N_{Re,D} = 145 \times 10^4$

Figure 41.- Streamline measurements from oil flow patterns on AD461M-1 delta wings.



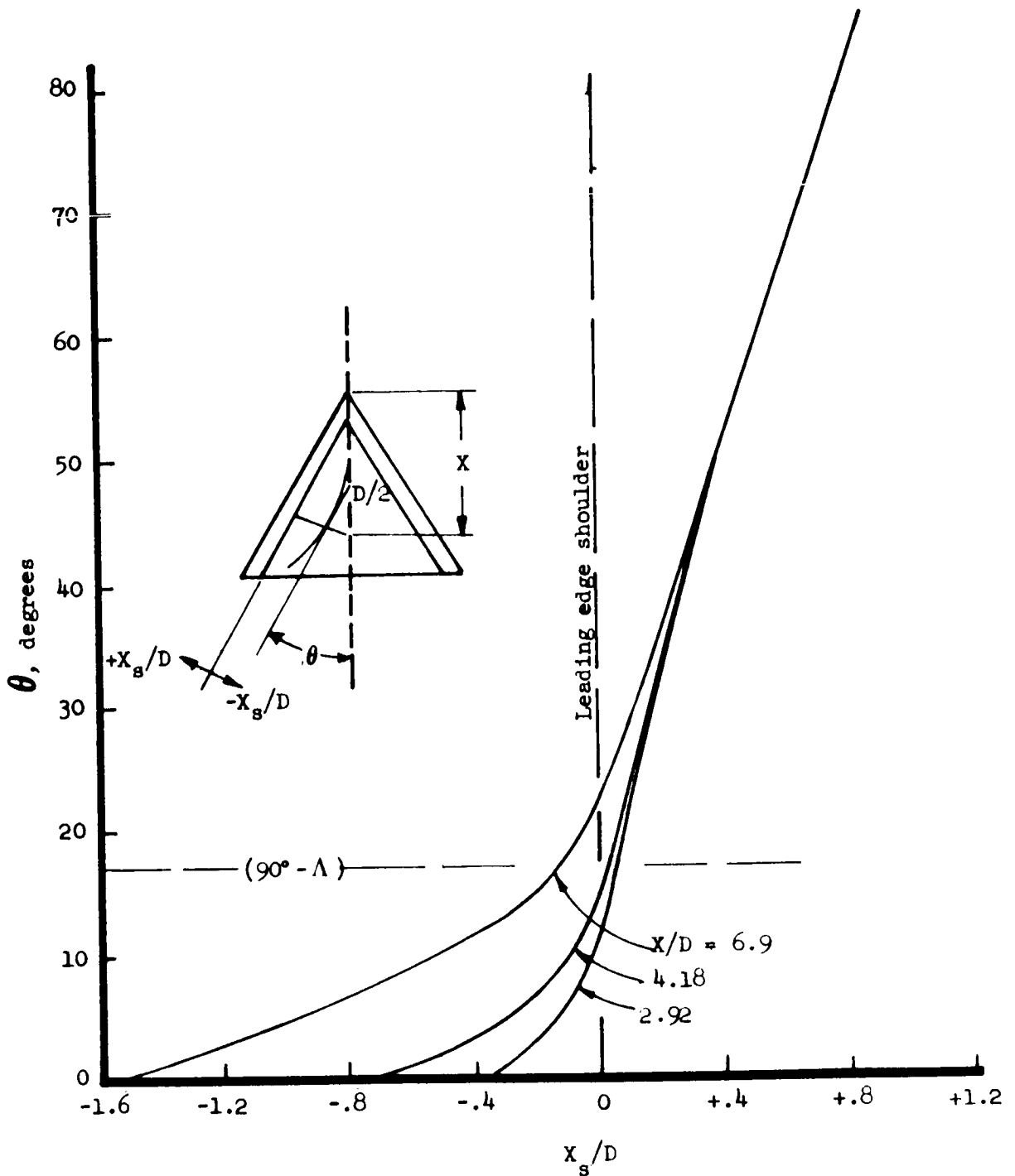
(b) Blunt-prow model W_2 ; $\alpha = 30^\circ$; $\Lambda = 73^\circ$; $M_\infty = 7.0$; $N_{Re,D} = 94.5 \times 10^4$

Figure 41.- Continued.



(c) Blunt-prow model W_2 ; $\alpha = 45^\circ$; $\Lambda = 73^\circ$;
 $M_\infty = 7.0$; $N_{Re,D} = 94.5 \times 10^4$

Figure 41.- Concluded.

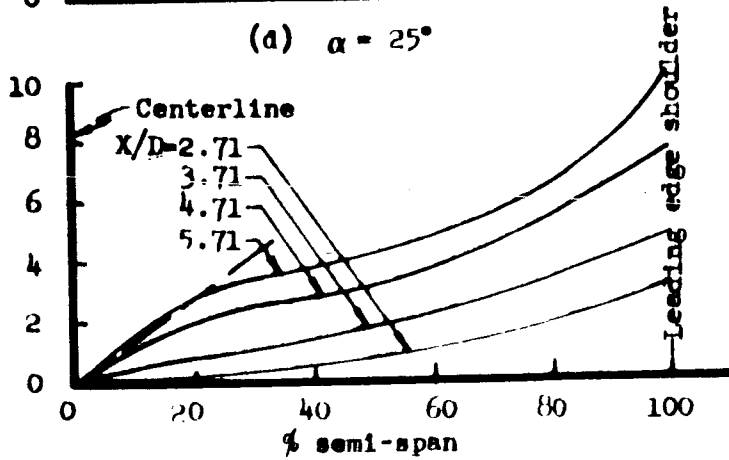
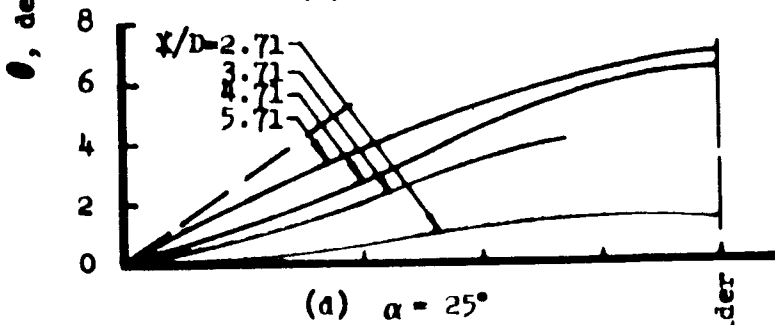
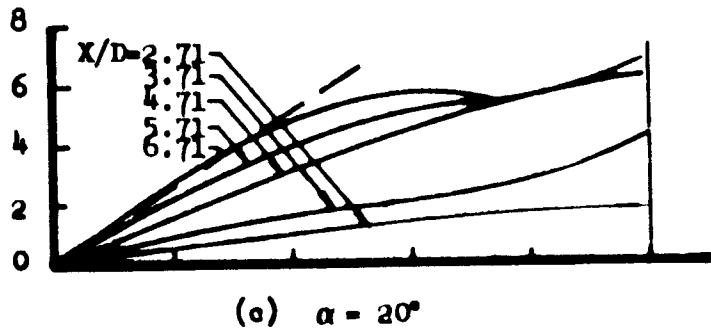
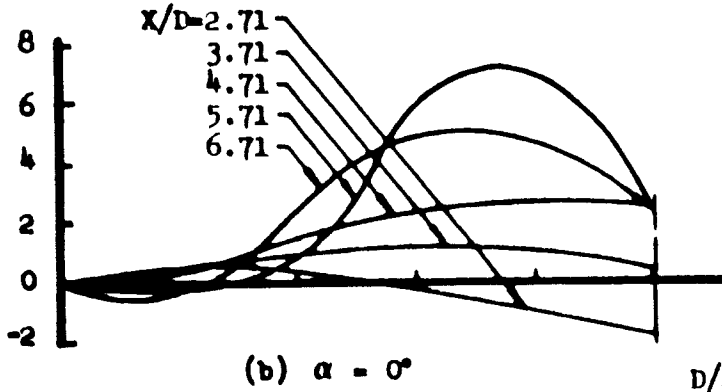


(a) Sharp-prow delta wing model W_{9A} ; turbulent flow; $\alpha = 42^\circ$; $M_\infty = 6.08$;
 $\Lambda = 73^\circ$; $N_{Re,D} = 145 \times 10^4$

Figure 42.- Streamline measurements from oil flow patterns on delta wings.

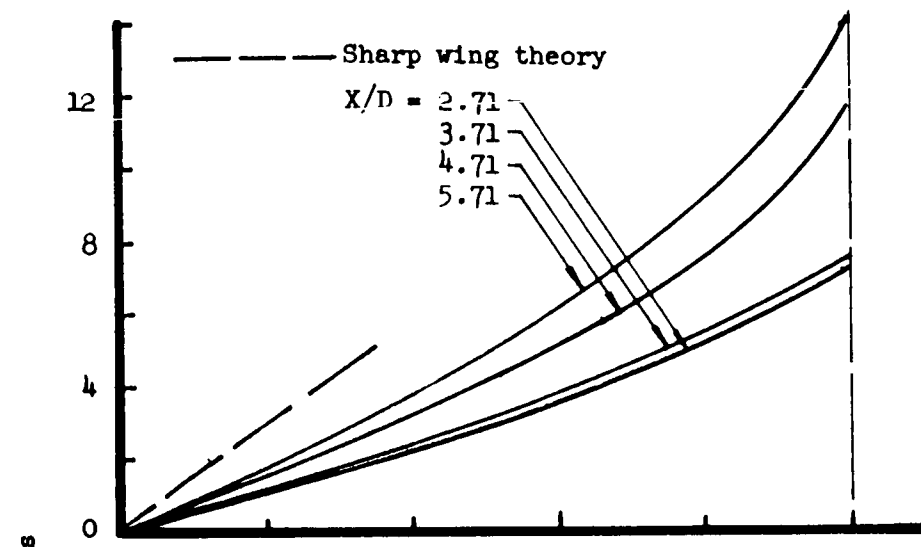
AD461M-1

----- Sharp-prov wing theory

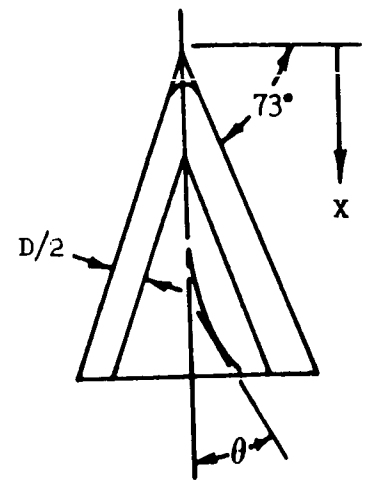


AD461M-1
Blunt delta wing
model W₂
M_∞ = 7.0
Λ = 73°
N_{Re,D} = 94.5 × 10⁴

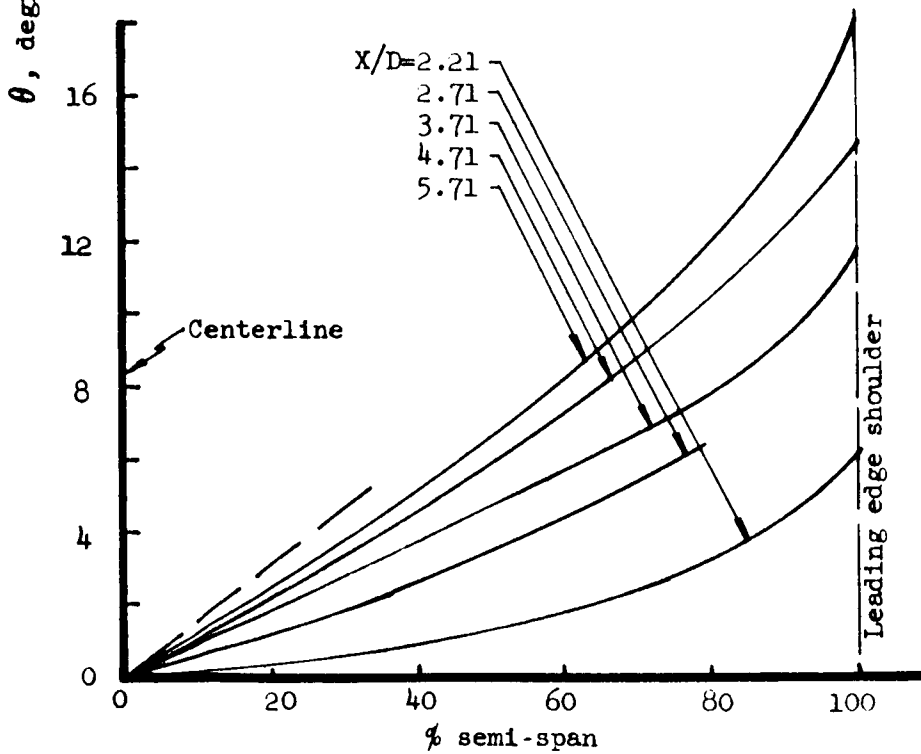
Figure 42.- Continued.



(f) $\alpha = 35^\circ$

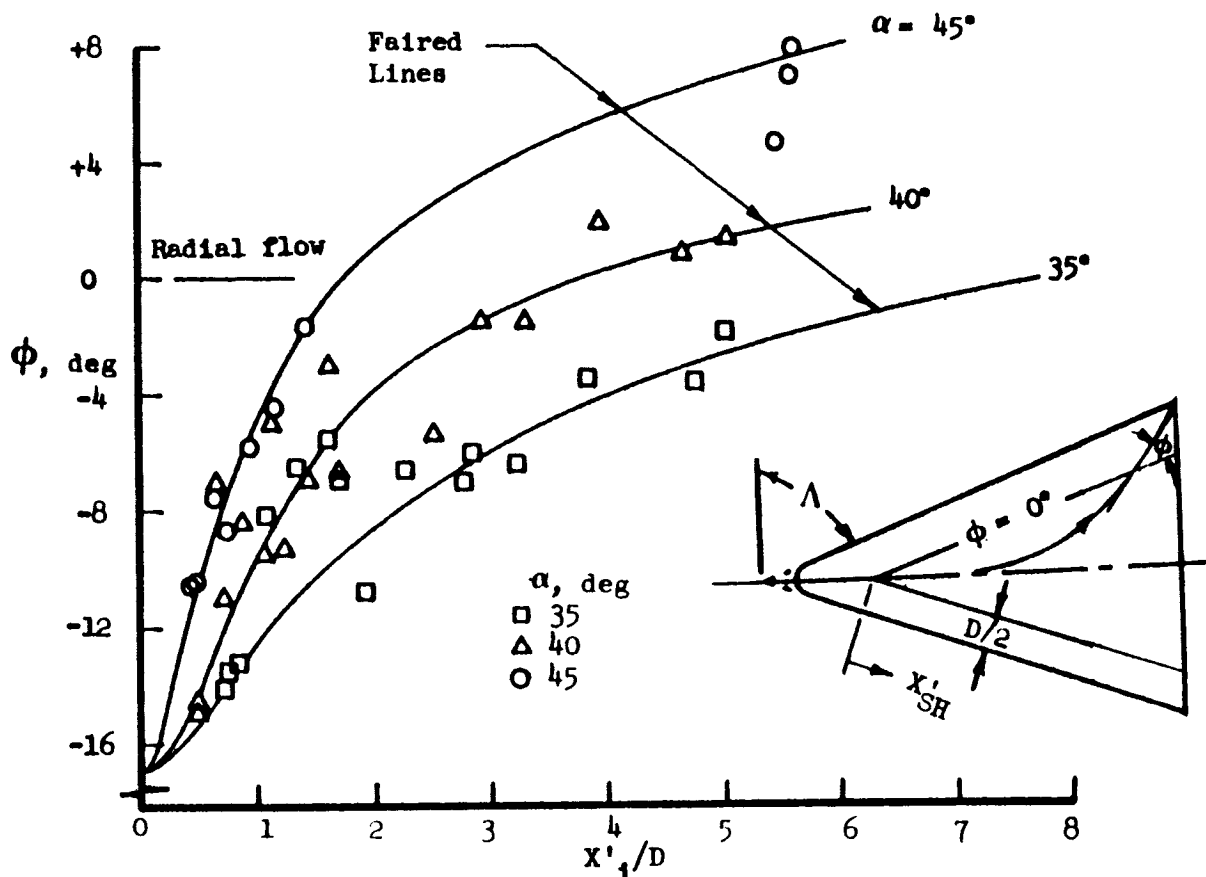


AD461M-1
 Blunt delta wing
 model W_2
 $M_\infty = 7.0$
 $\Lambda = 73^\circ$
 $N_{Re,D} = 94.5 \times 10^4$



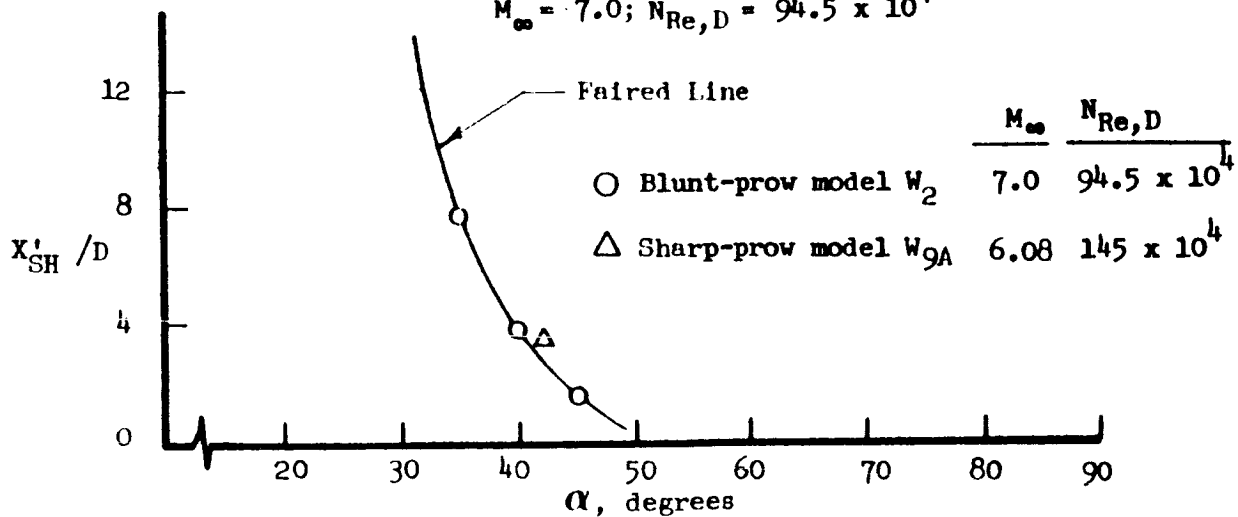
(g) $\alpha = 40^\circ$

Figure 42.- Concluded



(a) Streamline angles from the blunt-prow delta wing model W_2 .

$M_\infty = 7.0$; $N_{Re,D} = 94.5 \times 10^4$



(b) α required for radial flow, $\phi = 0^\circ$

Figure 43.- Measured streamline angle at the leading edge shoulder.

AD461M-1; $\Lambda = 73^\circ$

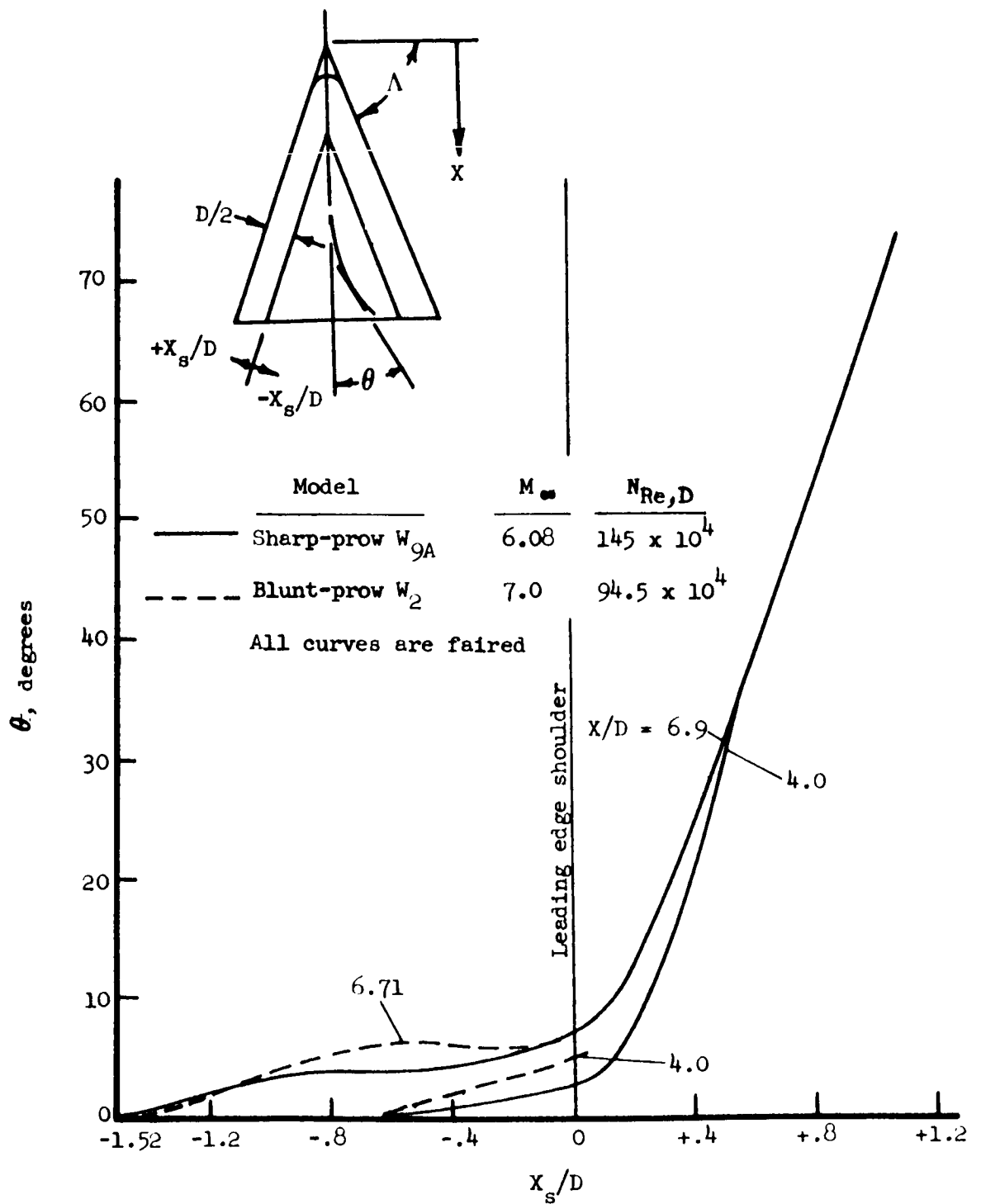


Figure 44.- Comparison of streamline angles on blunt and sharp-prow delta wings. AD461M-1; $\alpha = 20^\circ$; $\Lambda = 73^\circ$

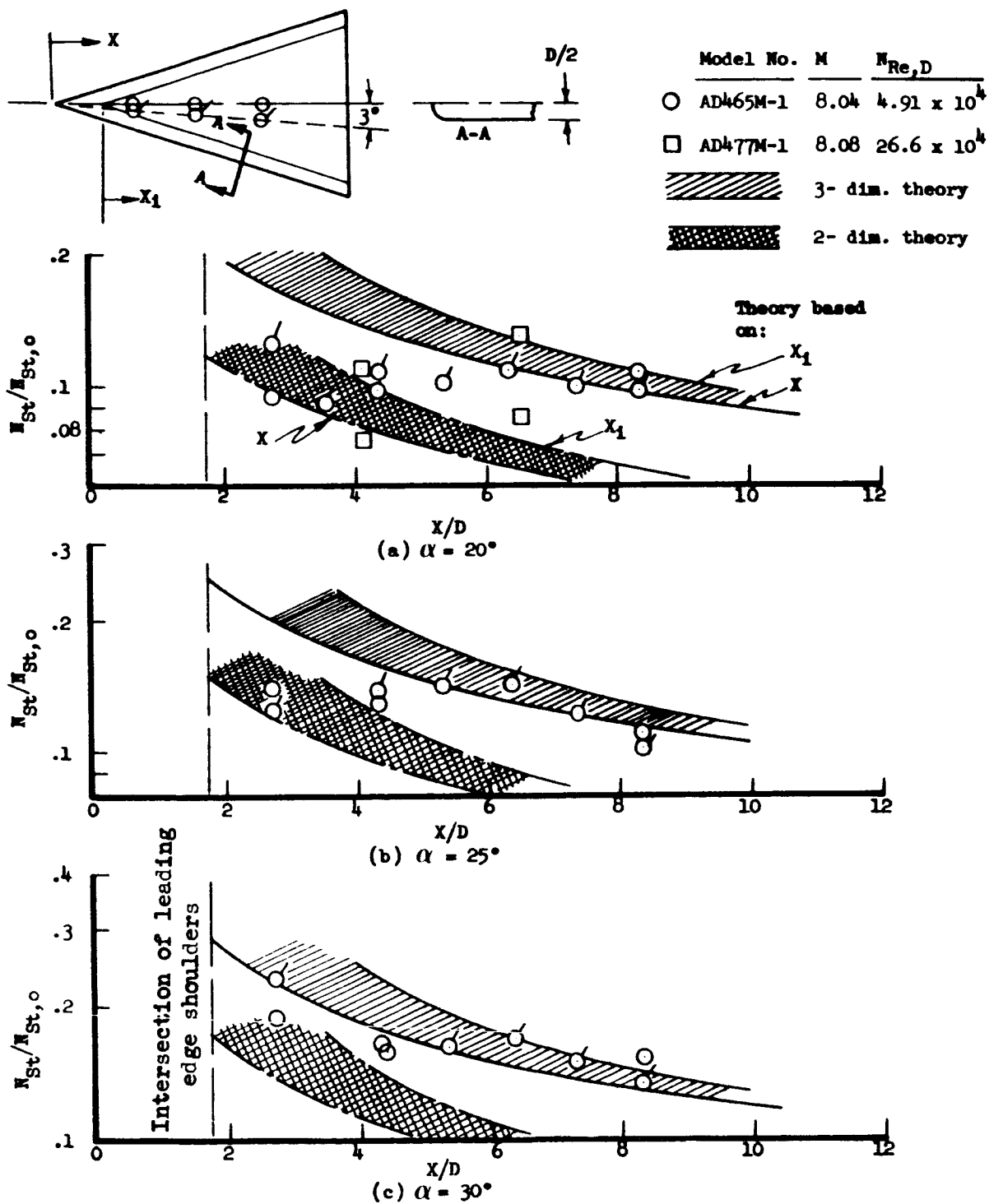


Figure 45.- Laminar heating on the lower surface of a sharp-prow delta wing.

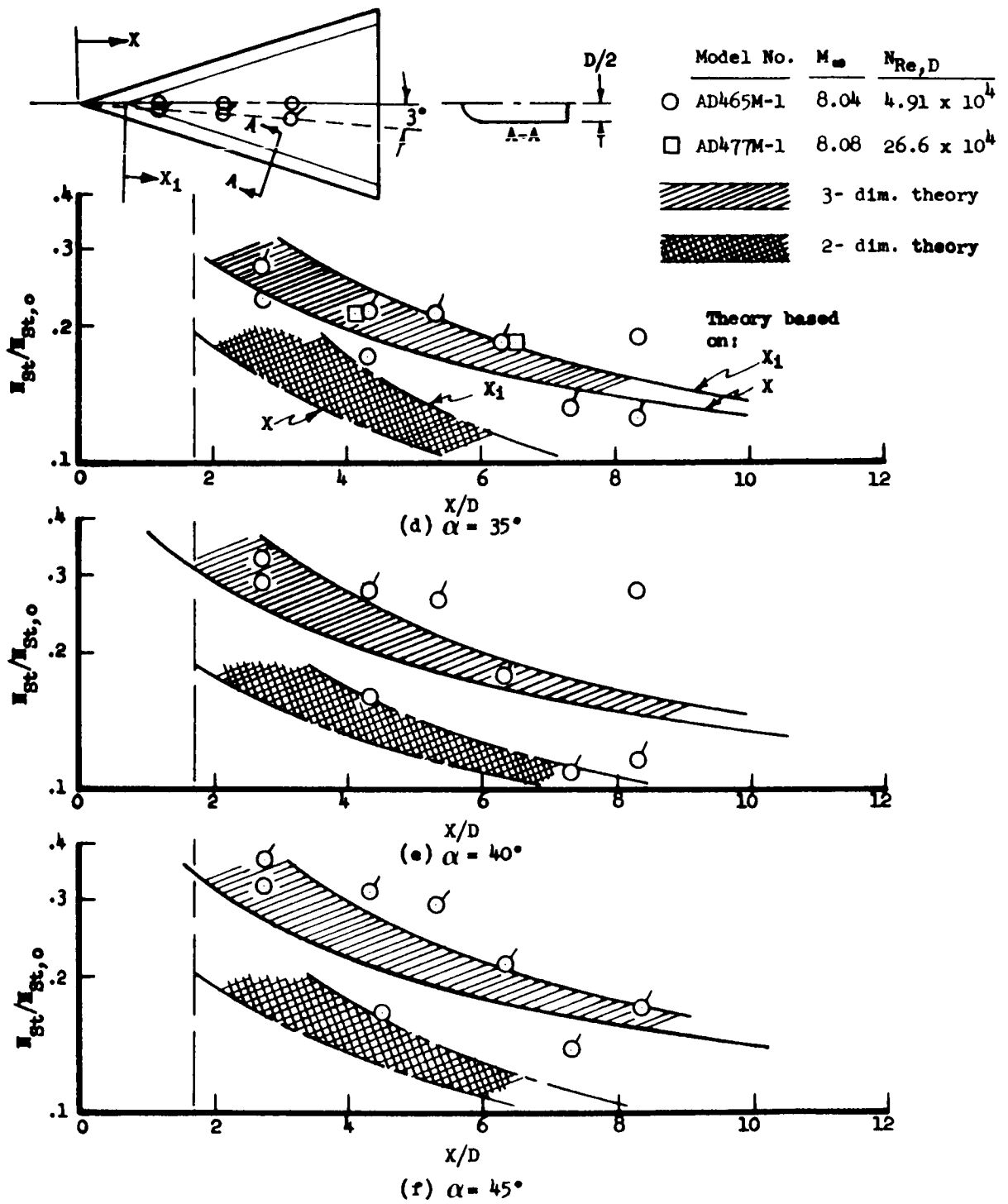


Figure 45.- Concluded.

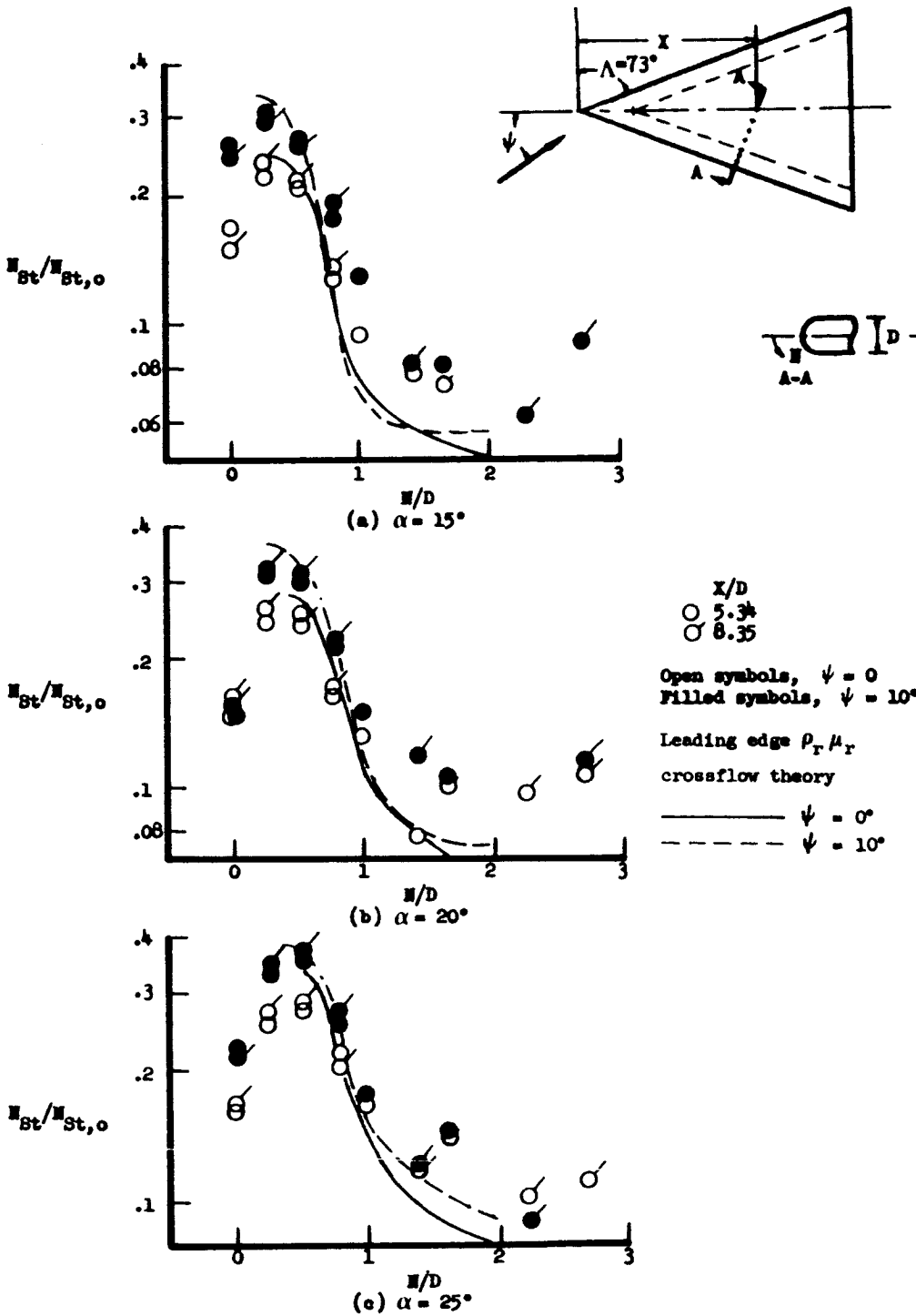


Figure 46.- Effect of yaw on sharp-prow delta wing heating in laminar flow AD477M-1; $M_\infty = 8.08$; $N_{Re,D} = 26.6 \times 10^4$.

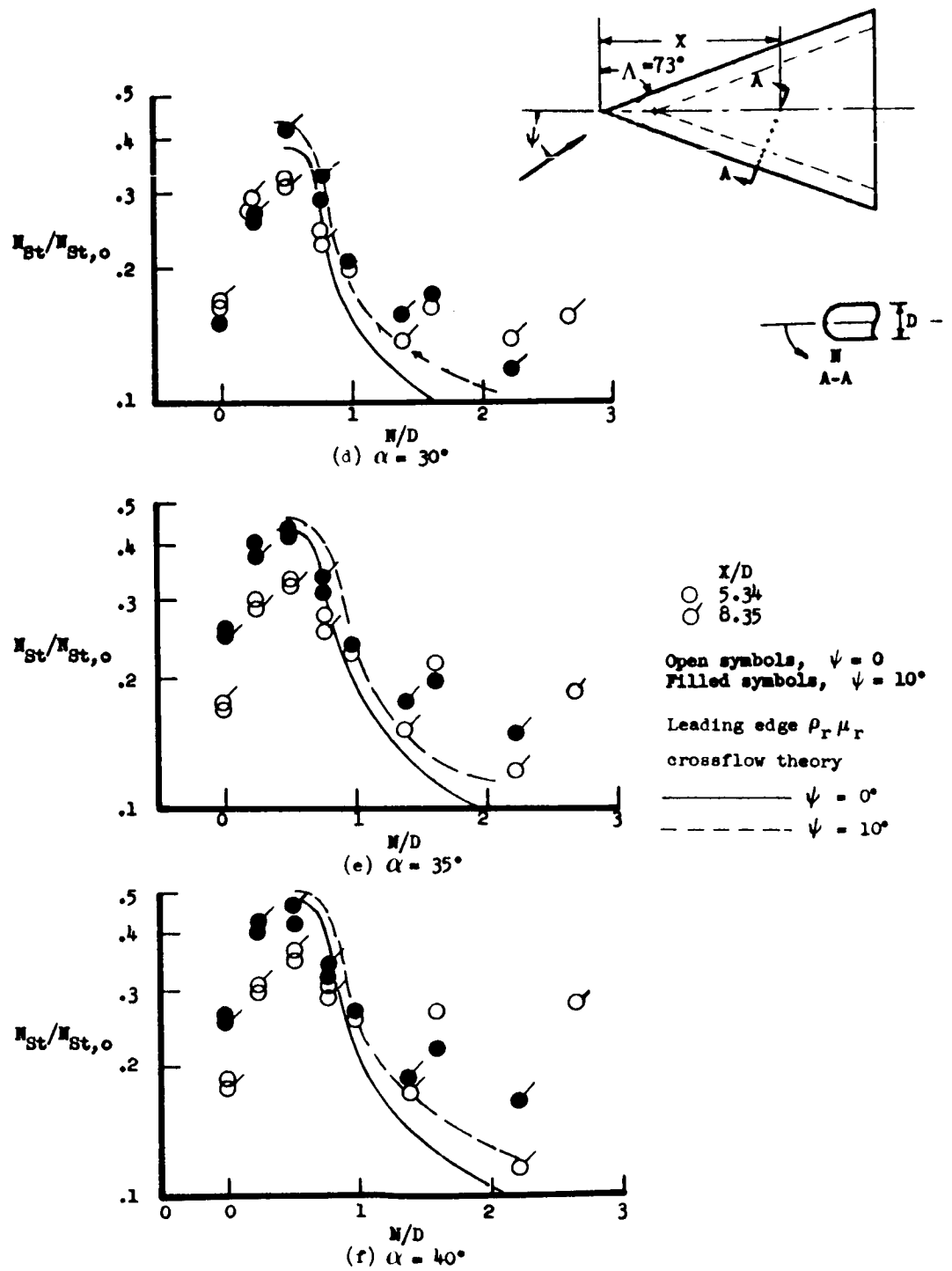


Figure 46.- Concluded.

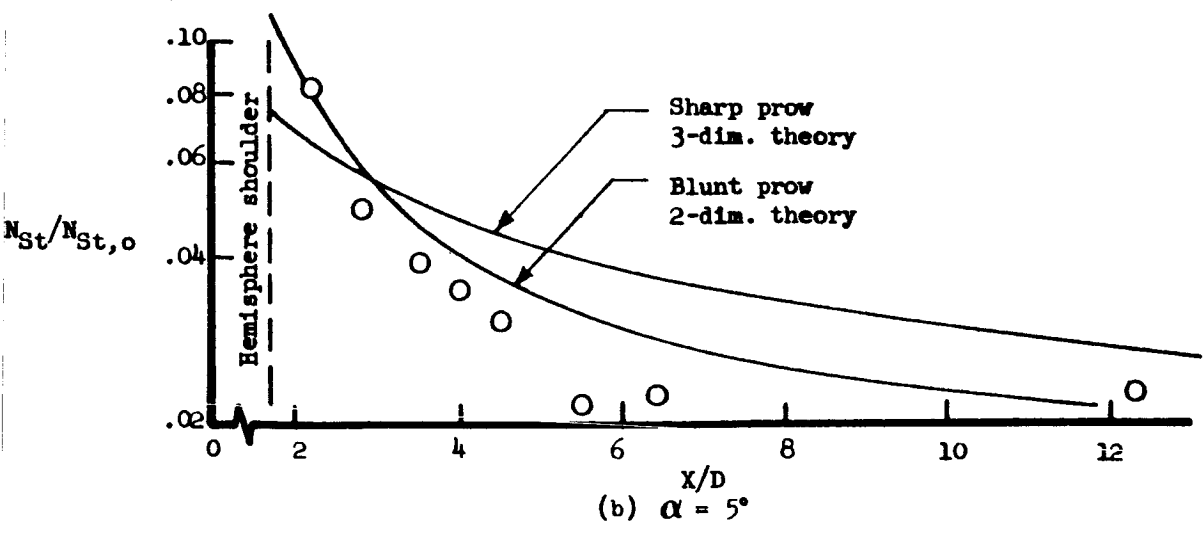
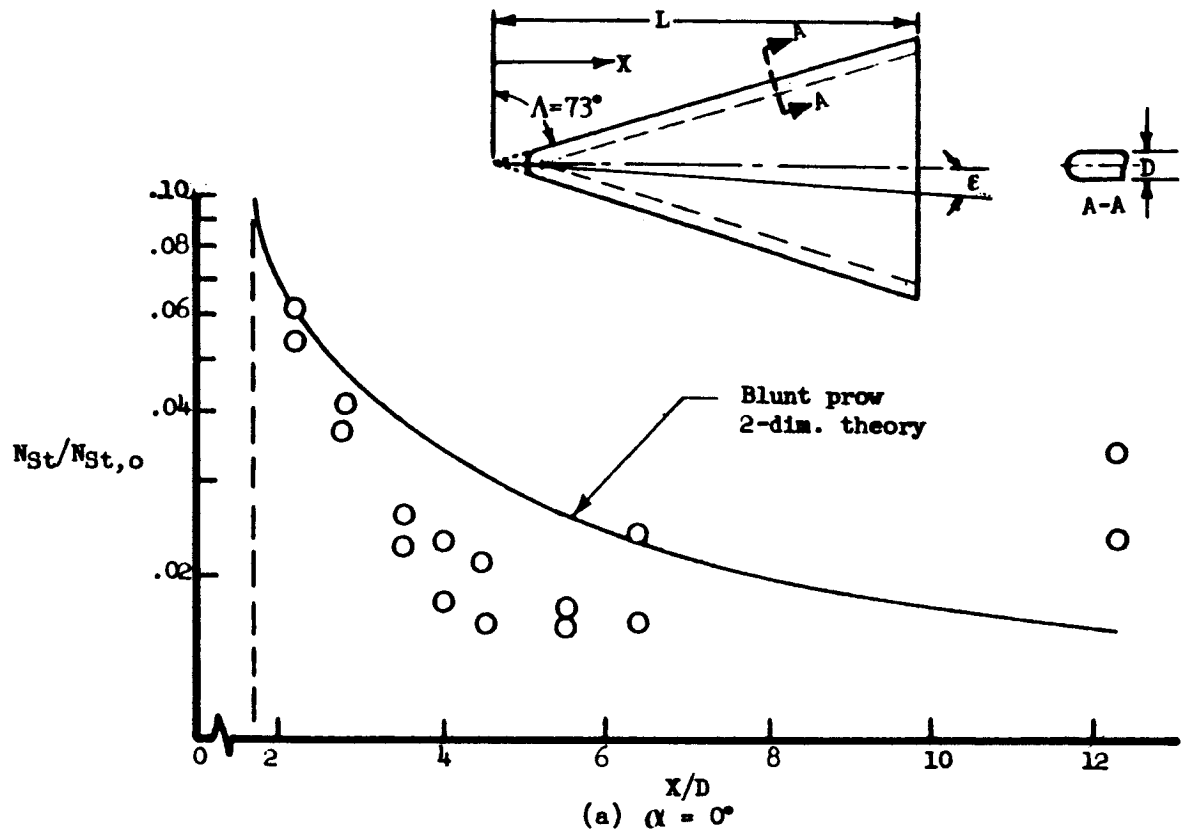


Figure 47.- Laminar heating data on the lower surface centerline of a blunt-prow delta wing. AD 462M-1; $M_\infty = 8.08$; $N_{Re,D} = 8.38 \times 10^4$

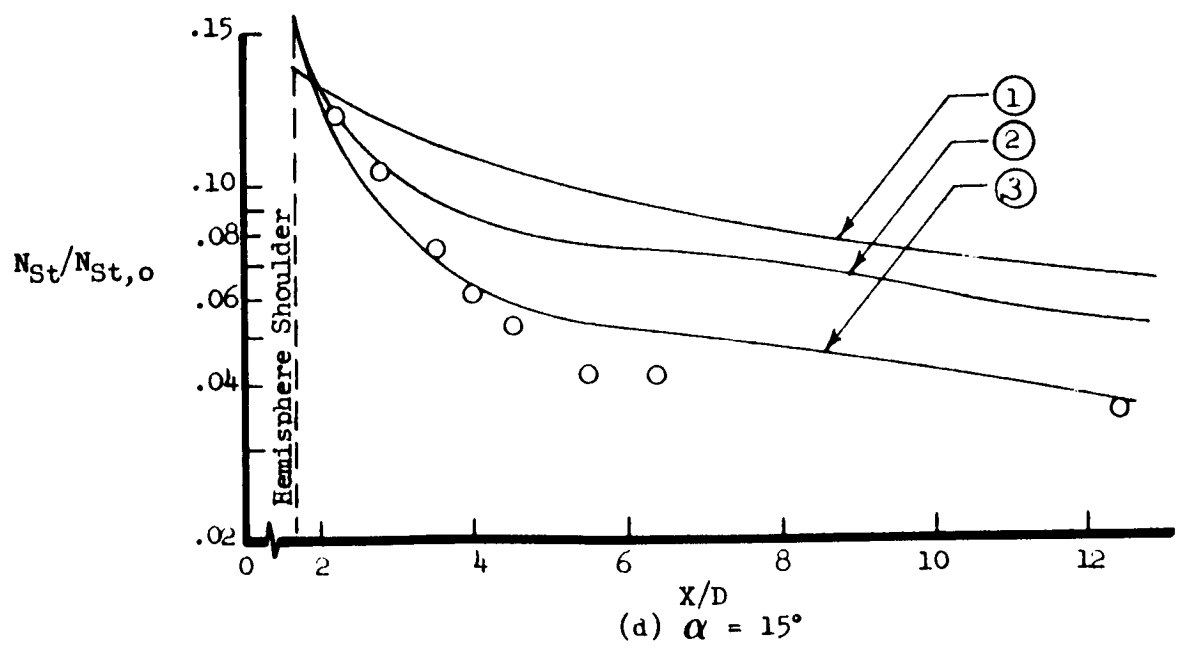
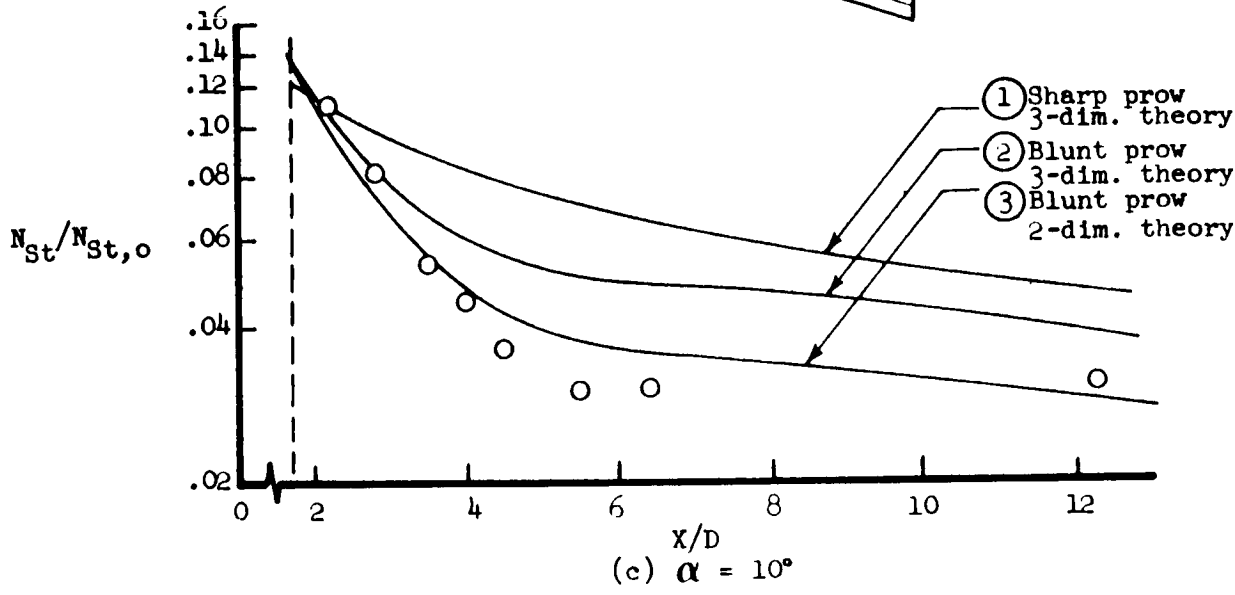
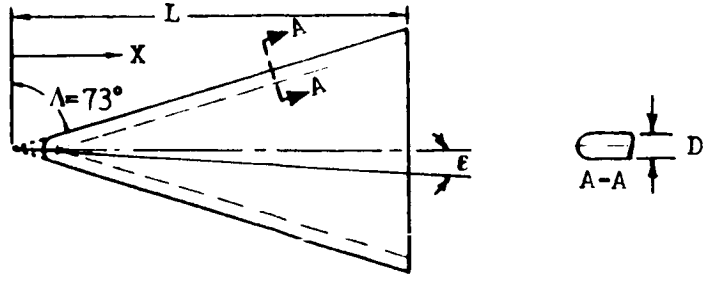


Figure 47.- Continued

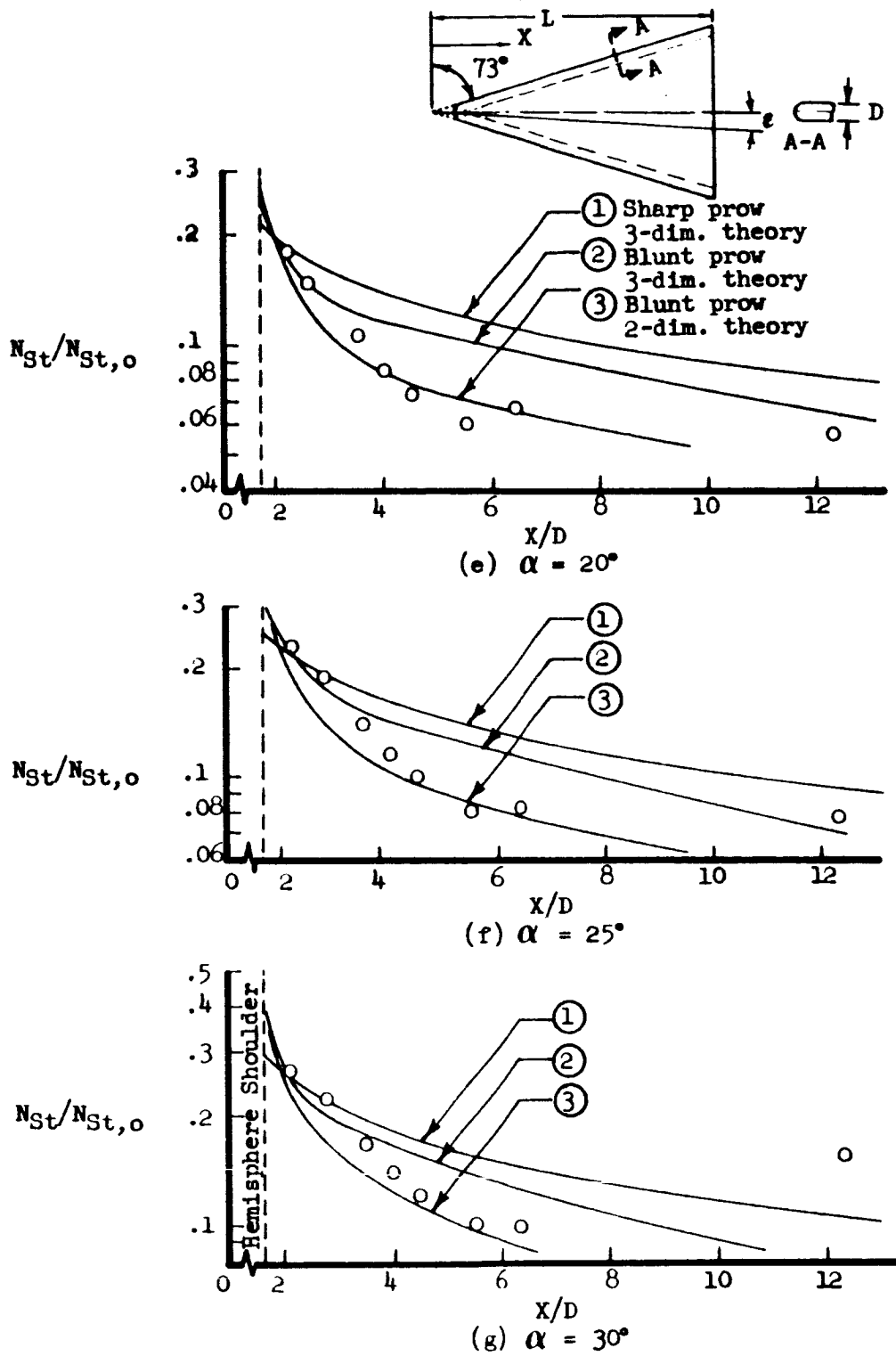
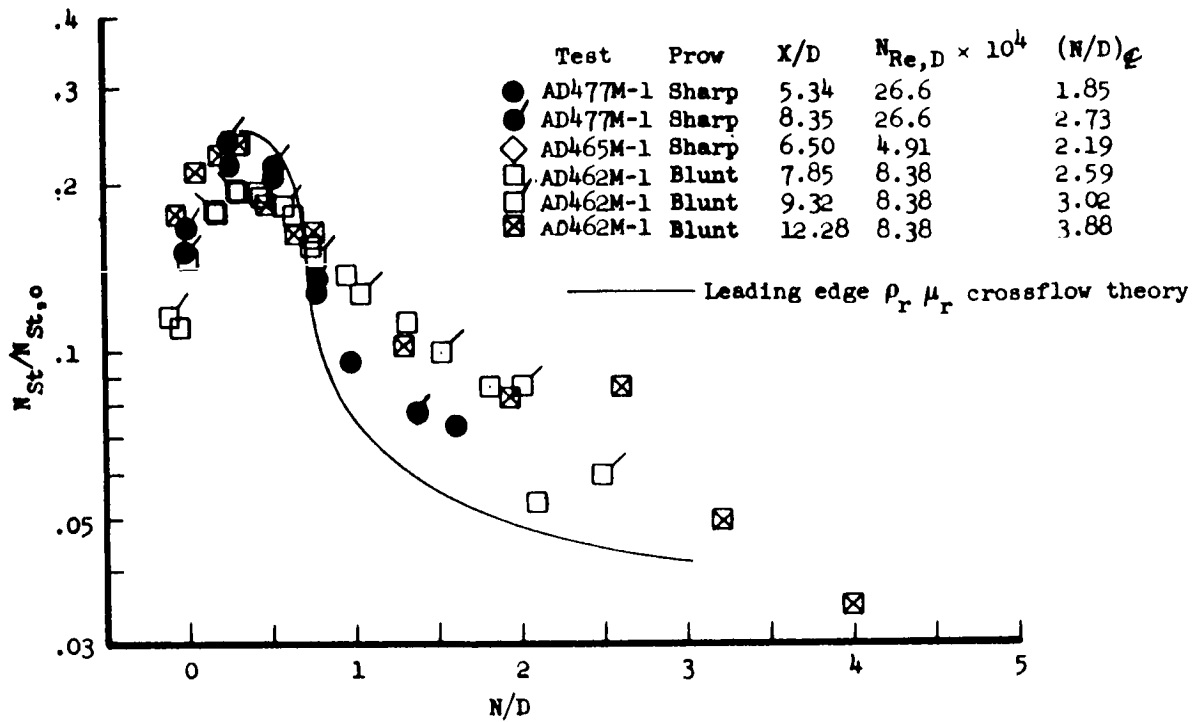
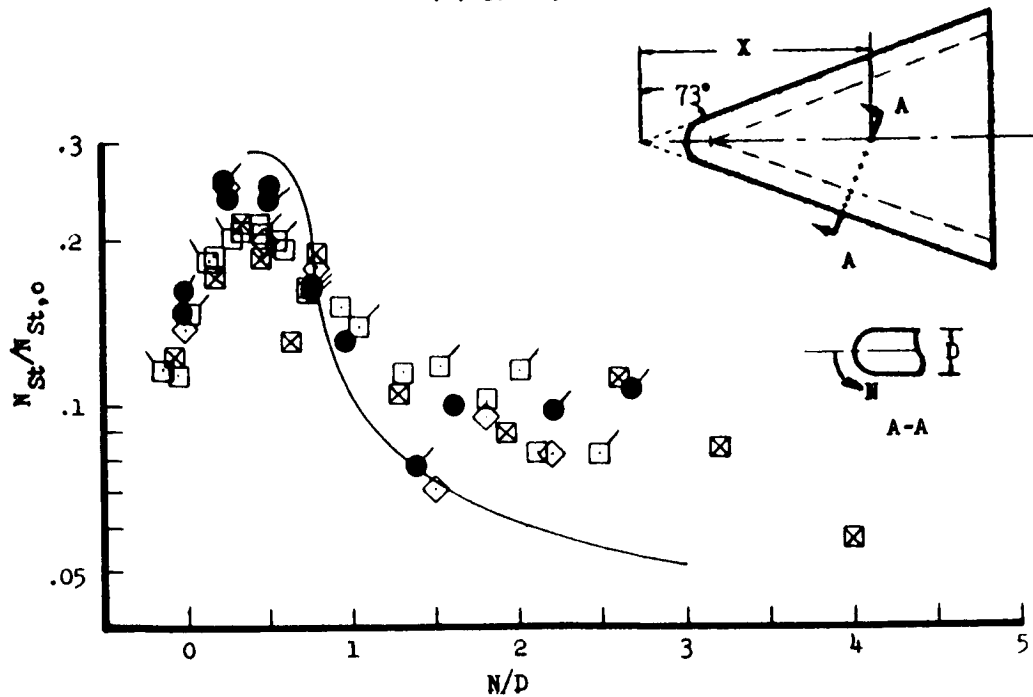


Figure 47.- Concluded.



(a) $\alpha = 15^\circ$



(b) $\alpha = 20^\circ$

Figure 48.- Comparison of laminar heating data on the lower surface of blunt and sharp prow delta wings. $M_\infty = 8$; $\Lambda = 73^\circ$; $\psi = 0^\circ$.

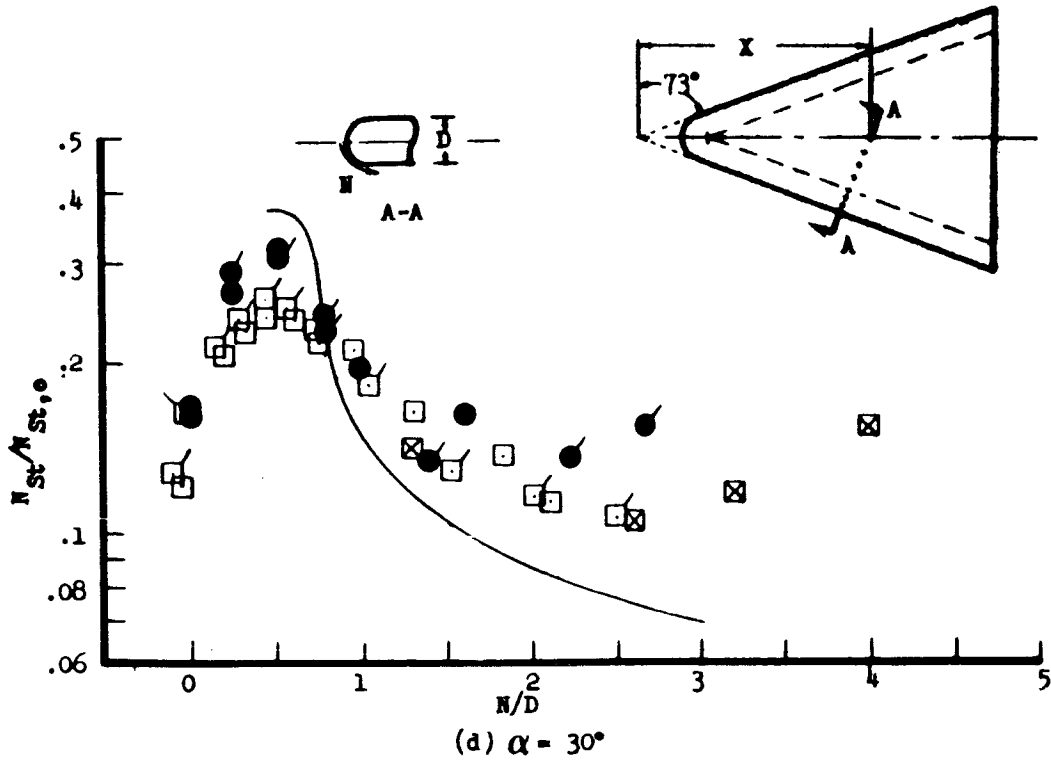
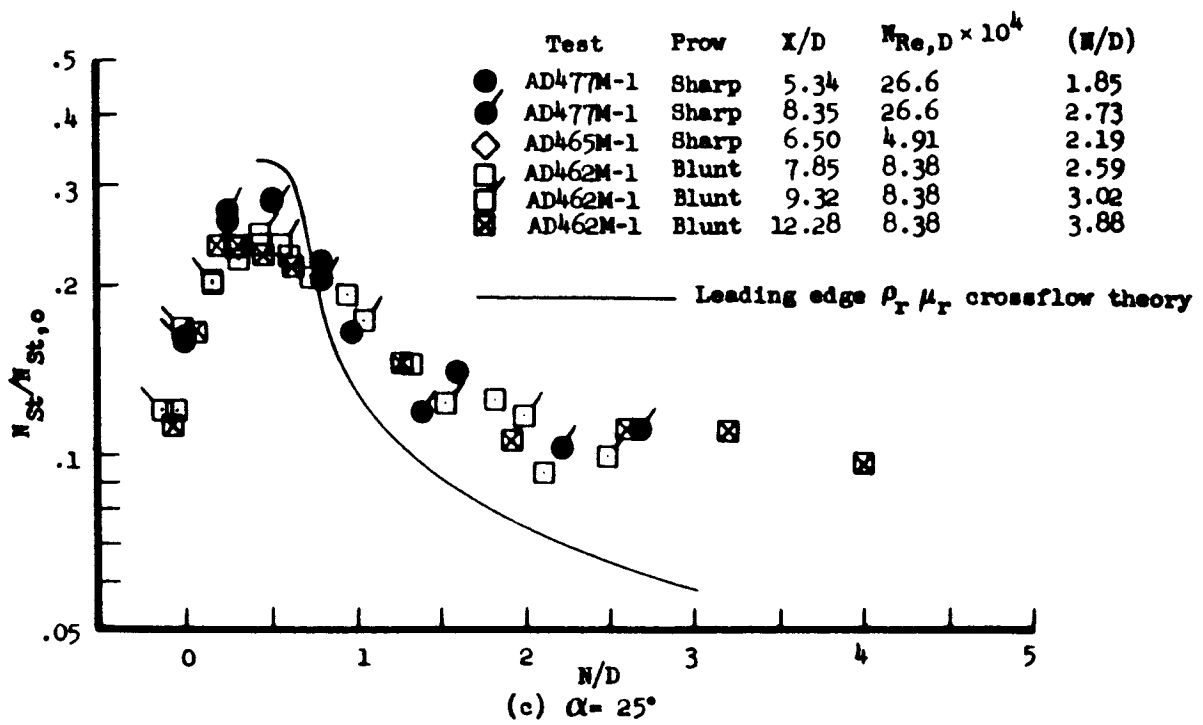
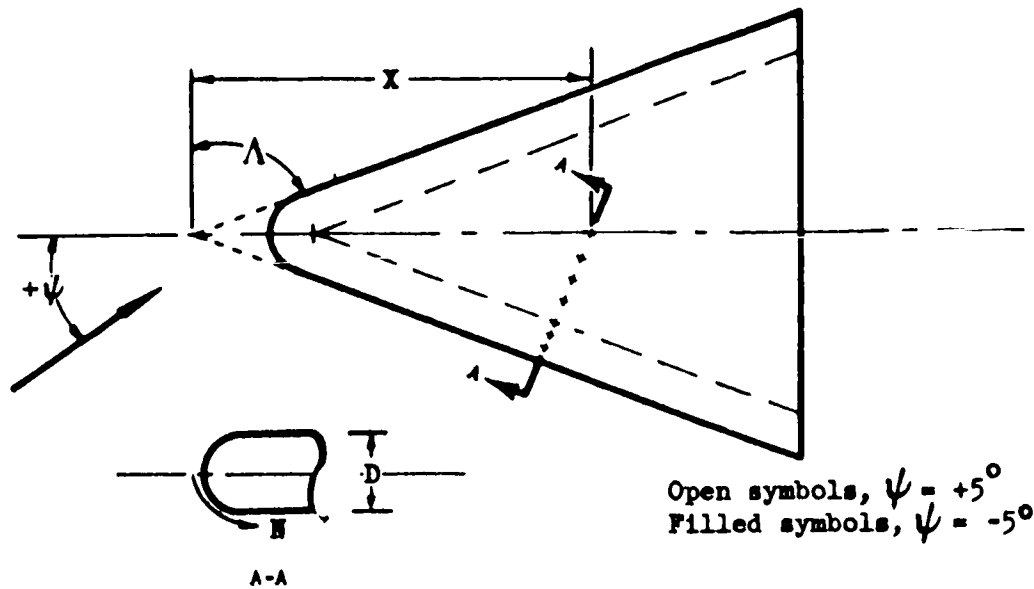


Figure 48.- Concluded.



Leading edge crossflow theory

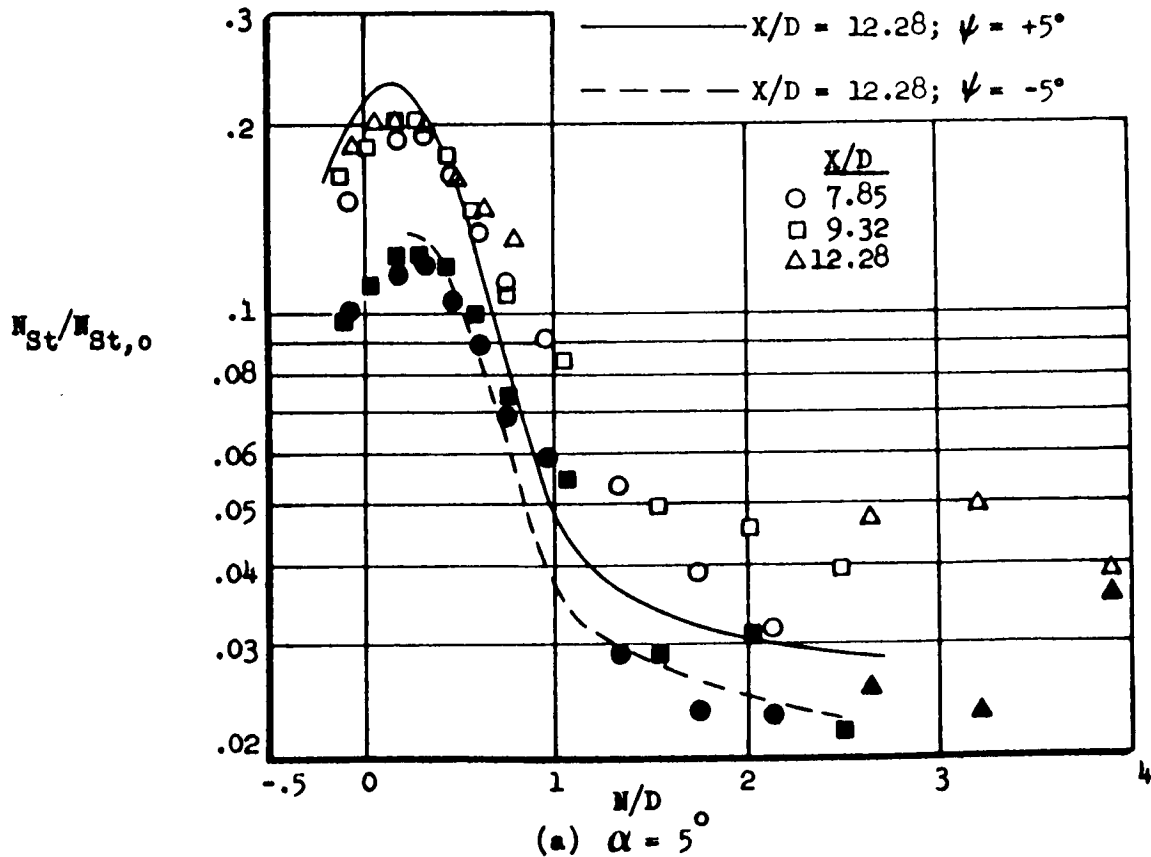


Figure 49. - Comparison of windward and leeward side heating data on a yawed blunt-prow delta wing in laminar flow. $M_\infty = 8.08$; $Re_{D} = 8.38 \times 10^4$.

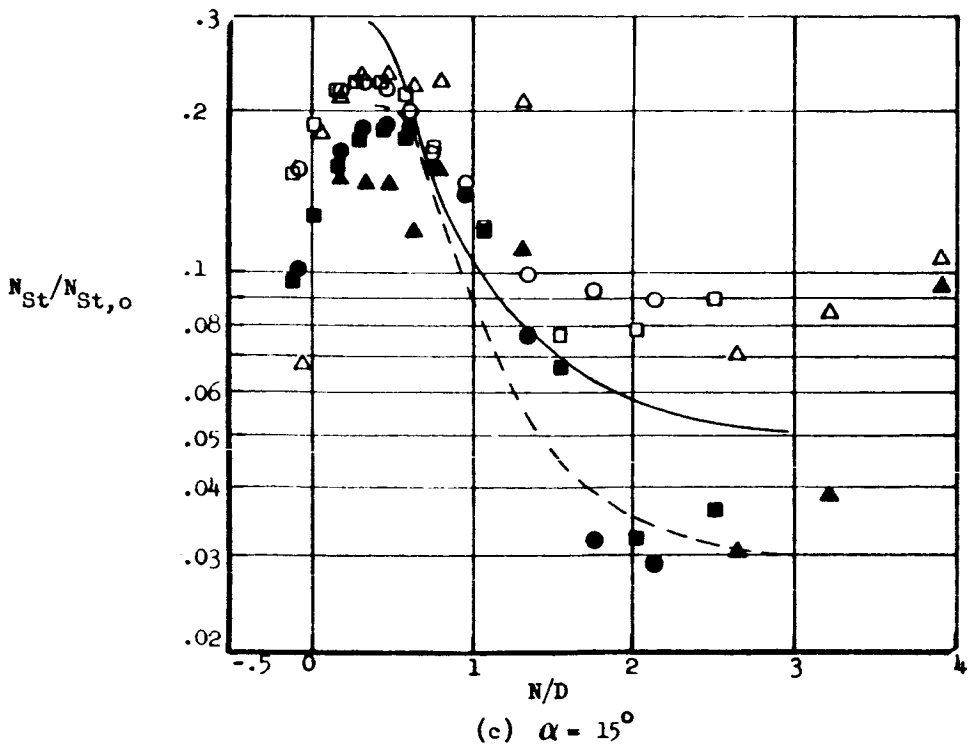
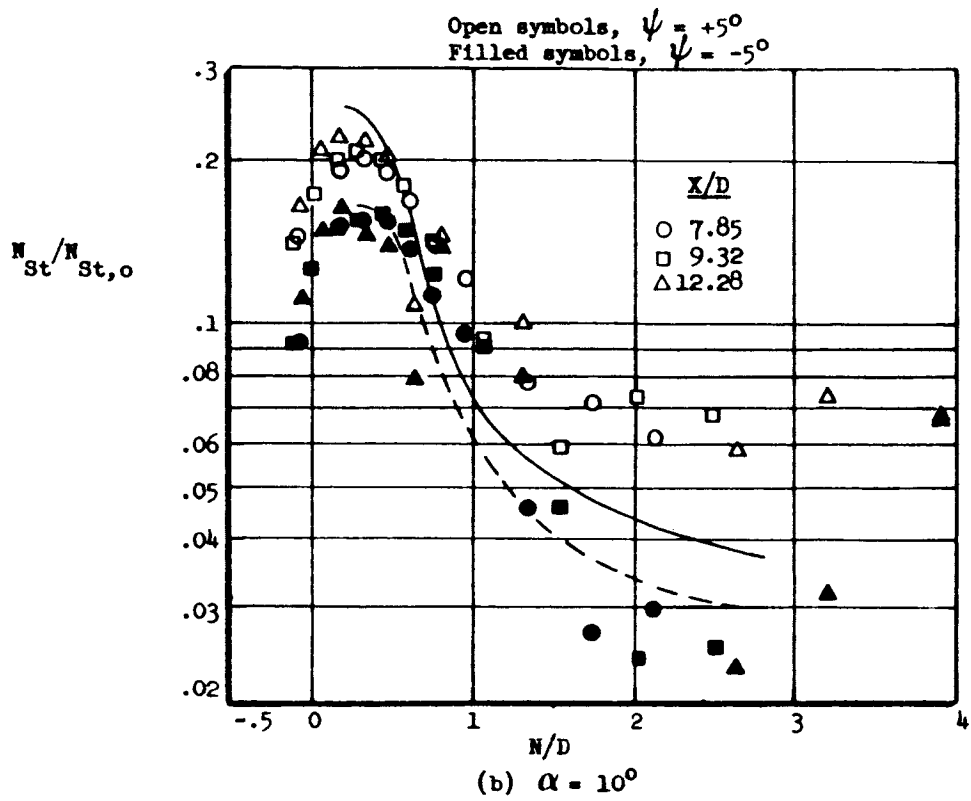


Figure 49.- Continued.

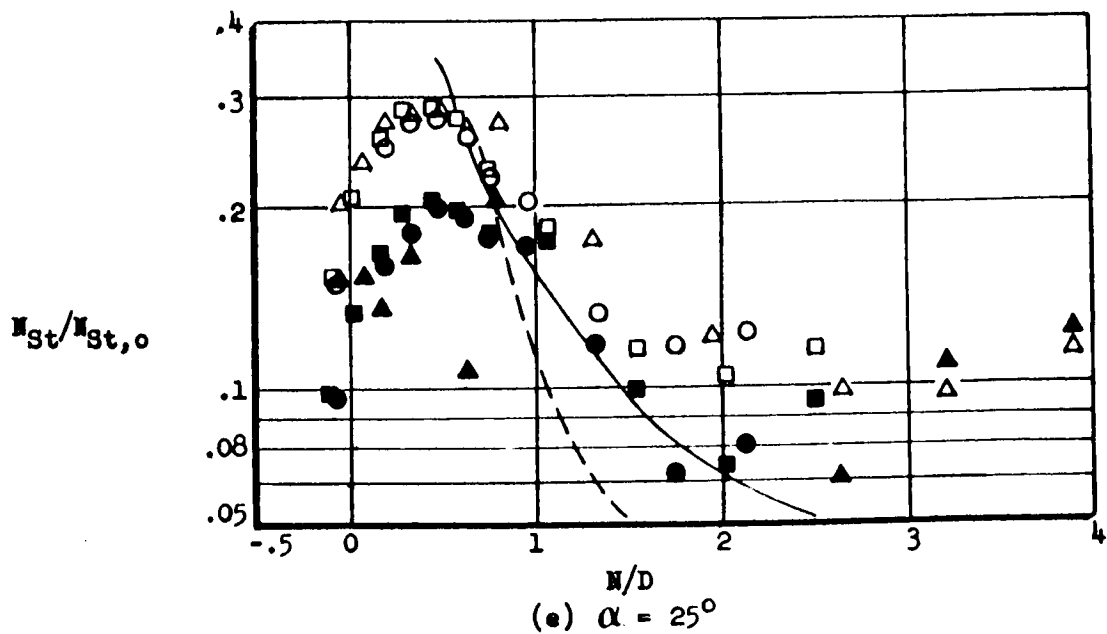
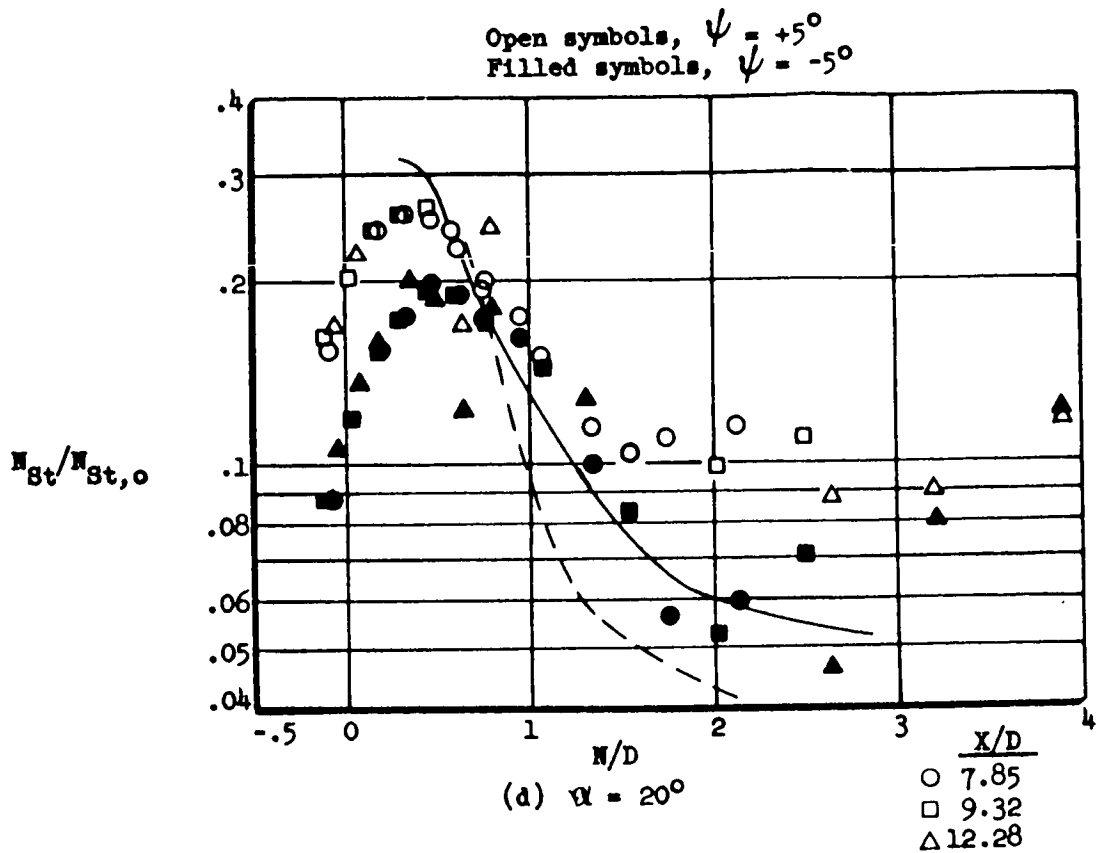
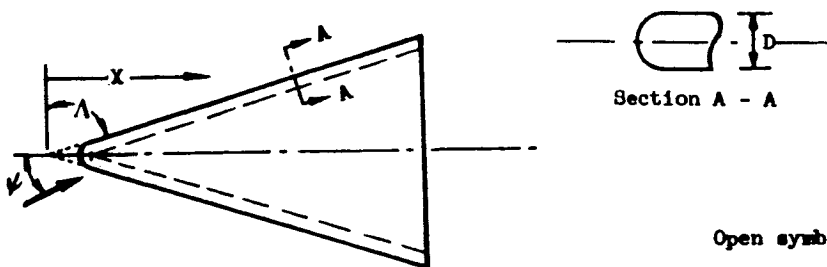


Figure 49. - Concluded.



Open symbols, $\psi = 0^\circ$
 Filled symbols, $\psi = 5^\circ$

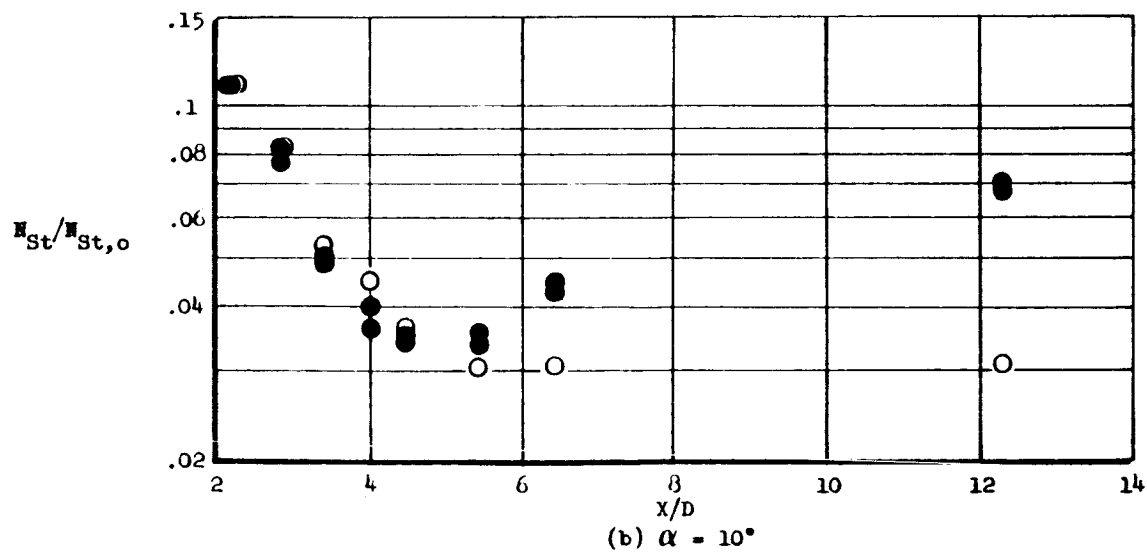
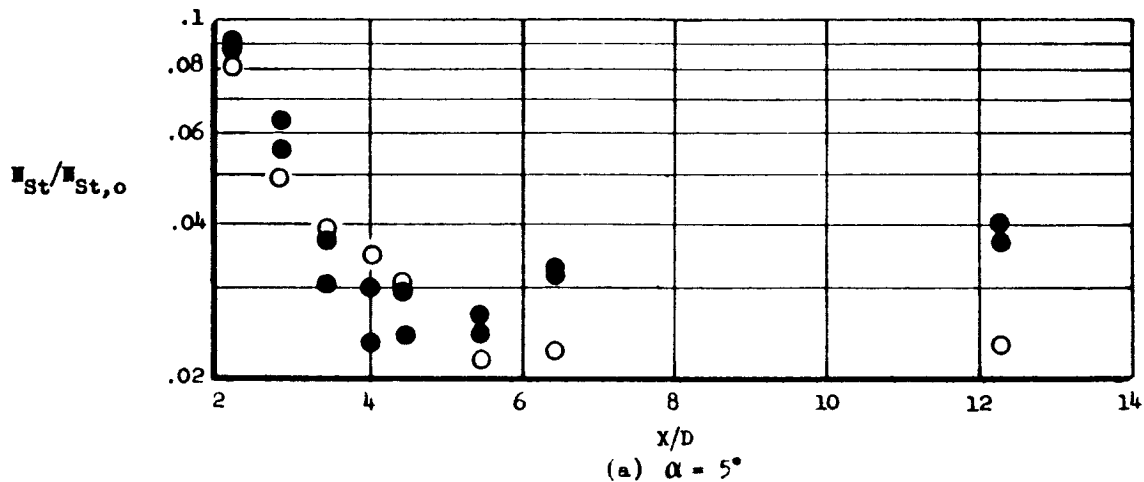
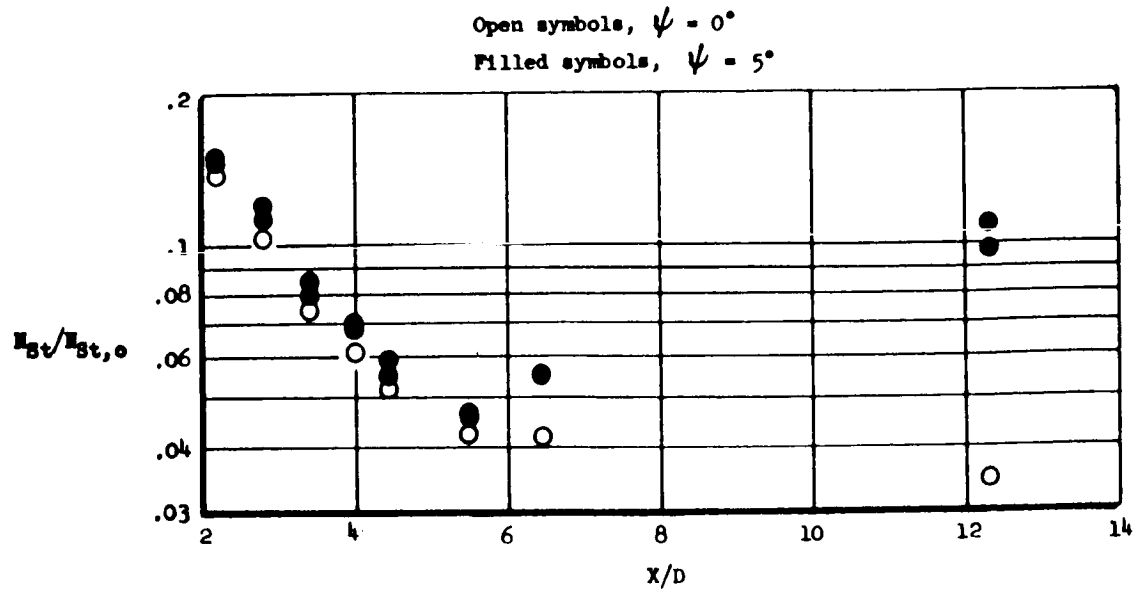
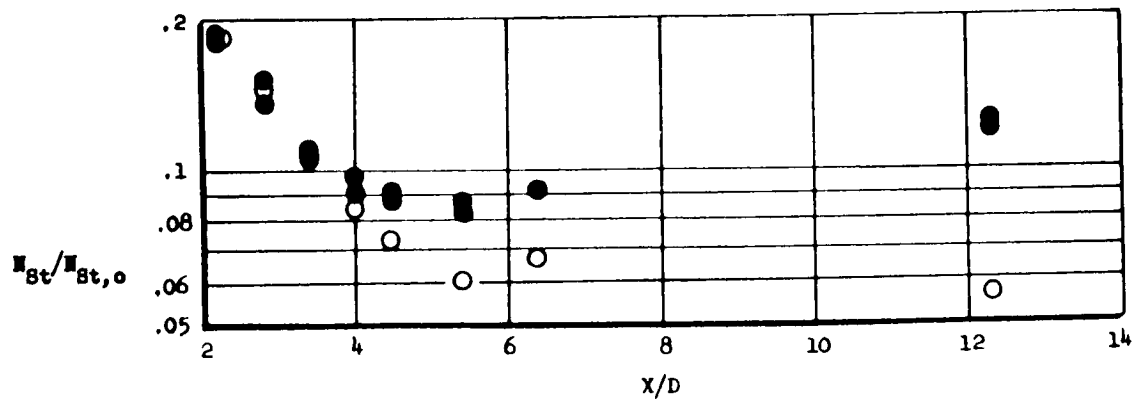


Figure 50.- Comparison of centerline heating data on a blunt-prow delta wing in laminar flow.

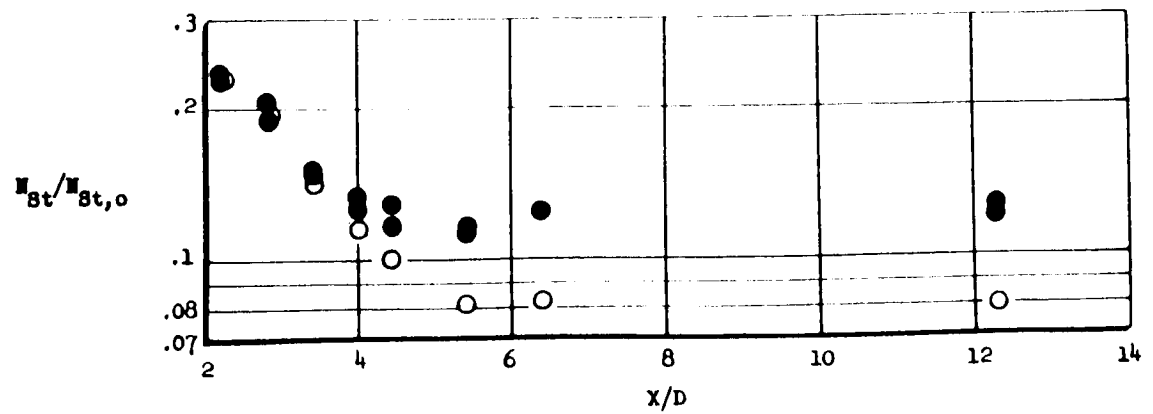
AD462M-1; $M_\infty = 8.08$; $N_{Re,D} = 8.38 \times 10^4$.



(c) $\alpha = 15^\circ$



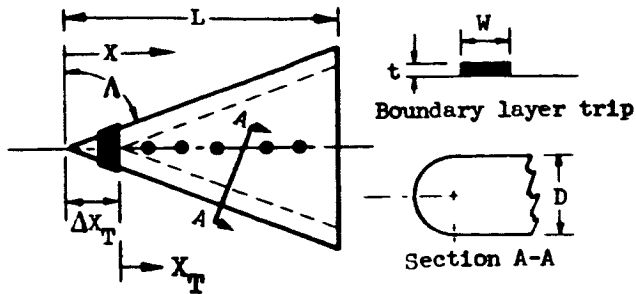
(d) $\alpha = 20^\circ$



(e) $\alpha = 25^\circ$

Figure 50.- Concluded.

——— 3-dim. $\rho_r \mu_r$ theory based on X .
 - - - 3-dim. $\rho_r \mu_r$ theory based on X_T at $\Delta X_T/D = 3$.
 - · - 2-dim. $\rho_r \mu_r$ theory based on X_T at $\Delta X_T/D = 3$.



	$N_{Re,D}$	L/D	$\Delta X_T/D$	t/D	W/D
▲	28.5×10^4	16.2	3.0	.06	.301
●	34.8×10^4	16.2	3.0	.06	.301
■	77.2×10^4	7.2	2.3	.022	.110
■	77.2×10^4	7.2	1.35	.022	1.110

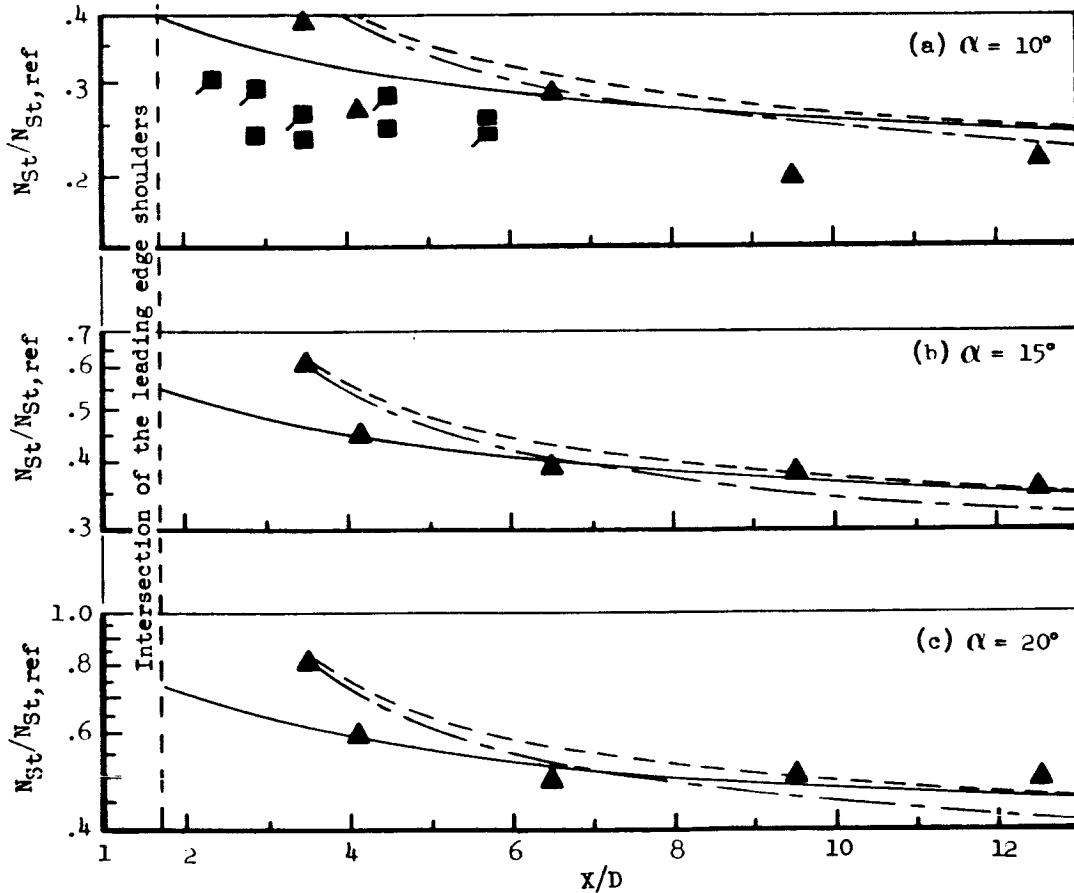


Figure 51.- Turbulent heating data on the centerlines of sharp-prow delta wings. AD461M-1; $M_\infty = 7.04$; $\Lambda = 73^\circ$.

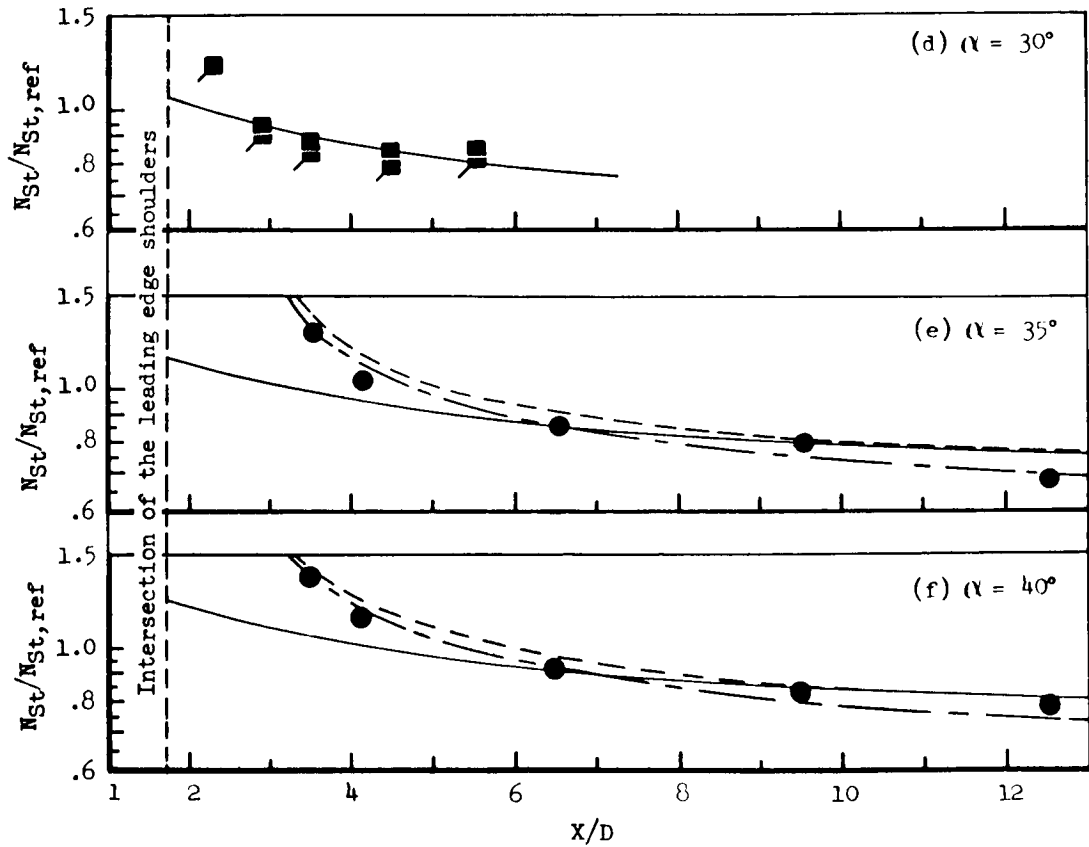
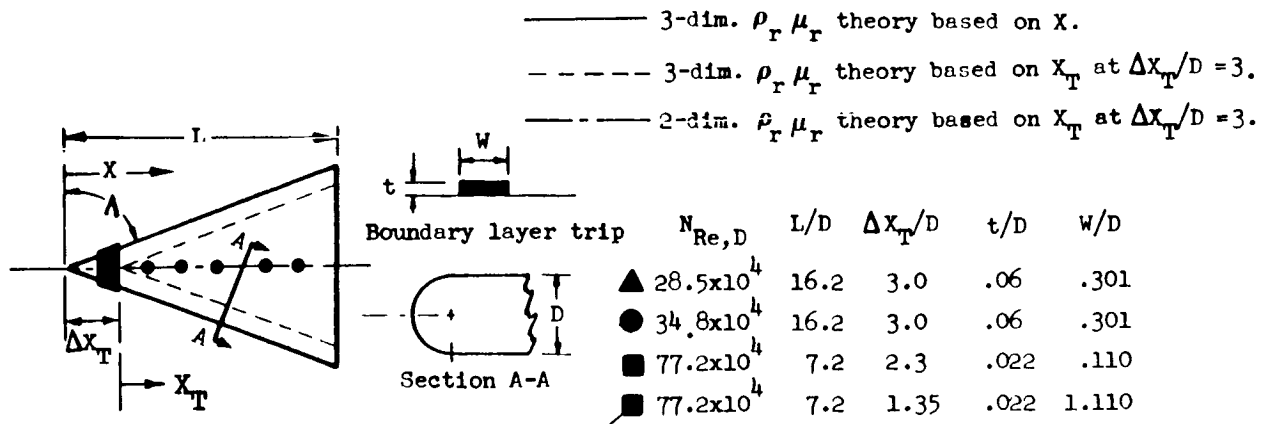
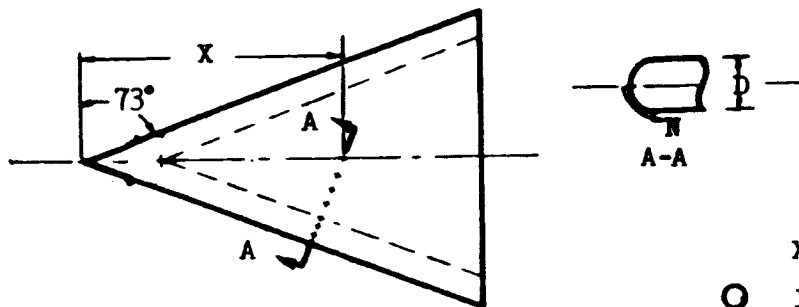
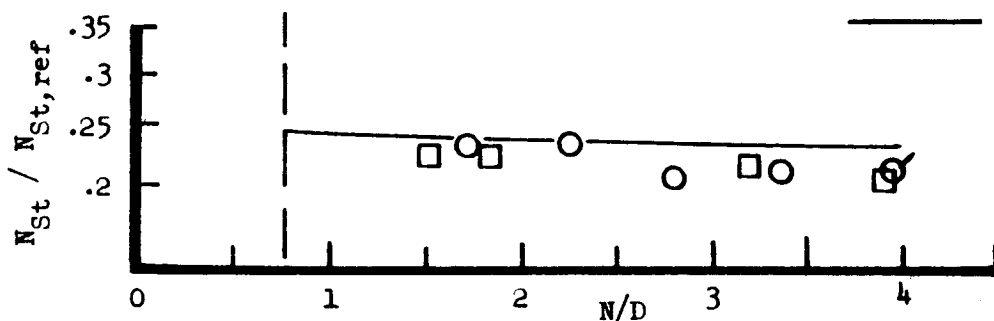


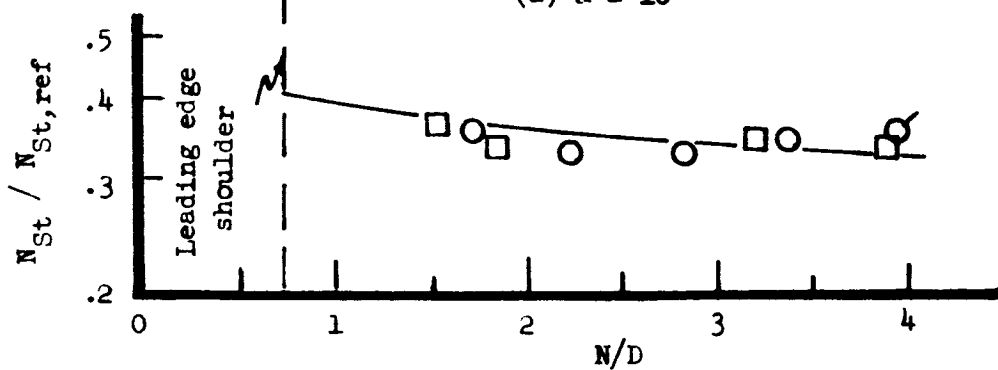
Figure 51.- Concluded.



X/D
 ○ 12.55
 □ 14.9
 Flagged symbols
 denote wing
 centerline
 — Eq. (14)
 $X/D = 12.55$



(a) $\alpha = 10^\circ$



(b) $\alpha = 15^\circ$

Figure 52.- Lower surface heating on a sharp-prow delta wing in turbulent flow. AD461M-1; $M_\infty = 7.0$; $N_{Re,D} = 28.5 \times 10^4$

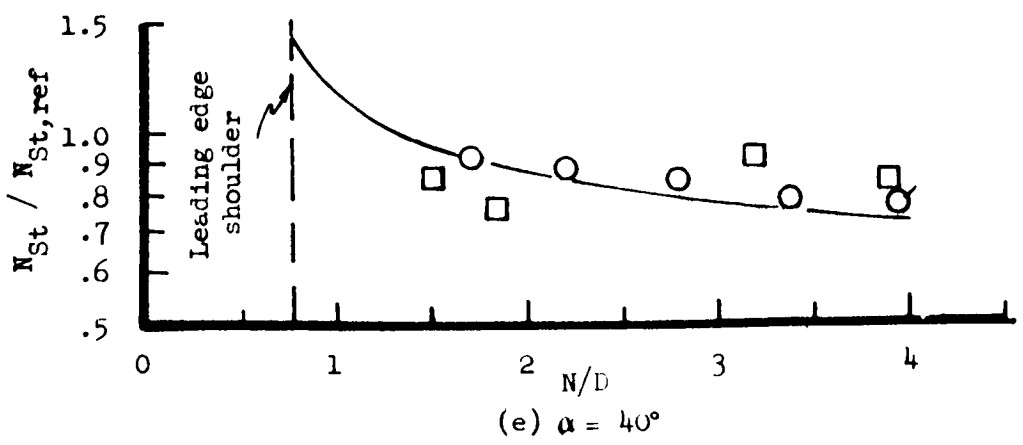
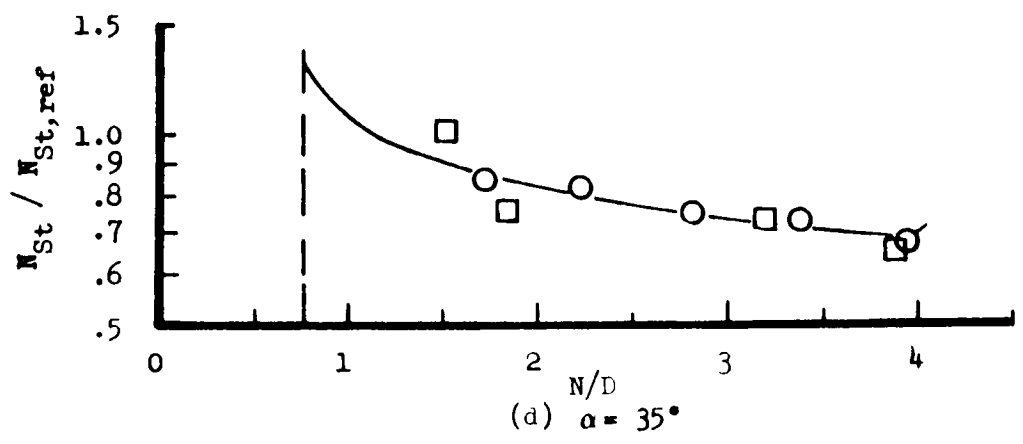
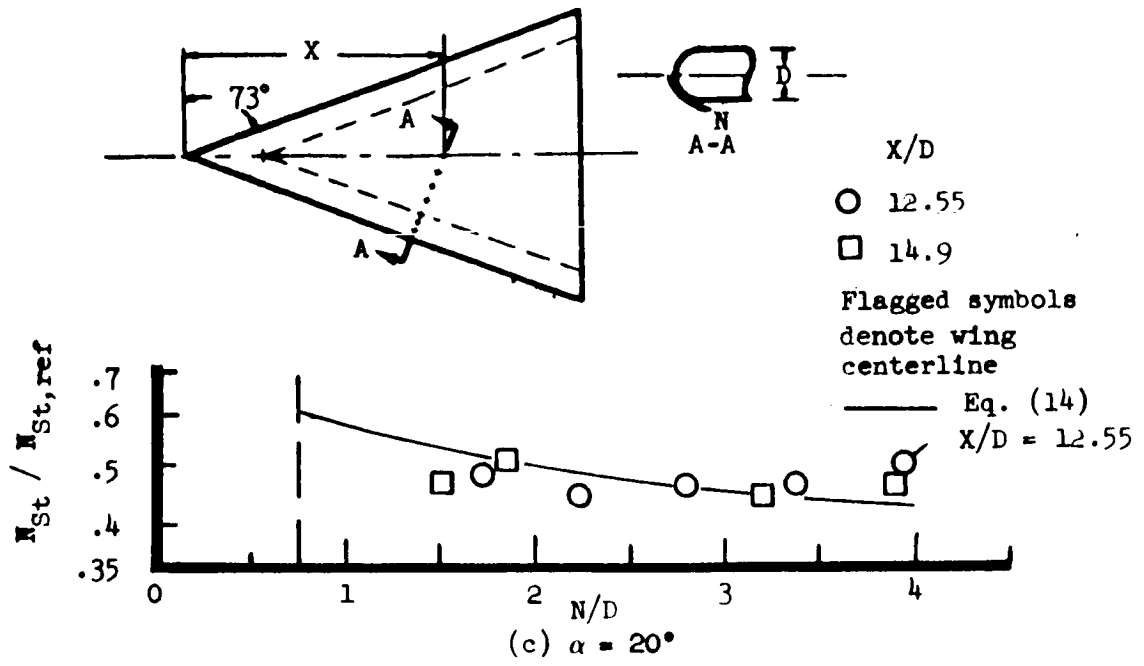
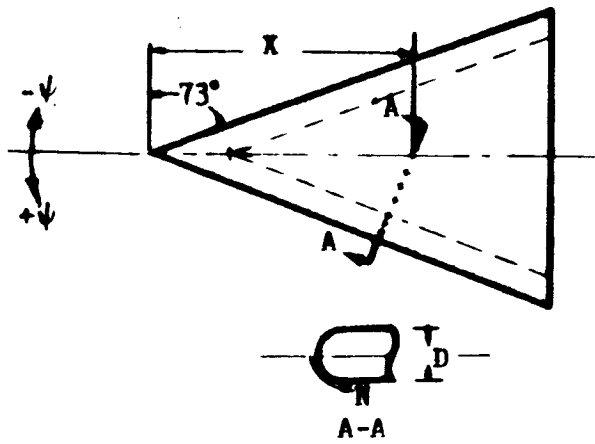
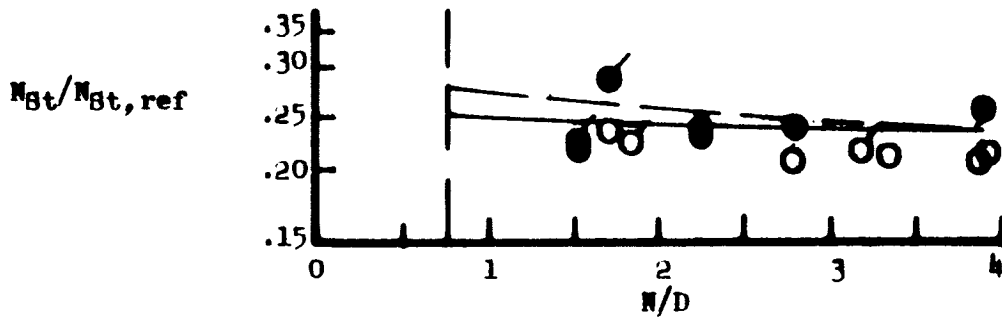


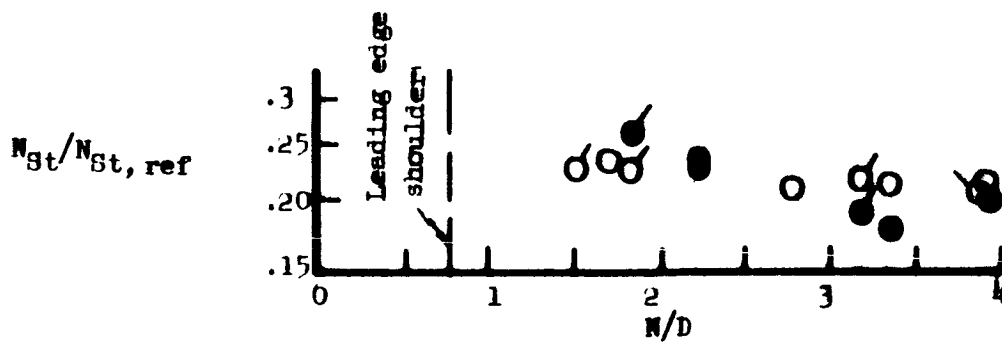
Figure 52.- Concluded.



- | | |
|-------|----------------------------|
| | x/D |
| ○ | 12.55 |
| ⊙ | 14.89 |
| ● | $\psi = +10^\circ$ |
| ○ | $\psi = 0^\circ$ |
| — | Theory, $\psi = 0^\circ$ |
| - - - | Theory, $\psi = +10^\circ$ |

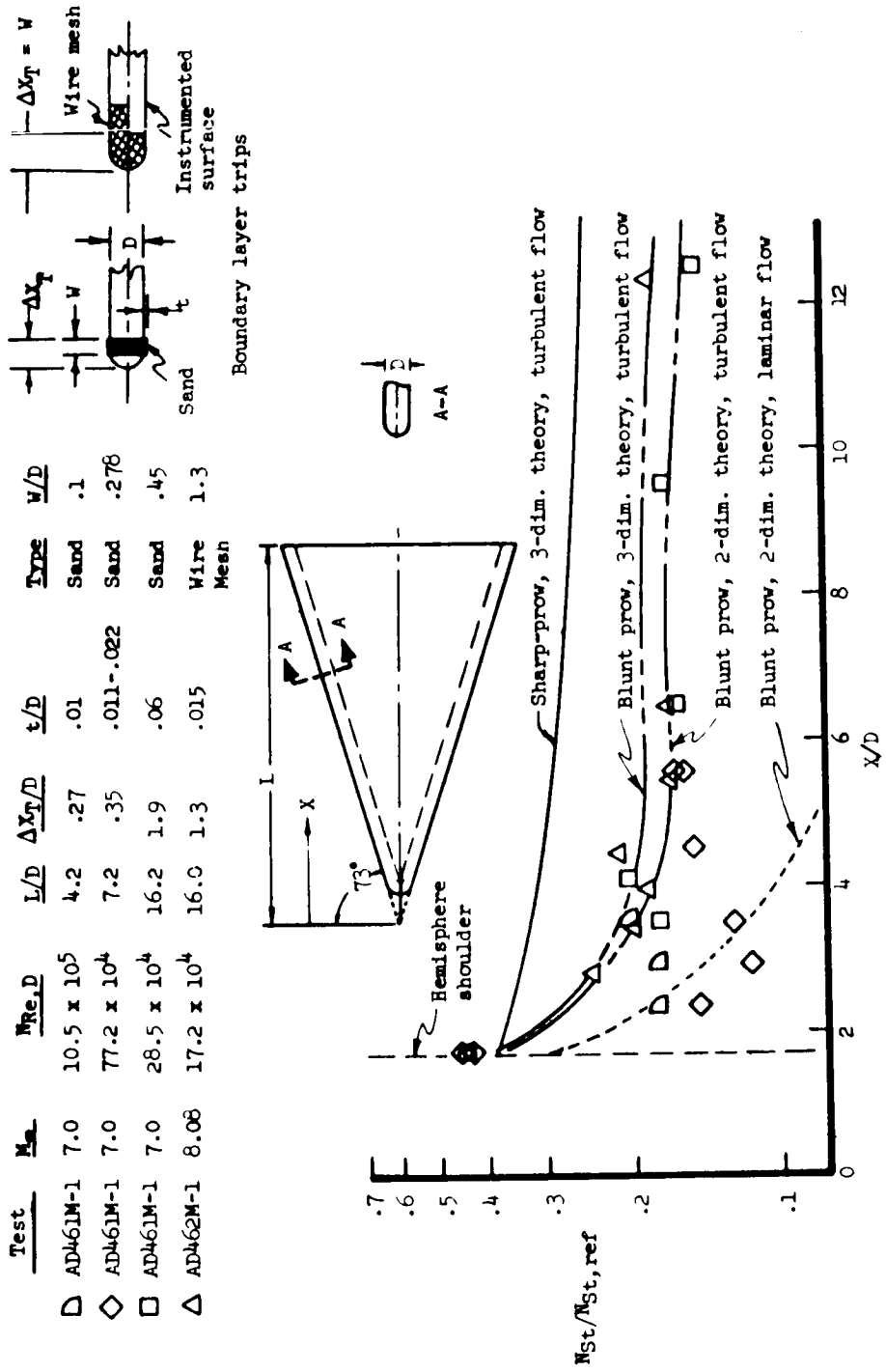


(a) $\psi = +10^\circ$



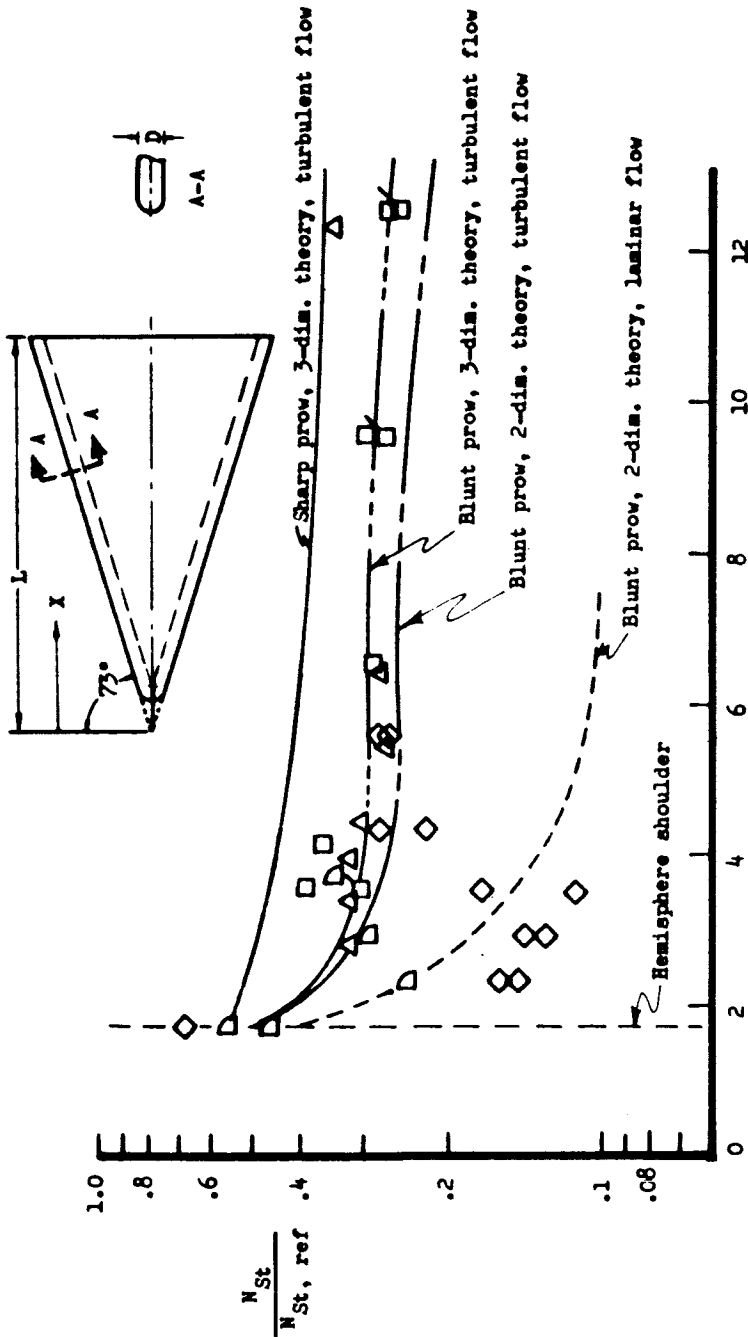
(b) $\psi = -10^\circ$

Figure 53.- Effect of yaw on turbulent heating data on a sharp-prow delta wing, AD461M-1; $M_\infty = 7.0$; $\alpha = 10^\circ$; $N_{Re,D} = 28.5 \times 10^4$

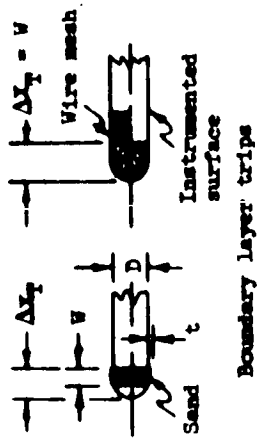


(a) $\alpha = 10^\circ$
 Figure 54.- Turbulent heating on the centerlines of blunt-prow delta wings.

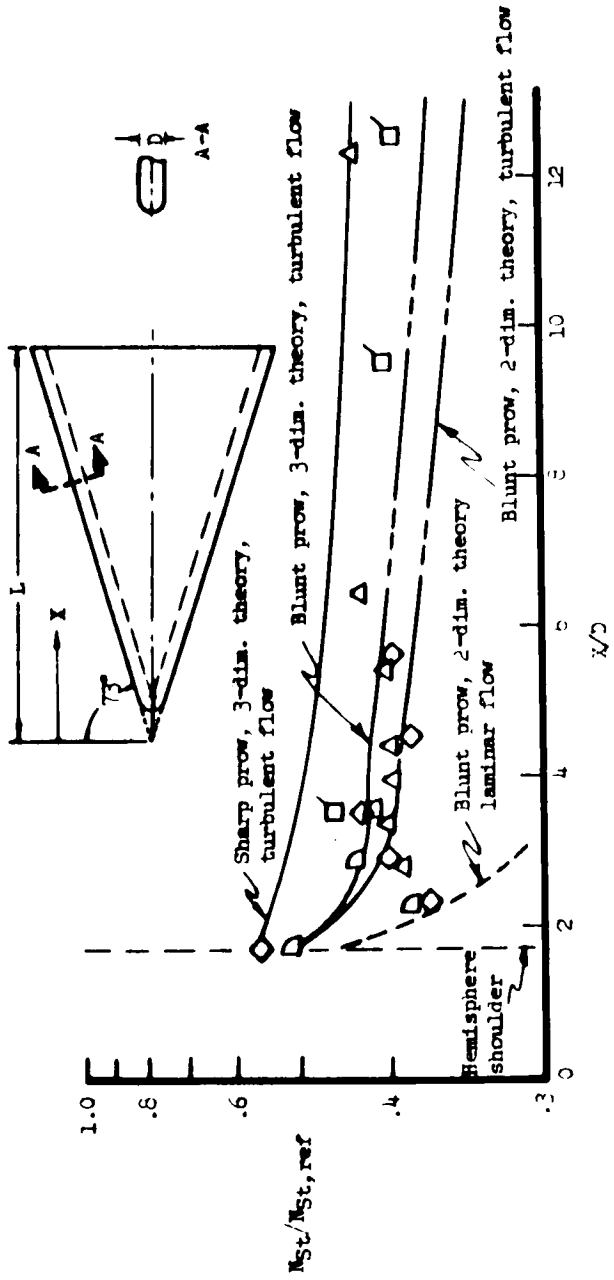
Test	M_{∞}	$N_{Re, D}$	L/D	$\Delta X_T/D$	t/D	Type	W/D
□	AD461M-1	7.0	10.5×10^5	4.2	.27	Sand	.1
◇	AD461M-1	7.0	77.2×10^4	7.2	.35	Sand	.278
□	AD461M-1	7.0	34.8×10^4	16.2	1.8	Sand	.301
□	AD461M-1	7.0	28.5×10^4	16.2	1.9	Sand	.45
△	AD462M-1	8.08	17.2×10^4	16.0	1.3	Wire mesh	1.30



(b) $\alpha = 15^\circ$
Figure 54.- Continued.

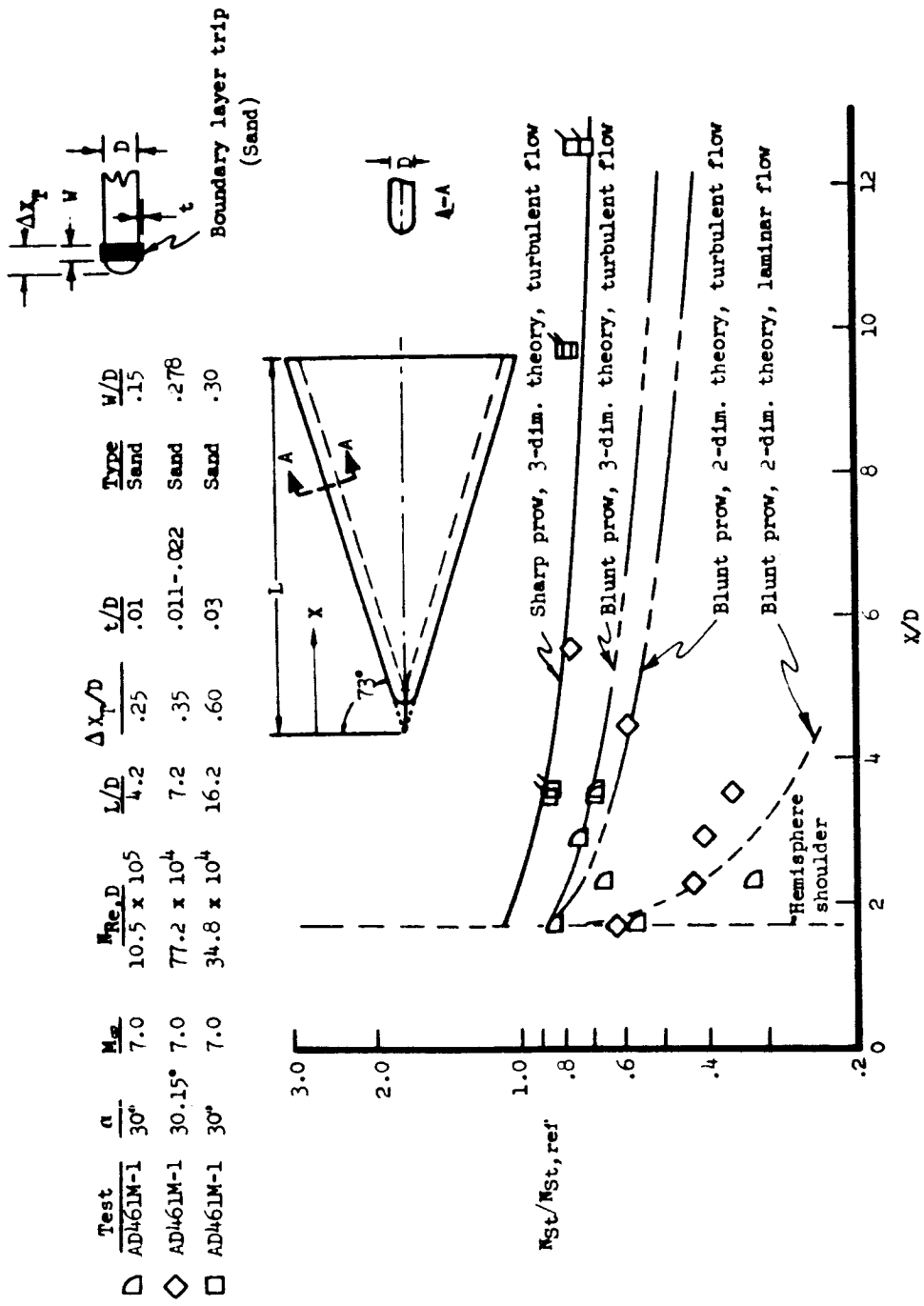


Test	α	M_p	$\frac{P_{st, D}}{M_p D}$	L/D	$\frac{\Delta Y/D}{L/D}$	t/D	Type	W/D
AD463M-1	20°	7.0	10.5×10^5	4.2	.25	.01	Sand	.15
AD463M-1	20°	7.0	77.2×10^4	7.2	.35	.011-.022	Sand	.278
AD461M-1	20°	7.0	34.8×10^4	16.2	.60	.03	Sand	.30
AD461M-1	20°	7.0	17.2×10^4	16.0	1.3	.015	Wire Mesh	1.30



(c) $\alpha = 20^\circ$

Figure 54.- Continued.



(d) $\alpha = 30^\circ$
 Figure 54.- Concluded.

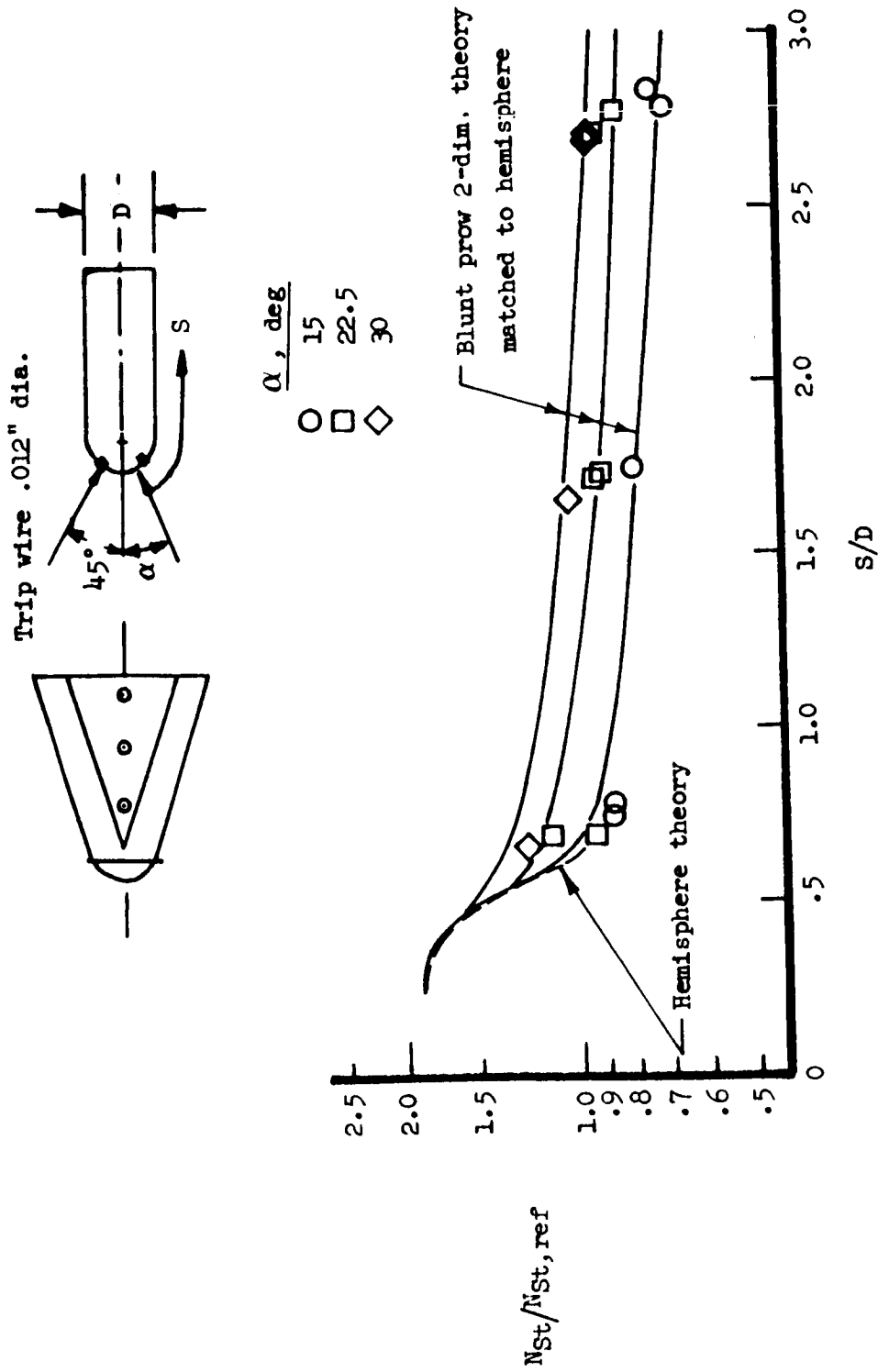


Figure 55.- Turbulent heating on a blunt-prov delta wing in high enthalpy flow.
 AD485M-1; $M_\infty = 2.4$; $i_0 = 3865$ btu/lb; $P_\infty = 203$ psia; $H_\infty = 2257$ btu/lb

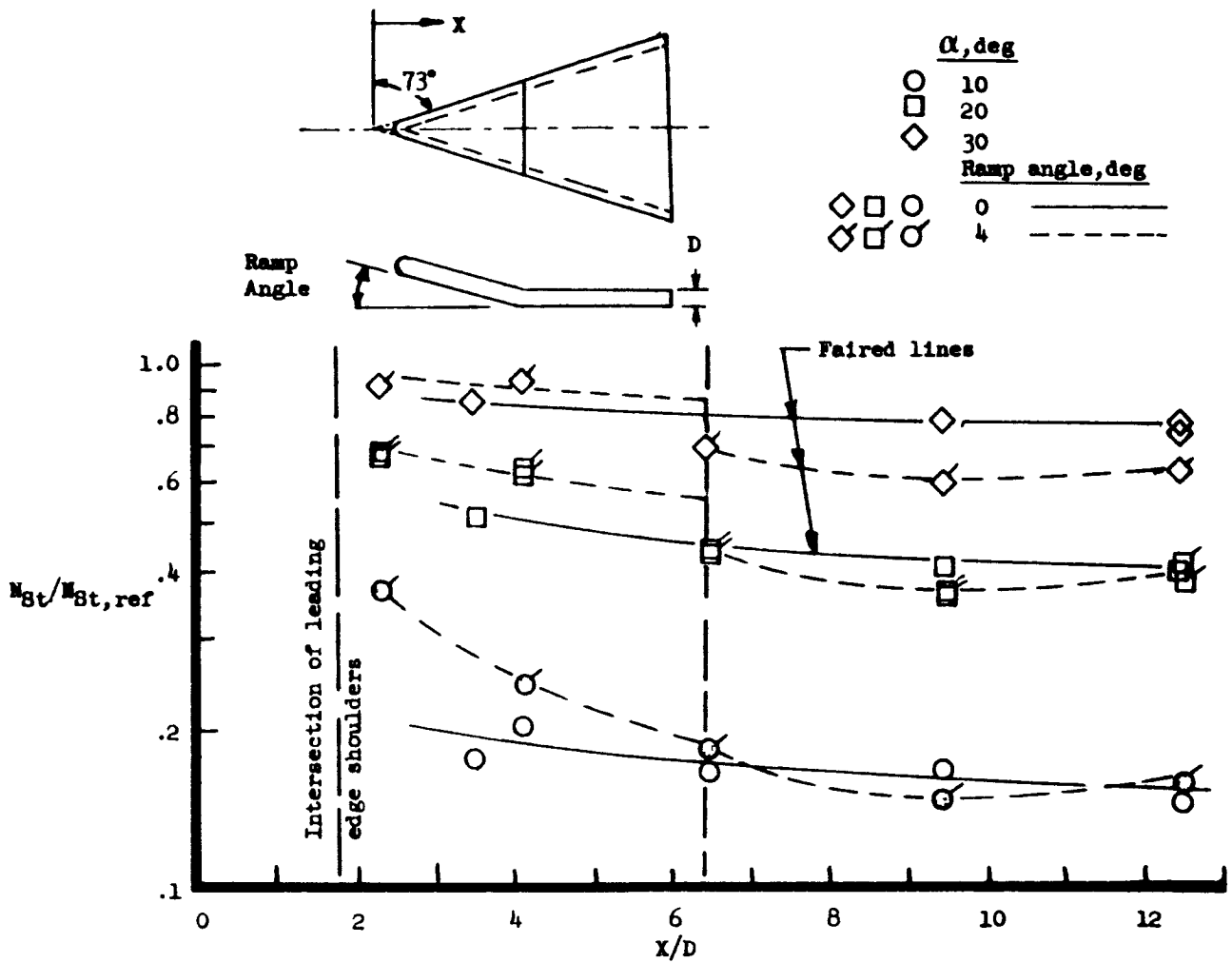


Figure 56.- Effect of ramp angle on a delta wing centerline heating.
 AD461M-1; $M_\infty = 7.0$; $N_{Re,D} = 28.5 \times 10^4$.

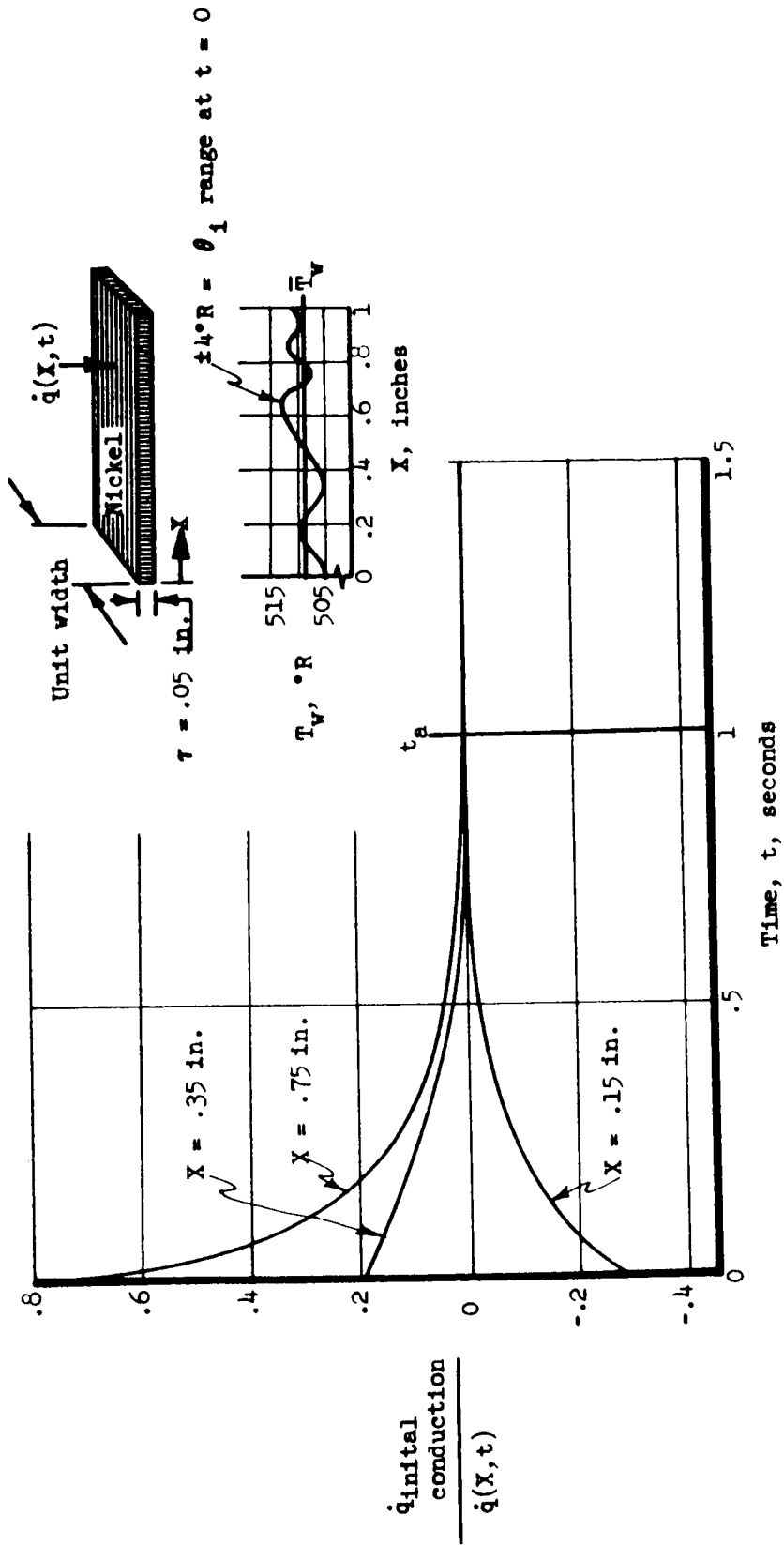


Figure 57.- Computer study of initial conduction.

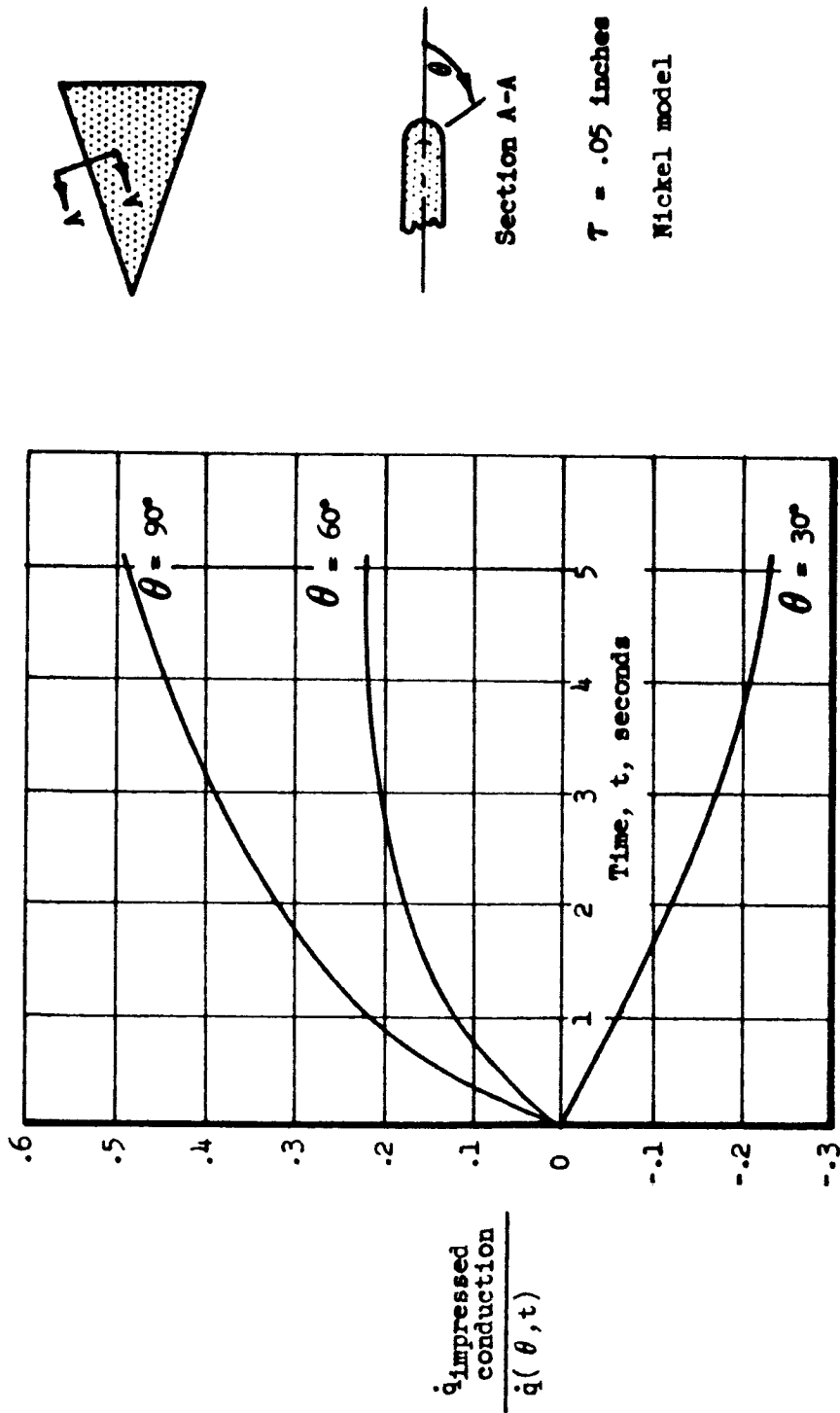


Figure 58.- Computer study of impressed conduction.

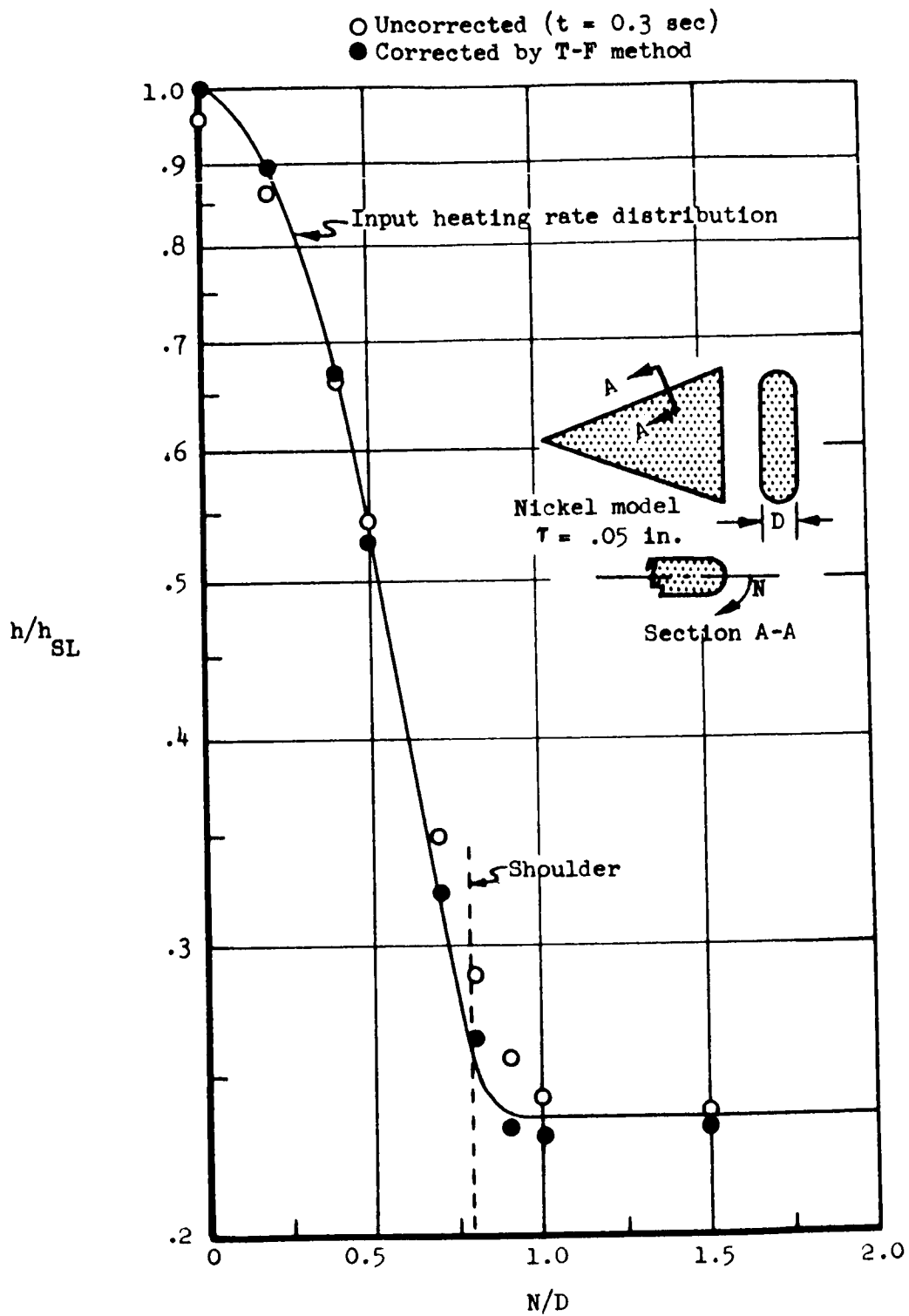


Figure 59.- Conduction corrections to computer temperature history.

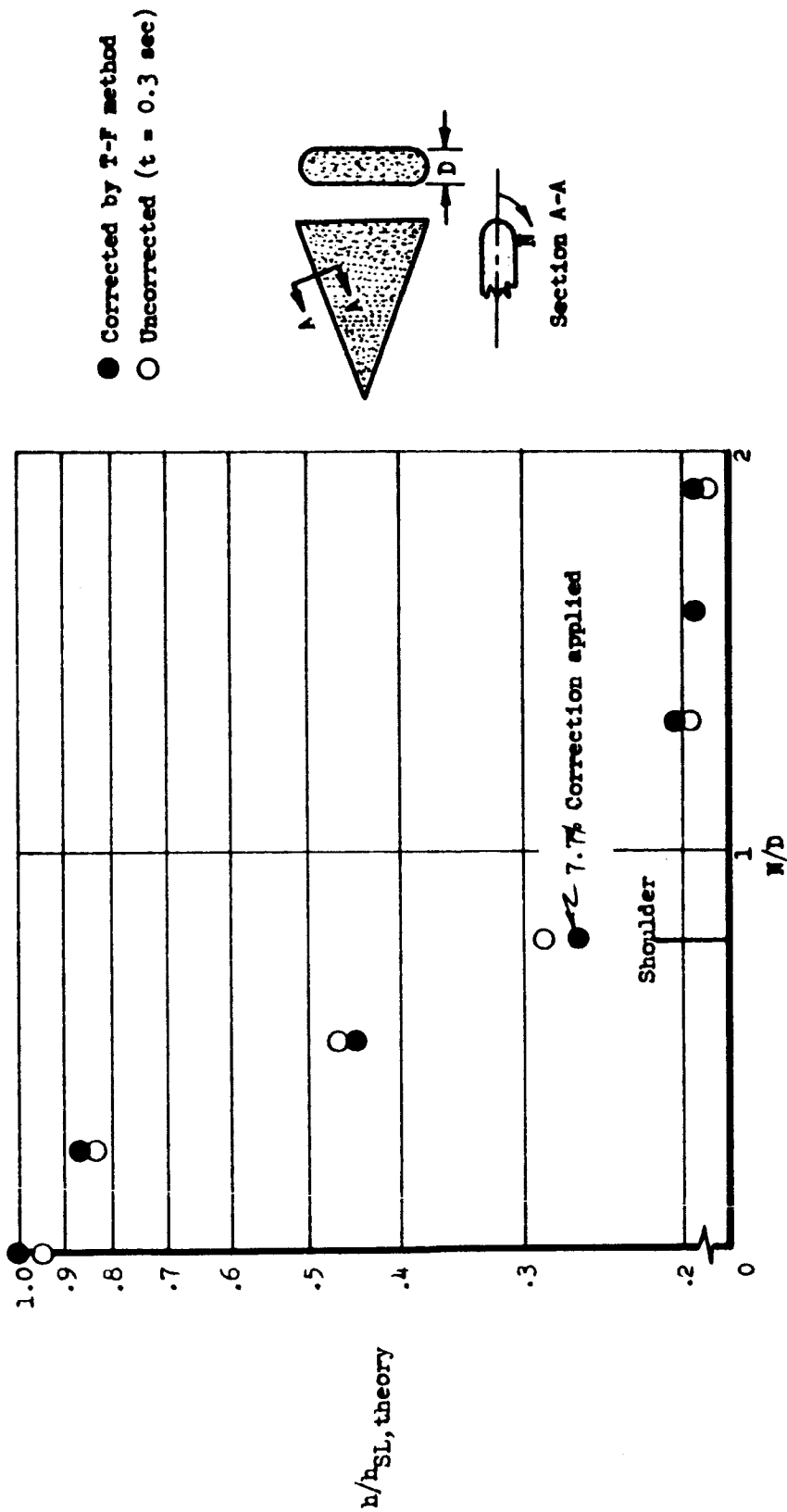


Figure 60.- Conduction corrections to experimental temperature history. AD46LM-1; $\Lambda = 73^\circ$; $\alpha = 0^\circ$; $\psi = 0^\circ$; $M_{\infty} = 6.08$

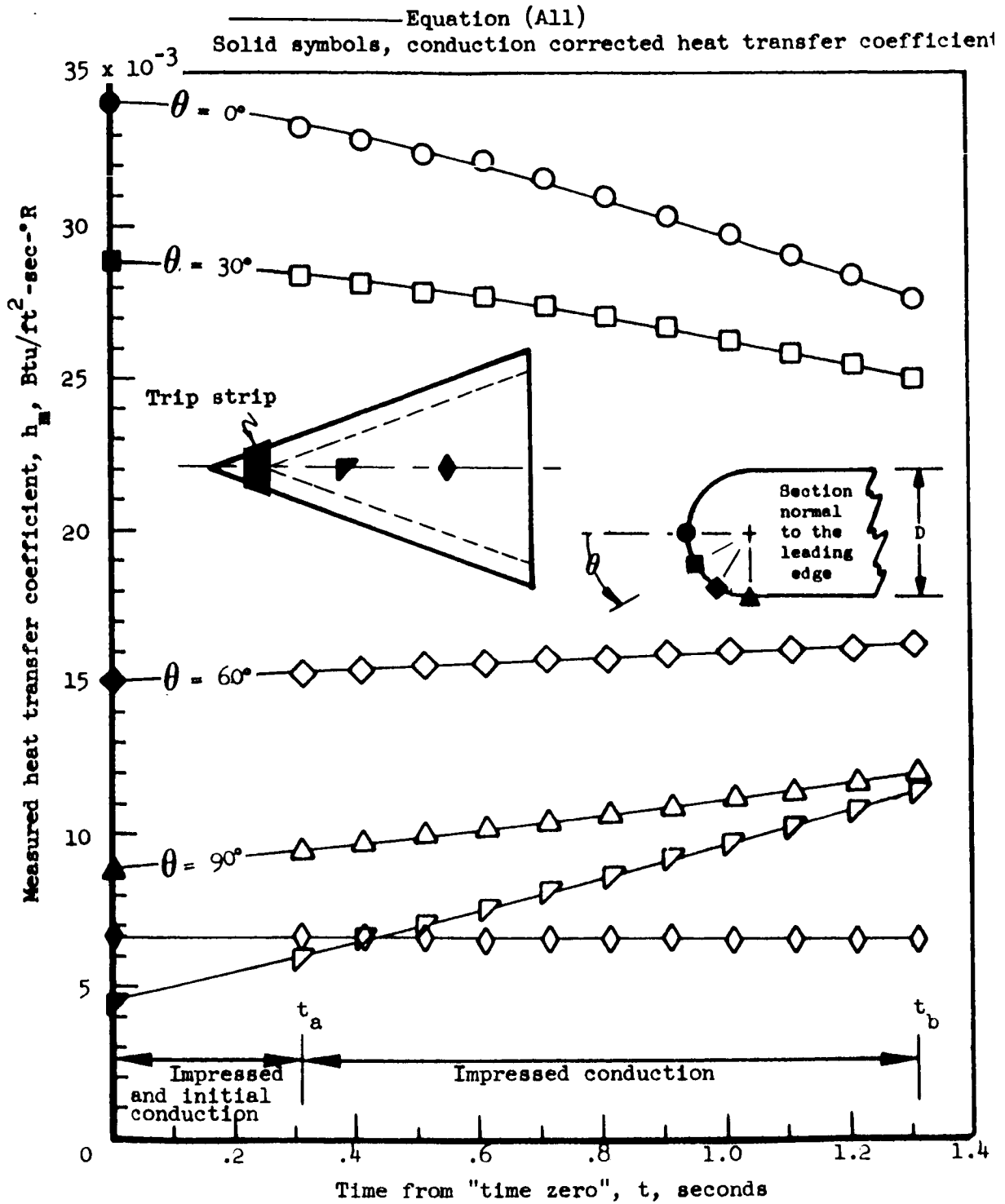
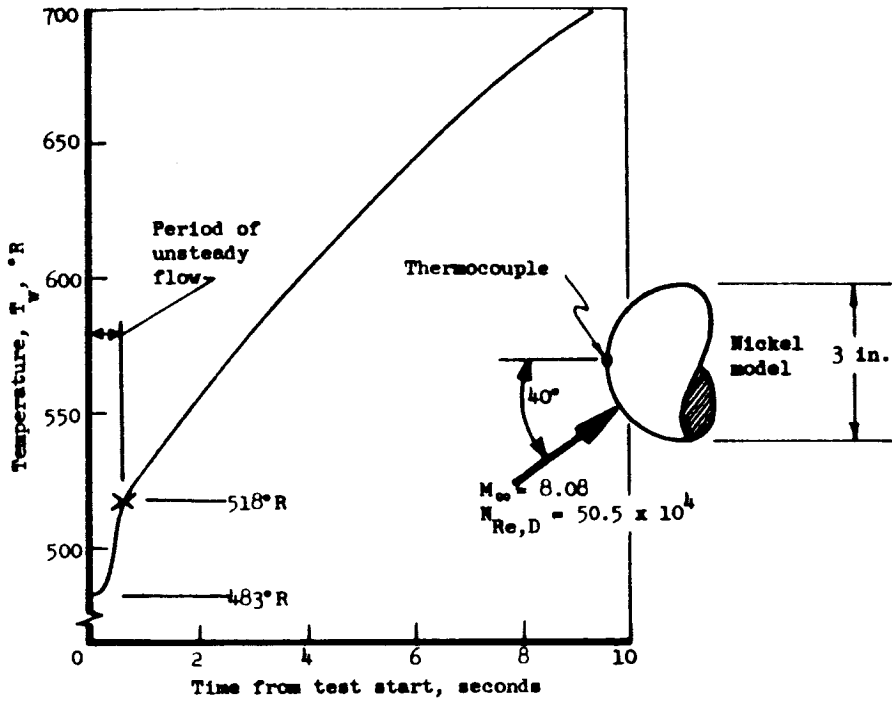
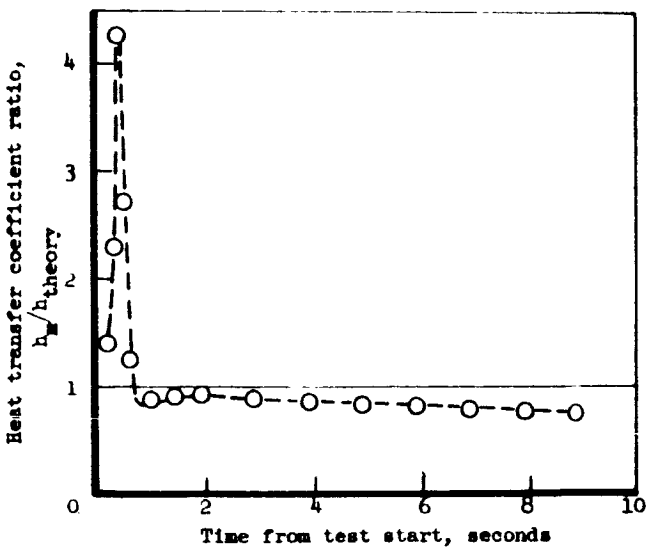


Figure 61.- Typical T-F method conduction correction. AD461M-1;
 $\Lambda = 73^\circ$; $\alpha = 0^\circ$; $\psi = 0^\circ$; $M_\infty = 6.08$.

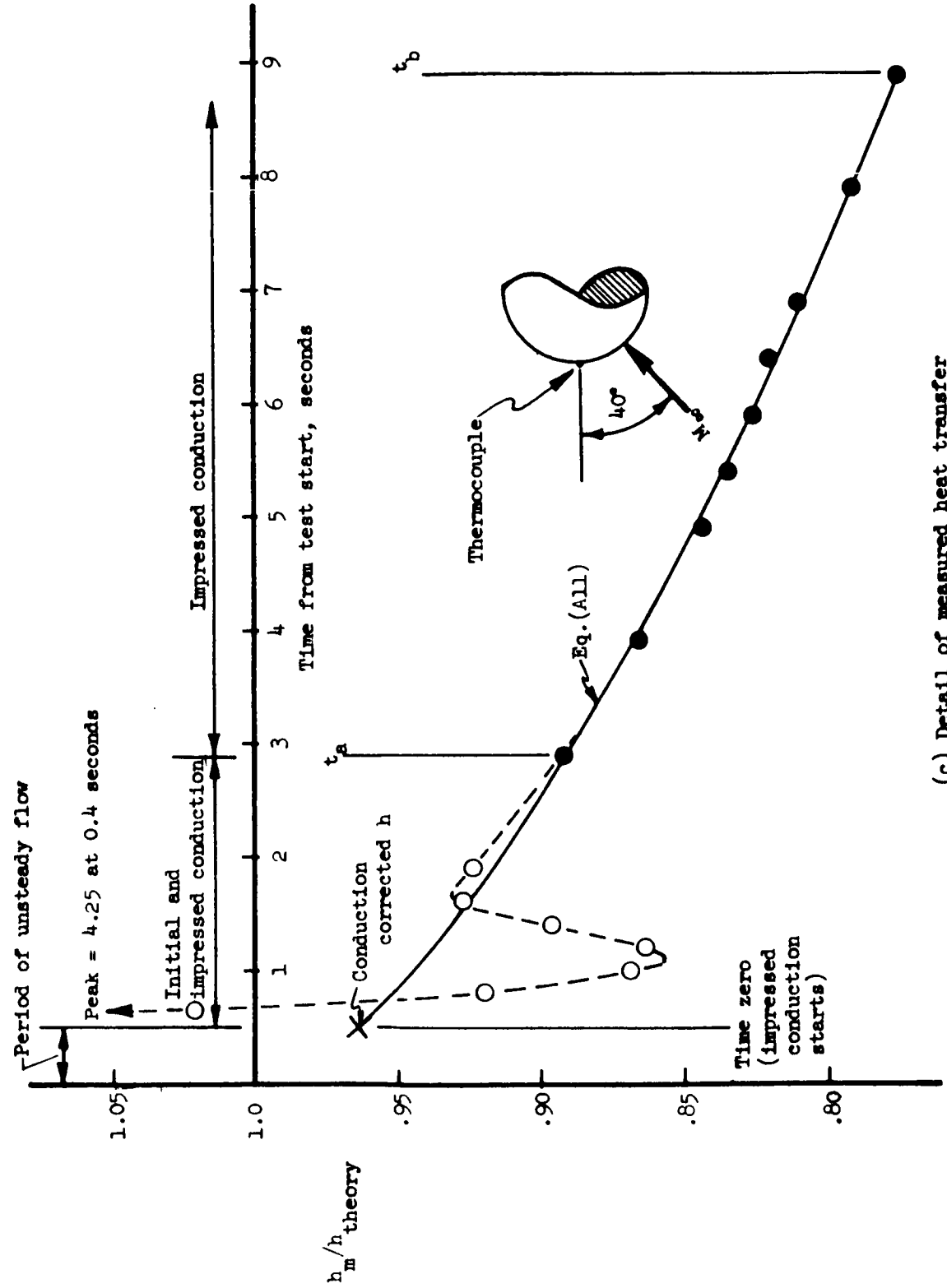


(a) Temperature history



(b) Measured heat transfer coefficient history

Figure 62.- Example of severe initial conduction on a nickel model.



(c) Detail of measured heat transfer coefficient history

Figure 62.- Concluded.

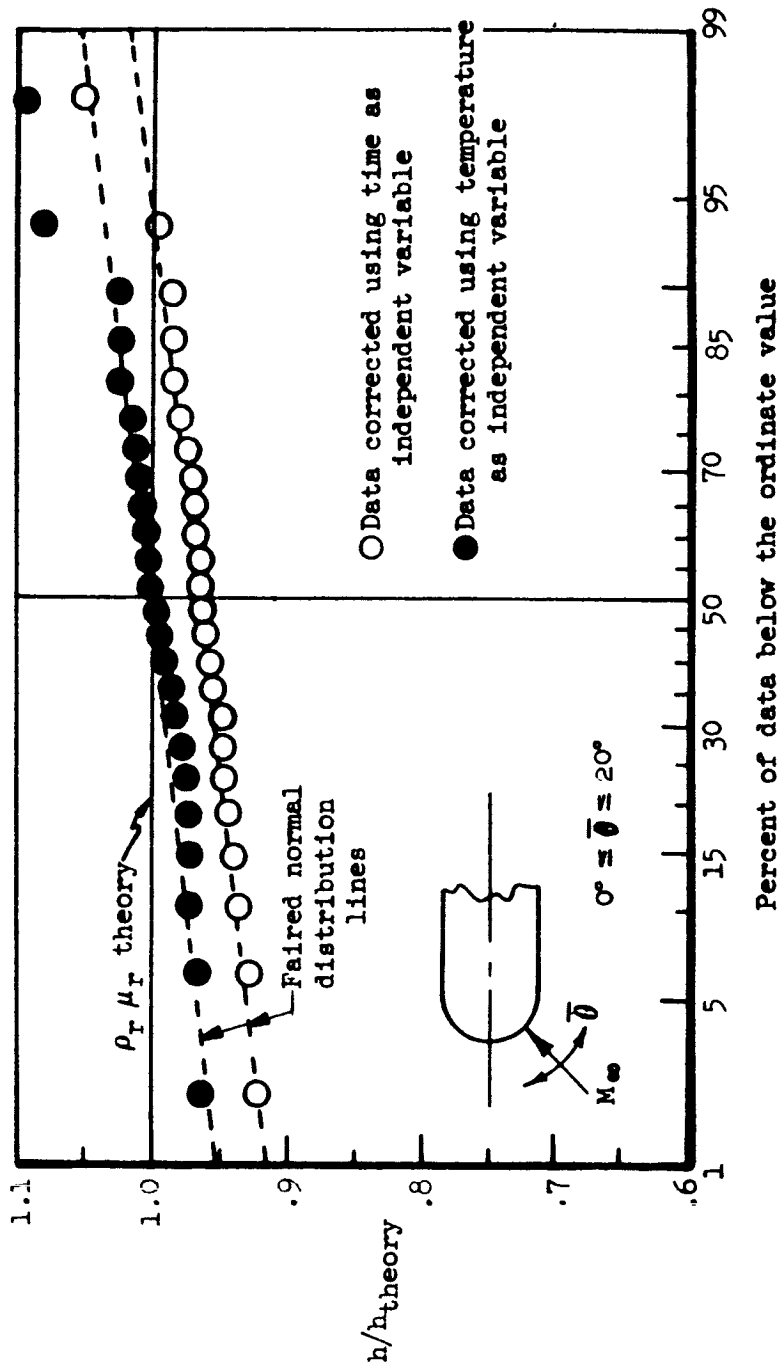


Figure 63.- Variations of the T-F method;
 $M_\infty = 8.08$; $N_{Re,D} = 50.5 \times 10^4$.

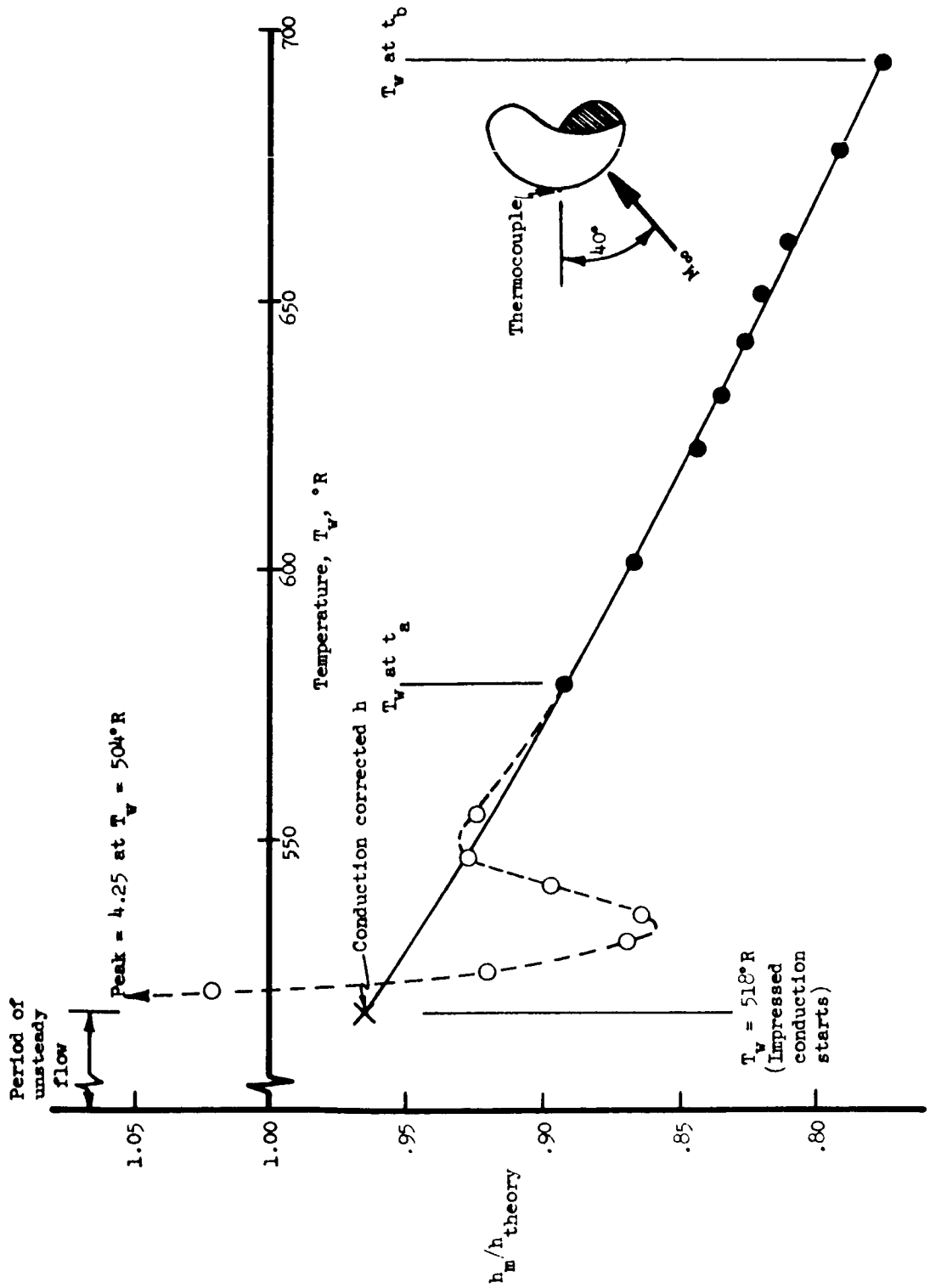


Figure 64.- Measured heat transfer coefficient versus temperature.

	□	○	◇
Reference	26	33	34
Prandtl Number	Constant	Constant	Variable
Specific Heat	Constant	Constant	Variable
$\rho \mu$ Product	Constant	Variable	Variable

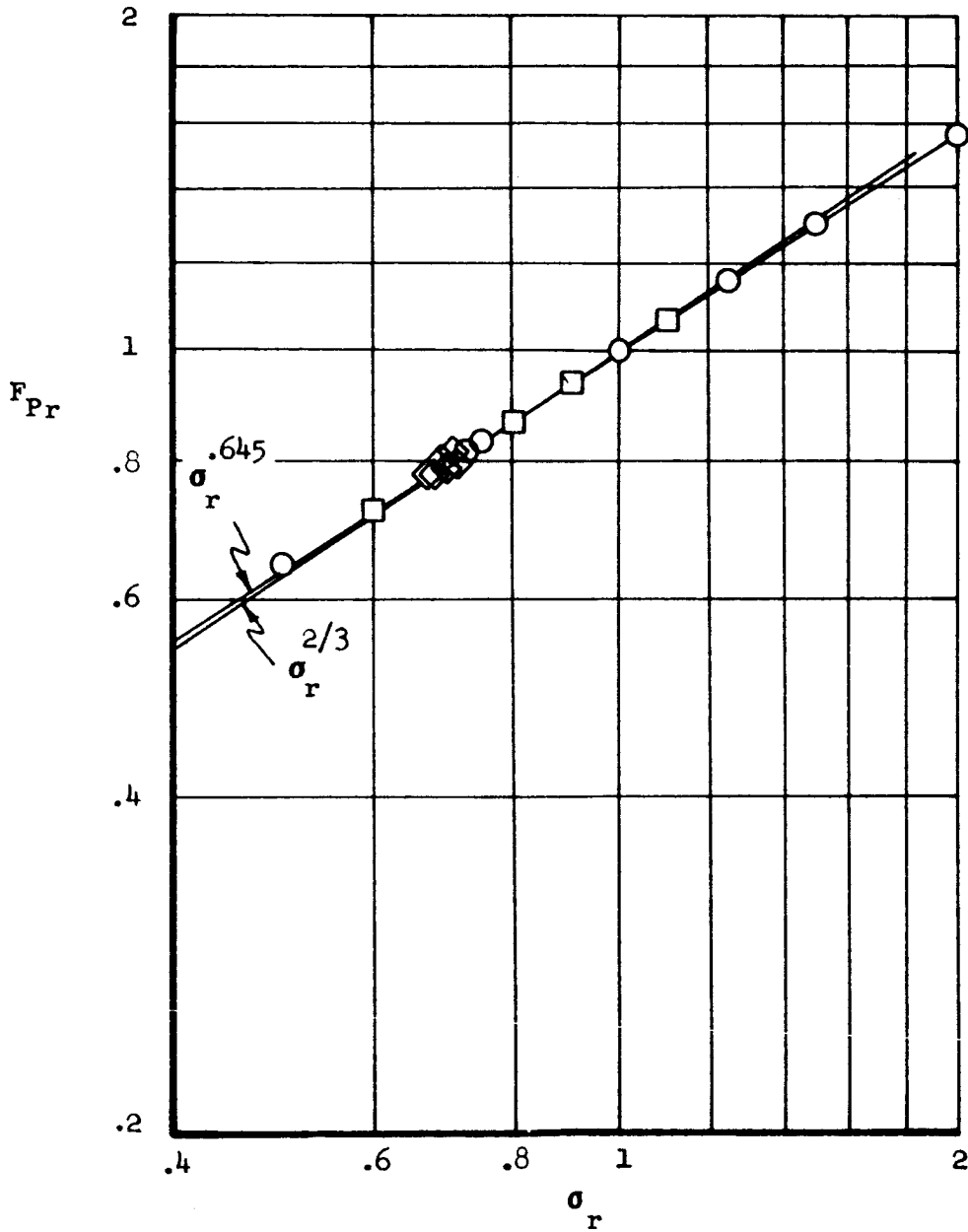


Figure 65.- Effect of Prandtl number on Reynolds analogy factor.

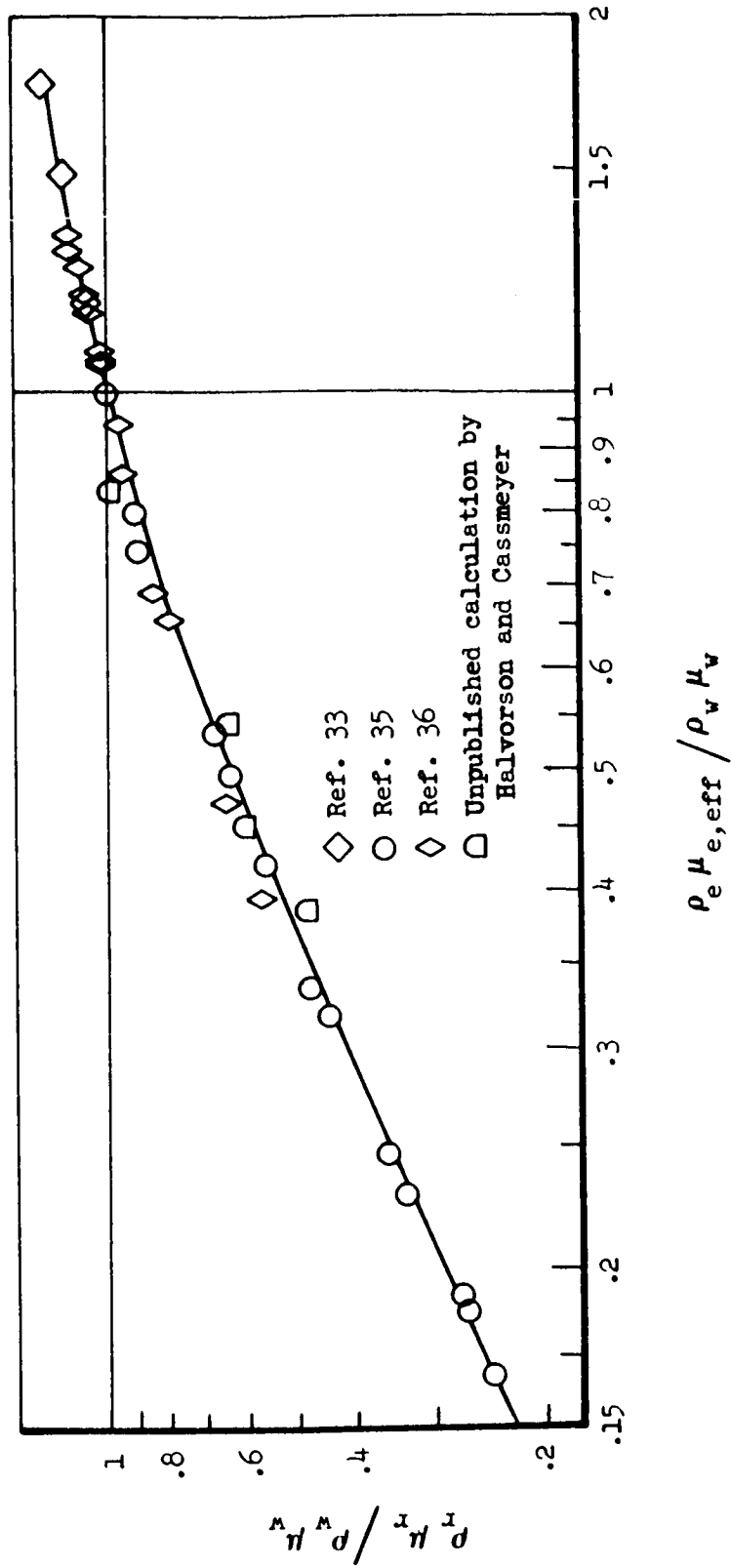
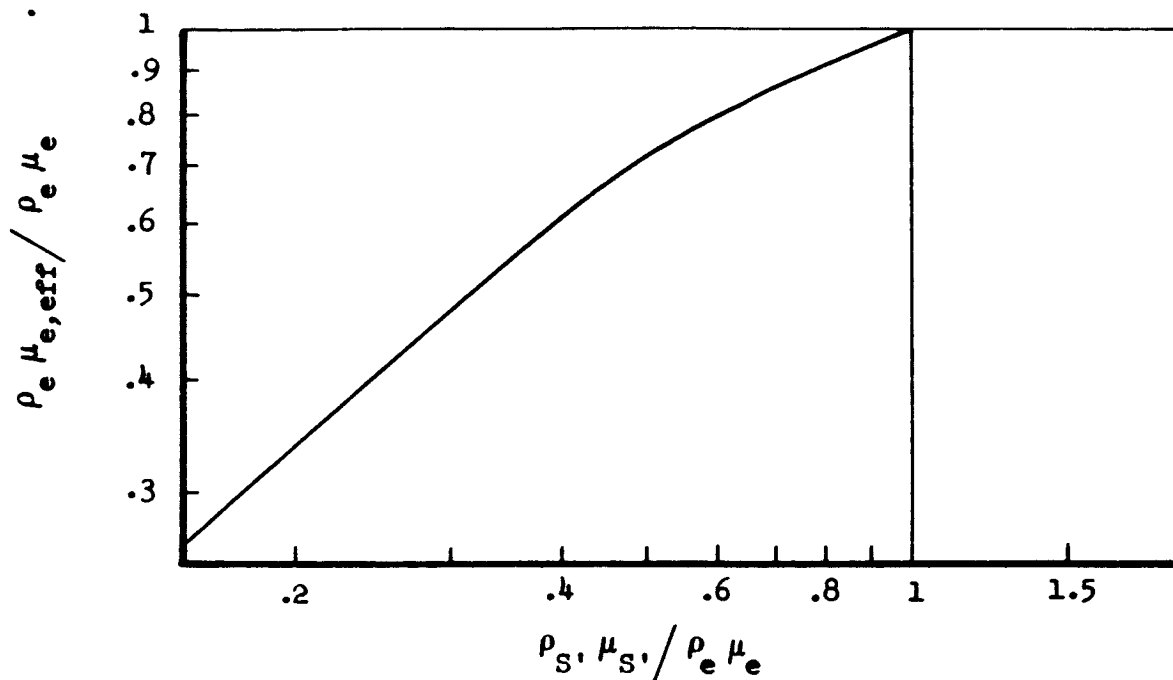
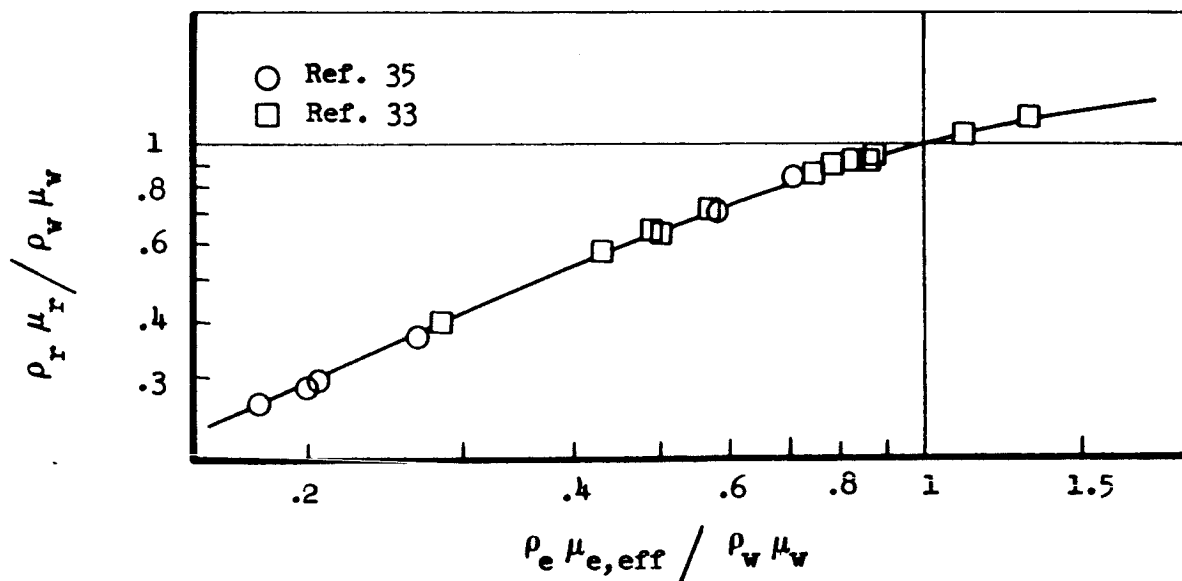


Figure 66.- Correlation of reference density-viscosity product. $M = 0$



(a) Effective density-viscosity product as a function of boundary layer edge and stagnation enthalpy conditions.



(b) Reference density-viscosity product as a function of effective edge values and wall conditions. $M > 0$

Figure 67.- Density-viscosity correlations.

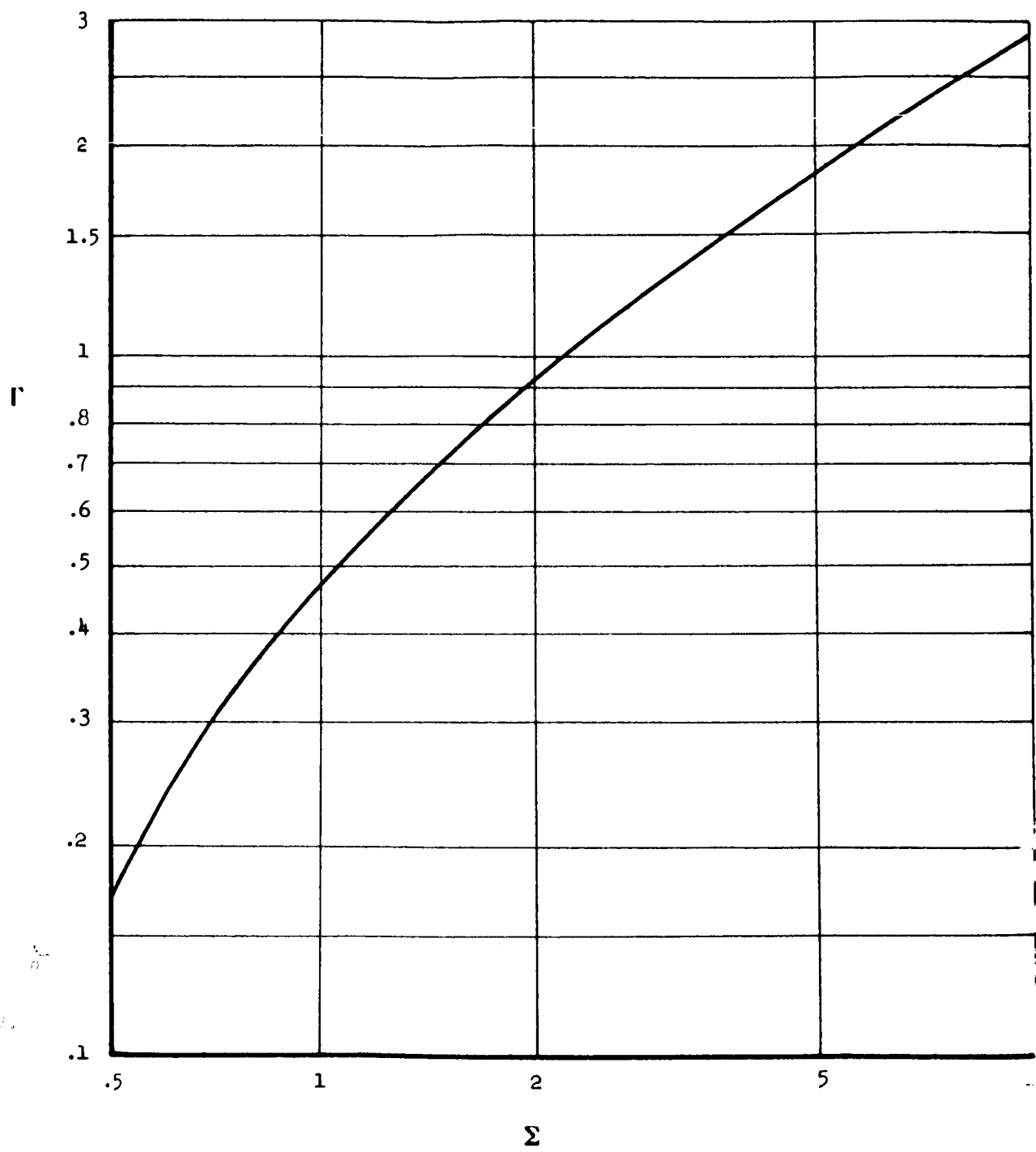


Figure 68.- Pressure gradient effect correlation parameters.

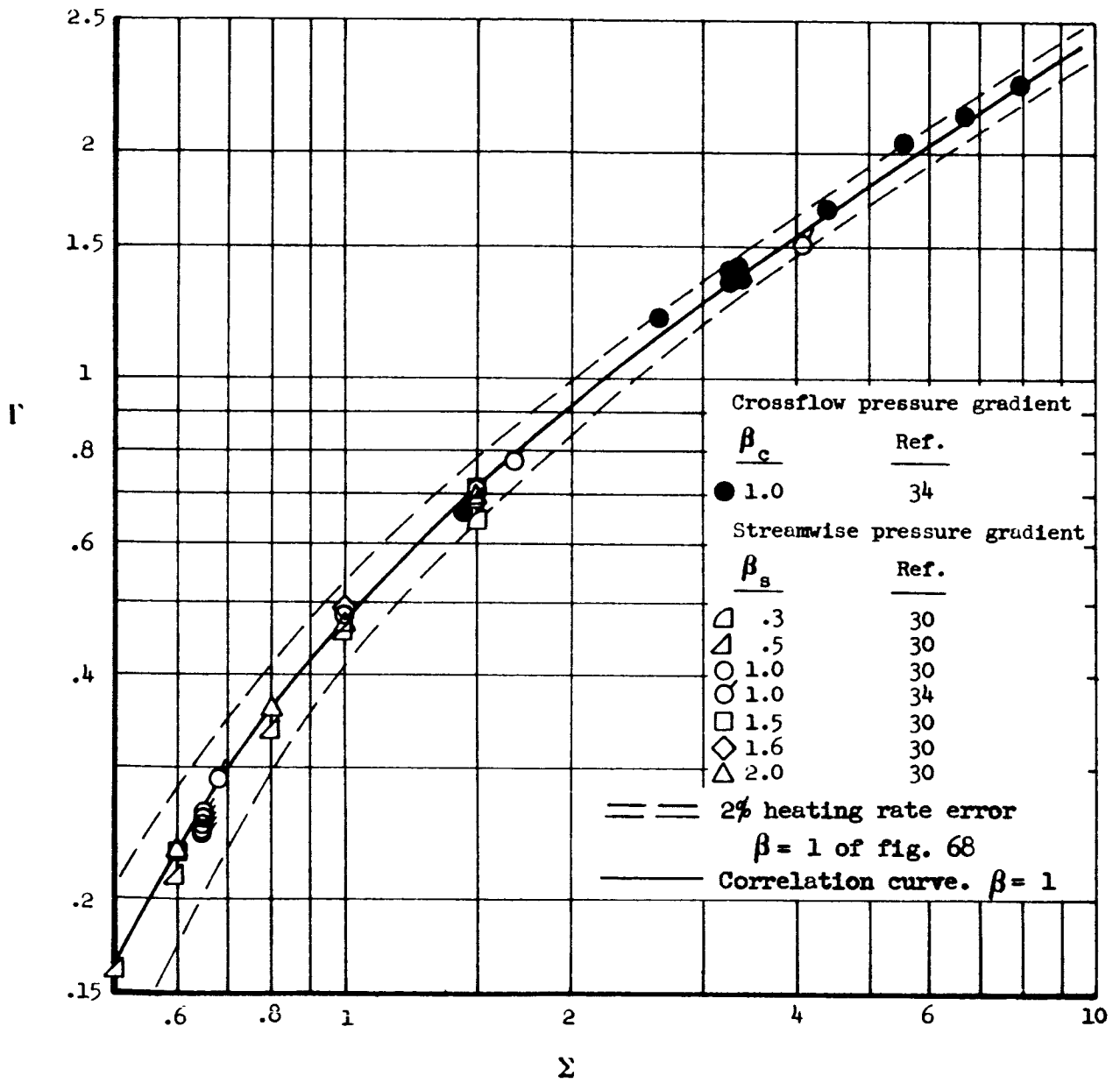


Figure 69.- Pressure-gradient effect correlation compared with exact solutions.

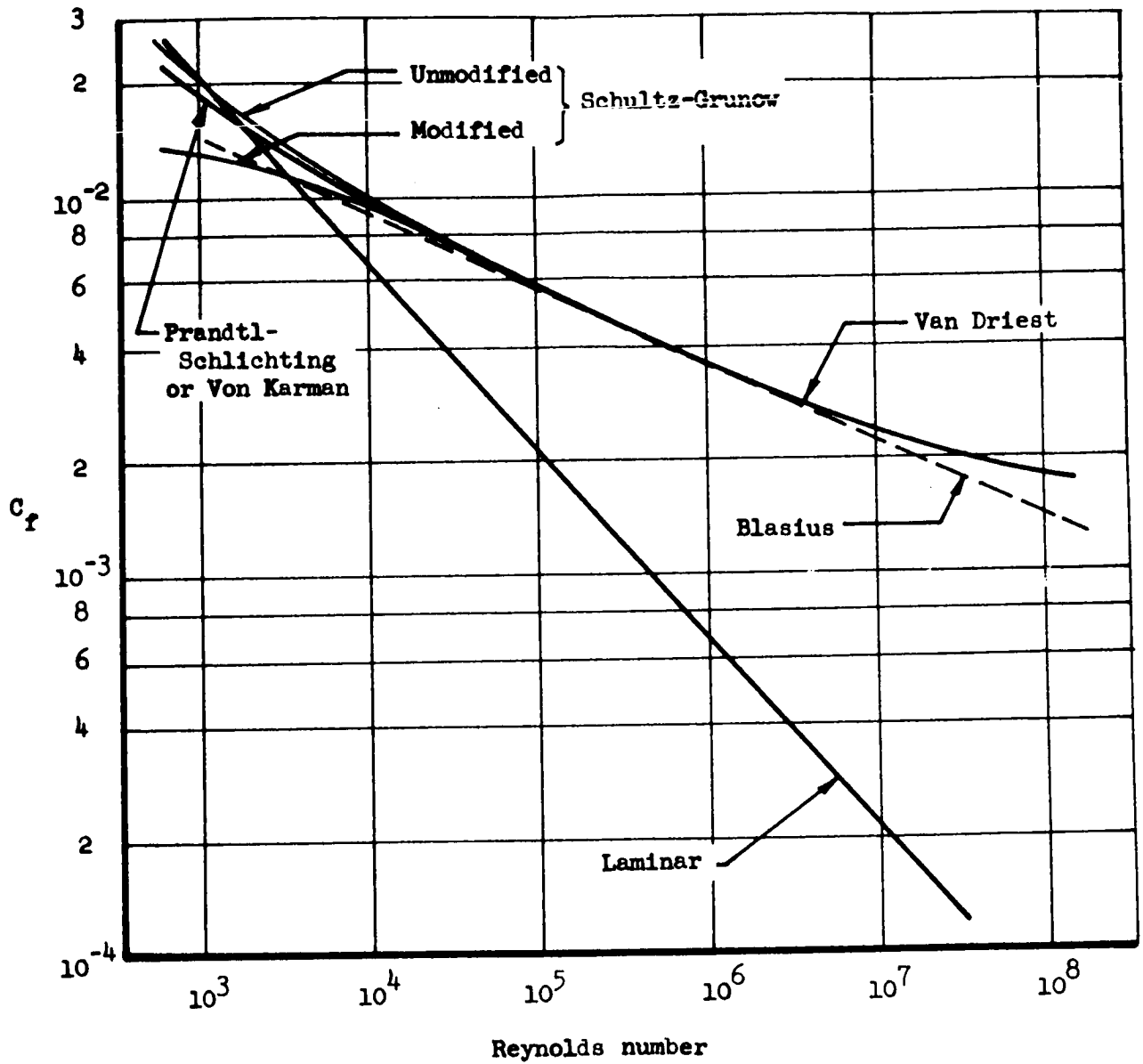


Figure 70.- Comparison of incompressible turbulent skin-friction formulas

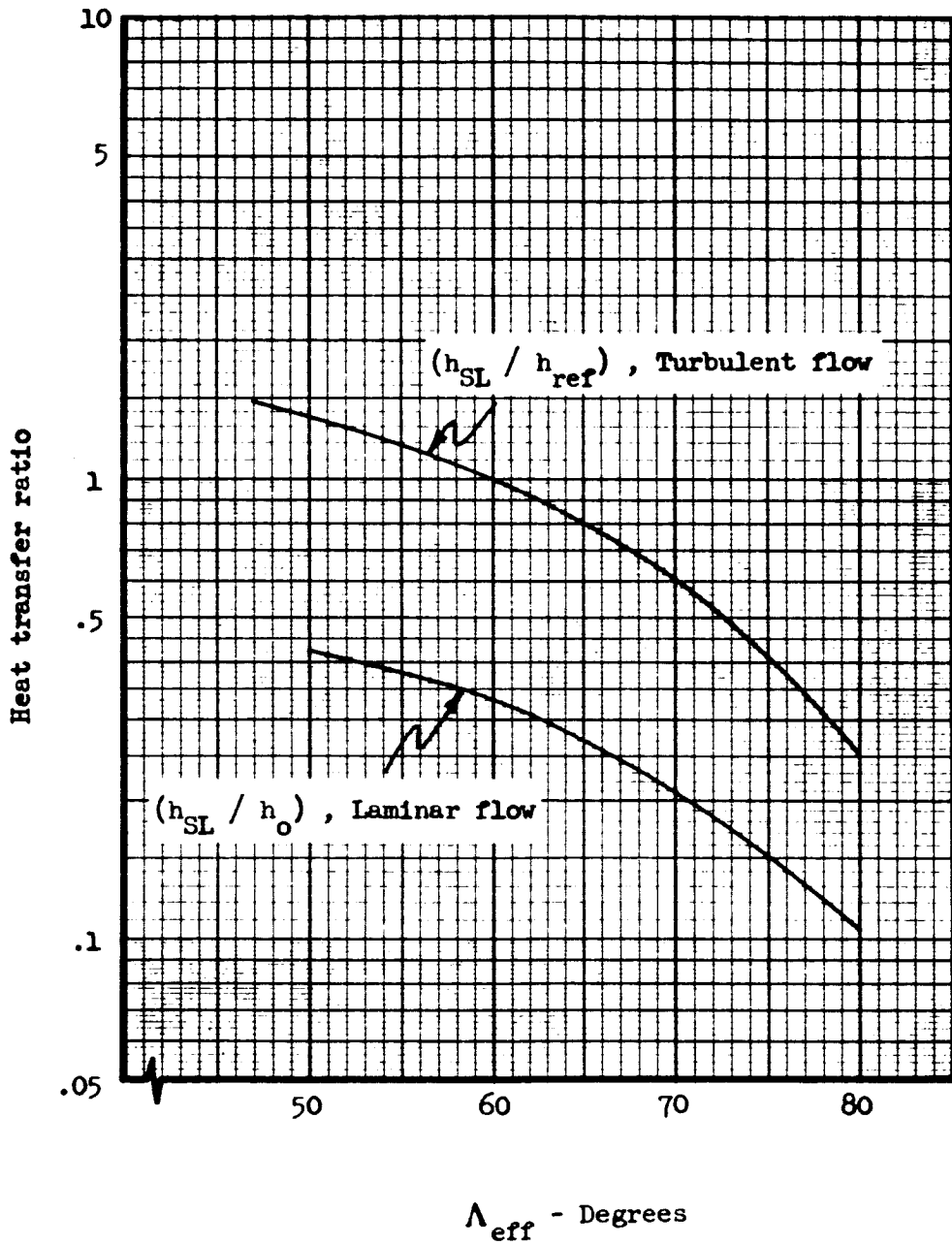


Figure 71.- Infinite cylinder stagnation line heat transfer.

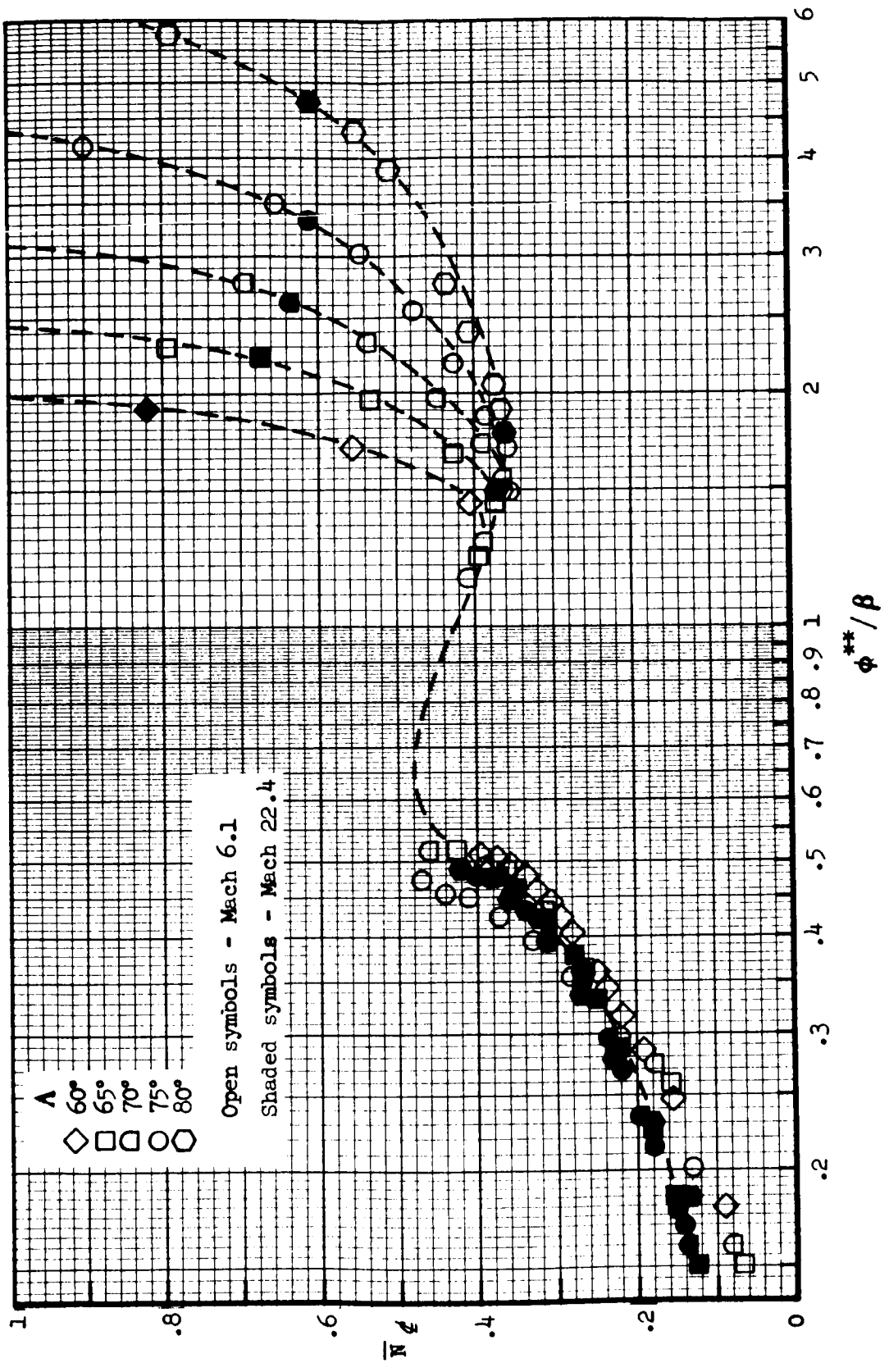


Figure 72.- Streamline Correlation.

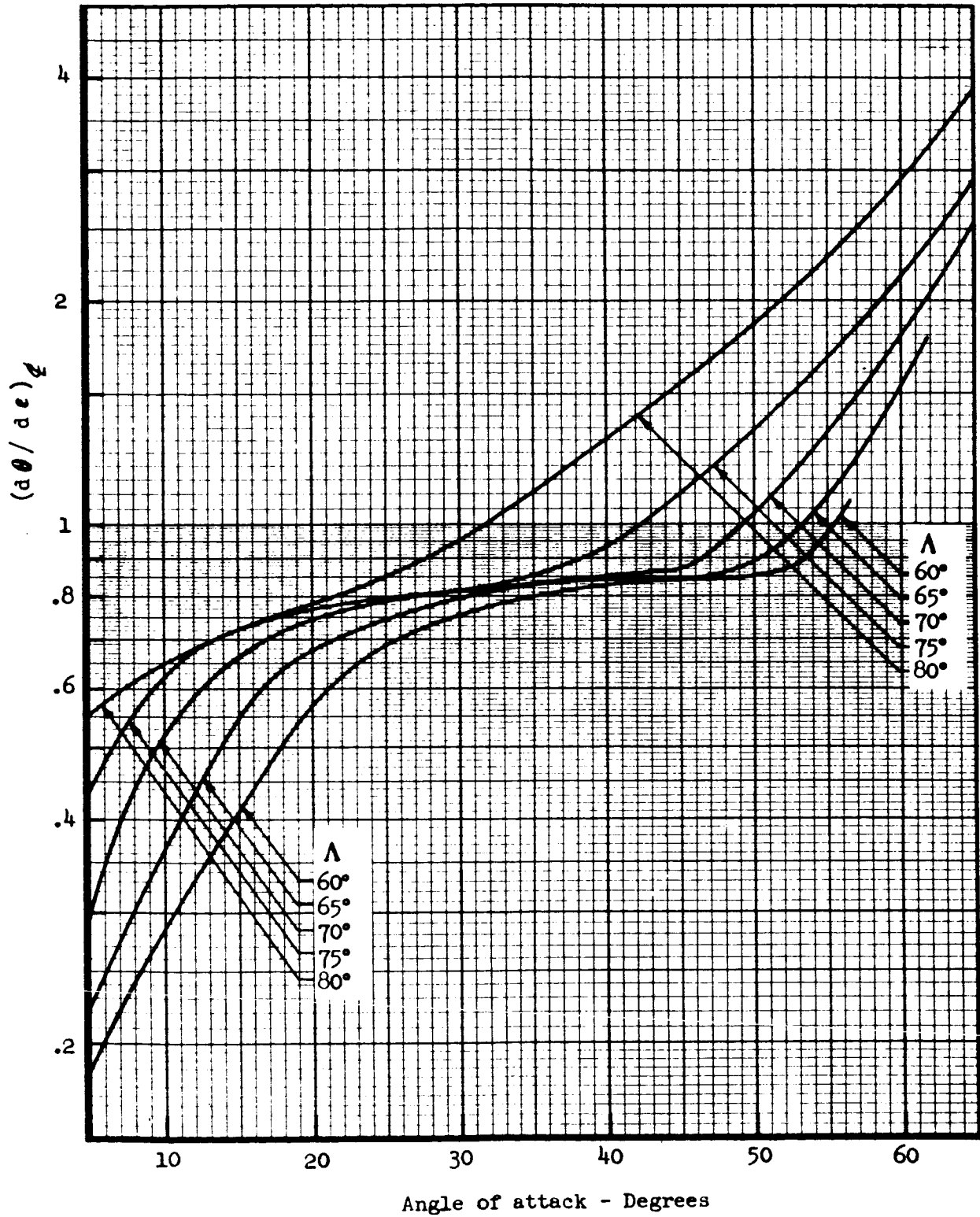


Figure 73.- Rate of change of inviscid streamline angle along the centerline of a sharp delta wing. $M_\infty = 6.1$

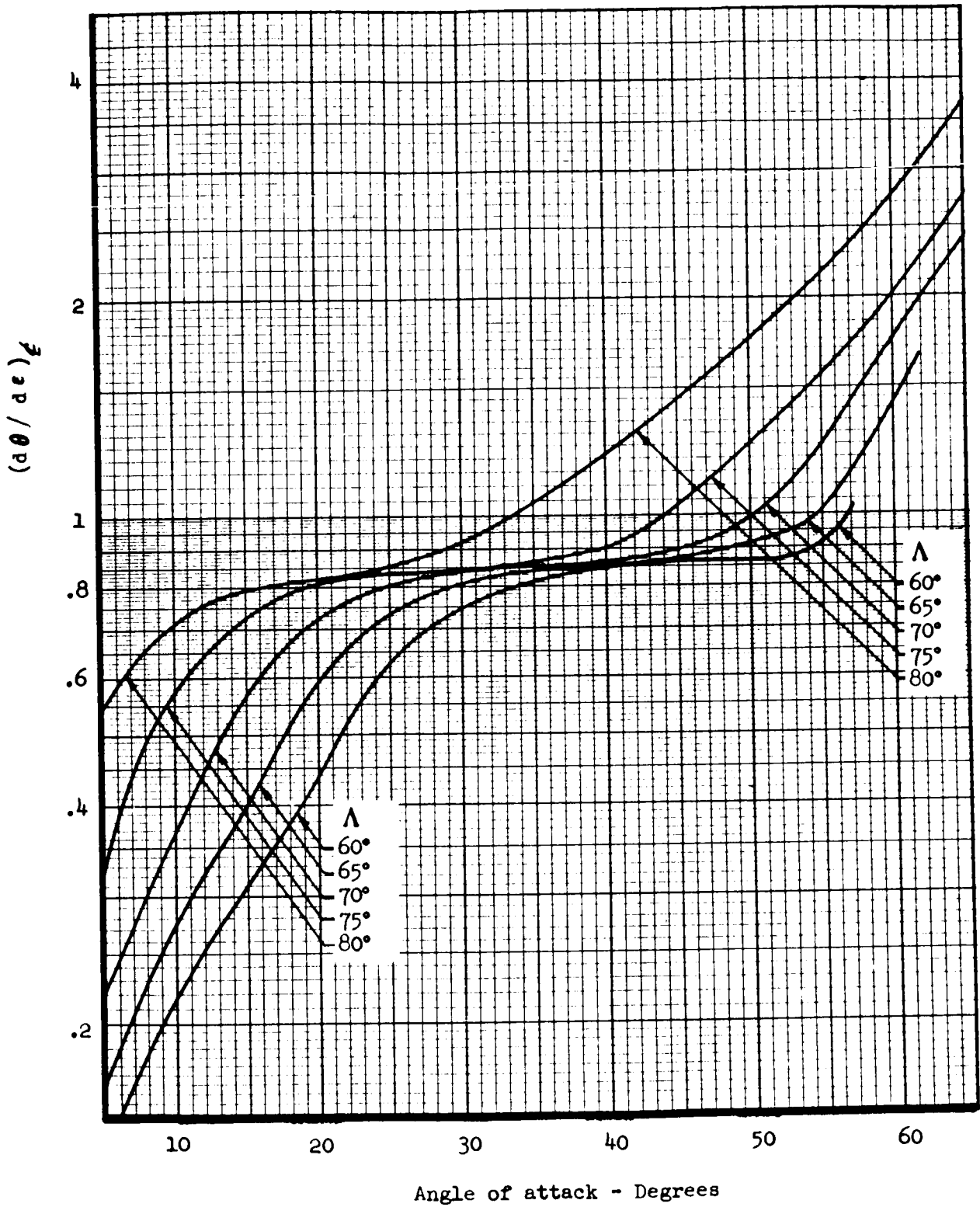


Figure 74.- Rate of change of inviscid streamline angle along the centerline of a sharp delta wing. $M_\infty = 9.6$

REFERENCES

1. Bertram, Mitchel H.; Everhart, Philip E.: An Experimental Study of the Pressure and Heat-Transfer Distribution on a 70° Sweep Slab Delta Wing in Hypersonic Flow, NASA TR R-153, 1963.
2. Whitehead, Allen H.; Dunavant, James C.: A Study of Pressure and Heat Transfer Over an 80° Sweep Slab Delta Wing in Hypersonic Flow, NASA TN D-2708, 1965.
3. Giles, H. L.; Thomas, John W.: Separated and Interfacing Hypersonic Flows for Flat Plates With Flaps and for Delta Wing Body Combinations With Elevons, Fins and Rudders. NASA CR-536, 1966.
4. Jaeck, C. L.: Analysis of Pressure and Heat Transfer Tests on Surface Roughness Elements with Laminar and Turbulent Boundary Layers, NASA CR-537, 1966.
5. Test Facilities Handbook. Arnold Engineering Development Center, 1963.
6. Description and Capabilities. Experimental Facilities Division Hypersonic Shock Tunnel. Cornell Aeronautical Laboratories 1964.
7. Weisblatt, Herbert: Dyna-Soar Real Gas Tests in the AVCO 4.0-inch Diameter Shock Tube. Technical Memorandum RAD-T-M-61-16. 1961.
8. Skinner, G. T.: Analog Network to Convert Surface Temperatures to Heat Transfer. Report No. 100, Cornell Aeronautical Laboratory, Feb. 1960.
9. Vidal, R. J.: Transient Surface Temperature Measurement. Report No. 114, Cornell Aeronautical Laboratory, March 1962.
10. Hodgman, Charles D. ed: Handbook of Chemistry and Physics. Chemical Rubber Publishing, 1957.
11. Giedt, Warren H.: Principles of Engineering Heat Transfer. Van Nostrand, 1957.
12. Eckert, E. R. G.; and Drake, R. M.: Heat and Mass Transfer. Second Edition. McGraw-Hill Book Co., 1959.
13. Busey, R. H.; and Giaouque, W. F.: The Heat Capacity of Nickel from 15 to 300°K. Entropy and Free Energy Functions. J. Am. Chem. Soc., vol. 74, pp. 3157-B.

14. Oelsen, Willy; Rieskamp, Karl Heins; and Oelsea, Olaf.: Thermodynamic Analysis II. The Heat Capacity Curve of a Material from a Single Calorimetric Test. Arch. Eisenhuttenn, vol. 26, pp. 253-66 (Germany).
15. Gregorek, G. M.; Korkan, K. D.: An Experimental Observation of the Mach and Reynolds Number Independence of Cylinders in Hypersonic Flow. AIAA Journal, vol. I, No. 1, January 1963.
16. Zakkay, Victor; Fields, Arthur K.: Pressure Distributions on a Two-Dimensional Blunt-Nosed Body at Various Angles of Attack. PIBAL Report No. 461 (AFOSR TN 58-1016 ASTIA No. AD 162281), Dept. of Aero. Eng. and Applied Mech., Polytech. Inst. of Brooklyn. 1958.
17. Anon: Unpublished Boeing Data
18. Kennet, Haim: The Inviscid Hypersonic Flow on the Windward Side of a Delta Wing. IAS Paper No. 63-55, 1963.
19. Bertram, M. H.: Hypersonic Laminar Viscous Interaction Effects on the Aerodynamics of Two-Dimensional Wedge and Triangular Planform Wings. Prospective NASA Langley Publication.
20. Bertram, Mitchel H.; Blackstock, Thomas A.: Some Simple Solutions to the Problem of Predicting Boundary-Layer Self-Induced Pressures. NASA TN D-798. 1961.
21. Baradell, Donald L.; Bertram, Mitchel H.: The Blunt Plate in Hypersonic Flow. NASA TND-408, 1960.
22. Van Hise, Vernon: Analytic Study of Induced Pressure on Long Bodies of Revolution With Varying Nose Bluntness at Hypersonic Speeds. NASA TR R-78, 1961.
23. Beckwith, E. I.: Similar Solutions for the Compressible Boundary Layer on a Yawed Cylinder with Transpiration Cooling, NACA TN 4345, September 1958.
24. Reshotko, E.: Laminar Boundary Layer with Heat Transfer on a Cone at Angle of Attack in a Supersonic Stream. NACA TN 4152, December 1957.
25. Conti, Raul: Approximate Temperature Distribution and Streamwise Heat Conduction Effects in the Transient Aerodynamic Heating of Thin Skin Bodies, NASA TN D-895, September 1961.
26. Schlichting, Herman: Boundary Layer Theory Fourth Edition, McGraw-Hill Book Co., New York, 1960.
27. Mager, A.: Transformation of the Compressible Turbulent Boundary Layer, Journal of Aeronautical Sciences, vol. 25, No. 5, May 1958, pp. 305-311.

28. Beckwith, I. E.; and Gallagher, J. J.: Local Heat Transfer and Recovery Temperatures on a Yawed Cylinder at a Mach Number of 4.15 and High Reynolds Numbers. NASA Memo 2-27-59L, April 1959.
29. Howarth, L.: Velocity and Temperature Distribution for a Flow Along a Flat Plate. Proc. Roy. Soc., London, 1936.
30. Cohen, C. B.; Reshotko, E. : Similar Solutions for Compressible Laminar Boundary Layer with Heat Transfer and Pressure Gradient, NACA TN 3325, February 1955.
31. Reshotko, E; Beckwith, I. E.: Compressible Laminar Boundary Layer Over a Yawed Infinite Cylinder with Heat Transfer, NACA TN 3986, June 1957.
32. Fay, J. A.; Riddell, F. R.: Theory of Stagnation Point Heat Transfer in Dissociated Air, Research Report No. 1, AVCO Research Laboratory, April 1957.
33. Van Driest, E. R.: Investigation of Laminar Boundary Layer in Compressible Flow Using the Crocco Method, NACA TN 2597, January 1952.
34. Cohen, N. B.: Boundary Layer Similar Solutions and Correlation Equations for Laminar Heat Transfer Distribution in Equilibrium Air at Velocities up to 41,000 Feet Per Second, NASA TR R-118, 1961.
35. Kemp, N. H.; Rose, P. H.; Detra, R. W.: Laminar Heat Transfer Around Blunt Bodies in Dissociated Air, AVCO Research Laboratory, Research Report 15, May 1958.
36. Young, G. B. W.; Janssen, E.: The Compressible Boundary Layer, Journal of Aeronautical Sciences, vol. 19, No. 4, April 1952,
37. Trella, M.; and Libby, P. A.: Similar Solutions for the Hypersonic Laminar Boundary Layer Near A Plane of Symmetry. AIAA Journal, vol. 3, No. 1, January 1965.
38. Vaglio-Laurin, R.: Laminar Heat Transfer on Three-Dimensional Blunt Nosed Bodies in Hypersonic Flow. ARS Journal, vol. 29, No. 2, February 1959.
39. Schultz-Grunow, F.: New Frictional Resistance Law for Smooth Plates. NACA Memorandum No. 986, August 1940.
40. Hanks, R. A.; Savage, R. T.: Thermal Design Methods for Recoverable Launch Vehicles with Consideration of Arbitrary Wall Temperatures and Surface Conditions. Boeing Document D2-90770-1, August 1965.
41. Hansen, C. F.: Approximations for the Thermodynamic and Transport Properties of High Temperature Air. NACA TN 4150, March 1958.